

Evaluation of gas sorption techniques and computational methods utilized in the analysis of porous compounds

by

Dewald Pepler van Heerden

Promoter: Prof. L. J. Barbour

Co-Promoter: Prof. C. Esterhuysen



*Submitted in partial fulfilment of the requirements for the degree
Master of Science*

Department of Chemistry and Polymer Science

Faculty of Science

Stellenbosch University

F gego dgt '2014

DECLARATION

By submitting this dissertation electronically, I Dewald P. van Heerden hereby declare that the entirety of the work contained herein is my own, original work, that I am the owner of the copyright thereof (unless to the extent explicitly stated otherwise) and that I have not previously in its entirety or in part submitted it for obtaining any qualification.

.....
Dewald Pepler van Heerden

Copyright © 2014 Stellenbosch University
All rights reserved

Abstract

A recently proposed mechanism responsible for anomalous thermal expansion in a metal-organic framework (compound **1**) is examined through theoretical calculations. A mechanistic model that reproduces the convergent expansion of the material's coordination spiral is developed. In order to decide on a suitable theoretical method, specifically at the Density Functional Theory (DFT) level of theory, a tricyclicorthoamide that presents a unique nearly-eclipsed methyl group in the solid state (compound **2**) is investigated. Since the anhydrous solid form of this molecule presents with the expected staggered conformation, the nearly-eclipsed conformation is ascribed to the presence of water molecules in the trihydrate form. An evaluation of the potential energy profile for rotation of the methyl group by the *ab initio* wave function methods HF, MP2 and CCSD revealed the global minimum to indeed be the nearly-eclipsed conformation ($\omega_{hccn} \approx 10^\circ$) with a barrier to rotation (ΔE_{rot}) of 1.24 kcal. mol^{-1} located at $\sim 85^\circ$ at the MP2/6-31+G(d) level of theory. The CCSD potential energy profiles also feature a local minimum at $\sim 55^\circ$ that is ascribed to a dispersive intramolecular interaction. Since the Kohn-Sham implementation of DFT functionals ignores the dynamic electron correlation required to describe dispersion, semi-empirical dispersion-correction schemes to the density-dependent energy are evaluated.

The mechanistic model describing the thermal expansion of **1** is evaluated with the B3LYP (hybrid GGA) and M06 (hybrid meta-GGA) density functionals augmented by the GD2 and GD3 dispersion correction schemes, respectively, in addition to the dispersion-corrected ω B97XD (LC-hybrid GGA) functional in conjunction with various basis sets. The resulting energy trends are found to compare favorably to the four energies obtained by periodic DFT evaluations of the 100, 190, 280 and 370 K crystal structures of **1**.

The thermodynamic data for carbon dioxide adsorption measured on a previously constructed in-house volumetric isosteric sorption technique (SIT) device are compared to those obtained through conventional gravimetric instrumentation. Two metallocyclic compounds (**3** and **4**) that maintain their crystallinity upon generation of the porous apohost, are evaluated. A comparison of the various methodologies that exist in the literature to determine isosteric heats of adsorption (Q_{st}) from adsorption isotherms are presented. In particular, the temperature-dependent dual-site Langmuir and virial-type isotherm equations are compared for the first time and found to be complementary. The Q_{st} values at zero occupancy are determined to be 29.2 and 35.5 kJ. mol^{-1} for compounds **3** and **4**, respectively, and trends in Q_{st} as a function of occupancy plots are accounted for.

Uittreksel

'n Meganisme wat onlangs voorgestel is om die buitengewone termiese uitsetting van 'n metaal-organiese raamwerk (verbinding **1**) te verduidelik, word ondersoek deur teoretiese berekening. 'n Meganistiese model wat die konvergente uitrekking van dié materiaal se koördinasie spiraal naboots word ontwikkel. Om op 'n gepaste teoretiese metode te besluit, spesifiek op die dighteidsfunksionaliteit (DFT) vlak, is 'n trisikliesorto-amied wat 'n metiel groep in die amper-versteekte konformasie in die vaste fase toon (verbinding **2**) ondersoek. Aangesien die anhidriese vaste-vorm van hierdie molekuul die verwagte verspringde konformasie besit, word die amper-versteekte konformasie aan die teenwoordigheid van water molekules in die trihidraat toegeskryf. 'n Evaluering van die potensiële energie profiel vir rotasie van die metiel groep met behulp van die *ab initio* golffunksie metodes HF, MP2 en CCSD het tentoongestel dat die globale minimum inderdaad die amper-versteekte konformasie is ($\omega_{hccn} \approx 10^\circ$) met 'n hindernis tot rotasie (ΔE_{rot}) van $1.24 \text{ kcal.mol}^{-1}$ geposisioneer by $\sim 85^\circ$ by die MP2/6-31G(d) vlak van teorie. Die CCSD potensiële energie profiele beskik ook oor 'n lokale minimum by $\sim 55^\circ$ wat aan 'n dispersie intramolekulêre interaksie toegeskryf word. Aangesien die Kohn-Sham implementering van (DFT) funksionale die dinamiese elektronkorrelasie wat nodig is om dispersie te beskryf, ignoreer, word semi-empiriese dispersie-korreksie metodes tot die dighteidsafhanklike energie ondersoek.

Die meganistiese model wat die termiese uitsetting van **1** beskryf word met die B3LYP (hibried GGA) en die M06 (hibried meta-GGA) digtheidsfunksionale, onderskeidelik met die GD2 en GD3 dispersie korreksie metodes aangevul, asook die inherente dispersiegekorigeerde ω B97XD (LC-hibried GGA) funksional in kombinasie met verskeie basisstelle ondersoek. Die verkrygde energietense vergelyk goed met die vier energieë verkry deur evaluering van die 100, 190, 280 en 370 K kristal strukture van **1** met behulp van periodiese DFT.

Die termodinamiese groothede vir koostofdioksied adsorpsie, voorheen bepaal op 'n tuis-ontwerpte volumetriese sorpsie isosteriese tegniek (SIT) toestel, word met dié verkry deur konvensionele gravimetriese instrumentasie vergelyk. Twee metaalsikliese verbinding (3 en 4) wat hul kristalliniteit behou tydens ontwikkeling van die poreuse apo-vorm, is geëvalueer. Verskeie metodologië wat gebruik word om die isosteriese hitte van adsorpsie (Q_{st}) vanaf adsorpsie isoterme te bepaal word vergelyk. Meer spesifiek word die temperatuur-afhanklike twee-setel Langmuir- en die viriale-tipe isotermsvergelykings vergelyk vir die eerste keer, en hul word as komplementêr beskou. Die Q_{st} waardes by nul-besetting word as 29.2 en 35.5 kJ.mol^{-1} onderskeidelik vasgestel vir verbinding 3 en 4, en tendense in die Q_{st} as 'n funksie van besetting kurwes word omskryf.

Acknowledgements

I would like to thank my supervisors, Prof. Leonard J. Barbour and Prof. Catharine Esterhuyzen, for the insightful discussion and guidance during the course of this study. Thank you for giving me the opportunity to conduct research in a group where dogmas are challenged and free-thinking scientists are moulded. I am looking forward to continuing my academic career under your supervision.

Thank you to all the members (past and present) of the Supramolecular Materials Group at Stellenbosch University for all the help you provided throughout this study.

A special thanks to my family for their love and support during this turmoil.

Finally, I wish to thank Stellenbosch University, the NRF and the Harry Crossley Foundation for funding.

Glossary

List of abbreviations and general symbols

ΔE_{rot}	Barrier to rotation
BSSE	Basis Set Superposition Error
QEeq	Charge equilibration
cp	Counterpoise scheme
$C_{AB,n}$	n^{th} -order isotropic dispersion coefficient of atom-pair AB
CCSD	Coupled Cluster with Single and Double excitations
DFT	Density Functional Theory
DF	Density functional
DIIS	Direct Inversion in an Iterative Subspace
ECP	Effective Core Potential
ΔH_{ad}	Enthalpy of adsorption
GD2	Grimme's second generation DFT-D
GD3	Grimme's third generation DFT-D
GD3BJ	GD3 with Becke-Johnson damping
HF	Hartree-Fock
Q_{st}	Isosteric heat of adsorption
GGA	Generalized Gradient Approximation
KS	Kohn-Sham
LC	Long-range Corrected functional
lr	Long-range
LSDA	Local Spin-Density Approximation
MD	Molecular Dynamics
MM	Molecular Mechanics
MOF	Metal-Organic Framework
MP2	Møller-Plesset perturbation theory with second order corrections
NTE	Negative Thermal Expansion
PTE	Positive Thermal Expansion
SCF	Self-Consistent Field
SIT	Sorption Isosteric Technique
sr	Short-range
TS	Dispersion-correction scheme of Tkatchenko and Scheffler

List of key symbols in theoretical methods overview (Chapter 2)

\vec{r}_i	Three dimensional spatial vector of electron i
\vec{s}_i	Spin of electron i
\vec{x}_i	Four dimensional state vector of electron i
$\Psi_e(\mathbf{r})$	Electronic Schrödinger wave function of a system
\mathbf{r}	Three dimensional space
$\phi_i(\vec{x}_i)$	Spin orbital i
$\varphi_A(\vec{r}_A)$	Spatial orbital a
$\sigma_i(s_i)$	Spin function, α or β
$\chi_\beta(\vec{r}_i)$	Basis function β of spatial orbital i : $\varphi_i(\vec{r}_i)$
$\chi_\alpha(\vec{r}_A)$	Basis function α of complex conjugate of spatial orbital i : $\varphi_i^*(\vec{r}_i)$
ε_i	Pseudo-energy of Fock operator
ρ_σ	σ -spin charge-density
$\nabla\rho_\sigma$	Gradient of charge-density
g_σ	Gradient correction factor
s_σ	Reduced spin-density gradient
u_σ	Remapped gradient correction
τ_σ	Kinetic energy chargedensity
$\vartheta_i(\vec{x}_i)$	Kohn-Sham spin orbital i
$\epsilon_{xc}(\rho_\sigma)$	Exchange-correlation energy density
c_x	Coefficient reserved for the fraction of exact exchange

Table of Contents

Declaration	i
Abstract	ii
Uittreksel	iii
Acknowledgments	vi
Glossary	v
Chapter 1: Introduction	1
1.1 Theoretical considerations: DFT and the dispersion interaction	2
1.2 Thermal expansion	5
1.3 Isosteric heat of adsorption, Q_{st}	8
1.4 Aims and objectives	9
1.5 Outline	9
1.6 References	11
Chapter 2: Overview of theoretical methods	14
2.1 Quantum Mechanics	14
2.1.1 The Schrödinger equation	15
2.1.2 The Born-Oppenheimer approximation	16
2.1.3 Introducing electron spin and indistinguishability	17
2.1.4 The energy of a Slater determinant	18
2.1.5 The variational principle	19
2.1.6 The Hartree-Fock (HF) approximation	19
2.1.7 HF energy of a closed-shell system	20
2.1.8 The basis set approximation and Roothaan-Hall Equations	21
2.1.9 The SCF procedure	23
2.2 Density Functional Theory (DFT)	24
2.2.1 Electron density and the Hohenberg-Kohn theorems	24
2.2.2 The Kohn-Sham (KS) approach	25
2.2.3 Exchange-correlation energy	27
2.2.4 Hybrid functionals	28
2.2.5 Generalized Gradient Approximation functionals; Becke's systematic optimization procedure	29
2.3 The dispersion interaction	32
2.4 Grimme's B97D functional	33
2.4.1 The exchange-correlation functional	33
2.4.2 The GD2 dispersion-correction scheme	34
2.5 Explicit long-range correction	35
2.5.1 The partitioned Coulomb operator	35
2.5.2 The ω B97X functional	37

2.5.3	The dispersion-corrected ω B97XD functional	39
2.6	Non-empirical dispersion correction	39
2.6.1	The GD3 dispersion-correction scheme	40
2.6.2	The dispersion-correction scheme of Tkatchenko and Scheffler	43
2.7	Summary	44
2.8	References	45
Chapter 3: Materials and methods		47
3.1	Molecular graphics	47
3.2	Compounds investigated	48
3.2.1	[Zn(4-(1 <i>H</i> -naphtho[2,3- <i>d</i>]imidazole-1-yl)benzoic acid)(OH)] _n ·nCH ₃ OH	48
3.2.2	[Cd ₂ (4,4'-bis(2-methylimidazol-1-ylmethyl)-1,1'-biphenyl) ₂ Cl ₄]	50
3.2.3	[Cu ₂ (1,3-bis(imidazol-1-ylmethyl)-2,4,6-trimethylbenzene) ₂ Cl ₄]	51
3.3	Volumetric Sorption Isosteric Technique (SIT) device	53
3.3.1	Adsorption to equilibrium: isothermal experiment	54
3.3.2	Determining thermodynamic parameters: isochoric temperature ramp	55
3.4	Gravimetric gas adsorption	55
3.5	Models and their internal coordinates	55
3.6	Definitions of internal coordinates	56
3.7	VB Script for generating a Z-matrix	59
3.7.1	Reading in Atom1-Number, -type, and XYZ coordinates	60
3.7.2	Determination of Atom2	60
3.7.3	Determining dihedral angle <i>W1234</i>	62
3.7.4	Identifying <i>unique</i> dihedral angles	63
3.8	Anisotropic thermal expansion mechanistic model	64
3.9	Density functionals and basis sets	69
3.10	Summary	69
3.11	References	70
Chapter 4: Investigation of eclipsed methyl in the solid state		73
4.1	Background	75
4.2	CCSD investigation	76
4.3	Comprehensive model of 2·3H ₂ O	78
4.4	Comparison of basis set performance at the HF level of theory	79
4.5	Comparison of different DFT methods using various basis sets	82
4.5.1	Oscillations in potential energy surfaces of meta-GGAs	83
4.5.2	Potential Energy profiles of dispersion-corrected B97D and ω B97XD	84
4.6	Møller-Plesset perturbation theory with 2 nd order corrections (MP2)	85

4.7	Eliminating the BSSE: the counterpoise scheme	87
4.8	Choice of dispersion correction scheme	89
4.9	Summary	91
4.10	References	92
Chapter 5:	Anisotropic thermal expansion in a MOF	94
5.1	Vibrational origin of thermal expansion	94
5.1.1	Bond-stretching effect	95
5.1.2	Tension effect	95
5.1.3	Bond-rotation effect	96
5.1.4	Rigid bonds	96
5.2	Anisotropic thermal expansion in a MOF	97
5.2.1	Comparison to mechanistic model	99
5.2.2	Considerations for theoretical modelling	100
5.3	Investigation of the crystal structure of 2·3H ₂ O	101
5.3.1	Molecular Mechanics investigation of 2·3H ₂ O	101
5.3.2	DFT-D investigation of the crystal structure and minimal model of 2·3H ₂ O	104
5.4	Molecular Dynamics (MD) on MOF 1 _{apo}	106
5.5	Mechanistic model for anisotropic thermal expansion in 1 _{apo}	107
5.6	Summary	110
5.7	References	111
Chapter 6:	Adsorption techniques and methodologies	112
6.1	Isotherm models	112
6.2	Thermodynamic parameters of adsorption	113
6.3	Volumetric SIT study of CO ₂ sorption on compounds 3 and 4	115
6.4	The isosteric heat of adsorption	117
6.4.1	Graphical interpolation of gravimetric CO ₂ adsorption data	118
6.4.2	Temperature-dependent dual-site Langmuir (dsL) adsorption equation	121
6.4.3	The virial-type isotherm equation	122
6.5	Global fits to gravimetric data for CO ₂ sorption on 3 and 4	123
6.6	Discussion	124
6.7	Summary	126
6.8	References	127
Chapter 7:	Concluding remarks	128
Appendix A.	Supplements to discussions in order of appearance in main-text	A.1
A.1	Addendum to Chapter 3	A.1
A.1.1	Calibration of volumetric SIT device	A.1
A.1.2	VB script for determining internal coordinates	A.3

A.1.3	Derivation of key equations for mechanistic thermal expansion model	A.9
A.2	Addendum to Chapter 4	A.11
A.2.1	Utility of Dummy atoms	A.11
A.2.2	CCSD investigation	A.12
A.2.3	Basis set dependence of potential energy profile for the B97D functional	A.13
A.2.4	Integration-grid effects on DFT potential energy profiles	A.14
A.2.5	The counterpoise correction for BSSE	A.15
A.2.6	BSSE of the minimal model at the MP2 and HF levels of theory	A.16
A.2.7	B97D in conjunction with GD2, GD3 and GD3BJ potential energy profiles	A.19
A.3	Addendum to Chapter 5	A.22
A.3.1	Comparison of variable temperature 1_{apo} crystal structures	A.22
A.3.2	Perl Scripts to scan the W_{hccn} dihedral angle in $2\cdot3\text{H}_2\text{O}$	A.23
A.3.3	Additional evaluations of mechanistic model	A.25
A.4	Additional fittings to gravimetric sorption data	A.26
Appendix B.	Contents of Supplementary DVD	B.1

Chapter 1: Introduction

A sharp increase in atmospheric carbon dioxide levels from anthropogenic emissions is of great concern due to its harmful effects on the environment. The current energy sector is almost entirely based on the burning of fossil fuels¹ and a shift in global infrastructure toward cleaner and sustainable energy sources is crucial. However, such a transition will take many years to accomplish and present efforts are focussed on mitigation of rising atmospheric levels through capture and storage of CO₂.²

Captured CO₂ is subjected to permanent sequestration in geological formations such as coal seams, salt water aquifers and depleted oil and gas reservoirs.³ A handful of such sequestration projects are in progress with the European Commission funded RECOPOL project already completed. Over the period August 2004 to June 2005 760 metric tons of CO₂ was injected into the Upper Silesian Coal Basin (near Kaniow, Poland) and observation is ongoing to establish long-term effects.⁴

The enthalpy of adsorption, ΔH_{ad} , is a measure of the affinity of an adsorbent for an adsorbate and, in the current context, can be used to predict the performance of a material in CO₂ capture. A large ΔH_{ad} value is required to ensure a high selectivity, but the enthalpy of adsorption must not be too large so as to impair regeneration of the adsorbent. Existing CO₂ capture technologies based on aqueous alkanolamide solutions (amine scrubbing)⁵ consume as much as 40% of the energy output of a power plant.² The mechanism of CO₂ capture involves the formation of a C-N bond⁶ and the enthalpy of adsorption was indeed found to fall in the chemisorption (as opposed to physisorption) regime of -50 to -100 kJ.mol⁻¹.⁷ High temperatures, the source of the large energy penalty, are therefore required to evolve CO₂ from these solutions.

The transport sector is responsible for 23% of energy-related CO₂ emissions.¹ However, alternatives to petroleum such as natural gas (consisting mainly of CH₄) and hydrogen is still not viable for reasons regarding the safe and efficient storage and release of these gases. Current technology based on compression or liquefaction (requiring cryogenic cooling in addition to compression) is not economically feasible and entails complex fuel-tanks (with heat-insulation to prevent boil-off) and expensive operating machinery.

A workable solution to the above stated problems is to use adsorbents packed into light-weight, conformable fuel-tanks or large-scale stationary reservoirs for the selective capture and transient storage of adsorbates at moderate temperature and pressure conditions. Porous solids retain gases by physisorption, a non-activated process that warrants the fast and reversible association of an adsorbate on the surface or inside a pore of an adsorbent through weak van der Waals forces such as dispersion and induction.⁸

Chapter 1: Introduction

The water susceptibility of zeolites and the limited capacity of activated carbons have made investigation of metal-organic frameworks (MOFs) a topical research area for gas storage and separation. The seemingly unlimited potential architectures, topologies and pore sizes attainable with MOFs allows for the development of porous structures that are fine-tuned for specific applications.⁹ Control over functionalities within the pores of MOFs enables an optimal ΔH_{ad} to be achieved that maintains high selectivity, but reduces the energy required to regenerate the evacuated adsorbent.

However, it is still difficult to predict the properties of a MOF resulting from a particular choice of organic linker(s) and metal salt(s), or even if a MOF will be obtained.¹⁰ An alternative is post-synthetic modification of an existing MOF to enhance the adsorption performance thereof.¹¹ Zhang *et al.*, for example, recently found an increased CO₂ capacity and larger CO₂/N₂ selectivity in ethylenediamine treated ZIF-8 ([Zn(2-methylimidazole)₂]_n, first reported by Yaghi and coworkers),¹² labelled ED-ZIF-8.¹³ Another advantage of the post-synthetic modification approach is that functional groups that might interfere with the crystallization process can be introduced after the framework scaffold has been formed.¹⁴

Determination of the enthalpy of adsorption allows for a greater understanding of an adsorption system and prediction of its industrial performance. The differential enthalpy of adsorption can be measured directly with a Tian-Calvet type microcalorimetry apparatus.¹⁵ However, due to its low value for physisorption (typically -25 to -60 kJ.mol⁻¹ for CO₂,¹⁶ -15 to -25 kJ.mol⁻¹ for CH₄¹⁷ and -5 to -12 kJ.mol⁻¹ for H₂,¹⁸ at zero coverage) ΔH_{ad} is usually determined indirectly from fitting of physisorption models to adsorption isotherms.

In the next section a brief introduction to the field of DFT, commonly used to predict properties of MOFs, is given, followed by a discussion of key concepts concerning the thermal expansion behavior of solids. The isosteric heat of adsorption, Q_{st} , commonly used to approximate ΔH_{ad} by assuming ideal gas behavior and temperature invariance, is discussed, followed by a summary of the aims and objectives of this work. The chapter concludes with an outline of this dissertation.

1.1 Theoretical considerations: DFT and the dispersion interaction

The weakly attractive, ubiquitous dispersion interaction (London force) is an important ingredient of the total energy of attraction between species. Although it is only dominant for inert gas solids and the crystalline phases of many organic molecules, the dispersion interaction is indispensable for obtaining the correct shape of the potential energy surface.¹⁹ It also plays an important role in the description of many physical and chemical phenomena such as adhesion, surface tension, physical adsorption, the secondary structures of biomolecules,²⁰ crystal packing, and the orientation of molecules on surfaces or in molecular films.²¹ In the guise of π - π stacking interactions, dispersion is paramount in the reversible DNA binding of intercalation anti-cancer drugs²² and the conductivity of self-assembling carbon nanowires.²³

Chapter 1: Introduction

Dispersion is a consequence of correlated fluctuations in nonoverlapping (widely separated) electron densities and can be thought of as a multitude of fleeting dipole-dipole interactions that result from the instantaneous shift of the electron densities of neighboring polarizable species in the same direction.²⁴ Highly correlated wave function methods, wherein electrons are simultaneously excited into virtual orbitals, are required to successfully describe dispersion. Due to the poor scaling of such high levels of theory with the size of a system, Density Functional Theory (DFT) provides a viable alternative to move beyond the Hartree-Fock (HF) approximation, the most basic Quantum Mechanics method.

In DFT the electronic energy is expressed as a function of charge density ρ_σ ($\sigma = \alpha$ or β to represent up- or down-spin). However, although proven to exist,²⁵ the exact relation between the ground-state density and ground-state energy remains elusive. In the rudimentary spin-density approximation (LSDA), density functionals are only dependent on ρ_σ . Generalized gradient approximation functionals (GGAs) are, in addition, dependent on the gradient of the charge density, $\nabla\rho_\sigma$, to move beyond a uniform electron gas approximation. Further improvements in the performance of functionals has been found by including a dependence on the spin kinetic-energy density, τ_σ , to yield so-called meta-GGAs. However, LSDAs, GGAs, and meta-GGAs are all *local* functionals because they only use information at, or near to, a single spatial point. Since dispersion is a consequence of dynamic electron-correlation, it is entirely nonlocal and successes achieved by these functionals are mainly due to a cancellation of errors.²⁶ As justified by the adiabatic connection theory, admixture of nonlocal HF exchange,²⁷ producing *hybrid* functionals, have been found to make density functionals (DFs) more accurate than *pure* functionals for main-group thermochemistry.²⁸

The accurate modelling of dispersion remains a challenging problem for DFT.²⁹ In a recent assessment of popular DFs, including GGAs, meta-GGAs, and hybrid functionals, Johnson *et al.* found all DFs to be incapable of describing van der Waals dimers when compared to results at the CCSD(T) level of theory.³⁰ Several groups have developed fundamental approaches for the modelling of dispersion by DFT.³¹ However, due to the complexity of these methods, the most widely used approach is the robust DFT-D scheme developed by Grimme wherein an empirical dispersion correction is added to the density-dependent energy at negligible additional computational cost.³² Various DFT-D schemes are discussed in Chapter 2 and results obtained with their application compared in subsequent chapters of this study.

Chapter 1: Introduction

The importance of the choice of dispersion-correction scheme was recently highlighted by a computational analysis of 1,1-diamino-2,2-dinitroethelene (FOX-7,³³ monoclinic $P2_1/n$ ($Z = 4$); asymmetric unit comprises one $(\text{NH}_2)_2\text{CC}(\text{NO}_2)_2$ molecule) by Appalakondaiah *et al.* who used the CASTEP code[†] to calculate the ground state geometry of FOX-7.³⁷ In FOX-7 there are two intramolecular nitro-amino hydrogen bonds that render the molecules planar, while they pack in infinite two-dimensional wave-shaped layers that are extensively hydrogen bonded.[‡] These layers pack in an *ABAB* fashion along [010] with only weak van der Waals interactions between them.³³

The PW91PW91 functional,³⁸ for which the Ortmann, Bechstedt and Schmidt dispersion-correction scheme (OBS)³⁹ is available, and the PBEPBE functional,⁴⁰ for which Grimme's DFT-D2 (GD2)^{32b} and the Tkatchenko and Scheffler (TS)⁴¹ dispersion-correction schemes are available, were assessed. Appalakondaiah *et al.* found that the standard DFs underestimate the density of FOX-7 mostly due to a large overestimation of the b unit cell parameter, due to an inability to correctly model the dispersion interactions between stacked layers. Application of the DFT-D schemes greatly improves the situation with the errors in unit cell volume (+28.4% and +26.8% for the PW91PW91 and PBEPBE, respectively) reduced to -0.6%, +2.7%, and -0.1% for PW91PW91+OBS, PBEPBE+TS and PBEPBE+GD2, respectively. Further investigations of structural and vibrational properties of FOX-7 under hydrostatic pressure using PBEPBE+GD2 showed accurate agreement with experiment, whereas the standard GGA functionals (and the LDA)[§] failed to reproduce observed trends.

[†] CAmbridge Serial Total Energy Package, or CASTEP, is a Quantum Mechanics first-principle code that uses plane-wave representations to model the electron density of periodic structures with pseudopotential approximations to inner electrons.³⁴ Appalakondaiah *et al.* employed ultrasoft pseudopotentials³⁵ with a plane wave kinetic energy cutoff of 540 eV and sampled the first Brillouin zone with a Monkhorst-Pack³⁶ grid of minimum spacing 0.04 Å⁻¹.³⁷

[‡] Here follows a list of the hydrogen bond geometries, $d_{N \cdots O}$ and $\theta_{N-H \cdots O}$, of the two intramolecular hydrogen bonds, and the six independent intermolecular hydrogen bonds separated by direction. Intramolecular hydrogen bond geometries: (1) $N_a\text{-H} \cdots O_a$, 2.608(2) Å, 128.8(19)°; (2) $N_b\text{-H} \cdots O_b$, 2.636(2) Å, 128.8(19)°. Intermolecular hydrogen bond geometries in direction-1: (1) $N_a\text{-H} \cdots O_c^i$, 3.000(2) Å, 156(2)°; (2) $N_b\text{-H} \cdots O_d^i$, 2.901(2) Å, 146(2)°. Intermolecular hydrogen bond geometries in direction-2: (1) $N_a\text{-H} \cdots O_b^{ii}$, 3.012(2) Å, 117.7(18)°; (2) $N_a\text{-H} \cdots O_d^{ii}$, 3.009(2) Å, 140.3(19)°; (3) $N_b\text{-H} \cdots O_c^i$, 3.191(2) Å, 147(2)°; (4) $N_b\text{-H} \cdots O_a^{iii}$, 3.026(2) Å, 136(2)°. Symmetry codes: (i) $x - \frac{1}{2}, \frac{1}{2} - y, z - \frac{1}{2}$; (ii) $\frac{1}{2} + x, \frac{1}{2} - y, z - \frac{1}{2}$; (iii) $x - 1, y, z$.

[§] Appalakondaiah *et al.* evaluated the local density approximation (LDA) in the Perdew-Zunger parameterization⁴² of results from Monte Carlo simulations carried out by Ceperley and Alder.⁴³

1.2 Thermal expansion

Most solids expand in all three dimensions upon an increase in temperature, that is, undergo positive thermal expansion (PTE).⁴⁴ Each atom i vibrates about its mean position $\langle \mathbf{r}_i \rangle$, and, as the amplitudes of vibration increase with increasing temperature, the anharmonic nature of interatomic potential wells causes distances between these mean positions to increase.⁴⁵ At the macroscopic level this manifests as an increase in volume.⁴⁶ The linear and volumetric coefficients of thermal expansion are defined as $\alpha = \frac{\Delta L}{l_0 \Delta T}$ and $\beta = \frac{\Delta V}{V_0 \Delta T}$, respectively, where ΔL represents the change in length and ΔV the change in volume from initial values l_0 and V_0 , respectively, over a temperature increment ΔT .⁴⁴ Isotropic solids (with cubic symmetry) have $\beta = 3\alpha$, but the situation is more complicated in the case of anisotropic solids where the linear expansion in the three orthogonal directions can be of different magnitudes and/or signs.⁴⁶

It is important to distinguish between *apparent* and *true* bond distances. The apparent bond length is the distance between the mean position of two atoms: $d_{app} = |\langle \mathbf{r}_2 \rangle - \langle \mathbf{r}_1 \rangle|$.⁴⁴ This is the distance obtained from X-ray diffraction data whereby atoms undergoing thermal motion are located by maxima in the electron density distribution.⁴⁷ The true bond length, on the other hand, is the mean distance between atoms, $d_{true} = |\langle \mathbf{r}_2 - \mathbf{r}_1 \rangle|$, and can, for example, be obtained from radial distribution functions from extended X-ray absorption fine-structure data.* Since components of motion perpendicular to the bond only affect the apparent bond length, d_{app} is always shorter than d_{true} . Negative thermal expansion, or a decrease of d_{app} with increasing temperature, can therefore still occur even when d_{true} increases with increasing temperature.

Elucidation of the mechanism of thermal expansion could provide insight into the design of thermo-responsive materials for use in sensors and actuators. The supramolecular structure of a solid is potentially the determining factor responsible for its thermal behavior.⁴⁶ Rubber, for example, shows negative thermal expansion (NTE) due to an increase in the amplitude of thermal vibrations perpendicular to the *n*-alkane chains. These vibrations cause the chains to shorten, and, because rubber is amorphous, this NTE is isotropic.⁴⁸ The majority of structures that are known to exhibit NTE feature the planar M-O-M linkage.⁴⁶ To exhibit NTE, vibration modes transverse to the linkage must outweigh those occurring along it, resulting in a decrease in the effective M···M distance – the so-called “guitar string” effect.⁴⁸⁻⁴⁹

* In gas-phase electron-diffraction experiments the true bond length, r_g , is calculated from the measured apparent bond length (r_a) by incorporating spectroscopic amplitude (u , mean-square amplitude of vibration) and shrinkage ($D = r_a - r_g$) corrections: $r_a = r_g - (u^2/r)$.

Chapter 1: Introduction

Isotropic NTE has been identified in the intensely studied MOF-5⁵⁰ ($[Zn_4O(1,4\text{-benzenedicarboxylate})_3]$, cubic crystal system, $Fm\bar{3}m$, $a = 25.6690(3)$ Å).⁵¹ This three dimensional framework is composed of aromatic rings linking tetranuclear $Zn_4O(COO)_6$ clusters, wherein each zinc atom is bonded to three carboxylate oxygen atoms and a central oxygen dianion in a distorted tetrahedral fashion. Dubbeldam *et al.* successfully reproduced the observed NTE behavior through Molecular Dynamics (MD) simulations on one unit cell of MOF-5 in the NTP ensemble using Ewald summation for electrostatics.* Subsequent MD simulations carried out by Han *et al.*,⁵⁶ employing the Dreiding force field⁵⁷ in the NTP ensemble,♦ confirmed the findings of Dubbeldam *et al.* and found negligible changes in covalent bond lengths, while the Zn-O coordination bond lengths increase by only ~ 0.010 Å as the temperature was increased from 10 K to 600 K. Han *et al.* postulated a cooperative rotational motion of the $Zn_4O(COO)_6$ nodes of the framework, connected by rigid linkers, as the mechanism responsible for NTE in MOF-5. Compared to the value of $\alpha = -20 \text{ MK}^{-1}$ (where $1 \text{ MK} = 1 \times 10^6 \text{ K}$) predicted by Dubbeldam *et al.*, Han *et al.* found $\alpha = -8 \text{ MK}^{-1}$.

The accuracy of these simulation results was confirmed by variable temperature synchrotron powder X-ray diffraction studies on the apohost conducted by Lock *et al.* who quantified the NTE over the 80 to 500 K range to be $-13.1(1) \text{ MK}^{-1}$.⁶⁰ Analysis of atomic displacement parameters, as obtained from conventional single crystal X-ray diffraction studies (between 100 K and 500 K in 20 K increments), and harmonic vibrational energies calculated at the B3LYP/LANL2DZ level of theory (using the same model as Dubbeldam *et al.* discussed in footnote ♦ optimized at this level of theory) lead Lock *et al.* to conclude that the rigid Zn_4O clusters and aromatic linkers are connected through flexible carboxylate groups, allowing the benzene rings to vibrate orthogonally, effectively reducing the mean distance between metal clusters, thus causing NTE in MOF-5.⁶⁰⁻⁶¹

Mechanisms other than vibrational modes must be responsible for colossal ($|\alpha| \geq 100 \text{ MK}^{-1}$) thermal expansion.⁶² For instance, it has been shown that the triply interpenetrated framework $Ag_3[Co(CN)_6]$ displays colossal PTE in the basal plane of the trigonal unit cell with $\alpha_1 = 132 \text{ MK}^{-1}$ and colossal NTE for the orthogonal c axis with $\alpha_3 = -130 \text{ MK}^{-1}$.⁶³ The framework, based on the crystal structure proposed by Pauling and Pauling,⁶⁴ consists of a network of Co-CN-Ag-NC-Co linkages whereby CoC_6 octahedra are connected through linear N-Ag-N bridges.

* The Zn_4O cluster was modelled using Lennard-Jones and Coulombic potentials between individual atoms while the 1,4-benzenedicarboxylate linker was simulated by parameters from the CVFF force field.⁵² Quantum mechanical charges (determined for a model consisting of two Zn_4O clusters linked by a complete 1,4-benzenedicarboxylate, but terminated otherwise by methyl groups in sp^3 geometry, at the PBEPBE/6-31+G(d) level of theory according to the CHelpG scheme⁵³ employing atomic radii from Bondi *et al.*)⁵⁴ were employed in the Molecular Dynamics simulations. The NTP ensemble was maintained by the reversible measure-preserving integrator of Martyna *et al.*⁵⁵

♦ Temperature was maintained by the Nosé-Hoover thermostat^{58(a)(b)(c)} and pressure by the Andersen barostat.⁵⁹

Chapter 1: Introduction

In an attempt to elucidate the mechanism behind the colossal thermal expansion, Goodwin *et al.* carried out periodic DFT calculations employing the PBE/PBE density functional.[•] The crystal structures obtained from variable temperature powder X-ray diffraction studies were optimized either with or without relaxation of lattice parameters.⁶⁶ A contour of the energy surface was obtained for fixed values of the a and c unit cell parameters, with a steep-walled, but flat valley that does not coincide with the locus of the experimental lattice parameters. Goodwin *et al.* recognized the possibility of a dispersive argentophilic interaction, with the Ag···Ag separation of 3.5 Å close to the van der Waals limit of 3.4 Å, despite Coulomb repulsion.⁶³ As briefly discussed in Section 1.1, the local nature of standard density functionals prohibits their modelling of dispersion interactions. Indeed, with the addition of a *post hoc* dispersive interaction term of the form $C_{AB,6}R_{AB}^{-6}$ (similar to the DFT-D schemes), the valley of the predicted a - c contour was found to coincide exactly with the experimental values.^{42,47}

Structural analysis by Conterio *et al.* revealed that the Co···Co chains remain linear with little extension over the range of lattice parameters considered.⁶⁷ However, relatively large changes were identified in the C-Co-C valence angles. An anisotropic thermal expansion mechanism whereby rigid Co-CN-Ag-NC-Co linkages flex like a garden trellis, therefore seems likely.⁶⁶ The similar magnitudes of the linear thermal coefficients α_1 and α_3 corroborate such a mechanism whereby any expansion in the basal plane drives a contraction in the orthogonal direction.

Anisotropic thermal expansion was identified in a MOF synthesized in our group (compound **1**, Figure 1.1) that shows colossal positive thermal expansion along the crystallographic c -axis and moderate negative thermal expansion in the ab plane, with linear expansion coefficients $\alpha_c = 123 \text{ MK}^{-1}$ and $\alpha_a = \alpha_b = -21 \text{ MK}^{-1}$.⁶⁸ Grobler *et al.* suggested that the mechanism responsible for the anisotropic thermal expansion is associated with the zinc-hydroxide-zinc coordination spiral that lies along the crystallographic c -axis.⁶⁸ Labile coordination bonds are able to stretch further than covalent bonds with increasing thermal energy due to their shallower potential energy wells.^{45b} Upon stretching of the coordination spiral, the ligands, acting as rigid linkers in the ab plane, are pulled closer together.

One of the primary aims of this study was to substantiate the proposed mechanism for the anomalous thermal expansion of **1**. In order to decide on a level of theory, an organic compound with a nearly eclipsed methyl group in the solid state (compound **2**, Figure 1.1) was evaluated. Comparison of results obtained employing various basis sets with various wave function theory methods and different density functionals revealed key scientific insights regarding the shallow potential energy surface of complexes wherein van der Waals interactions dominate.

[•] The CASTEP code was employed using an energy cut-off of 680 eV and a $3\times3\times3$ Monkhorst-Pack k-point grid.³⁶ Goodwin *et al.* found small discrepancies when using ultrasoft³⁵ or norm-conserving^{65(a)(b)(c)} pseudopotentials.

Chapter 1: Introduction

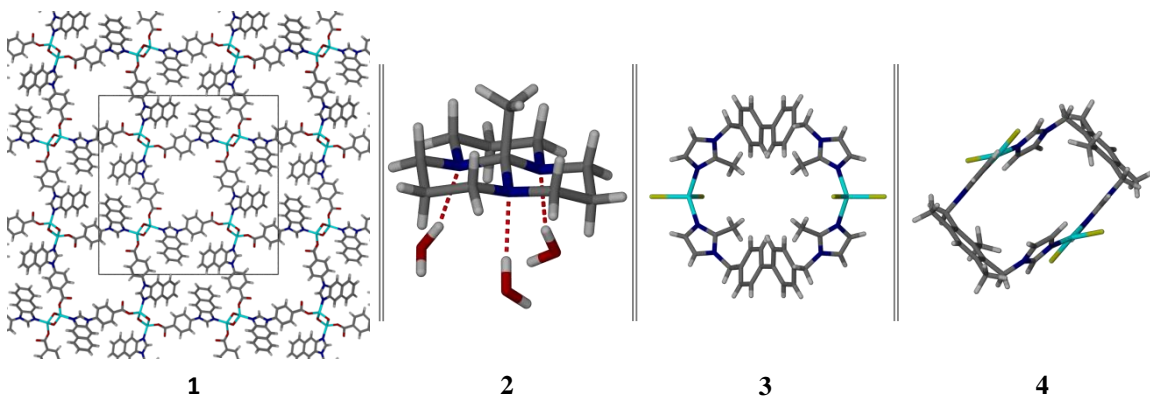


Figure 1.1: Collection of the compounds investigated in this study. More detailed discussions on MOF compound **1** and metallocyclic compounds **3** and **4** can be found in Section 3.2 while compound **2** is discussed in the introduction of Chapter 4.

1.3 Isosteric heat of adsorption, Q_{st}

A novel volumetric sorption isosteric technique (SIT) device was previously developed in-house for the measurement of adsorption isotherms and the simplified determination of thermodynamic parameters of adsorption.⁶⁹ Owing to the high cost of commercial instruments, usually accompanied by software that is not very user-friendly, this device, constructed from readily available components, offers a robust methodology for evaluating porous materials.

This study aims to validate the novel SIT device by comparing thermodynamic parameters obtained using it⁷⁰ to isosteric heats of CO₂ adsorption determined using conventional gravimetric adsorption techniques. Two metallocyclic compounds, compounds **3** and **4** (to be introduced in Sections 3.2.2 and 3.2.3, respectively) were evaluated. Q_{st} is an approximation of the enthalpy of adsorption, ΔH_{ad} , and its value at zero loading gives an indication of the affinity of an adsorbent for an adsorbate. The value of Q_{st} can be related to various interaction energies, including dispersion, short range repulsion, polarization and electrostatic interactions.⁷¹ Due to its higher polarizability, the Q_{st} values for carbon dioxide are larger than other frequently investigated gases (CH₄ and H₂, for example). The important contribution of quadrupolar interactions in CO₂ was recognised early on by Barrer *et al.* who compared experimental initial heats of CO₂ adsorption of different zeolites to the overall initial heats predicted in terms of intermolecular forces.⁷²

By fitting the virial-type isotherm equation⁷³ to CO₂ adsorption isotherms recorded in the temperature range 298–328 K, Zhang *et al.* found a larger onset Q_{st} value for ED-ZIF-8 than for ZIF-8 (-33 kJ·mol⁻¹ vs. -27 kJ·mol⁻¹).¹³ This indicates a stronger interaction of CO₂ with ED-ZIF-8 than ZIF-8, which Zhang *et al.* ascribed to the presence of N-H groups in the modified ED-ZIF-8 framework.¹³

Chapter 1: Introduction

The sensitivity of the isosteric heat of CO₂ adsorption to the identity of the metal cation was recently investigated by Wade *et al.*⁷⁴ who synthesized and analysed members of the M₃(BTC)₂ isostructural series (BTC ≡ 1,3,5-benzenetricarboxylate) with M = Cr, Ni, Mo, Ru and Cu (the well-known HKUST-1 first reported by Chui *et al.*).⁷⁵ Carbon dioxide adsorption isotherms up to 800 Torr were recorded between 313 and 334 K. Simultaneous regression fitting by the virial equation yielded nearly linear $Q_{st}^{CO_2}$ vs. occupancy profiles that maintained the order Mo < Cr < Cu < Ru < Ni from onset values, which ranged 25.6 to 36.8 kJ.mol⁻¹, to maximum CO₂ occupancy. However, the presence of enclathrated donor solvent molecules, that could also contribute to a large Q_{st} value, in Ni₃(BTC)₂(DMA)₂(H₂O), Mo₃(BTC)₂(DMF)_{0.5} and [Ru₃(BTC)₂][BTC]_{0.5}, means the observed order cannot solely be ascribed to M-CO₂ interactions (DMA ≡ dimethylamine, DMF ≡ N,N'-dimethylformamide).⁷⁴ Wade *et al.* also stated that the higher formal charge of the diruthenium unit (or paddlewheel), +5 as opposed to +4 for the other dimetal units, allows for stronger electrostatic interactions to occur.⁷⁴

Trends in the Q_{st} vs. occupancy profiles obtained for compounds **3** and **4** in this study will be rationalized in a similar fashion.

1.4 Aims and objectives

The aim of this dissertation is to evaluate commonly used procedures in the study of porous compounds, with a focus on computational methods used to predict geometric conformations in the solid state and techniques used to determine isosteric heats of adsorption from gas sorption isotherms. The main objectives of this study were to (i) identify suitable density functionals for the study of porous metal organic frameworks by assessment of an organic compound with an anomalous methyl conformation in the solid state, (ii) confirm a proposed mechanism of anisotropic thermal expansion observed in a MOF by envisaging a simple molecular mechanistic model and comparing potential energy profiles and (iii) validate the thermodynamic parameters obtained by a novel volumetric technique by comparison to Q_{st} values measured by conventional means.

1.5 Outline

The dissertation largely follows the order in which the aims and objectives were presented. Background to the theoretical methods used is given in Chapter 2 with a focus on those approximations necessary to realize a practical quantum mechanical theory. These include the Born-Oppenheimer, mean-field and basis set approximations. The density functional theory is elaborated on, with a discussion of certain functionals and the details of different dispersion-correction schemes for DFT are presented.

The compounds investigated are presented in Chapter 3 along with the models used in theoretical assessments and how their internal coordinates were derived. The volumetric SIT device is described and a summary of the density functionals and basis sets used in this study given in the conclusion.

Chapter 1: Introduction

Chapter 4 comprises results obtained in assessing a molecular representation of an organic compound (**2**) that uniquely displays a nearly eclipsed methyl group in the solid state. Various methods (CCSD, MP2, HF, DFT) and levels of theories (methods in combination with a plethora of basis sets) are evaluated and key considerations, including, for example, effects of basis set augmentation and the basis set superposition error, are discussed.

In Chapter 5 the vibrational origin of thermal expansion is discussed, followed by a Molecular Mechanics and DFT investigation of the crystal structures of (i) compound **2**, which was assessed on a molecular level in Chapter 4 and (ii) compound **1**, the metal-organic framework that displays anomalous thermal expansion. The chapter is concluded with results obtained for the mechanistic model, developed in Section 3.8, for emulating the temperature dependent variation in compound **1**.

Different isotherm equations are presented in Chapter 6, along with results obtained from gravimetric CO₂ adsorption experiments. The previously obtained thermodynamic parameters of CO₂ adsorption by compounds **3** and **4** using the volumetric SIT device are presented, followed by an evaluation of different ways in which isosteric heats of adsorption are determined from adsorption isotherms. A comparison is then made of all the Q_{st} plots as a function of occupancy profiles obtained in the chapter.

Chapter 1: Introduction

1.6 References

1. U.S. Environmental Protection Agency: <http://www.iea.org/statistics/>.
2. Haszeldine, R.S., *Science* **2009**, 325, 1647.
3. Klara, S.M.; Srivastava, R.D.; McIlvried, H.G., *Energy Convers. Manage.* **2003**, 44, 2699.
4. Anon, *Science* **2009**, 325, 1644.
5. Rochelle, G.T., *Science* **2009**, 325, 1652.
6. da Silva, E.F.; Svendsen, H.F., *Int. J. Greenhouse Gas Control* **2007**, 1, 151.
7. Blanchon le Bouhelec, E.; Mougin, P.; Barreau, A.; Solimando, R., *Energy Fuels* **2007**, 21, 2044.
8. van den Berg, A.W.C.; Arean, C.O., *Chem. Commun.* **2008**, 668.
9. Rowsell, J.L.C.; Yaghi, O.M., *Microporous Mesoporous Mater.* **2004**, 73, 3.
10. Greathouse, J.A.; Allendorf, M.D., *J. Phys. Chem. C* **2008**, 112, 5795.
11. (a) Wang, Z.; Cohen, S.M., *Chem. Soc. Rev.* **2009**, 38, 1315; (b) Tanabe, K.K.; Cohen, S.M., *Chem. Soc. Rev.* **2011**, 40, 498.
12. Park, K.S.; Ni, Z.; Cote, A.P.; Choi, J.Y.; Huang, R.; Uribe-Romo, F.J.; Chae, H.K.; O'Keeffe, M.; Yaghi, O.M., *Proc. Natl. Acad. Sci. U. S. A.* **2006**, 103, 10186.
13. Zhang, Z.; Xian, S.; Xia, Q.; Wang, H.; Li, Z.; Li, J., *AICHE J.* **2013**, 59, 2195.
14. (a) Garibay, S.J.; Wang, Z.; Tanabe, K.K.; Cohen, S.M., *Inorg. Chem.* **2009**, 48, 7341; (b) Garibay, S.J.; Wang, Z.; Cohen, S.M., *Inorg. Chem.* **2010**, 49, 8086.
15. (a) Llewellyn, P.L.; Maurin, G., *C. R. Chim.* **2005**, 8, 283; (b) Tian, A., *Bull. Soc. Chim. Fr.* **1923**, 33, 427; (c) Calvet, E.; Prat, H., *Récents progrès en microcalorimétrie*. Dunod: **1958**.
16. Sumida, K.; Rogow, D.L.; Mason, J.A.; McDonald, T.M.; Bloch, E.D.; Herm, Z.R.; Bae, T.-H.; Long, J.R., *Chem. Rev.* **2012**, 112, 724.
17. Mason, J.A.; Veenstra, M.; Long, J.R., *Chem. Sci.* **2014**, 5, 32.
18. Bimbo, N.; Sharpe, J.E.; Ting, V.P.; Noguera-Diaz, A.; Mays, T.J., *Adsorption* **2014**, 20, 373.
19. Sinnokrot, M.O.; Valeev, E.F.; Sherrill, C.D., *J. Am. Chem. Soc.* **2002**, 124, 10887.
20. (a) Dąbkowska, I.; Gonzalez, H.V.; Jurečka, P.; Hobza, P., *J. Phys. Chem. A* **2005**, 109, 1131; (b) Vondrášek, J.; Bendová, L.; Klusák, V.; Hobza, P., *J. Am. Chem. Soc.* **2005**, 127, 2615.
21. Brutschy, B.; Hobza, P., *Chem. Rev.* **2000**, 100, 3861.
22. Brana, M.F.; Cacho, M.; Gradillas, A.; De Pascual-Teresa, B.; Ramos, A., *Curr. Pharm. Des.* **2001**, 7, 1745.
23. Van de Craats, A.M.; Warman, J.M.; Muellen, K.; Geerts, Y.; Brand, J.D., *Adv. Mater.* **1998**, 10, 36.
24. (a) Stone, A., *The theory of intermolecular forces*. Clarendon Press: Oxford, **1996**; (b) Pellenq, R.J.-M.; Nicholson, D., *Mol. Phys.* **1998**, 95, 549.
25. Hohenberg, P.; Kohn, W., *Phys. Rev.* **1964**, 136, B864.
26. Chai, J.-D.; Head-Gordon, M., *J. Chem. Phys.* **2008**, 128, 84106.
27. Becke, A.D., *J. Chem. Phys.* **1993**, 98, 5648.
28. Zhao, Y.; Truhlar, D.G., *Acc. Chem. Res.* **2008**, 41, 157.

Chapter 1: Introduction

29. Johnson, E.R.; Becke, A.D.; Sherrill, C.D.; DiLabio, G.A., *J. Chem. Phys.* **2009**, *131*, 34111.
30. Johnson, E.R.; Wolkow, R.A.; DiLabio, G.A., *Chem. Phys. Lett.* **2004**, *394*, 334.
31. (a) Becke, A.D.; Johnson, E.R., *J. Chem. Phys.* **2007**, *127*, 154101; (b) Vydrov, O.A.; Wu, Q.; Van Voorhis, T., *J. Chem. Phys.* **2008**, *129*, 14106; (c) Zaremba, E.; Kohn, W., *Phys. Rev. B* **1976**, *13*, 2270; (d) Dobson, J.F.; Dinte, B.P., *Phys. Rev. Lett.* **1996**, *76*, 1780.
32. (a) Grimme, S., *J. Comput. Chem.* **2004**, *25*, 1463; (b) Grimme, S., *J. Comput. Chem.* **2006**, *27*, 1787; (c) Grimme, S.; Antony, J.; Ehrlich, S.; Krieg, H., *J. Chem. Phys.* **2010**, *132*, 154104; (d) Grimme, S.; Ehrlich, S.; Goerigk, L., *J. Comput. Chem.* **2011**, *32*, 1456.
33. Bemm, U.; Östmark, H., *Acta Crystallogr., Sect. C Cryst. Struct. Commun.* **1998**, *C54*, 1997.
34. Segall, M.D.; Lindan, P.J.D.; Probert, M.J.; Pickard, C.J.; Hasnip, P.J.; Clark, S.J.; Payne, M.C., *J. Phys. Condens. Matter* **2002**, *14*, 2717.
35. Vanderbilt, D., *Phys. Rev. B* **1990**, *41*, 7892.
36. Monkhorst, H.J.; Pack, J.D., *Physical Rev. B* **1976**, *13*, 5188.
37. Appalakondaiah, S.; Vaitheeswaran, G.; Lebégue, S., *J. Chem. Phys.* **2014**, *140*, 014105/1.
38. Perdew, J.P.; Wang, Y., *Physical Rev. B* **1992**, *45*, 13244.
39. Ortmann, F.; Bechstedt, F.; Schmidt, W.G., *Phys. Rev. B* **2006**, *73*, 205101.
40. Perdew, J.P.; Burke, K.; Ernzerhof, M., *Phys. Rev. Lett.* **1996**, *77*, 3865.
41. Tkatchenko, A.; Scheffler, M., *Phys. Rev. Lett.* **2009**, *102*, 73005.
42. Perdew, J.P.; Zunger, A., *Phys. Rev. B Condens. Matter* **1981**, *23*, 5048.
43. Ceperley, D.M.; Alder, B.J., *Phys. Rev. Lett.* **1980**, *45*, 566.
44. Barrera, G.D.; Bruno, J.A.O.; Barron, T.H.K.; Allan, N.L., *J. Phys. Condens. Matter* **2005**, *17*, R217.
45. (a) Brown, I.D., *Acta Crystallogr.* **1992**, *B48*, 553; (b) Brown, I.D.; Dabkowski, A.; McCleary, A., *Acta Crystallogr.* **1997**, *B53*, 750.
46. Miller, W.; Smith, C.W.; Mackenzie, D.S.; Evans, K.E., *J. Mater. Sci.* **2009**, *44*, 5441.
47. Busing, W.R.; Levy, H.A., *Acta Crystallogr.* **1964**, *17*, 142.
48. Sleight, A.W., *Endeavour* **1995**, *19*, 64.
49. Mary, T.A.; Evans, J.S.O.; Vogt, T.; Sleight, A.W., *Science* **1996**, *272*, 90.
50. Li, H.; Eddaoudi, M.; O'Keeffe, M.; Yaghi, M., *Nature* **1999**, *402*, 276.
51. Rowsell, J.L.C.; Spencer, E.C.; Eckert, J.; Howard, J.A.K.; Yaghi, O.M., *Science* **2005**, *309*, 1350.
52. Dauber-Osguthorpe, P.; Roberts, V.A.; Osguthorpe, D.J.; Wolff, J.; Genest, M.; Hagler, A.T., *Proteins Struct., Funct., Genet.* **1988**, *4*, 31.
53. Reed, A.E.; Curtiss, L.A.; Weinhold, F., *Chem. Rev.* **1988**, *88*, 899.
54. Bondi, A., *J. Phys. Chem.* **1964**, *68*, 441.
55. Martyna, G.J.; Tuckerman, M.E.; Tobias, D.J.; Klein, M.L., *Mol. Phys.* **1996**, *87*, 1117.
56. Han, S.S.; Goddard, W.A., III, *J. Phys. Chem. C* **2007**, *111*, 15185.
57. Mayo, S.L.; Olafson, B.D.; Goddard, W.A., III, *J. Phys. Chem.* **1990**, *94*, 8897.
58. (a) Nosé, S., *Mol. Phys.* **1984**, *52*, 255; (b) Nosé, S., *J. Chem. Phys.* **1984**, *81*, 511; (c) Nosé, S., *Prog. Theor. Phys. Suppl.* **1991**, *103*, 1.

Chapter 1: Introduction

59. Andersen, H.C., *J. Chem. Phys.* **1980**, *72*, 2384.
60. Lock, N.; Wu, Y.; Christensen, M.; Cameron, L.J.; Peterson, V.K.; Bridgeman, A.J.; Kepert, C.J.; Iversen, B.B., *J. Phys. Chem. C* **2010**, *114*, 16181.
61. Lock, N.; Christensen, M.; Wu, Y.; Peterson, V.K.; Thomsen, M.K.; Piltz, R.O.; Ramirez-Cuesta, A.J.; McIntyre, G.J.; Noren, K.; Kutteh, R.; Kepert, C.J.; Kearley, G.J.; Iversen, B.B., *Dalton Trans.* **2013**, *42*, 1996.
62. Takenaka, K.; Takagi, H., *Appl. Phys. Lett.* **2005**, *87*, 261902.
63. Goodwin, A.L.; Calleja, M.; Conterio, M.J.; Dove, M.T.; Evans, J.S.O.; Keen, D.A.; Peters, L.; Tucker, M.G., *Science* **2008**, *319*, 794.
64. Pauling, L.; Pauling, P., *Proc. Natl. Acad. Sci. U. S. A.* **1968**, *60*, 362.
65. (a) Rappé, A.M.; Rabe, K.M.; Kaxiras, E.; Joannopoulos, J., *Phys. Rev. B* **1990**, *41*, 1227; (b) Hamann, D.R.; Schlueter, M.; Chiang, C., *Phys. Rev. Lett.* **1979**, *43*, 1494; (c) Lin, J.S.; Qteish, A.; Payne, M.C.; Heine, V., *Phys. Rev. B* **1993**, *47*, 4174.
66. Calleja, M.; Goodwin, A.L.; Dove, M.T., *J. Phys. Condens. Matter* **2008**, *20*, 255226.
67. Conterio, M.J.; Goodwin, A.L.; Tucker, M.G.; Keen, D.A.; Dove, M.T.; Peters, L.; Evans, J.S.O., *J. Phys. Condens. Matter* **2008**, *20*, 255225.
68. Grobler, I.; Smith, V.J.; Bhatt, P.M.; Herbert, S.A.; Barbour, L.J., *J. Am. Chem. Soc.* **2013**, *135*, 6411.
69. Atwood, J.L.; Barbour, L.J.; Thallapally, P.K.; Wirsig, T.B., *Chem. Commun.* **2005**, 51.
70. Marais, C.G. MSc thesis, *Thermodynamics and Kinetics of Sorption*; Stellenbosch University, **2008**.
71. Roque-Malherbe, R., *Microporous Mesoporous Mater.* **2000**, *41*, 227.
72. Barrer, R.M.; Gibbons, R.M., *Trans. Faraday Soc.* **1965**, *61*, 948.
73. Czepirski, L.; Jagiełło, J., *Chem. Eng. Sci.* **1989**, *44*, 797.
74. Wade, C.R.; Dincă, M., *Dalton Trans.* **2012**, *41*, 7931.
75. Chui, S.S.Y.; Lo, S.M.F.; Charmant, J.P.H.; Orpen, A.G.; Williams, I.D., *Science* **1999**, *283*, 1148.

Chapter 2: Overview of theoretical methods

A brief discussion on the theoretical methods used in this study is given in this chapter. In Section 2.1 fundamentals of Quantum Mechanics and the simplest wave function theory, that of the Hartree-Fock approximation, are discussed. The section is concluded with an outline of the self-consistent field procedure that forms the basis of all computational applications. Density Functional Theory (DFT), which presents an efficient way of overcoming certain shortcomings of the Hartree-Fock level of theory, is subsequently discussed in Section 2.2. The books by Jensen¹ and Koch and Holthausen² were used extensively, but not exclusively, in compiling these sections.

Substantial progress has been made in the refinement of density functionals (DFs) and DFT has become a viable alternative to conventional quantum mechanical techniques for the reproduction of spectroscopic and thermochemical data.³ For some weakly bound systems, such as hydrogen-bonded systems, DFs still yield reasonable results for energetics and geometries. However, they give insufficient binding or even unbound results for van der Waals systems where the dispersion interaction is dominant. This weak but omnipresent attractive force dominates the interaction between atoms, molecules, surfaces, and other neutral fragments of matter.⁴

Calculation of structural properties of open systems such as porous metal organic frameworks poses a special problem for DFT. The framework encloses large regions of very low electron density, where errors in the density are amplified. Such large differences in the absolute values of densities takes to an extreme the preliminary assumption used in the parameterizations of DFs, namely the use of a uniform electron gas as the reference system.⁴ Means to address these inadequacies, namely admixing a fraction of exact exchange (hybrid), generalised gradient corrected (GGA) and long-range corrected (LC) functionals are elaborated on in this chapter. The development of a systematic optimization procedure by Becke (Section 2.2.5), Grimme's pure-GGA B97D functional (Section 2.4) and Chai and Head-Gordon's LC-hybrid ω B97XD functional (Section 2.5) are discussed. The empirical dispersion correction schemes used in B97D and ω B97XD functionals are discussed in Sections 2.4.2 and 2.5.3, respectively. Grimme's third generation chemical environment dependent DFT-D3 (Section 2.6.1) and the Tkatchenko-Scheffler (Section 2.6.2) dispersion correction schemes are discussed in the concluding section.

2.1 Quantum Mechanics

At the subatomic level electrons, protons, neutrons and light all behave as both waves and particles. This wave-particle duality is what distinguishes quantum from classical mechanics and allows a multinuclear, multielectron system to be represented by a wave function. In mathematics, an *eigenfunction* of an operator \hat{O} is any function f_n that can be acted on by the operator and be returned unaltered except for a scaling factor: $\hat{O}f_n = a_n f_n$. The scalar result a_n is called the *eigenvalue*: $a_n = \int f_n^* \hat{O} f_n$, where f_n^* represents the complex conjugate of f_n . For every quantifiable property of a system, there exists in quantum mechanics a

Chapter 2: Overview of theoretical methods

corresponding operator that yields the *observable* (result) as an eigenvalue when the wave function of the system is subjected to it. The time-independent Schrödinger equation is an eigenvalue equation for the total energy E of the system. The corresponding total energy operator is called the *Hamiltonian*.

2.1.1 The Schrödinger equation

The Schrödinger equation is the basis of quantum chemistry, but it does not account for relativistic effects or recognize electron spin directly. This simplifies the situation considerably as, initially, only spatial dimensions need be considered. The multinuclear, multielectron, time-independent Schrödinger equation is written as

$$\hat{H}\Psi(\vec{r}_1, \vec{r}_2, \dots, \vec{r}_n, \vec{R}_1, \vec{R}_2, \dots, \vec{R}_m) = E\Psi(\vec{r}_1, \vec{r}_2, \dots, \vec{r}_n, \vec{R}_1, \vec{R}_2, \dots, \vec{R}_m) \quad 2.1$$

where E is the total energy of the system containing N electrons and M nuclei represented by wave function Ψ . The positional vectors \vec{r}_i and \vec{R}_k define the spatial coordinates of electron i and nucleus k , respectively. The Hamiltonian operator \hat{H} encompasses the information necessary to obtain the total energy and has the following components:

$$\hat{H} = \hat{T}_n + \hat{T}_e + \hat{V}_{ne} + \hat{V}_{ee} + \hat{V}_{nn} \quad 2.2a$$

$$\hat{T}_n = -\frac{\hbar^2}{2} \sum_k^M \frac{1}{M_k} \nabla_{\vec{R}_k}^2 \quad 2.2b$$

$$\hat{T}_e = -\frac{\hbar^2}{2m_e} \sum_i^N \nabla_{\vec{r}_i}^2 \quad 2.2c$$

$$\hat{V}_{ne} = -\frac{e^2}{4\pi\epsilon_0} \sum_i^N \sum_k^M \frac{Z_k}{r_{ik}} \quad 2.2d$$

$$\hat{V}_{ee} = \frac{e^2}{4\pi\epsilon_0} \sum_i^N \sum_{j>i}^N \frac{1}{r_{ij}} \quad 2.2e$$

$$\hat{V}_{nn} = \frac{e^2}{4\pi\epsilon_0} \sum_k^M \sum_{l>k}^M \frac{Z_k Z_l}{R_{kl}} \quad 2.2f$$

The kinetic energy operators of the nuclei (T_n) and electrons (T_e) are given in Eqs. 2.2b and 2.2c, respectively. In these expressions, \hbar is the Planck constant, h , divided by 2π , m_e is the mass of an electron, M_k is the mass of nucleus k , and ∇^2 represents the Laplace operator defined as the sum of differential operators in Cartesian coordinates: $\nabla^2 = \frac{\partial^2}{\partial x^2} + \frac{\partial^2}{\partial y^2} + \frac{\partial^2}{\partial z^2}$.

Equations 2.2d, 2.2e and 2.2f give the potential energy operators for the Coulomb interactions between nuclei and electrons (V_{ne}), electrons (V_{ee}) and nuclei (V_{nn}), respectively,

Chapter 2: Overview of theoretical methods

where, e is the charge of one electron, ε_0 the permittivity of free space, Z_k is the atom number of nucleus k and $r_{ik} = |\vec{r}_i - \vec{R}_k|$ is the distance between electron i and nucleus k . The distance between electrons i and j is given by $r_{ij} = |\vec{r}_i - \vec{r}_j|$, while $R_{kl} = |\vec{R}_k - \vec{R}_l|$ is the separation between nuclei k and l .

The Schrödinger equation (Eq. 2.1) cannot be solved exactly for the many-electron case because the electron-electron repulsion term in the potential energy does not have spherical symmetry. Thus, in order to realize a practical Quantum Mechanics theory, it is necessary to make certain approximations. These are discussed in the following sections.

2.1.2 The Born-Oppenheimer approximation

Since the mass of a proton is about 2000 times that of an electron, the nuclei are almost stationary with respect to the electrons. A reasonable simplification of the Schrödinger equation would therefore be to decouple the very different time-scales of nuclear and electronic motion by fixing the positions of all nuclei. In the Born-Oppenheimer approximation⁵ the total wave function is factored into two parts: one that depends only on the position of the nuclei ($\vec{R}_1, \vec{R}_2, \dots, \vec{R}_m$) and another that depends on the positions of the electrons ($\vec{r}_1, \vec{r}_2, \dots, \vec{r}_n$) relative to the stationary nucleic field:

$$\Psi(\vec{r}_1, \vec{r}_2, \dots, \vec{r}_n, \vec{R}_1, \vec{R}_2, \dots, \vec{R}_m) = \Psi_{nuclear}(\vec{R}_1, \vec{R}_2, \dots, \vec{R}_m) \times \Psi_e(\vec{r}_1, \vec{r}_2, \dots, \vec{r}_n, \vec{R}_1^{fixed}, \vec{R}_2^{fixed}, \dots, \vec{R}_m^{fixed}) \quad 2.3$$

In this approximation, the kinetic energy contribution of the nuclei (T_n) becomes zero, and the potential energy of the internuclear interaction (V_{nn}) a constant. Collecting the remaining operators of Eq. 2.2 according to their electron indices, the electronic Hamiltonian can be written as

$$\hat{H}_e = \hat{T}_e + \hat{V}_{ne} + \hat{V}_{ee} = \sum_i^N \hat{h}_1(i) + \sum_i^N \sum_{j>i}^N \hat{g}_{12}(ij) \quad 2.4a$$

where

$$\hat{h}_1(i) = -\frac{\hbar^2}{2m_e} \nabla_{\vec{r}_i}^2 - \frac{e^2}{4\pi\varepsilon_0} \sum_k^M \frac{Z_k}{r_{ik}} \quad 2.4b$$

$$\hat{g}_{12}(ij) = \frac{e^2}{4\pi\varepsilon_0} \frac{1}{r_{ij}} \quad 2.4c$$

Chapter 2: Overview of theoretical methods

The one-electron operator \hat{h}_1 describes the motion of an electron in the field of all the nuclei, and \hat{g}_{12} is the two-electron operator representing electron-electron repulsion. The solution of the Schrödinger equation as given by $\hat{H}_e \Psi_e = E_e \Psi_e$ is the electronic energy. The total energy is then obtained after addition of the nuclear repulsion energy:

$$E = E_e + V_{nn} = \int \Psi_e^* \hat{H}_e \Psi_e d^3r + \frac{1}{4\pi\epsilon_0} \sum_k^M \sum_{l>k}^M \frac{Z_k Z_l}{R_{kl}} \quad 2.5$$

2.1.3 Introducing electron spin and indistinguishability

Since the Schrödinger equation is non-relativistic, it does not account for electron spin directly. In the orbital approximation, the N -electron wave function can be expressed as N one-electron spin orbitals,

$$\Psi_e(\vec{x}_1, \vec{x}_2, \dots, \vec{x}_n) = \phi_1(\vec{x}_1)\phi_2(\vec{x}_2) \cdots \phi_n(\vec{x}_n) \quad 2.6$$

where $\vec{x}_i = (x_i, y_i, z_i, s_i)$ is the four dimensional state vector representing the position and spin of electron i . Equation 2.6 is also referred to as the *Hartree product*. A spin orbital ϕ is constructed by multiplying the spatial orbital φ by a spin function,

$$\phi_i(\vec{x}_i) = \phi_i(\vec{r}_i, s_i) = \varphi_i(\vec{r}_i)\sigma_i(s_i) \quad 2.7$$

where σ represents either the α (“spin up”) or β (“spin down”) spin function.

The wave function itself is not an observable, but a physical interpretation can be associated with the square thereof: $|\Psi_{elec}(\vec{x}_1, \vec{x}_2, \dots, \vec{x}_n)|^2 d\vec{x}_1 d\vec{x}_2 \cdots d\vec{x}_n$ represents the probability of simultaneously finding electrons $1, 2, \dots, n$ in volume elements $d\vec{x}_1 d\vec{x}_2 \cdots d\vec{x}_n$. This probability must not change if any two electrons (here i and j) were to switch places, that is

$$|\Psi_e(\vec{x}_1, \vec{x}_2, \dots, \vec{x}_i, \vec{x}_j, \dots, \vec{x}_n)|^2 = |\Psi_e(\vec{x}_1, \vec{x}_2, \dots, \vec{x}_j, \vec{x}_i, \dots, \vec{x}_n)|^2 \quad 2.8a$$

This is a result of the indistinguishability of electrons and can be satisfied either by two identical wave functions (symmetric case), or by two wave functions with opposite signs (antisymmetric case). The Pauli exclusion principle states that the wave function describing a many-electron system must change sign (be antisymmetric) upon exchange of any two electrons:

$$\Psi_e(\vec{x}_1, \vec{x}_2, \dots, \vec{x}_i, \vec{x}_j, \dots, \vec{x}_n) = -\Psi_e(\vec{x}_1, \vec{x}_2, \dots, \vec{x}_j, \vec{x}_i, \dots, \vec{x}_n) \quad 2.8b$$

Chapter 2: Overview of theoretical methods

Hartree products (Eq. 2.6) do not satisfy the antisymmetry condition. Antisymmetrical wave functions can be constructed using Slater determinants, which have the following form for an N electron system:

$$\Phi = \frac{1}{\sqrt{N!}} \begin{vmatrix} \phi_1(\vec{x}_1) & \phi_2(\vec{x}_1) & \cdots & \phi_n(\vec{x}_1) \\ \phi_1(\vec{x}_2) & \phi_2(\vec{x}_2) & \cdots & \phi_n(\vec{x}_2) \\ \vdots & \vdots & & \vdots \\ \phi_1(\vec{x}_n) & \phi_2(\vec{x}_n) & \cdots & \phi_n(\vec{x}_n) \end{vmatrix} \quad 2.9$$

The N one-electron spin orbitals are listed going across each row, with one row for each electron. The determinant changes sign if any two rows are interchanged, while it is zero if any two rows are identical. The factor in front of the determinant is a normalization constant, requiring that the probability of finding the N electrons anywhere in space must be exactly unity, that is

$$\int \cdots \int |\Psi_e(\vec{x}_1, \vec{x}_2, \dots, \vec{x}_n)|^2 d\vec{x}_1 d\vec{x}_2 \cdots d\vec{x}_n = 1 \quad 2.10$$

2.1.4 The energy of a Slater determinant

The electronic energy, $E_e = \int \Phi^* \hat{H}_e \Phi d^3r$, of a single Slater determinant can be shown to be

$$E_e = \sum_i^N h_1(i) + \frac{1}{2} \sum_{i,j}^N (J_{ij} - K_{ij}) \quad 2.11a$$

The first summation in Eq. 2.11a represents the kinetic energy of the electrons, as well as their attractive interaction with a field of nuclei. These energies are a function of only one electron's state and are calculated by the *core* integral:

$$h_1(i) = \int \phi_i^*(\vec{x}_1) \hat{h}_1(i) \phi_i(\vec{x}_1) d\vec{x}_1 \quad 2.11b$$

The second summation in Eq. 2.11a represents the repulsive electron-electron interaction. The first term is the *Coulomb* integral:

$$J_{ij} = \int \int \phi_i^*(\vec{x}_1) \phi_j^*(\vec{x}_2) \hat{g}_{12}(ij) \phi_i(\vec{x}_1) \phi_j(\vec{x}_2) d\vec{x}_1 d\vec{x}_2 \quad 2.11c$$

and represents the classical repulsion between two charge distributions $\rho(1)$ and $\rho(2)$ given by $\phi_i^2(\vec{x}_1)$ and $\phi_j^2(\vec{x}_2)$, respectively. The second term is the *exchange* integral:

$$K_{ij} = \int \int \phi_i^*(\vec{x}_1) \phi_j^*(\vec{x}_2) \hat{g}_{12}(ij) \phi_i(\vec{x}_2) \phi_j(\vec{x}_1) d\vec{x}_1 d\vec{x}_2 \quad 2.11d$$

wherein the electron coordinates are interchanged between orbitals. It has no classical analogue and is a manifestation of the fact that the wave function must be antisymmetric.

Chapter 2: Overview of theoretical methods

2.1.5 The variational principle

The electron repulsion terms in the Hamiltonian preclude an analytical solution to the many-electron Schrödinger equation. Numerical methods must therefore be employed to get as good an estimate of the exact solution as possible. According to the variational principle, the energy, E_{trial} , of any approximate wave function, Ψ_{trial} , will always be greater than or equal to the true ground state energy, E_0 , of a particular system:

$$\int \Psi_{trial}^* \hat{H} \Psi_{trial} d^3r = E_{trial} \geq E_0 = \int \Psi_0^* \hat{H} \Psi_0 d^3r \quad 2.12$$

The strategy for finding the ground state energy and wave function, Ψ_0 , is then to search through all acceptable N -electron wave functions in order find a suitable Ψ_{trial} that minimizes E_{trial} .

A logical continuation of separating electronic and nuclear motion (the Born-Oppenheimer approximation), is to assume that electrons move independently of each other. This simplification is introduced in the Hartree-Fock approximation, in which it is assumed that the trial wave function can be represented by a single Slater determinant.

2.1.6 The Hartree-Fock (HF) approximation

The second essential approximation towards a practical quantum mechanical description is to neglect electron correlation and to include electron repulsion only as an average effect. This is accomplished by employing the effective one-electron Fock operator defined as follows:

$$\hat{F}_1(i) = \hat{h}_1(i) + V_{HF}(i) \quad 2.13a$$

In this expression, $\hat{h}_1(i)$ is defined as in Eq. 2.4b to encompass the electron kinetic energy and electron-nuclear attraction, while V_{HF} is the Hartree-Fock potential representing the average repulsive potential experienced by the i^{th} electron due to the remaining $N - 1$ electrons. The cumbersome two-electron repulsion operator \hat{g}_{12} in the Hamiltonian (Eq. 2.4c) is substituted for the simple one-electron operator V_{HF} with the following form:

$$V_{HF}(i) = \sum_j^N (\hat{J}_j - \hat{K}_j) \quad 2.13b$$

The Coulomb and exchange operators, \hat{J}_j and \hat{K}_j , are defined in the following manner:

$$\hat{J}_j \phi_i(\vec{x}_1) = \int \phi_j^*(\vec{x}_2) \hat{g}_{12}(ij) \phi_j(\vec{x}_2) d\vec{x}_2 \phi_i(\vec{x}_1) \quad 2.13c$$

$$\hat{K}_j \phi_i(\vec{x}_1) = \int \phi_j^*(\vec{x}_2) \hat{g}_{12}(ij) \phi_i(\vec{x}_2) d\vec{x}_2 \phi_j(\vec{x}_1) \quad 2.13d$$

Chapter 2: Overview of theoretical methods

The Coulomb operator represents the potential that electron 1 in spin orbital ϕ_i experiences as a result of the charge distribution of electron 2 in ϕ_j , while the \hat{K}_j operator exchanges the two electrons, $\phi_i(\vec{x}_1) \rightarrow \phi_j(\vec{x}_1)$. Applying these operators yields their respective integrals, that is: $\int \phi_i^*(\vec{x}_1) \hat{J}_j \phi_i(\vec{x}_1) d\vec{x}_1 = J_{ij}$ and $\int \phi_i^*(\vec{x}_1) \hat{K}_j \phi_i(\vec{x}_1) d\vec{x}_1 = K_{ij}$.

The summation over the Coulomb and exchange operators represents an average potential experienced by a single electron in the field provided by the other $N - 1$ electrons. The HF method is therefore referred to as a *mean-field* method. After applying the Fock operator, a set of *pseudo*-eigenvalue equations is obtained:

$$\hat{F}_1(i)\phi_i(\vec{x}_1) = \varepsilon_i \phi_i(\vec{x}_1) \quad 2.14$$

where ε_i $[= \int \phi_i^*(\vec{x}_1) \hat{F}_1(i) \phi_i(\vec{x}_1) d\vec{x}_1]$ has the dimension of energy. The total HF energy, after including nuclear repulsion, is given by

$$E = \sum_i^N \varepsilon_i - \frac{1}{2} \sum_{i,j}^N (J_{ij} - K_{ij}) + V_{nn} \quad 2.15$$

The HF equations cannot be solved in closed form, because the Fock operator of spin orbital i is dependent on the values of all $N - 1$ other ϕ_j spin orbitals. In other words, the spin orbitals are derived from their own effective potential. This problem is solved by applying the HF equations in an iterative fashion to improve an initial-guess set of spin orbitals. This is repeated until the input and output spin orbitals differ by less than a predetermined threshold, resulting in a set of orbitals that are self-consistent. However, since the expressions for one-electron spin orbitals of a many-electron system are unknown, further approximations are required.

2.1.7 HF energy of a closed-shell system

The Schrödinger equation does not account for electron spin directly. This allows for the spin dimension to be removed. In closed shell systems, an even number of N electrons is restricted to occupy $N/2$ spatial orbitals as spin balanced pairs with identical spatial coordinates. The sum over N spin orbitals can then be written as follows:

$$\Psi_e(\vec{x}_1, \vec{x}_2, \dots, \vec{x}_n) = \sum_i^N \phi_i(\vec{x}_i) = \sum_A^{N/2} \varphi_A(\vec{r}_A) \sigma(\alpha) + \sum_A^{N/2} \varphi_A(\vec{r}_A) \sigma(\beta) \quad 2.16$$

Chapter 2: Overview of theoretical methods

The Fock operator is now expressed by

$$\hat{F}_1(A) = \hat{h}_1(A) + \sum_B^{N/2} (2\hat{J}_B - \hat{K}_B) \quad 2.17a$$

with the HF equations and total energy given as follows:

$$\hat{F}_1(A)\varphi_A(\vec{r}_1) = \varepsilon_A \varphi_A(\vec{r}_1) \quad 2.17b$$

$$E = 2 \sum_A^{N/2} \varepsilon_A - \sum_{A,B}^{N/2} (2J_{AB} - K_{AB}) + V_{nn} \quad 2.17c$$

Using the same spatial orbital φ_A for both α and β spin electrons is known as performing a *spin-restricted* calculation. All systems discussed in this dissertation are closed-shell; hence open-shell systems will not be discussed here. The HF equations can only be solved numerically for small, highly symmetrical cases. For larger molecules, spatial orbitals are necessarily approximated as linear combinations of atomic orbitals.

2.1.8 The basis set approximation and Roothaan-Hall Equations

The final approximation towards a practical quantum mechanical description is the transformation of the HF equations into a set of algebraic equations. These algebraic equations can furthermore be collected into matrices to significantly simplify their manipulation. The true wave function of a many-electron system is not known, but it is expected that the N one-electron solutions for the N -electron system will resemble the exact one-electron wave functions of the hydrogen atom. In the basis set approximation, the spatial orbitals are expressed as linear combinations of known functions:

$$\varphi_A(\vec{r}_1) \approx \sum_{\beta}^{N_{basis}} c_{\beta A} \chi_{\beta}(\vec{r}_1) \quad 2.18$$

The χ_{β} functions are called basis functions and remain fixed, while their coefficients $c_{\beta A}$ are optimized towards self-consistency. Subscript β refers to the β^{th} basis function and has no relation to electron-spin function β . The set of functions in Eq. 2.18 is known as the *basis set* and is complete (exact) if the number of basis functions, N_{basis} , goes to infinity. The HF equations (Eq. 2.17b) can be written in the basis-set expansion as

$$\hat{F}_1(A) \sum_{\beta}^{N_{basis}} c_{\beta A} \chi_{\beta}(\vec{r}_1) = \varepsilon_A \sum_{\beta}^{N_{basis}} c_{\beta A} \chi_{\beta}(\vec{r}_1) \quad 2.19a$$

Chapter 2: Overview of theoretical methods

Multiplying from the left by $\chi_\alpha^*(\vec{r}_1)$ (the α^{th} basis function in the basis set of the complex conjugate of φ_A , that is: $\varphi_A^*(\vec{r}_1) \approx \sum_{\alpha}^{N_{\text{basis}}} c_{\alpha A} \chi_\alpha^*(\vec{r}_1)$) and then integrating results in the Roothaan-Hall equations for closed-shell systems:

$$\sum_{\alpha}^{N_{\text{basis}}} c_{\beta A} \int \chi_\alpha^*(\vec{r}_1) \hat{F}_1(A) \chi_\beta(\vec{r}_1) d\vec{r}_1 = \varepsilon_A \sum_{\alpha}^{N_{\text{basis}}} c_{\beta A} \int \chi_\alpha^*(\vec{r}_1) \chi_\beta(\vec{r}_1) d\vec{r}_1 \quad 2.19\text{b}$$

These equations represent the HF equations (Eq. 2.17b) expanded in the basis-set approximation. All N_{basis} equations can be collected in matrix notation as

$$\mathbf{FC} = \mathbf{SCE} \quad 2.19\text{c}$$

where \mathbf{F} is the Fock matrix; \mathbf{C} is the matrix of unknown coefficients; \mathbf{S} is the overlap matrix with elements $S_{\alpha\beta} = \int \chi_\alpha^*(\vec{r}_1) \chi_\beta(\vec{r}_1) d\vec{r}_1$; and \mathbf{E} is a diagonal matrix with elements ε_A . Each element of \mathbf{F} ($F_{\alpha\beta} = \int \chi_\alpha^*(\vec{r}_1) \hat{F}_1(A) \chi_\beta(\vec{r}_1) d\vec{r}_1$) contains the one-electron integrals of kinetic and attractive potential energy (\hat{h}_1), as well as the sum over occupied orbitals of coefficients multiplied by the two-electron integrals of electron repulsion (see Eq. 2.17a). By writing the latter as a product of the spin-restricted density matrix (\mathbf{D}) and two-electron integrals, the Fock matrix elements are calculated as follows:

$$\begin{aligned} F_{\alpha\beta} &= \int \chi_\alpha^*(\vec{r}_1) \hat{h}_1(A) \chi_\beta(\vec{r}_1) d\vec{r}_1 \\ &+ \sum_{\gamma, \delta}^{N_{\text{basis}}} D_{\gamma\delta} \left(\int \int \chi_\alpha^*(\vec{r}_1) \chi_\gamma^*(\vec{r}_2) \hat{g}_{12}(AB) \chi_\beta(\vec{r}_1) \chi_\delta(\vec{r}_2) d\vec{r}_1 d\vec{r}_2 \right. \\ &\quad \left. - \frac{1}{2} \int \int \chi_\alpha^*(\vec{r}_1) \chi_\gamma^*(\vec{r}_2) \hat{g}_{12}(AB) \chi_\beta(\vec{r}_2) \chi_\delta(\vec{r}_1) d\vec{r}_1 d\vec{r}_2 \right) \end{aligned} \quad 2.20\text{a}$$

Notice the double summation over the number of basis functions (δ and γ) in the expansion of spatial orbital B , $\varphi_B(\vec{r}_1) \approx \sum_{\delta}^{N_{\text{basis}}} c_{\delta B} \chi_\delta^*(\vec{r}_1)$, and its complex conjugate, $\varphi_B^*(\vec{r}_1) \approx \sum_{\gamma}^{N_{\text{basis}}} c_{\gamma B} \chi_\gamma^*(\vec{r}_1)$. Elements of the spin-restricted density matrix are given by

$$D_{\gamma\delta} = 2 \sum_B^{N/2} c_{\gamma B} c_{\delta B} \quad 2.20\text{b}$$

Chapter 2: Overview of theoretical methods

2.1.9 The SCF procedure

The Roothaan-Hall equations are used to determine the N_{basis} coefficients of each spatial orbital approximated by a basis set. Values for the unknown coefficients and corresponding orbital energies, ε_A , are obtained by diagonalization of the Fock matrix. However, the Fock matrix can only be constructed if all the coefficients are known. To overcome this, the Roothaan-Hall equations are applied in an iterative fashion to improve an initial-guess density matrix. This is repeated until the density matrix used to construct the Fock matrix is equal to that resulting from diagonalization, to within a certain convergence limit. The resulting density matrix therefore determines a self-consistent field (SCF) solution.

Using the SCF density matrix, the electronic energy is then computed as

$$\begin{aligned} E_e = & \sum_{\alpha,\beta}^{N_{basis}} D_{\alpha\beta} \int \chi_\alpha^*(\vec{r}_1) \hat{h}_1(A) \chi_\beta(\vec{r}_1) d\vec{r}_1 + \frac{1}{2} \sum_{\alpha,\beta,\gamma,\delta}^{N_{basis}} D_{\alpha\beta} D_{\gamma\delta} \\ & \times \left[\int \int \chi_\alpha^*(\vec{r}_1) \chi_\gamma^*(\vec{r}_2) \hat{g}_{12}(AB) \chi_\beta(\vec{r}_1) \chi_\delta(\vec{r}_2) d\vec{r}_1 d\vec{r}_2 \right. \\ & \left. - \int \int \chi_\alpha^*(\vec{r}_1) \chi_\gamma^*(\vec{r}_2) \hat{g}_{12}(AB) \chi_\beta(\vec{r}_2) \chi_\delta(\vec{r}_1) d\vec{r}_1 d\vec{r}_2 \right] \end{aligned} \quad 2.21$$

with: $D_{\alpha\beta} = 2 \sum_A^{N/2} c_{\alpha A} c_{\beta A}$. Equation 2.21 can be simplified to

$$\begin{aligned} E_e = & \sum_{\alpha,\beta}^{N_{basis}} D_{\alpha\beta} \int \chi_\alpha^*(\vec{r}_1) \hat{h}_1(A) \chi_\beta(\vec{r}_1) d\vec{r}_1 + \frac{1}{2} \sum_{\alpha,\beta,\gamma,\delta}^{N_{basis}} (D_{\alpha\beta} D_{\gamma\delta} - D_{\alpha\delta} D_{\gamma\beta}) \\ & \times \int \int \chi_\alpha^*(\vec{r}_1) \chi_\gamma^*(\vec{r}_2) \hat{g}_{12}(AB) \chi_\beta(\vec{r}_1) \chi_\delta(\vec{r}_2) d\vec{r}_1 d\vec{r}_2 \end{aligned} \quad 2.22a$$

where new density matrices are constructed from the obtained coefficients:

$$D_{\alpha\delta} = 2 \sum_{A,B}^{N/2} c_{\alpha A} c_{\delta B}; D_{\gamma\beta} = 2 \sum_{A,B}^{N/2} c_{\beta A} c_{\gamma B} \quad 2.22b$$

In order to construct a Fock matrix, one-electron integrals between all pairs of basis functions and the \hat{h}_1 operator, as well as two-electron integrals over four basis functions and the \hat{g}_{12} operator, are required. However, since the integrals are a function only of the fixed basis function expressions, the N_{basis}^4 two-electron integrals are computed beforehand and reused at each SCF iteration to construct the Fock matrix. This provides a significant gain in computational efficiency.

Chapter 2: Overview of theoretical methods

The difference between the limiting HF energy, as calculated by a complete basis set, and the energy from an exact solution to the Schrödinger equation is called the *correlation* energy. In the HF approximation the instantaneous interactions between electrons are replaced by interactions of electrons with a static mean field made up of all the other electrons. This decreases the flexibility of electrons to spread out in order to minimize Coulomb repulsion, resulting in a total energy that is too large, or, in other words, not negative enough. Especially for large systems, the most feasible attempt at incorporating electron correlation is that of density functional theory.

2.2 Density Functional Theory (DFT)

In DFT the electronic energy is expressed as a function of the charge density:

$$E_e^{DFT}[\rho] = E_T[\rho] + E_{ne}[\rho] + E_J[\rho] + E_{xc}[\rho] \quad 2.23$$

The first three terms follow directly from the Hartree-Fock approximation, that is, expressions for the kinetic energy (E_T) and the electron-nuclear (E_{ne}) and electron-electron (E_J) Coulomb potential energies. Since both exchange symmetry and correlation results in a lowering of the energy, they are grouped together into the exchange-correlation energy denoted by E_{xc} . The precise form of E_{xc} needed to make Eq. 2.23 an exact solution of the many-electron problem remains elusive, and approximations must be made. The most successful implementation of DFT is based on the Kohn-Sham (KS) approach wherein the electron density is denoted by a set of one-electron spin orbitals. Here follows a short discussion on the fundamentals of DFT, in turn followed by an outline of the procedure used by Becke to arrive at an exchange-correlation functional by parameter fitting to experimental data. The application of this scheme in the recent development of two density functionals is also presented.

2.2.1 Electron density and the Hohenberg-Kohn theorems

The local electron density is defined as the square of the wave function integrated over the spin dimensions (\vec{s}_i) of all N electrons and over the spatial coordinates (\vec{r}_i) of $N - 1$ electrons:

$$\rho(\vec{r}_1) = N \int \cdots \int |\Psi_e(\vec{x}_1, \vec{x}_2, \dots, \vec{x}_n)|^2 d\vec{s}_1 d\vec{x}_2 \cdots d\vec{x}_n \quad 2.24$$

Recall that $\vec{x}_i = (x_i, y_i, z_i, s_i)$ is the four dimensional state vector of electron i representing its position and spin. The multiple integral in the above expression represents the probability of finding a particular electron with arbitrary spin in the volume element $d\vec{r}_1$. Since electrons are indistinguishable, the probability of finding any electron within $d\vec{r}_1$ is N times the probability of finding a single electron therein. The electron density $\rho \equiv \rho(\mathbf{r})$ is a non-negative function of only three spatial coordinates that integrates to the number of electrons, $\int \rho(\mathbf{r}) d\mathbf{r} = N$, and vanishes at infinity, $\rho(\mathbf{r} \rightarrow \infty) = 0$.

Chapter 2: Overview of theoretical methods

In their 1964 paper,⁶ Hohenberg and Kohn showed that (i) the electron density uniquely determines the Hamiltonian, and therefore all properties of the system, and (ii) the energy of an approximate electron density will always be an overestimate of the true ground state energy: $E_{\text{trial}}[\rho_{\text{trial}}(\mathbf{r})] \geq E_0[\rho_0(\mathbf{r})]$. The first of these statements is known as the *proof of existence* theorem, and the second allows for use of the variational principle. These theorems state that an exact relationship exists between the ground-state density and the ground-state energy, but provide no clues as to its functional form.

2.2.2 The Kohn-Sham (KS) approach

In order to improve on earlier attempts at evaluating the energy of a system based only on electron density, Kohn and Sham⁷ introduced the concept of a fictitious non-interacting reference system given by a Slater determinant:

$$\Phi = \frac{1}{\sqrt{N!}} \begin{vmatrix} \vartheta_1(\vec{x}_1) & \vartheta_2(\vec{x}_1) & \cdots & \vartheta_n(\vec{x}_1) \\ \vartheta_1(\vec{x}_2) & \vartheta_2(\vec{x}_2) & \cdots & \vartheta_n(\vec{x}_2) \\ \vdots & \vdots & & \vdots \\ \vartheta_1(\vec{x}_n) & \vartheta_2(\vec{x}_n) & \cdots & \vartheta_n(\vec{x}_n) \end{vmatrix} \quad 2.25$$

The N fictitious KS one-electron spin orbitals ϑ are used to calculate the approximate electron density; that is, ρ_{appr} at a point \vec{r}_1 is equal to the sum of the squares of all the spin orbitals at that point:

$$\sum_i^N |\vartheta_i(\vec{r}_1, s_i)|^2 = \rho_{\text{appr}}(\vec{r}_1) \quad 2.26$$

The closer the expression for the exchange-correlation energy is to the unknown correct form, the more accurate the KS orbitals will be, and, therefore, the closer the approximate density will be to the true ground state electron density. To obtain the unknown KS orbitals, the KS equations are solved iteratively,

$$\hat{f}_1^{KS}(i)\vartheta_i = \varepsilon_i\vartheta_i \quad 2.27a$$

with the one-electron KS operator defined by

$$\hat{f}_1^{KS}(i) = -\frac{\hbar^2}{2m_e}\nabla_{\vec{r}_i}^2 - \frac{e^2}{4\pi\varepsilon_0}\sum_k^M \frac{Z_k}{r_{ik}} + \frac{e^2}{4\pi\varepsilon_0}\int \frac{\rho(\vec{r}_j)}{r_{ij}} d\vec{r}_j + V_{xc}(\vec{r}_i) \quad 2.27b$$

Chapter 2: Overview of theoretical methods

The KS model is closely related to the HF method, with the kinetic energy, electron-nuclear potential and the classical electron-electron Coulomb energies sharing identical expressions. The only term for which no explicit form can be given is the potential due to the exchange-correlation energy, $E_{xc}[\rho]$. The unknown potential is simply defined as the functional derivative of the unknown energy with respect to the electron density, *i.e.*,

$$V_{xc}(\vec{r}_i) = \frac{\delta E_{xc}}{\delta \rho(\vec{r}_i)} \quad 2.27c$$

The electronic energy is now given by

$$\begin{aligned} E_e[\rho(\vec{r}_i)] &= \sum_i^N \int \vartheta_i^*(\vec{r}_i) \left[-\frac{\hbar^2}{2m_e} \nabla_{\vec{r}_i}^2 \right] \vartheta_i(\vec{r}_i) d\vec{r}_i + \sum_i^N \int \sum_k^M \left[-\frac{e^2}{4\pi\epsilon_0} \frac{Z_k}{r_{ik}} \right] \rho(\vec{r}_i) d\vec{r}_i \\ &\quad + \frac{1}{2} \sum_{j>i}^N \int \int \rho(\vec{r}_i) \left[\frac{e^2}{4\pi\epsilon_0} \frac{1}{r_{ij}} \right] \rho(\vec{r}_j) d\vec{r}_i d\vec{r}_j + E_{xc}[\rho(\vec{r}_i)] \end{aligned} \quad 2.28a$$

or, after expanding each KS orbital as a set of basis functions (designated as before (Section 2.1.8) by subscripts α, β, γ and δ for ϑ_i^* , ϑ_i , ϑ_j^* and ϑ_j , respectively), by

$$\begin{aligned} E_e[\rho(\vec{r}_1)] &= \sum_{\alpha,\beta}^{N_{basis}} D_{\alpha\beta} \int \chi_\alpha^*(\vec{r}_1) \left[-\frac{\hbar^2}{2m_e} \nabla_{\vec{r}_1}^2 + \sum_k^M \int \chi_\alpha^*(\vec{r}_1) \left[-\frac{e^2}{4\pi\epsilon_0} \frac{Z_k}{r_{1k}} \right] \right] \chi_\beta(\vec{r}_1) d\vec{r}_1 \\ &\quad + \frac{1}{2} \sum_{\alpha,\beta,\gamma,\delta}^{N_{basis}} D_{\alpha\beta} D_{\gamma\delta} \int \int \chi_\alpha^*(\vec{r}_1) \chi_\gamma^*(\vec{r}_2) \left[\frac{e^2}{4\pi\epsilon_0} \frac{1}{r_{12}} \right] \chi_\beta(\vec{r}_1) \chi_\delta(\vec{r}_2) d\vec{r}_1 d\vec{r}_2 + E_{xc}[\rho(\vec{r}_1)] \end{aligned} \quad 2.28b$$

Similar to the Roothaan-Hall equations (Eq. 2.19b), minimizing the electronic energy with respect to unknown orbital coefficients can conveniently be done by matrix manipulation:

$$\mathbf{F}^{KS} \mathbf{C} = \mathbf{SCE} \quad 2.29$$

Chapter 2: Overview of theoretical methods

That is, by diagonalization of the Kohn-Sham Fock matrix, \mathbf{F}^{KS} , until the density matrix is returned self consistently. Elements of \mathbf{F}^{KS} are given by

$$\begin{aligned} F_{\alpha\beta} = & \int \chi_{\alpha}^*(\vec{r}_1) \left[-\frac{\hbar^2}{2m_e} \nabla_{\vec{r}_1}^2 - \sum_k^M \frac{e^2}{4\pi\varepsilon_0 r_{1k}} Z_k \right] \chi_{\beta}(\vec{r}_1) d\vec{r}_1 \\ & + \sum_{\gamma,\delta}^{N_{basis}} D_{\gamma\delta} \int \int \chi_{\alpha}^*(\vec{r}_1) \chi_{\gamma}^*(\vec{r}_2) \left[\frac{e^2}{4\pi\varepsilon_0} \frac{1}{r_{12}} \right] \chi_{\beta}(\vec{r}_1) \chi_{\delta}(\vec{r}_2) d\vec{r}_1 d\vec{r}_2 \\ & + E_{xc}(\alpha\beta) \end{aligned} \quad 2.30$$

where the form of the exchange-correlation energy, $E_{xc}(\alpha\beta)$ depends on the particular density functional employed.

2.2.3 Exchange-correlation energy

The exchange-correlation energy can conveniently be separated into exchange and correlation parts. The parts are functionalized independently, allowing for different combinations of f_x and f_c to yield an array of complete density functionals:

$$E_{xc}[\rho] = E_x[\rho] + E_c[\rho]$$

where

$$E_x[\rho] = E_x^{\alpha}[\rho_{\alpha}] + E_x^{\beta}[\rho_{\beta}] \quad 2.31$$

$$E_c[\rho] = E_c^{\alpha\alpha}[\rho_{\alpha}] + E_c^{\beta\beta}[\rho_{\beta}] + E_c^{\alpha\beta}[\rho_{\alpha}, \rho_{\beta}]$$

Exchange only involves electrons with parallel spin, whereas correlation occurs between all electrons. Parallel-spin correlation, $E_c^{\sigma\sigma}$ (where σ refers to electron-spin α or β), gives the smallest contribution to the exchange-correlation energy, making it the most difficult to express. The opposite spin correlation, $E_c^{\alpha\beta}$, is larger because it involves both intra- and inter-orbital contributions.

It is useful to write the functional dependence of $E_{xc}[\rho]$ in terms of the exchange-correlation energy per particle, $\epsilon_{xc}(\rho)$:

$$E_{xc}[\rho] = \int \epsilon_{xc}(\rho) d^3\mathbf{r} \quad 2.32$$

In the local spin-density approximation (LSDA), the assumption is made that the electron density can be treated as a uniform spin-polarized electron gas with spin-density equal to its local value ρ_{σ} . The σ -spin exchange-energy density per unit volume is given by

$$\epsilon_{x\sigma}^{LSDA}(\rho_{\sigma}) = -\frac{3}{2} \left(\frac{3}{4\pi} \right)^{1/3} \rho_{\sigma}^{4/3} \quad 2.33$$

Chapter 2: Overview of theoretical methods

The correlation part cannot be expressed in a similarly explicit way, but various parameterizations are available. A popular example is the parameterization that Vosko, Wilk and Nusair⁸ (VWN) derived from Monte Carlo simulations carried out by Ceperley and Alder.⁹

2.2.4 Hybrid functionals

The exchange energy is larger, usually significantly so, than the correlation energy, making the correct expression for $E_x[\rho]$ critical. Fortunately, the exact exchange energy of a Slater determinant can be calculated using the exchange integral of HF theory (K_{ij} , Eq. 2.11d). In terms of one-electron KS spin orbitals, the exact exchange energy is given by

$$E_x^{exact} = -\frac{1}{2} \sum_{i,j}^N \int \int \vartheta_i^*(\vec{x}_1) \vartheta_j^*(\vec{x}_2) \left[\frac{e^2}{4\pi\epsilon_0} \frac{1}{r_{ij}} \right] \vartheta_i(\vec{x}_2) \vartheta_j(\vec{x}_1) d\vec{x}_1 d\vec{x}_2 \quad 2.34$$

In hybrid functionals, a fraction of the exact exchange energy is incorporated as follows:

$$E_x = E_x[\rho] + a_x E_x^{exact} \quad 2.35$$

where the variable a_x is usually determined by fitting to accurate experimental data. The exchange energy cannot, however, be completely represented by the exact expression, due to incompatibility with DFT approximations for the correlation energy. The fraction of exact exchange typically ranges from 20-25% when used for thermochemistry¹⁰ to as high as 40-60% for applications in kinetics.¹¹ The very popular B3LYP functional is denoted by¹²

$$E_{xc}^{B3LYP} = (1 - c_x) E_x^{LSDA} + c_0 E_x^{B88} + c_x E_x^{exact} + (1 - c_c) E_c^{VWN} + c_c E_c^{LYP} \quad 2.36$$

with $E_x^{LSDA} = \sum_{\sigma} \int \epsilon_{x\sigma}^{LSDA}(\rho_{\sigma}) d^3\mathbf{r}$, E_x^{B88} the exchange functional of Becke¹³ and E_c^{LYP} the correlation functional of Lee, Yang and Parr.¹⁴ The values of the scaling factors are $c_0 = 0.72$, $c_x = 0.20$ and $c_c = 0.81$.

Chapter 2: Overview of theoretical methods

2.2.5 Generalized Gradient Approximation functionals; Becke's systematic optimization procedure

To move beyond the LSDA, the energy density of generalized gradient approximation (GGA) functionals is represented as a nonuniform electron gas by also expressing ϵ_{xc} as a function of the gradient of electron density, $\epsilon_{xc\sigma}^{GGA}(\rho_\sigma, \nabla\rho_\sigma)$. In his 1997 paper,¹⁵ Becke presented a procedure that allows for fitting to experimental data to arrive at an exchange-correlation functional at the hybrid-GGA level, namely B97. The exchange part thereof is expressed as follows:

$$E_x^{B97} = \sum_{\sigma} \int \epsilon_{x\sigma}^{LSDA}(\rho_\sigma) g_{x\sigma}(s_\sigma^2) d^3r \quad 2.37$$

where the gradient correction factor, $g_{x\sigma}$, has as its argument the dimensionless reduced spin-density gradient s_σ designated by

$$s_\sigma = \frac{|\nabla\rho_\sigma|}{\rho_\sigma^{4/3}} \quad 2.38$$

The correlation partner of the exchange energy is separated into opposite and parallel spin functions as follows:

$$E_c^{B97} = E_{c\alpha\beta}^{B97} + \sum_{\sigma} E_{c\sigma\sigma}^{B97} \quad 2.39a$$

$$\text{where } E_{c\alpha\beta}^{B97} = \int \epsilon_{c\alpha\beta}^{LSDA}(\rho_\alpha, \rho_\beta) g_{c\alpha\beta}(s_{avg}^2) d^3r \quad 2.39b$$

$$E_{c\sigma\sigma}^{B97} = \int \epsilon_{c\sigma\sigma}^{LSDA}(\rho_\sigma) g_{c\sigma\sigma}(s_\sigma^2) d^3r \quad 2.39c$$

The opposite spin, $\epsilon_{c\alpha\beta}^{LSDA}(\rho_\alpha, \rho_\beta)$, and parallel spin, $\epsilon_{c\sigma\sigma}^{LSDA}(\rho_\sigma)$, local correlation energy densities are derived from the Perdew-Wang¹⁶ parameterization of the LSDA correlation energy using the approach of Stoll *et al.*,¹⁷

$$\epsilon_{c\sigma\sigma}^{LSDA}(\rho_\sigma) = \epsilon_c^{LSDA}(\rho_\sigma, 0) \quad 2.40a$$

$$\epsilon_{c\alpha\beta}^{LSDA} = \epsilon_c^{LSDA}(\rho_\alpha, \rho_\beta) - \sum_{\sigma} \epsilon_c^{LSDA}(\rho_\sigma, 0) \quad 2.40b$$

Stoll *et al.* argued that, because the correlation energies for atoms and molecules are overestimated in the LSDA by roughly a factor of two, the LSDA should only be used for the description of correlation between electrons of different spins. This is accomplished, as shown in Eq. 2.40b, by subtracting the correlation-energy density of the pure spin systems, $\epsilon_c^{LSDA}(\rho_\sigma, 0)$, from the full correlation-energy density, $\epsilon_c^{LSDA}(\rho_\alpha, \rho_\beta)$.

Chapter 2: Overview of theoretical methods

As implemented in Eq. 2.39, the opposite-spin gradient correction, $g_{c\alpha\beta}(s_{avg}^2)$, is assumed to depend on the single variable $s_{avg}^2 = (s_\alpha^2 + s_\beta^2)/2$, whereas the like-spin gradient correction factors are assumed to depend on s_α^2 and s_β^2 independently.

The expressions for the gradient correction factors are given by,

$$g_{x\sigma}(s_\sigma^2) = \frac{(1 + b_{x\sigma}s_\sigma^2)}{(1 + \gamma_{x\sigma}s_\sigma^2)} \quad 2.41a$$

$$g_{c\alpha\beta}(s_{avg}^2) = (1 + \gamma_{c\alpha\beta}s_{avg}^2)^{-1} \quad 2.41b$$

$$g_{c\sigma\sigma}(s_\sigma^2) = (1 + \gamma_{c\sigma\sigma}s_\sigma^2)^{-1} \quad 2.41c$$

The parameters were optimized to reproduce HF atomic energies and are summarized in Eq. 2.42. The gradient correction of Eq. 2.41a is based on Becke's 1986 empirical exchange-energy function,¹⁸ " $X_{\alpha\beta\gamma}$ ", which he optimized by a least squares fit to the HF exchange energy of atomic systems. The parameters of $X_{\alpha\beta\gamma}$ are implemented in B97 without change. The functions used to correct the LSDA opposite- and parallel-spin correlation energy densities are given by Eqs. 2.41b and 2.41c, respectively. The non-linear opposite-spin correlation parameter, $\gamma_{c\alpha\beta}$, is chosen to give the correct correlation energy for helium when $E_{c\alpha\beta}^{B97}$ (Eq. 2.39b) is used as a standalone function. For like-spin correlation, $\gamma_{c\sigma\sigma}$ is chosen to reproduce the total correlation energy E_c^{B97} (Eq. 2.39a) of Ne.

$$b_{x\sigma} = 0.00787 \quad ; \quad \gamma_{x\sigma} = 0.004 \quad 2.42a$$

$$\gamma_{c\alpha\beta} = 0.006 \quad 2.42b$$

$$\gamma_{c\sigma\sigma} = 0.2 \quad 2.42c$$

Due to the semi-infinite domain of the gradient correction argument $s_\sigma \in [0, \infty)$ is remapped to a new variable according to

$$u_\sigma = \frac{\gamma s_\sigma^2}{(1 + \gamma s_\sigma^2)} \quad 2.43a$$

where u_σ has the finite domain $[0, 1]$:

$$\lim_{s_\sigma^2 \rightarrow 0} u_\sigma = 0 \leq u \leq 1 = \lim_{s_\sigma^2 \rightarrow \infty} u_\sigma \quad 2.43b$$

Chapter 2: Overview of theoretical methods

Employing the non-linear atomic optimized parameters of Eq. 2.42, the new arguments of the gradient corrections in terms of u_σ become

$$u_{x\sigma} = \frac{\gamma_{x\sigma} s_\sigma^2}{(1 + \gamma_{x\sigma} s_\sigma^2)} \quad 2.44a$$

$$u_{c\alpha\beta} = \frac{\gamma_{c\alpha\beta} s_{avg}^2}{(1 + \gamma_{c\alpha\beta} s_{avg}^2)} \quad 2.44b$$

$$u_{c\sigma\sigma} = \frac{\gamma_{c\sigma\sigma} s_\sigma^2}{(1 + \gamma_{c\sigma\sigma} s_\sigma^2)} \quad 2.44c$$

Substituting Eq. 2.43 into Eq. 2.41, the linearized gradient correction functions are now given by

$$g_{x\sigma}(u_{x\sigma}) = 1 + \left(\frac{b_{x\sigma}}{\gamma_{x\sigma}} - 1 \right) u_{x\sigma} = 1 + 0.967 u_{x\sigma} \quad 2.45a$$

$$g_{c\alpha\beta}(u_{c\alpha\beta}) = 1 - u_{c\alpha\beta} \quad 2.45b$$

$$g_{c\sigma\sigma}(u_{c\sigma\sigma}) = 1 - u_{c\sigma\sigma} \quad 2.45c$$

The final step in the systematic optimization scheme is the expansion of each gradient correction function of Eq. 2.45 in a power series as follows (subscripts omitted for brevity),

$$g = \sum_{i=0}^m c_i u^i \quad 2.46$$

where the coefficients c_i and expansion order m are determined by least-squares fitting to accurate experimental and/or theoretical data. As recommended by Becke himself, a fraction of exact exchange is included as follows:¹⁰

$$E_{xc}^{B97} = E_x^{B97} + c_x E_x^{HF} + E_c^{B97} \quad 2.47$$

where c_x is a linear parameter to be determined.

The uniform electron gas limit, which requires that all $c_0 = 1$, is not enforced and this ($i = 0$) leading term for each of $g_{x\sigma}$, $g_{c\alpha\beta}$ and $g_{c\sigma\sigma}$ is treated as a free parameter. If the series expansions are all truncated uniformly at order m , there are $(3m + 4)$ linear parameters to be determined by least-squares fitting. Becke used the augmented thermochemical data set G2 of Pople and co-workers¹⁹ as a training set and concluded that expansion order $m = 2$ is optimal.

2.3 The dispersion interaction

Although DFT within the KS scheme is, in principle, able to provide the exact ground state energy of a system, widely used density functional approximations cannot simulate the correlated motion of electrons and consequently fail when predicting dispersion bound complexes. A robust and efficient way to overcome this problem is to add an empirical atom-pairwise dispersion correction to the standard mean-field energy:²⁰

$$E_{DFT-D} = E_{DFT} + E_{dispersion} \quad 2.48$$

In the approximation that the charge distributions of the interacting species do not overlap appreciably, the dispersion potential between two ground state spherically symmetric species A and B can be expressed according to a multipole expansion approximation:²¹

$$V_{dispersion}(R_{AB}) = - \sum_{n=3,4,5,\dots}^{\infty} \sum_A^{N_{at}-1} \sum_{B>A}^{N_{at}} \frac{C_{AB,2n}}{R_{AB}^{2n}} \quad 2.49$$

where R_{AB} is the internuclear separation. The $C_{AB,2n}$ constants are dispersion coefficients where, of the leading terms, $C_{AB,6}$ describes the interaction between two instantaneous dipoles, $C_{AB,8}$ the interaction between a quadrupole and a dipole, and $C_{AB,10}$ includes the interaction between a dipole and an octupole and between two quadrupoles. When orbital overlap is substantial, the multipole expansion is no longer valid.²² Furthermore, in the short-range region standard density functionals already account for correlation to various extents. The multipole expansion approximation should therefore be restricted to the mid- and long-ranges to prevent *double counting* of correlation effects. A practical way to accomplish this is to incorporate a damping function into the multipolar expansion, as was first suggested by Brooks:²³

$$E_{dispersion}(R_{AB}) = - \sum_{n=3,4,5,\dots}^{\infty} \sum_A^{N_{at}-1} \sum_{B>A}^{N_{at}} f_{d,2n} \frac{C_{AB,2n}}{R_{AB}^{2n}} \quad 2.50$$

The always-positive value of the damping function, $f_{d,2n}$, is unity in the range where overlap is negligible and less than one for distances at which orbital overlap is appreciable. The magnitude of the dispersion energy is therefore effectively scaled, depending on the interatomic separation relative to some cut-off distance.

One of the most widely applied dispersion correction schemes is that of DFT-D developed by Grimme.²⁴ Here follows a short discussion of the GGA functional B97D he parameterized in conjunction with the second generation DFT-D scheme (referred to as GD2 in this work). The third generation DFT-D (GD3) will be elaborated on in Section 2.6.1. In addition, the dispersion correction of Chai and Head-Gordon's ω B97XD functional is discussed in Section 2.5.3, while the dispersion correction scheme of Tkatchenko and Scheffler is described in Section 2.6.2.

2.4 Grimme's B97D functional

2.4.1 The exchange-correlation functional

Grimme used the flexible power series of Becke discussed previously to develop a pure (nonhybrid) GGA functional, *i.e.*, with $c_x = 0$ in Eq. 2.47.²⁵ The gain in computational efficiency makes the pure functional applicable to very large systems. The density dependent part of the B97D functional is expressed as

$$E_{xc}^{B97D} = E_x^{B97D} + E_{c\alpha\beta}^{B97D} + \sum_{\sigma} E_{c\sigma\sigma}^{B97D} \quad 2.51$$

Each term in Eq. 2.51 is exactly the same as in Becke's B97 functional (*cf.* Eqs. 2.37 and 2.39) and, after the power series expansion (Eq. 2.46) is introduced, they are given by:

$$E_x^{B97D} = \sum_{\sigma} \int \epsilon_{x\sigma}^{LSDA}(\rho_{\sigma}) \sum_{i=0}^m c_{x\sigma,i} u_{x\sigma}^i d^3\mathbf{r} \quad 2.52a$$

$$E_{c\alpha\beta}^{B97D} = \int \epsilon_{c\alpha\beta}^{LSDA}(\rho_{\alpha}, \rho_{\beta}) \sum_{i=0}^m c_{c\alpha\beta,i} u_{c\alpha\beta}^i d^3\mathbf{r} \quad 2.52b$$

$$E_{c\sigma\sigma}^{B97D} = \sum_{\sigma} \int \epsilon_{c\sigma\sigma}^{LSDA}(\rho_{\sigma}) \sum_{i=0}^m c_{c\sigma\sigma,i} u_{c\sigma\sigma}^i d^3\mathbf{r} \quad 2.52c$$

The uniform electron gas σ -spin-polarized energy densities, ϵ_{σ}^{LSDA} , were defined in Eq. 2.33 for exchange, and in Eq. 2.40 for correlation. Recall that the respective remapped gradient arguments, u_{σ} , are given by $u_{\sigma} = \gamma s_{\sigma}^2 / (1 + \gamma s_{\sigma}^2)$ (Eq. 2.43), where s_{σ}^2 is the reduced spin gradient given by $s_{\sigma} = |\nabla \rho_{\sigma}| / \rho_{\sigma}^{4/3}$ (Eq. 2.38). Grimme reused the nonlinear γ -parameters that Becke optimized for atomic energies (Eq. 2.42) and also did not enforce the uniform electron gas limit. He supported use of expansion order $m = 2$ and redetermined the $3m + 3 = 9$ linear expansion coefficients, c_i , by least-squares fitting with respect to an expansive training set of atomic and molecular systems. This parameter fitting was carried out in the presence of the GD2 dispersion correction, to be discussed next.

Chapter 2: Overview of theoretical methods

2.4.2 The GD2 dispersion-correction scheme

In the same paper in which he presented the B97D functional, Grimme introduced the second generation of his DFT-D scheme.²⁵ Using a single global scaling factor, this correction can be combined with any density functional. The empirical correction is truncated after $n = 3$ (*cf.* Eq. 2.50) and is given by

$$E_{disp}^{GD2} = -s_6 \sum_A^{N_{at}-1} \sum_{B>A}^{N_{at}} \frac{C_{AB,6}}{R_{AB}^6} f_{dmp}(R_{AB}) \quad 2.53$$

Here $C_{AB,6}$ denotes the isotropic 6th order dispersion coefficient for atom pair AB , s_6 is a global scaling factor optimized for a specific DF, and R_{AB} is the interatomic distance. In order to avoid near-singularities for small R , a damping function of the following form is used:^{20a}

$$f_{dmp} = \frac{1}{1 + e^{-d(R_{AB}/R_{AB,0} - 1)}} \quad 2.54$$

where $R_{AB,0}$ is the sum of atomic van der Waals radii based on the radius of the $0.01a_0^{-3}$ electron density contour from ROHF/TZV computations of the atoms in their ground states, scaled by a factor of 1.10. A value of $d = 20$ makes the damping function sufficiently steep to quickly reduce the magnitude of the correction in the short-range.

To calculate the composed $C_{AB,6}$ coefficients, the geometric mean of the atomic coefficients is used as the combination rule:

$$C_{AB,6} = \sqrt{C_{A,6} C_{B,6}} \quad 2.55$$

The atomic $C_{i,6}$ coefficients are derived from the London formula for dispersion,²⁶ based on PBE0 calculations²⁷ of atomic ionization potentials, I^P , and static dipole polarizabilities, α . The C_6 coefficient for atom A (in $\text{J nm}^6 \text{ mol}^{-1}$) is then given as

$$C_{A,6} = 0.05 N I_A^P \alpha_A \quad 2.56$$

where N has values 2, 10, 18, 36, and 54 respectively for atoms from rows 1-5 of the periodic table. The free atom coefficients of Group I and II elements and transition metals differ considerably from their values in bonding situations. To overcome this, the coefficients of these elements are taken as the average of the coefficients of the preceding rare gas and the following Group III element.

The s_6 scale factors were determined through least squares fitting of interaction energies of 40 noncovalent complexes to be 1.25, 0.75 and 1.05 for s_6^{B97D} , s_6^{PBE0} and s_6^{B3LYP} , respectively. The GD2 parameterization works well with all DFs considered, but B97D was found to yield the best overall results. This is because the short-range, density-dependent part of B97D has been adjusted in the presence of the long-range correction.

2.5 Explicit long-range correction

DFT and wave function methods are, to some extent, complementary. DFT provides a reliable treatment of dynamical correlation effects, but cannot describe long-range van der Waals interactions correctly. On the other hand, wave function methods accurately treat static correlation as well as long-range correlation effects.²⁸ To properly describe the two-electron interaction, $1/r_{ij}$ (in terms of atomic units), which has a singularity for $r_{ij} \rightarrow 0$, arduous wave function methods must be employed. One approach to overcome this is to replace $1/r_{ij}$ with $h(r_{ij})/r_{ij}$, where $h(r_{ij})$ is a suitable cut-off function for $r_{ij} \rightarrow 0$.²⁹ Thereby only the long-range part of the electron-electron interaction is retained. The short-range part of r_{ij} can, however, not simply be neglected. DFT presents an accurate means of implicitly treating $[1 - h(r_{ij})]/r_{ij}$ without taking explicit care of the correlation cusp ($r_{ij} \rightarrow 0$). In long-range corrected density functionals, the long-range exchange energy is treated explicitly by Hartree-Fock theory (E_x^{lr-HF}), while a density functional approximation is maintained for the short-range exchange and full correlation energy ($E_x^{sr-DFT} + E_c^{DFT}$).³⁰ In order to avoid double counting of long-range exchange-correlation effects, a generally accurate E_x^{sr-DFT} that is compatible with the full E_c^{DFT} and E_x^{lr-HF} needs to be constructed. Here follows a discussion on how the two-electron operator is efficiently partitioned into short-range and long-range parts. The development of the ω B97X functional of Chai and Head-Gordon³¹ is then presented in Section 2.5.2, along with its dispersion corrected form ω B97XD³² in Section 2.5.3.

2.5.1 The partitioned Coulomb operator

The Coulomb operator describing the electron-electron interaction, $v_{ee}(\vec{r}_1, \vec{r}_2)$ (denoted $\hat{g}_{12}(ij)$ in Eq. 2.4c in SI units), is partitioned into a nonsingular, slowly decaying long-range part and a singular short-range part using the standard error function $\text{erf}(z) = \frac{2}{\sqrt{\pi}} \int_0^z e^{-t^2} dt$ as follows:³³

$$v_{ee} = v_{ee}^{lr} + v_{ee}^{sr} \quad 2.57a$$

where, in atomic units,[▼]

$$v_{ee}^{lr} = \frac{\text{erf}(\omega r_{12})}{r_{12}} \quad 2.57b$$

$$v_{ee}^{sr} = \frac{1 - \text{erf}(\omega r_{12})}{r_{12}} \quad 2.57c$$

The parameter ω defines the reach of the short-range component of the interaction, which is roughly proportional to $1/\omega$. Therefore, the smaller the value of ω , the longer will be the range of the short-range operator (v_{ee}^{sr}).

[▼] In atomic units $\hbar = e^2 = m_e = 1$, energies are in hartrees (= 627.5095 kcal.mol⁻¹) and distances are in Bohr (= 5.291×10^{-11} m), as derived from terms in the Hamiltonian, Eq. 2.2.

Chapter 2: Overview of theoretical methods

The exact long-range exchange is represented by the following integral of Hartree-Fock theory (Eq. 2.11d; *cf.* Eq. 2.34 for the unpartitioned exchange integral in SI units):

$$E_x^{lr-HF} = -\frac{1}{2} \sum_{i,j}^N \int \int \phi_i^*(\vec{x}_1) \phi_j^*(\vec{x}_2) \frac{\text{erf}(\omega r_{12})}{r_{12}} \phi_i(\vec{x}_2) \phi_j(\vec{x}_1) d\vec{x}_1 d\vec{x}_2 \quad 2.58$$

In DFT, this integral is substituted by an exchange functional that is generally defined as

$$E_x^{DFT} = -\frac{1}{2} \sum_{\sigma} \int K_{\sigma} \rho_{\sigma}^{4/3}(\mathbf{r}) d^3\mathbf{r} \quad 2.59$$

where ρ_{σ} is the density of the σ -spin (α or β) electrons. K_{σ} is a dimensionless parameter that is given by $K_{\sigma}^{LSDA} = 3[3/(4\pi)]^{1/3}$ for the LSDA (*cf.* Eq. 2.33).

Evaluation of the first-order density matrix (1DM) is necessary to define the dependence of the exchange functional on the electron-electron distance r_{12} .³⁴ In the Bardeen model of a metal surface with electrons confined by an infinite planar barrier, the 1DM for the LSDA exchange functional is given by³⁵

$$P_{1\sigma}^{LSDA}(\mathbf{R}) = 3 \frac{j_1(k_{\sigma} r_{12})}{k_{\sigma} r_{12}} \rho_{\sigma}(\mathbf{R}) \quad 2.60$$

where $\mathbf{R} = (\vec{r}_1 + \vec{r}_2)/2$, $j_1(x) = (\sin x - x \sin x)/x^2$ is the first-order spherical Bessel function, and k_{σ} is the averaged relative momentum, written for the LSDA as the Fermi momentum:

$$k_{\sigma}^{LSDA} = k_{F\sigma} = (6\pi^2 \rho_{\sigma}(\mathbf{r}))^{1/3} \quad 2.61$$

A general short-range exchange energy expression is given by

$$E_x^{sr-DFT} = -\frac{1}{2} \sum_{\sigma} \int K_{\sigma} \rho_{\sigma}^{4/3}(\mathbf{r}) \int_0^{\infty} |P_{1\sigma}^{LSDA}(\mathbf{R})|^2 \times \frac{1 - \text{erf}(\omega r_{12})}{r_{12}} d^3\mathbf{R} d^3\mathbf{r} \quad 2.62$$

Integration of the square of the LSDA 1DM multiplied by the v_{ee}^{sr} operator results in³⁶

$$E_x^{sr-DFT} = -\frac{1}{2} \sum_{\sigma} \int K_{\sigma} \rho_{\sigma}^{4/3}(\mathbf{r}) F(a_{\sigma}) d^3\mathbf{r} \quad 2.63$$

where $a_{\sigma} = \omega/(2k_{\sigma})$ is a dimensionless parameter controlling the values of the attenuation function $F(a_{\sigma})$:

$$F(a_{\sigma}) = 1 - \frac{8}{3} a_{\sigma} \left[\sqrt{\pi} \text{erf} \left(\frac{1}{2a_{\sigma}} \right) - 3a_{\sigma} + 4a_{\sigma}^3 + (2a_{\sigma} - 4a_{\sigma}^3) e^{\left(\frac{-1}{4a_{\sigma}^2} \right)} \right] \quad 2.64$$

Chapter 2: Overview of theoretical methods

A general expression for a long-range corrected hybrid (LC-hybrid) functional can be given as follows:

$$E_{xc}^{LC-DFT} = E_x^{lr-HF} + E_x^{sr-DFT} + E_c^{DFT} \quad 2.65$$

where exchange is treated explicitly by wave function theory in the long-range, and approximated by DFT in the short-range. Correlation is described at the DFT level of theory. Here follows a discussion on the commonly applied ω B97X LC-hybrid functional.

2.5.2 The ω B97X functional

Chai and Head-Gordon used the flexible power series expansion of Becke¹⁵ to arrive at a robust LC-hybrid functional, ω B97X.³¹ Similar to Becke's adiabatic-connection argument for admixing a fraction of exact exchange in hybrid functionals,¹⁰ mixing a fraction of short-range HF exchange with the short-range DFT exchange should also improve the performance of LC-hybrids for thermochemistry. The ω B97X functional is expressed as

$$E_{xc}^{\omega\text{B97X}} = E_x^{lr-HF} + c_x E_x^{sr-HF} + E_x^{sr-B97} + E_c^{B97} \quad 2.66$$

where c_x is a fractional number to be determined. The terms for ω B97X are expressed as follows:

$$E_x^{lr-HF} = -\frac{1}{2} \sum_{i,j}^N \int \int \phi_i^*(\vec{x}_1) \phi_j^*(\vec{x}_2) \frac{\text{erf}(\omega r_{12})}{r_{12}} \phi_i(\vec{x}_2) \phi_j(\vec{x}_1) d\vec{x}_1 d\vec{x}_2 \quad 2.67\text{a}$$

$$E_x^{sr-HF} = -\frac{1}{2} \sum_{i,j}^N \int \int \phi_i^*(\vec{x}_1) \phi_j^*(\vec{x}_2) \frac{1 - \text{erf}(\omega r_{12})}{r_{12}} \phi_i(\vec{x}_2) \phi_j(\vec{x}_1) d\vec{x}_1 d\vec{x}_2 \quad 2.67\text{b}$$

$$E_x^{sr-B97} = \sum_{\sigma} \int \epsilon_{x\sigma}^{sr-LSDA}(\rho_{\sigma}) \sum_{i=0}^m c_{x\sigma,i} u_{x\sigma}^i d^3\mathbf{r} \quad 2.67\text{c}$$

$$E_{c\alpha\beta}^{B97} = \int \epsilon_{c\alpha\beta}^{LSDA}(\rho_{\alpha}, \rho_{\beta}) \sum_{i=0}^m c_{c\alpha\beta,i} u_{c\alpha\beta}^i d^3\mathbf{r} \quad 2.67\text{d}$$

$$E_{c\sigma\sigma}^{B97} = \sum_{\sigma} \int \epsilon_{c\sigma\sigma}^{LSDA}(\rho_{\sigma}) \sum_{i=0}^m c_{c\sigma\sigma,i} u_{c\sigma\sigma}^i d^3\mathbf{r} \quad 2.67\text{e}$$

Chapter 2: Overview of theoretical methods

The uniform electron gas σ -spin-polarized exchange-energy density of Eq. 2.67c is defined as in Eq. 2.63 by

$$\epsilon_{x\sigma}^{sr-LSDA}(\rho_\sigma) = -\frac{3}{2} \left(\frac{3}{4\pi} \right)^{1/3} \rho_\sigma^{4/3}(\mathbf{r}) \times F(a_\sigma) \quad 2.68$$

with the argument of the attenuation function ($F(a_\sigma)$, Eq. 2.64) given as before by $a_\sigma = \omega(48\pi\rho_\sigma(\mathbf{r}))^{-1/3}$. This exchange-energy density expression reduces to the original LSDA definition (Eq. 2.33) in the limit $\omega = 0$. The total correlation energy, E_c^{B97} , of Eq 2.66 is made up of the opposite-spin and parallel-spin contributions from Eqs. 2.67d and 2.67e, respectively, with the correlation energy-densities expressed as in their original forms defined in Eq. 2.40). Recall that in order to linearize the gradient correction functionals the reduced spin gradient, $s_\sigma = |\nabla\rho_\sigma|/\rho_\sigma^{4/3}$, was remapped to u_σ according to $u_\sigma = \gamma s_\sigma^2/(1 + \gamma s_\sigma^2)$ (Eq. 2.43). Chai *et al.* retained the nonlinear γ -parameters that Becke optimized for atomic energies (Eq. 2.42).

The uniform electron gas limit is enforced by restraining the leading terms of the expansions of the gradient correction as follows:

$$c_{ca\beta,0}^{\omega B97X} = 1 \quad 2.69a$$

$$c_{c\sigma\sigma,0}^{\omega B97X} = 1 \quad 2.69b$$

$$c_{x\sigma,0}^{\omega B97X} + c_x^{\omega B97X} = 1 \quad 2.69c$$

For a fixed range-separation parameter ω and with a uniform truncation imposed at expansion order m , there are $3m + 1$ linear parameters to be optimized by least-squares fitting. Chai *et al.* used a training set of 412 accurate experimental and theoretical results and found an expansion order of $m = 4$ to be optimal, along with a range partitioning parameter of $\omega = 0.3$ bohr⁻¹.

In a performance comparison, ω B97X showed an improved description of kinetics and thermochemistry. Long-range correlation effects, however, are not treated correctly.³¹ To overcome this, Chai and Head-Gordon subsequently introduced an empirical dispersion correction to the ω B97X functional to afford the ω B97XD functional.

Chapter 2: Overview of theoretical methods

2.5.3 The dispersion-corrected ω B97XD functional

Chai and Head-Gordon based their dispersion correction on the GD2 correction, Section 2.4.2, but without a global scaling factor, *i.e.*, $s_6 = 1$, and a damping function of the following form (*cf.* Eq. 2.54):³²

$$f_{dmp}(R_{AB}) = \frac{1}{1 + a(R_{AB}/R_{AB,0})^{-12}} \quad 2.70$$

This form for f_{dmp} fixes undesirable divergence of the dispersion correction at small interatomic separations. The nonlinear parameter a controls how sharply the dispersion corrections are scaled and a value $a = 6$ was chosen. The GD2 scheme's constants $C_{AB,6}$ and $R_{AB,0}$ were employed without change. To prevent double-counting of correlation effects from the KS-DFT and the dispersion correction, all 14 parameters in ω B97X were redetermined in the presence of the dispersion correction by a least-squares fitting procedure.

It is interesting to compare some aspects of the optimized parameters of the ω B97X and ω B97XD functionals. The value of ω is reduced from 0.3 bohr⁻¹ in ω B97X to 0.2 bohr⁻¹ in ω B97XD. The fraction of short-range exact exchange (c_x) simultaneously increases from 0.16 in ω B97X to 0.22 in ω B97XD. Inclusion of the dispersion correction therefore increases the optimal length from which exact long-range exchange is used while, to compensate, the fraction of exact exchange admixed at short distances is increased.

In an assessment of the distance dependence of hydrogen bonding between bimolecular complexes of formic acid, formamide and formamidine, Thanthiriwatte *et al.* found that, among the DFT-D schemes, ω B97XD gave the best overall results in comparison to CCSD(T) interaction energies extrapolated to the complete basis set limit.³⁷

2.6 Non-empirical dispersion correction

In order to decrease the empiricism of the dispersion correction, Grimme proposed calculation of $C_{AB,6}$ coefficients from first principles.³⁸ In his third-generation dispersion correction scheme, DFT-D3 (designated GD3 in this work), 8th-order dispersion coefficients,⁴ calculated recursively from the $C_{AB,6}$ values, are included. The contribution of an atom to the dispersion interaction of a molecule depends on its chemical environment. To incorporate this into GD3, Grimme developed the ansatz of a fractional coordination number. Here follows a short discussion of how this was accomplished, followed by a description of another *ab initio* dispersion correction, *i.e.* that of Tkatchenko and Scheffler.

⁴ The contribution of $C_{AB,8}$ terms was recently found to be non-negligible,³⁹ but the damping optimization procedure partially account for the missing dispersion energy in the 6th-order truncated correction schemes.

Chapter 2: Overview of theoretical methods

2.6.1 The GD3 dispersion-correction scheme

The following atom-pairwise interaction expression is used for the third generation of Grimme's DFT-D dispersion correction:³⁸

$$E_{disp}^{GD3} = - \sum_{n=3,4} \sum_A^{N_{at}-1} \sum_{B>A}^{N_{at}} s_{2n} \frac{C_{AB,2n}}{R_{AB}^{2n}} f_{d,2n}(R_{AB}) \quad 2.71$$

where the terms have the same meaning as before. The s_6 scaling factor is set to unity while the s_8 factor is adjusted empirically for a specific density functional. A variant of the damping function $f_{d,2n}$ proposed by Chai and Head-Gordon (Eq. 2.70),³² which is numerically stable and convenient also for higher dispersion orders, is employed:

$$f_{d,2n}(R_{AB}) = \frac{1}{1 + 6(R_{AB}/(s_{r,2n} R_{AB,0}))^{-\alpha_{2n}}} \quad 2.72$$

where $s_{r,2n}$ is an order-dependent scaling factor of the cutoff radii, $R_{AB,0}$. The $s_{r,6}$ factor is adjusted for each DF, while it was decided to fix $s_{r,8}$ to unity. The *steepness* parameters have values of $\alpha_6 = 14$ and $\alpha_8 = 16$.

In the GD3 scheme, the C_6 dispersion coefficients are computed *ab initio* by time-dependent DFT. According to the Casimir-Polder formula,⁴⁰ the orientation-averaged $C_{AB,6}$ dispersion coefficient between atoms A and B can be expressed in terms of their respective frequency-dependent polarizabilities as follows:⁴¹

$$C_{AB,6} = \frac{3}{\pi} \int_0^{\infty} \alpha_A(i\omega) \alpha_B(i\omega) d\omega \quad 2.73$$

where $\alpha_A(i\omega)$ is the isotropic average dipole polarizability of atom A at imaginary frequency ω :

$$\alpha_A(i\omega) \equiv \bar{\alpha}_A(i\omega) = \frac{\alpha_{A,xx}(i\omega) + \alpha_{A,yy}(i\omega) + \alpha_{A,zz}(i\omega)}{3} \quad 2.74$$

Each term in the above expression is a diagonal element of the dipole polarizability tensor. Calculation of the $C_{AB,6}$ dispersion coefficient therefore involves determination of the frequency-dependent dipole polarizability tensor at a range of imaginary frequencies (through time-dependent DFT), followed by evaluation of the Casimir-Polder integral by numerical quadrature.

Chapter 2: Overview of theoretical methods

The $\alpha_A(i\omega)$ values of free atoms are easy to determine, but can be very large due to energetically low-lying atomic states. These states are mostly quenched during bond formation in that fractionally occupied atomic orbitals become doubly occupied, energetically lower-lying molecular orbitals. The $\alpha_A(i\omega)$ values are therefore computed for simple molecules with well-defined electronic structures. Apart from the noble gases, every element forms at least one stable hydride: A_mH_n , where m and n are stoichiometric factors. The elemental polarizabilities are then calculated from the polarizabilities of reference hydrides after removal of the hydrogen contribution:

$$\alpha_A(i\omega) = \frac{1}{m} \left[\alpha_{A_mH_n}(i\omega) - \frac{n}{2} \alpha_{H_2}(i\omega) \right] \quad 2.75$$

where $\alpha_{A_mH_n}(i\omega)$ and $\alpha_{H_2}(i\omega)$ are the averaged dipole polarizability at frequency $i\omega$ of the reference A_mH_n and dihydrogen molecules, respectively. The two-body 6th order dispersion coefficient for the AB pair is then calculated using the Casimir-Polder integral:

$$C_{AB,6} = \frac{3}{\pi} \int_0^{\infty} \frac{1}{m} \left[\alpha_{A_mH_n}(i\omega) - \frac{n}{2} \alpha_{H_2}(i\omega) \right] \times \frac{1}{k} \left[\alpha_{B_kH_l}(i\omega) - \frac{l}{2} \alpha_{H_2}(i\omega) \right] d\omega \quad 2.76$$

where $\alpha_{B_kH_l}(i\omega)$ is the polarizability of the reference hydride of element B. The environment of an atom can greatly influence its contribution to the dispersion coefficient of a molecule. Elements that can undergo various modes of bonding, *i.e.* exhibit several hybridization states, or coordination numbers (CNs), require several representative hydrides. For carbon, for example, ethane, ethene and ethyne are used for CNs 2 to 4. Values for C-H and C complete the set of five *reference molecules* for carbon. Each element is then represented by a set of $\alpha_A(i\omega)$ values (Eq. 2.75, five for carbon) that span the normal bonding modes of that element. All combinations of reference molecules are used to precompute $C_{AB,6}^{ref}(CN_i^A, CN_j^B)$ values according to Eq. 2.76, where CN_i^A is the coordination number of element A in reference molecule i and CN_j^B the coordination number of element B in reference molecule j . A total of 254 reference molecules for elements up to $Z = 94$ have been computed, giving about 3.2×10^4 different $C_{AB,6}^{ref}(CN_i^A, CN_j^B)$ values.⁴²

The *fractional* coordination number (*fCN*) of an atom is used to infer its chemical environment in the system under investigation. The *fCN* an atom A is determined using a distance-dependent counting function:

$$fCN^A = \sum_{B \neq A}^{N_{at}} \left[1 + e^{-k_1 \left(\frac{k_2(R_{A,cov} + R_{B,cov})}{R_{AB}} - 1 \right)} \right]^{-1} \quad 2.77$$

where $R_{A,cov}$ is the covalent single-bond radius of atom A. The values of Pyykkö and Atsumi,⁴³ scaled by $k_2 = 4/3$, were used, with the covalent radii of metallic elements scaled by an additional 10%. A value of $k_1 = 16$ prevents very distant atoms from being “counted”.

Chapter 2: Overview of theoretical methods

The fCN s obtained for a specific pair of atoms (A and B) in a system are then used to obtain the $C_{AB,6}(fCN^A, fCN^B)$ coefficient that best describes the dispersion interaction between atoms A and B in their respective chemical environments. All the precomputed $C_{AB,6}^{ref}(CN_i^A, CN_j^B)$ values for the two elements of interest serve as supporting points in a two-dimensional interpolation procedure. A simple Gaussian-distance weighted average is used:

$$C_{AB,6}(fCN^A, fCN^B) = \frac{Z}{W} \quad 2.78a$$

$$Z = \sum_i^{N_A} \sum_j^{N_B} L_{ij} C_{AB,6}^{ref}(CN_i^A, CN_j^B) \quad 2.78b$$

$$L_{ij} = e^{-k_3[(fCN^A - CN_i^A)^2 + (fCN^B - CN_j^B)^2]} \quad 2.78c$$

$$W = \sum_i^{N_A} \sum_j^{N_B} L_{ij} \quad 2.78d$$

where N_A and N_B are the number of reference molecules for atoms A and B , respectively. As seen from its calculation in Eq. 2.78c, the scaling function L_{ij} is larger for value(s) of CN_i^A and/or CN_j^B close to fCN^A and/or fCN^B , respectively, thereby bestowing a greater weight to the corresponding precomputed $C_{AB,6}^{ref}(CN_i^A, CN_j^B)$ value in the summation of Eq. 2.78b. W is the normalizing factor, so that Z , made up of $(N_A + N_B)$ $C_{AB,6}^{ref}(CN_i^A, CN_j^B)$ factors, is scaled back to a *single* $C_{AB,6}(fCN^A, fCN^B)$ value. A value of $k_3 = 4$ allows for a smooth interpolation function, Eq. 2.78a with plateaus near integer CN values.

The 8th order dispersion coefficients are computed recursively from $C_{AB,6}(fCN^A, fCN^B)$ using values of $\langle r^n \rangle$, ground-state expectation values derived from atomic densities, according to⁴⁴

$$C_{AB,8} = 3C_{AB,6}(fCN^A, fCN^B)\sqrt{Q_A Q_B} \quad 2.79a$$

$$Q_j = s_{42}\sqrt{Z_j} \frac{\langle r^4 \rangle_j}{\langle r^2 \rangle_j} \quad 2.79b$$

$$\langle r^n \rangle = \int_0^{\infty} r^n \rho(r) dr \quad 2.79c$$

The value of factor s_{42} was chosen such that reasonable self-interaction $C_{AA,6}$ values for He, Ne, and Ar are obtained.

Chapter 2: Overview of theoretical methods

The GD3 scheme, after omitting those parameters set to unity, is given by

$$E_{disp}^{GD3} = - \sum_A^{N_{at}-1} \sum_{B>A}^{N_{at}} \left\{ \frac{C_{AB,6}}{R_{AB}^6 \left[1 + 6 \left(\frac{R_{AB}}{s_{r,6} R_{AB,0}} \right)^{-14} \right]} + \frac{s_8 C_{AB,8}}{R_{AB}^8 \left[1 + 6 \left(\frac{R_{AB}}{R_{AB,0}} \right)^{-16} \right]} \right\} \quad 2.80$$

where $C_{AB,6}$ is the $C_{AB,6}(fCN^A, fCN^B)$ value as computed by Eq. 2.78a for the atom pair of interest.

The GD3 scheme can be used to augment any density functional by adjusting the $s_{r,6}$ and s_8 parameters. For the B97D, PBEPBE and B3LYP functionals, the optimized parameters are $s_{r,6}^{B97D} = 0.892$, $s_8^{B97D} = 0.909$, $s_{r,6}^{PBEPBE} = 1.261$, $s_8^{PBEPBE} = 1.703$, $s_{r,6}^{B3LYP} = 1.217$ and $s_8^{B3LYP} = 0.722$, respectively.

2.6.2 The dispersion-correction scheme of Tkatchenko and Scheffler

In GD3 the ansatz of a fractional coordination number and an elaborate geometric counting function was employed to infer the chemical environment of an atom. In the Tkatchenko-Scheffler (TS) dispersion correction scheme⁴⁵ the direct relationship between polarizability, α_A , and volume is used:⁴⁶

$$V_A = \alpha_A \kappa_A \quad 2.81$$

where κ_A is the proportionality constant for atom A. The volume of an atom in a molecule is obtained by the Hirshfeld partitioning of electron density:⁴⁷

$$V_A = \int w_A(\mathbf{r}) \rho(\mathbf{r}) r^3 d^3 \mathbf{r} \quad 2.82$$

where $w_A(\mathbf{r})$ is the Hirshfeld atomic partitioning weight:

$$w_A(\mathbf{r}) = \frac{\rho_A^{free}(\mathbf{r})}{\sum_B \rho_B^{free}(\mathbf{r})} \quad 2.83$$

In these equations r is the distance from nucleus A and $\rho(\mathbf{r})$ is the total electron density and $\rho_A^{free}(\mathbf{r})$ is the electron density of free atom A *in vacuo* with corresponding volume:

$$V_A^{free} = \int \rho_A^{free}(\mathbf{r}) r^3 d^3 \mathbf{r} \quad 2.84$$

The sum in the denominator of Eq. 2.83 goes over all atoms in the system. The dispersion coefficient for an atom in a molecule is then determined from the free-atom value as

$$C_{AA,6} = \left(\frac{V_A}{V_A^{free}} \right)^2 C_{AA,6}^{free} \quad 2.85$$

Chapter 2: Overview of theoretical methods

The dispersion coefficient for the van der Waals interaction between two atoms is calculated from

$$C_{AB,6} = 2C_{6AA}C_{6BB}/\left(\frac{\alpha_B^0}{\alpha_A^0}C_{AA,6} + \frac{\alpha_A^0}{\alpha_B^0}C_{BB,6}\right) \quad 2.86$$

Tkatchenko and Scheffler used the database of scaled time-dependent DFT free atom reference values, α_m and $C_{mm,6}^{free}$, reported by Chu and Dalgarno.⁴⁸ The TS dispersion correction energy is given by

$$E_{disp}^{TS} = - \sum_A^{N_{at}-1} \sum_{B>A}^{N_{at}} f_{dmp} \frac{C_{AB,6}}{R_{AB}^6} \quad 2.87a$$

with R_{AB} the interatomic separation. The damping function has the following form:

$$f_{dmp} = \frac{1}{1 + e^{-20\left(\frac{R_{AB}}{s_r R_{AB,0}} - 1\right)}} \quad 2.87b$$

where s_r is an empirical parameter that determines the onset of the dispersion correction for a particular density functional by scaling of the cutoff distance $R_{AB,0} = R_{A,0} + R_{B,0}$. For the PBE/PBEPBE and B3LYP functionals, $s_r^{PBE/PBEPBE} = 0.94$ and $s_r^{B3LYP} = 0.84$, respectively.

2.7 Summary

A brief overview of the fundamentals of Quantum Mechanics with a focus on those approximations that enable its application to moderately sized models is given in this chapter. The versatile field of DFT is discussed and the systematic procedure developed by Becke to optimize (hybrid-) GGA exchange-correlation functionals by empirical fitting is elaborated. One of the shortcomings of DFT is an inability to describe correlated motion of electrons responsible for the omnipresent attractive dispersion force. Pragmatic dispersion correction schemes whereby an atom-pairwise semi-empirical energy correction is added to the mean-field energy are discussed. The second generation DFT-D scheme of Grimme, GD2, developed in conjunction with the B97D functional, is discussed, along with LC-hybrid functionals that combine the merits of wave function methods and DFT functionals. In the most general form of LC-hybrid functionals, the short-range electron-electron interaction is described by the LSDA and the long-range part by HF theory. The ω B97X functional of Chai and Head-Gordon, and subsequently the reparameterized dispersion corrected ω B97XD functional, are discussed. Finally, the GD3 and TS dispersion-correction schemes, wherein the chemical environment of an atom is inferred *ab initio*, is described.

Chapter 2: Overview of theoretical methods

2.8 References

1. Jensen, F., *Introduction to Computational Chemistry*. Second Edition.; Wiley: West Sussex, England, **2007**.
2. Koch, W.; Holthausen, M.C., *A Chemist's Guide to Density Functional Theory*. Wiley-VCH: Weinheim, **2000**.
3. Schmider, H.L.; Becke, A.D., *J. Chem. Phys.* **1998**, *108*, 9624.
4. Lima, N.A.; Caldas, M.J., *Phys. Rev. B* **2005**, *72*, 33109.
5. Born, M.; Oppenheimer, R., *Ann. Phys.* **1927**, *84*, 457.
6. Hohenberg, P.; Kohn, W., *Phys. Rev.* **1964**, *136*, B864.
7. Kohn, W.; Sham, L.J., *Phys. Rev.* **1965**, *140*, A1133.
8. Vosko, S.H.; Wilk, L.; Nusair, M., *Can. J. Phys.* **1980**, *58*, 1200.
9. Ceperley, D.M.; Alder, B.J., *Phys. Rev. Lett.* **1980**, *45*, 566.
10. Becke, A.D., *J. Chem. Phys.* **1993**, *98*, 5648.
11. Boese, A.D.; Martin, J.M.L., *J. Chem. Phys.* **2004**, *121*, 3405.
12. Stephens, P.J.; Devlin, F.J.; Chabalowski, C.F.; Frisch, M.J., *J. Phys. Chem.* **1994**, *98*, 11623.
13. Becke, A.D., *Phys. Rev. A* **1988**, *38*, 3098.
14. Lee, C.; Yang, W.; Parr, R.G., *Phys. Rev. B* **1988**, *37*, 785.
15. Becke, A.D., *J. Chem. Phys.* **1997**, *107*, 8554.
16. Perdew, J.P.; Wang, Y., *Physical Rev. B* **1992**, *45*, 13244.
17. (a) Stoll, H.; Pavlidou, C.M.E.; Preuss, H., *Theor. Chim. Acta* **1978**, *49*, 143; (b) Stoll, H.; Golka, E.; Preuss, H., *Theor. Chim. Acta* **1980**, *55*, 29.
18. Becke, A.D., *J. Chem. Phys.* **1986**, *84*, 4524.
19. Gill, P.M.W.; Johnson, B.G.; Pople, J.A.; Frisch, M.J., *Int. J. Quantum Chem., Quantum Chem. Symp.* **1992**, *26*, 319.
20. (a) Wu, Q.; Yang, W., *J. Chem. Phys.* **2002**, *116*, 515; (b) Wu, X.; Vargas, M.C.; Nayak, S.; Lotrich, V.; Scoles, G., *J. Chem. Phys.* **2001**, *115*, 8748; (c) Zimmerli, U.; Parrinello, M.; Koumoutsakos, P., *J. Chem. Phys.* **2004**, *120*, 2693.
21. (a) Eisenschitz, R.; London, F., *Z. Phys.* **1930**, *60*, 491; (b) Dalgarno, A.; Davison, W.D., *Adv. At. Mol. Phys.* **1966**, *2*, 1; (c) Dalgarno, A., *Adv. Chem. Phys.* **1967**, *12*, 143.
22. Pellenq, R.J.-M.; Nicholson, D., *Mol. Phys.* **1998**, *95*, 549.
23. (a) Brooks, F.C., *Phys. Rev.* **1952**, *86*, 92; (b) Ahlrichs, R., *Theor. Chim. Acta* **1976**, *41*, 7; (c) Tang, K.T.; Toennies, J.P., *J. Chem. Phys.* **1984**, *80*, 3726.
24. Grimme, S., *J. Comput. Chem.* **2004**, *25*, 1463.
25. Grimme, S., *J. Comput. Chem.* **2006**, *27*, 1787.
26. (a) London, F., *Z. Physik. Chem.* **1930**, *11*, 222; (b) London, F., *Z. Phys.* **1930**, *63*, 245; (c) Tang, K.T., *Phys. Rev.* **1969**, *177*, 108.
27. Adamo, C.; Barone, V., *J. Chem. Phys.* **1999**, *110*, 6158.
28. (a) Goll, E.; Werner, H.-J.; Stoll, H., *Phys Chem Chem Phys* **2005**, *7*, 3917; (b) Goll, E.; Werner, H.-J.; Stoll, H.; Leininger, T.; Gori-Giorgi, P.; Savin, A., *Chem. Phys.* **2006**, *329*, 276.

Chapter 2: Overview of theoretical methods

29. Leininger, T.; Stoll, H.; Werner, H.-J.; Savin, A., *Chem. Phys. Lett.* **1997**, 275, 151.
30. Angyan, J.G.; Gerber, I.C.; Savin, A.; Toulouse, J., *Phys. Rev. A* **2005**, 72, 12510.
31. Chai, J.-D.; Head-Gordon, M., *J. Chem. Phys.* **2008**, 128, 84106.
32. Chai, J.-D.; Head-Gordon, M., *Phys. Chem. Chem. Phys.* **2008**, 10, 6615.
33. Adamson, R.D.; Dombroski, J.P.; Gill, P.M.W., *J. Comput. Chem.* **1999**, 20, 921.
34. Iikura, H.; Tsuneda, T.; Yanai, T.; Hirao, K., *J. Chem. Phys.* **2001**, 115, 3540.
35. Bardeen, J., *Phys. Rev.* **1936**, 49, 653.
36. Gill, P.M.W.; Adamson, R.D.; Pople, J.A., *Mol. Phys.* **1996**, 88, 1005.
37. Thanthiriwatte, K.S.; Hohenstein, E.G.; Burns, L.A.; Sherrill, C.D., *J. Chem. Theory Comput.* **2011**, 7, 88.
38. Grimme, S.; Antony, J.; Ehrlich, S.; Krieg, H., *J. Chem. Phys.* **2010**, 132, 154104.
39. Adamovic, I.; Gordon, M.S., *Mol. Phys.* **2005**, 103, 379.
40. Casimir, H.B.G.; Polder, D., *Phys. Rev.* **1948**, 73, 360.
41. Mavroyannis, C.; Stephen, M.J., *Mol. Phys.* **1962**, 5, 629.
42. See www.uni-muenster.de/Chemie.oc/grimme for the latest version of DFT-D3 parameterization.
43. Pyykkö, P.; Atsumi, M., *Chem. Eur. J.* **2009**, 15, 186.
44. Starkschall, G.; Gordon, R.G., *J. Chem. Phys.* **1972**, 56, 2801.
45. Tkatchenko, A.; Scheffler, M., *Phys. Rev. Lett.* **2009**, 102, 73005.
46. Brinck, T.; Murray, J.S.; Politzer, P., *J. Chem. Phys.* **1993**, 98, 4305.
47. Hirshfeld, F.L., *Theor. Chim. Acta* **1977**, 44, 129.
48. Chu, X.; Dalgarno, A., *J. Chem. Phys.* **2004**, 121, 4083.

Chapter 3: Materials and methods

Details considered too technical for subsequent chapters are presented here. Initially, the compounds investigated are discussed, with the exception of compound **2**, which is elaborated on in Chapter 4. A novel volumetric sorption isosteric technique (SIT) device previously developed in-house is discussed, followed by a description of a conventional gravimetric instrument employed for this study. Background on internal coordinates and rudimentary vector mathematics is then presented together with a discussion of a Visual Basic script that was written to automate the generation of a Z-matrix from Cartesian coordinates. In the penultimate section a description of a mechanistic model used to investigate anisotropic thermal expansion is given, and the chapter is concluded with a summary of the density functionals and basis sets employed in this study.

3.1 Molecular graphics

The program MSROLL was used for the determination and visual representation of void space.¹ MSROLL, developed by Michael L. Connolly, maps the available volume using a spherical probe whose radius can be specified. In this work a probe radius of 1.4 Å was used and guest molecules within pockets created by the host molecules were deleted prior to each calculation. The van der Waals atom radii and color scheme presented in Table 3.1 was employed, where the van der Waals radius is defined as half the distance between two atoms at which exchange repulsion and (attractive) dispersion forces are balanced.² POV-RayTM was used to produce high quality molecular graphics.³ Both MSROLL and POV-RayTM were accessed via the X-Seed program.⁴

Table 3.1: Van der Waals radii and color scheme used in the present study.

Atom	Radius (Å)	Color	
H	1.20	white	
C	1.70	grey	
N	1.55	blue	
O	1.52	red	
Cl	1.80	yellow	
Cu	0.68		
Zn	0.74	cyan	
Cd	0.95		

Chapter 3: Materials and methods

3.2 Compounds investigated

The ligands shown below were synthesized by previous members of our group who used them for the formation of either frameworks (as in compound **1**) or discrete metallocycles (compounds **3** and **4**). For the latter case, bidentate ligands that bridge two metal centres in a C-shape conformation were envisaged.

3.2.1 $[\text{Zn}(\text{4-(1H-naphtho[2,3-d]imidazole-1-yl)benzoic acid})(\text{OH})]_n \cdot n\text{CH}_3\text{OH}$

Following the procedure developed by Grobler,⁵ 4,4'-bis(2-methylimidazol-1-ylmethyl)-1,1'-biphenyl (Ligand **L₁**, Figure 3.1) and an equimolar amount of $\text{Zn}(\text{NO}_3)_2 \cdot 4\text{H}_2\text{O}$ were dissolved in a mixture of dimethylformamide (1.0 mL), methanol (1.0 mL) and water (0.2 mL). Two days under solvothermal conditions within a Teflon-lined autoclave at 100 °C yielded crystals of the three dimensional MOF $[\text{Zn}(\text{L}_1)(\text{OH})]_n \cdot n\text{CH}_3\text{OH}$, **1_{MeOH}**, as confirmed by powder X-ray diffraction. From single-crystal X-ray diffraction structure elucidation,⁵ the benzoate moiety is disordered over two positions of equal occupancy as shown in Figure 3.1, with a (full occupancy) oxygen coordinating to a Zn^{2+} cation that is in a tetrahedral coordination sphere.

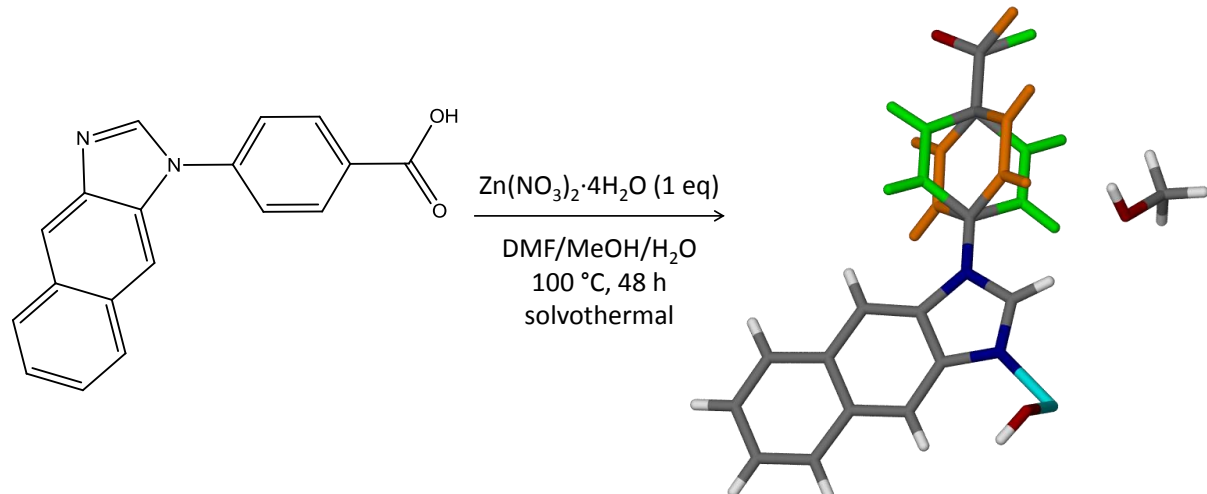


Figure 3.1: Synthesis of **1_{MeOH}** under solvothermal conditions with the asymmetric unit shown.⁵ The two positions of equal occupancy over which the benzoate moiety is disordered are shown in different colors.

The bridging hydroxide hydrogen bonds to the coordinating oxygen to form a hydrogen bond network that interlaces the coordination spiral along the crystallographic *c* axis, as depicted in Figure 3.2. It was shown that the methanol guest can be removed under reduced pressure and heating (150 °C) to yield the aphost, **1_{apo}**.⁵ Continuous channels could be mapped with a volume of $\sim 355 \text{ \AA}^3$ per $[\text{Zn}(\text{L}_1)_2(\text{OH})_2]$ formula unit, or 19% of the unit cell volume, as depicted in Figure 3.3.

Chapter 3: Materials and methods

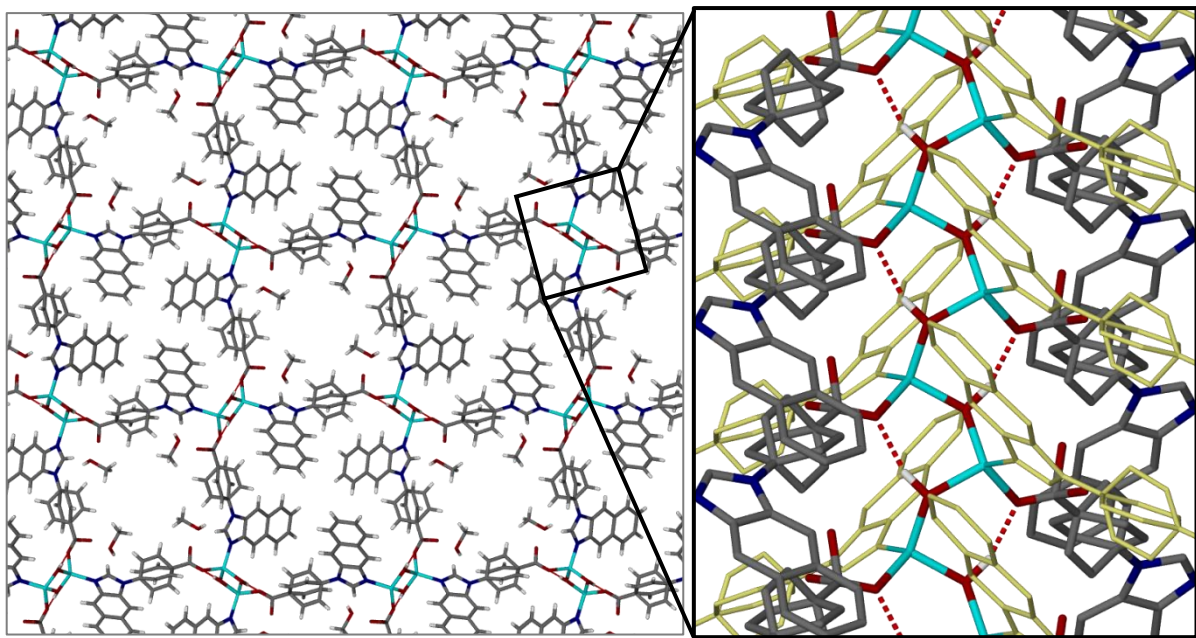


Figure 3.2: Left panel: view of *ab* plane showing packing of $\mathbf{1}_{\text{MeOH}}$ with alternating methanol filled square-shaped channels. Hydrogen bonds are shown as red dashed lines. Right panel: depiction of the hydrogen bond network in the coordination spiral along the *c* axis. Here, only hydroxide hydrogen atoms are shown and ligands coordinating through the imidazole moiety are shown in yellow.

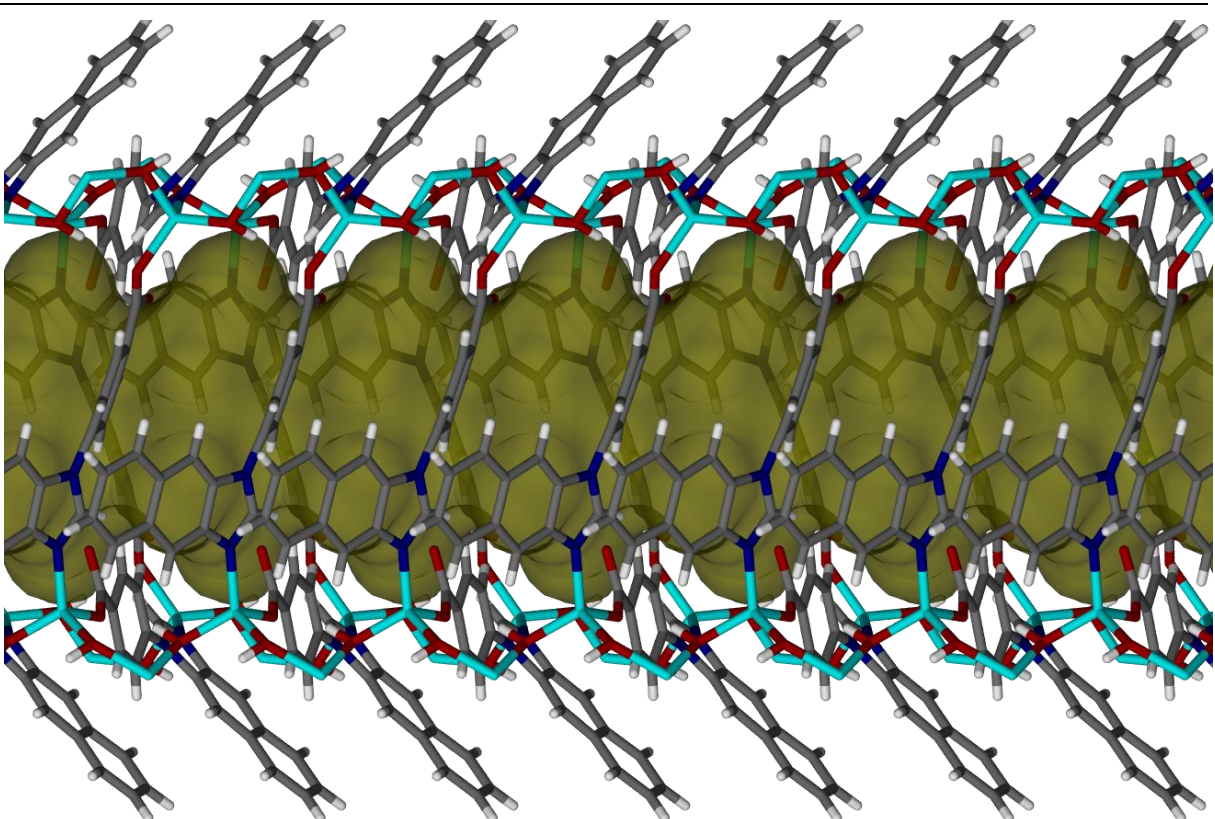


Figure 3.3: Depiction of the solvent-accessible space $\mathbf{1}_{\text{apo}}$ determined to be $\sim 710 \text{ \AA}^3$ per unit cell. The neutral framework of $[\text{Zn}(\mathbf{L}_1)_2(\text{OH})_2]_n$ is shown in capped-stick representation and a Connolly contact surface is shown in semi-transparent gold.

Chapter 3: Materials and methods

3.2.2 $[\text{Cd}_2(4,4'\text{-bis}(2\text{-methylimidazol-1-ylmethyl)-1,1'\text{-biphenyl})_2\text{Cl}_4]$

Synthesis of the exo-bidentate ligand 4,4'-bis(2-methylimidazol-1-ylmethyl)-1,1'-biphenyl (Ligand **L₃**, Figure 3.4) and subsequent crystallization was carried out by Jacobs.⁶ By dissolving **L₃** in chloroform and $\text{CdCl}_2 \cdot 2.5\text{H}_2\text{O}$ in methanol, crystals of $[\text{Cd}_2(\text{L}_3)_2\text{Cl}_4] \cdot 2\text{CH}_3\text{OH}$ (**3_{MeOH}**) were obtained by interdiffusion of the solvent layers. Single-crystal X-ray diffraction structure elucidation revealed discrete metallocycles that crystallize in the monoclinic space group *C2/m*. Each complex is composed of two cadmium cations that are tetrahedrally coordinated to two chloride anions and two bridging ligands, both in a converging conformation.

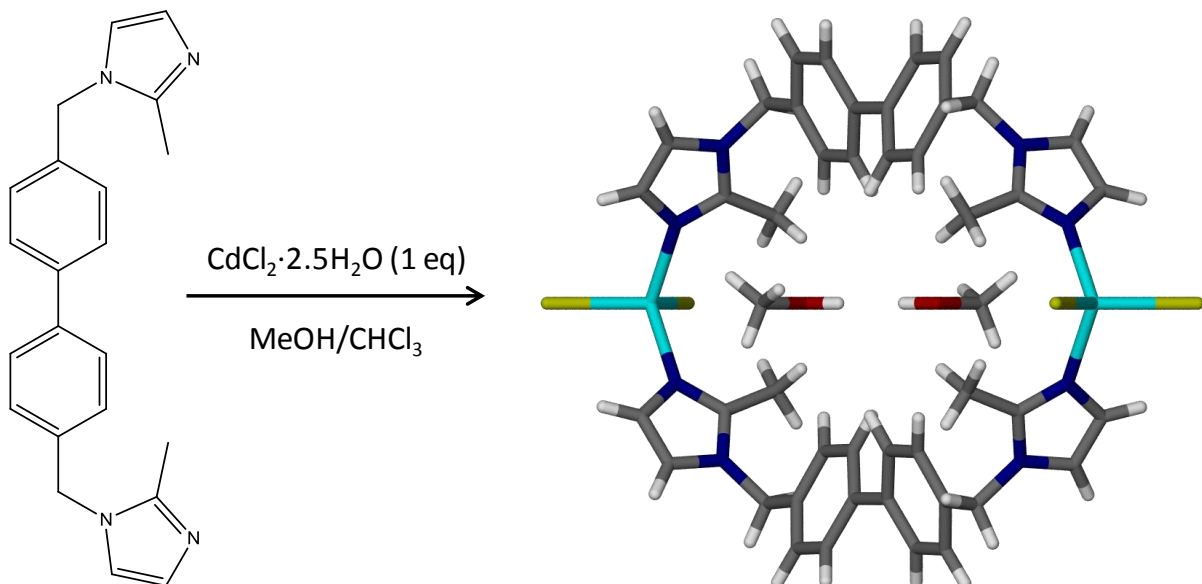


Figure 3.4: Formation of **3_{MeOH}** by layering a methanolic solution of $\text{CdCl}_2 \cdot 2.5\text{H}_2\text{O}$ over a chloroform solution of **L₃** to allow for slow interdiffusion.

The cyclic complexes stack along the crystallographic *c* axis to form a series of solvent-filled pockets each situated between two adjacent metallocycles. The apohost **3_{apo}** can be obtained overnight by desolvation under dynamic vacuum. The desolvation process occurs in a single-crystal to single-crystal fashion and the apohost structure was elucidated by single-crystal X-ray diffraction.⁶ The solvent filled pockets of **3_{MeOH}** and voids in **3_{apo}** are shown for comparison in Figure 3.5. Protrusion of the van der Waals surface of the methanol molecules beyond the Connolly surface in **3_{MeOH}** implies the presence of host-guest intermolecular interactions. The chloride anions that block off the pockets each form O-H \cdots Cl hydrogen bonds with methanol molecules ($d_{O \cdots Cl} = 3.173 \text{ \AA}$). The void-volume in **3_{apo}** was estimated to be $\sim 118 \text{ \AA}^3$ using a probe radius of 1.4 \AA , corresponding to 9.8% of the unit cell volume.

Chapter 3: Materials and methods

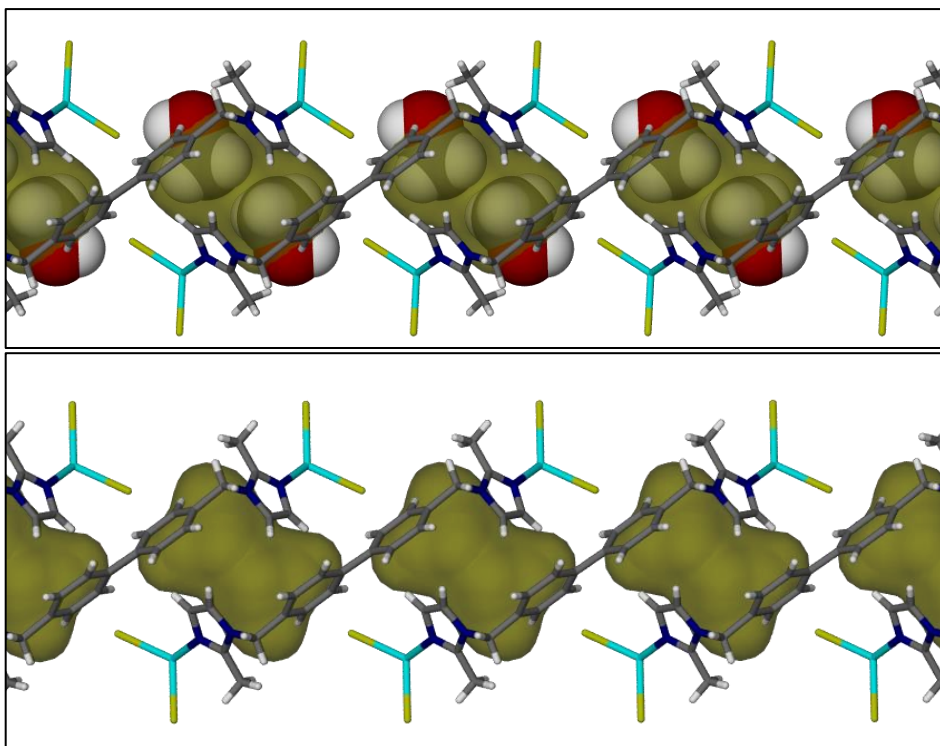


Figure 3.5: Comparison of the contact surfaces in (top panel) 3_{MeOH} and (bottom panel) 3_{apo} . Complexes of $[\text{Cd}_2(\text{L}_3)_2\text{Cl}_4]$ are shown as capped-sticks and the methanol guest molecules in van der Waals representation. Connolly contact surfaces are shown in semi-transparent gold.

3.2.3 $[\text{Cu}_2(1,3\text{-bis(imidazol-1-ylmethyl)-2,4,6-trimethylbenzene})_2\text{Cl}_4]$

In experiments carried out by Dobrzańska and Lloyd, the ligand 1,3-bis(imidazol-1-ylmethyl)-2,4,6-trimethylbenzene (Ligand **L₄**, Figure 3.6) was reacted with $\text{CuCl}_2 \cdot 2\text{H}_2\text{O}$ to yield a discrete dinuclear metallocycle that enclathrates a hydrogen-bonded ($d_{\text{O} \cdots \text{O}} = 2.769 \text{ \AA}$) $\text{MeOH} \cdots \text{H}_2\text{O}$ adduct, $[\text{Cu}_2(\text{L}_4)_2\text{Cl}_4] \cdot \text{CH}_3\text{OH} \cdot \text{H}_2\text{O}$, $4_{\text{MeOH}\cdot\text{H}_2\text{O}}$.⁷ Both Cu^{2+} ions of each metallocycle are coordinated in a distorted square-planar arrangement to two C-shaped ligands and two chloride anions. These complexes stack linearly to form columns along [100] with discrete voids centred within each complex.

The guest molecules can readily be removed by heating to 60°C under vacuum for one hour. This process occurs as a single-crystal-to-single-crystal transformation and the apohost structure 4_{apo} was elucidated by single-crystal X-ray diffraction.⁷ No significant change in the structure occurs upon desolvation of $4_{\text{MeOH}\cdot\text{H}_2\text{O}}$ except that the space previously occupied by guest molecules becomes devoid of appreciable electron density. As shown in Figure 3.7, the size of the pockets visibly shrinks upon desolvation from a volume of $\sim 142 \text{ \AA}^3$ in $4_{\text{MeOH}\cdot\text{H}_2\text{O}}$ to $\sim 107 \text{ \AA}^3$ (corresponding to 10% of the unit cell) in 4_{apo} . This can be understood as the structure adjusting in order to achieve more efficient packing. The $\text{Cu} \cdots \text{Cu}$ distance of the metallocyclic complex shrinks from 6.621 \AA in $4_{\text{MeOH}\cdot\text{H}_2\text{O}}$ to 6.598 \AA in 4_{apo} .

Chapter 3: Materials and methods

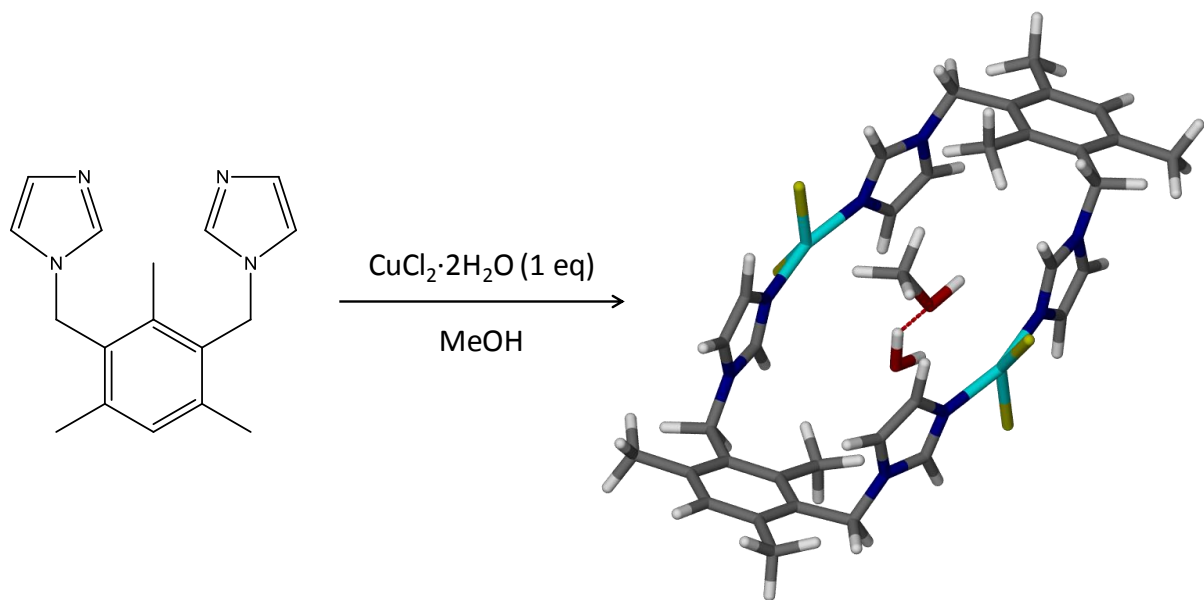


Figure 3.6: Formation of **4_{MeOH·H₂O}** by reacting **L₄** and CuCl₂·2H₂O in a 1:1 molar ratio in a slowly evaporating methanolic solution. The hydrogen bond in the heterodimer is shown as a red dashed line.

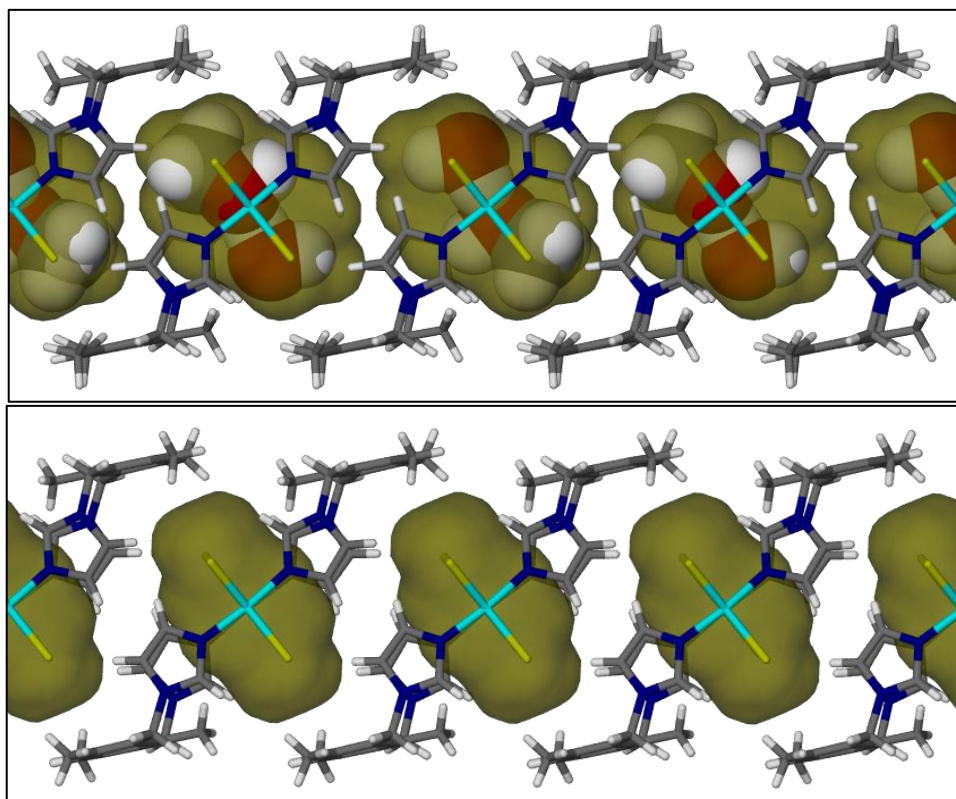


Figure 3.7: Comparison of the contact surfaces in (top panel) **4_{MeOH·H₂O}** and (bottom panel) **4_{apo}**. Complexes of [Cu₂(L₄)₂Cl₄] are shown as capped-sticks and the guest molecules in the van der Waals representation. Connolly contact surfaces are shown in semi-transparent gold.

3.3 Volumetric Sorption Isosteric Technique (SIT) device

A novel volumetric SIT device was developed by Barbour *et al.*⁸ for the determination of thermodynamic parameters of adsorption.⁹ The SIT involves the measurement of gas pressure changes in a calibrated and constant volume as a function of time. A schematic diagram of the volumetric SIT device is shown in Figure 3.8. The device was constructed from modular Swagelok® components with each of the two chambers connected to a high precision Wika® Eco-1 low pressure transducer. Ball valves separate the chambers from the environment and each other. The device is mounted against a wooden board, as shown in Figure 3.9, which in turn is housed in a thermostated cabinet.

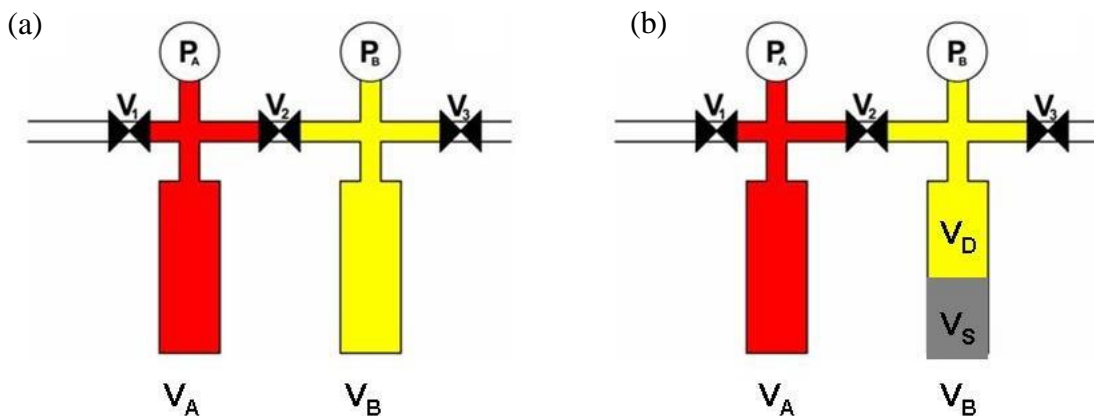


Figure 3.8: Schematic of the volumetric SIT device shown in (a) without sample and (b) with sample. P_A and P_B are pressure transducers; V_1 , V_2 and V_3 are ball valves; V_A represents the volume of chamber A (gas reservoir, shaded red) and V_B that of chamber B (sample cell, shaded yellow). In (b) V_S (shaded grey) is the sample volume and V_D (shaded yellow) the dead volume $V_D = V_B - V_S$. Adapted from Marais.⁹

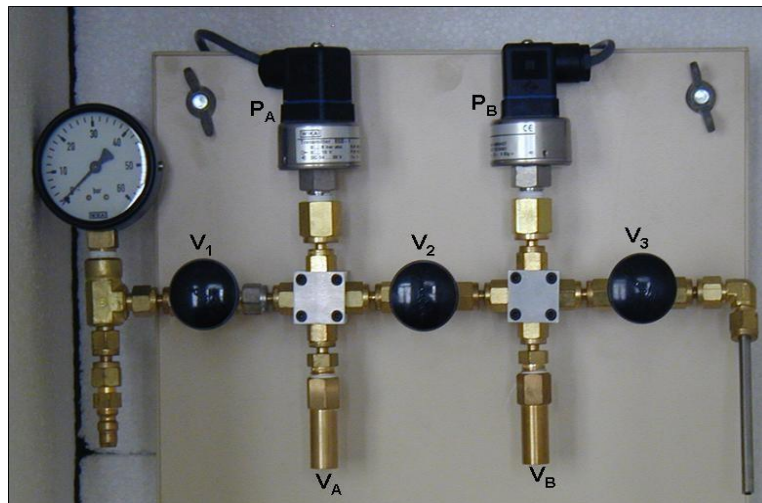


Figure 3.9: Photograph of the volumetric SIT device that was connected to a high pressure cylinder through valve V_1 and to a vacuum pump through valve V_3 .

Details regarding calibration of chamber volumes V_A and V_B is given in Section A.1.1. Two modes of experiment will be discussed here. In the first the temperature is kept constant while loading is increased to obtain an adsorption isotherm, and in the second the temperature is steadily increased while maintaining equilibrium in order to determine thermodynamic parameters of adsorption.

Chapter 3: Materials and methods

3.3.1 Adsorption to equilibrium: isothermal experiment

During a volumetric adsorption experiment the temperature and volume are kept constant in order to calculate the number of moles from pressure measurements using an appropriate equation of state. In a typical experiment, a powdered sample is placed in chamber B and the system evacuated. The pressure transducer P_B monitors the pressure in the dead volume where $V_D = V_B - V_S$. The volume of the sample, V_S , is calculated using the density obtained from crystallographic studies.* Following evacuation, all valves are closed and the selected gas is introduced to chamber A by opening and closing valve V_3 . After allowing the system to stabilise, the reading of pressure transducer P_A is recorded as $P_{A,start}$. Valve V_2 is briefly opened (for about one second) and then closed to introduce adsorbate into the sample cell. If the sample is porous, adsorption will take place and the pressure in chamber B will gradually decrease until equilibrium is reached. This is monitored *in situ* by pressure transducer P_B . Once equilibrium is established, the pressure transducer P_A reading is recorded as $P_{A,end}$ and the reading of pressure transducer P_B as $P_{B,eq}$.

The van der Waals equation is used to convert pressure to fugacity, and to calculate the amount of gas for each fugacity: $f_{A,start}$, $f_{A,end}$ and $f_{B,eq}$.[♦] The amount of gas introduced to the sample chamber, n_{intro} , is calculated as

$$n_{intro} = n_{f_{A,start}} - n_{f_{A,end}} \quad 3.1$$

while the amount of gas adsorbed by a porous sample, n_{ad} , at equilibrium loading $P_{B,eq}$ is obtained from

$$n_{ad} = n_{intro} - n_{f_{B,eq}} \quad 3.2$$

By repeating this experimental procedure with increasing input gas pressures ($P_{A,start}$) an adsorption isotherm, or plot of occupancy versus equilibrium loading ($P_{B,eq}$), can be obtained.

* $\rho(g.cm^{-3}) = \frac{Mr(g.mol^{-1}.UC^{-1}) \times 10^{24}(\text{\AA}^3.cm^{-3})}{v_{UC}(\text{\AA}^3.UC^{-1})N_A(mol^{-1})}$, where the UC^{-1} unit represents per unit cell and N_A is Avogadro's constant.

♦ Rewriting the van der Waals equation as $\frac{ab}{v^2}n^3 - \frac{a}{v}n^2 + (RT + bP)n - PV = 0$ enables use of the cubic equation, which has only one real root, to obtain n : For the equation $Ax^3 + Bx^2 + Cx + D = 0$, $x = -\{B + [(E + G)/2]^{1/3} + [(E - G)/2]^{1/3}\}/(3A)$ where $E = 2B^3 - 9ABC + 27A^2D$, $F = B^2 - 3AC$ and $G = \sqrt{E^2 - 4F^3}$.

Chapter 3: Materials and methods

3.3.2 Determining thermodynamic parameters: isochoric temperature ramp

The volumetric SIT device allows for the thermodynamic quantities ΔG_{ad}^0 , ΔH_{ad}^0 and ΔS_{ad}^0 to be experimentally determined for each point of the adsorption isotherm. After equilibrium is reached in chamber B, the temperature of the system is ramped from 25 to 50 °C and back down to 25 °C while the pressure reading of transducer P_B is recorded. Marais found a ramp rate of 0.20 °C.min⁻¹ to be sufficient for equilibrium to be maintained during the temperature ramp.⁹ By sequentially increasing the input gas pressure ($P_{A,start}$) and performing isochoric temperature ramp experiments after equilibrium was established isothermally, the dependence of the thermodynamic parameters of adsorption on equilibrium loading pressures ($P_{B,eq}$) can be determined.

3.4 Gravimetric gas adsorption

Gravimetric carbon dioxide adsorption isotherms were measured with an Intelligent Gravimetric Analyser (IGA-002) from Hiden Analytical, Warrington, UK.¹⁰ The instrument measures the change in sample mass under controlled pressure and temperature conditions. It is equipped with an enhanced pressure rating that allows measurements to be carried out up to 20 bar. Buoyancy effects are corrected for automatically by control software using the sample density. In the absence of single-crystal data, a buoyancy scan under helium pressure can be used to determine the density of the sample. The temperature is maintained to an accuracy of ±0.05 °C by a Grant refrigerated recirculation bath. Data collection is monitored by real-time processing computer software that continuously checks for pressure and weight equilibrium using least-squares regression to extrapolate a value of the asymptote.¹¹ For this study a Linear Driving Force relaxation model was used with an equilibrium point recorded once a 99% fit with the model was achieved, or the time-out (set to 120 minutes) was reached. The samples were subjected to an outgas sequence prior to adsorption runs and also between consecutive experiments of the same sample when the temperature was changed.

3.5 Models and their internal coordinates

Owing to their low electron density, hydrogen atom (nuclear) positions are poorly determined by X-ray crystallography. During structure refinement, hydrogen atoms are therefore usually placed geometrically (at a fixed bond length according to its chemical environment) using a riding model and refined with isotropic thermal parameters.¹² In order to make comparisons of crystal structures based on lattice energies, the hydrogen atom positions must first be optimized, usually while non-hydrogen atoms are constrained to their crystallographic positions.

Reducing the degrees of freedom of a model can expedite calculations. To this end it was decided to create input files with non-hydrogen atoms specified in Cartesian coordinates, and hydrogen atoms in Z-matrix format, *i.e.* internal coordinates (bond lengths, valence angles and dihedral angles). The benefit of using a Z-matrix is that variables can be transferred between different models and, by specifying atoms in the same chemical environment using the same variables, symmetry can inherently be enforced during optimizations. This is

Chapter 3: Materials and methods

especially helpful for molecular representations generated from the asymmetric unit of crystal structures. To circumvent making measurements through a graphical user interface, vector mathematics was used to calculate the necessary internal coordinates.

3.6 Definitions of internal coordinates

Vectors are values that have both magnitude and direction, while scalar quantities have only magnitude. The *dot*-product of two vectors, $\vec{J} \cdot \vec{K} = j_x k_x + j_y k_y + j_z k_z = |\vec{J}| |\vec{K}| \cos \theta_{JK}$, yields a scalar value.¹³ Here (j_x, j_y, j_z) is the vector extending from the origin to the centre of atom J , $|\vec{J}|$ represents the magnitude of vector \vec{J} and θ_{JK} is the angle between vectors \vec{J} and \vec{K} . The *cross*-product of two vectors, $\vec{J} \times \vec{K} = (j_y k_z - j_z k_y) \vec{e}_x + (j_z k_x - j_x k_z) \vec{e}_y + (j_x k_y - j_y k_x) \vec{e}_z$, results in a new vector that is perpendicular to both \vec{J} and \vec{K} .¹³ The unit vectors \vec{e}_x , \vec{e}_y , and \vec{e}_z are used to specify the direction of the new vector in Cartesian space. A bond distance, d_{21} , is specified by the magnitude of the vector connecting the two atoms:

$$d_{21} = |\vec{r}_{21}| = \sqrt{(x_1 - x_2)^2 + (y_1 - y_2)^2 + (z_1 - z_2)^2} \quad 3.3$$

while the valence angle, θ_{123} , is defined as the angle between two vectors pointing away from the central atom, as shown in Figure 3.10, by

$$\theta_{123} = \arccos \frac{\vec{r}_{21} \cdot \vec{r}_{23}}{|\vec{r}_{21}| |\vec{r}_{23}|} \quad 3.4$$

where $\vec{r}_{21} \cdot \vec{r}_{23} = (x_1 - x_2)(x_3 - x_2) + (y_1 - y_2)(y_3 - y_2) + (z_1 - z_2)(z_3 - z_2)$.

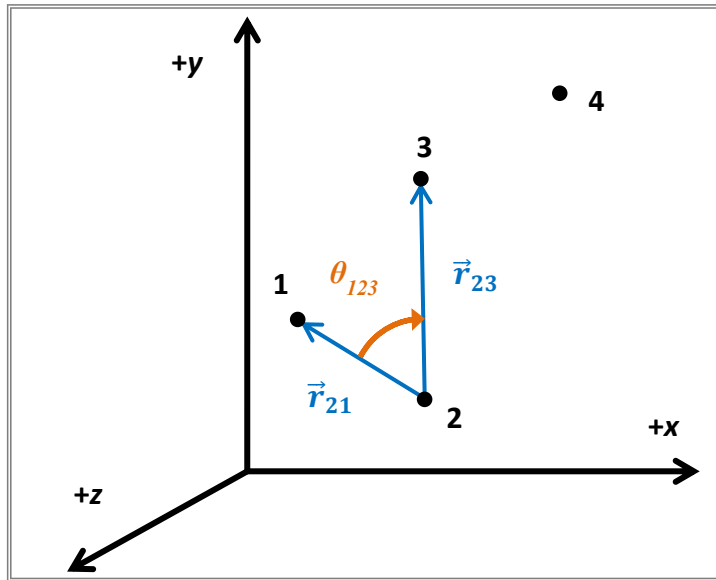


Figure 3.10: Illustration of the four atoms necessary to specify atom 1 in internal coordinates. The vectors used for calculating the bond angle between atoms 1, 2 and 3 are shown.

Chapter 3: Materials and methods

Specifying a dihedral angle is more complicated, because it also has an associated directionality component, or sign. First, two new vectors, each separately perpendicular to the planes created by the atoms 123 (vector \vec{A}) and 234 (vector \vec{B}), are specified:

$$\begin{aligned}\vec{A} &= \vec{r}_{21} \times \vec{r}_{23} = ((y_1 - y_2)(z_3 - z_2) - (z_1 - z_2)(y_3 - y_2))\vec{e}_x \\ &\quad + ((z_1 - z_2)(x_3 - x_2) - (x_1 - x_2)(z_3 - z_2))\vec{e}_y \\ &\quad + ((x_1 - x_2)(y_3 - y_2) - (y_1 - y_2)(x_3 - x_2))\vec{e}_z\end{aligned}\quad 3.5a$$

$$\begin{aligned}\vec{B} &= \vec{r}_{32} \times \vec{r}_{34} = ((y_2 - y_3)(z_4 - z_3) - (z_2 - z_3)(y_4 - y_3))\vec{e}_x \\ &\quad + ((z_2 - z_3)(x_4 - x_3) - (x_2 - x_3)(z_4 - z_3))\vec{e}_y \\ &\quad + ((x_2 - x_3)(y_4 - y_3) - (y_2 - y_3)(x_4 - x_3))\vec{e}_z\end{aligned}$$

This is depicted in Figure 3.11(a) and (b). The magnitude of the dihedral angle is given by the angle between these vectors:

$$|\omega_{1234}| = \theta_{AB} = \arccos \frac{\vec{A} \cdot \vec{B}}{|\vec{A}| |\vec{B}|} \quad 3.5b$$

To obtain the sign of ω_{1234} , the dot-product of the cross-product of \vec{A} and \vec{B} , $\vec{C} = \vec{A} \times \vec{B}$, with \vec{r}_{32} is evaluated,

$$\cos \theta_{Cr_{32}} = \frac{\vec{C} \cdot \vec{r}_{32}}{|\vec{C}| |\vec{r}_{32}|} \in \{1, -1\} \quad 3.5c$$

The expression in Eq. 3.5c can have one of only two values: if $\theta_{Cr_{32}} = 0^\circ$, the dihedral angle will have a positive sign; if $\theta_{Cr_{32}} = 180^\circ$ ω_{1234} will be negative Figure 3.11(d). The dihedral angle between any four atoms is therefore fully expressed by:

$$\omega_{1234} = \frac{(\vec{A} \times \vec{B}) \cdot \vec{r}_{32}}{|\vec{A} \times \vec{B}| |\vec{r}_{32}|} \arccos \frac{\vec{A} \cdot \vec{B}}{|\vec{A}| |\vec{B}|}, \quad \vec{A} = \vec{r}_{21} \times \vec{r}_{23}, \quad \vec{B} = \vec{r}_{32} \times \vec{r}_{34} \quad 3.5d$$

Chapter 3: Materials and methods

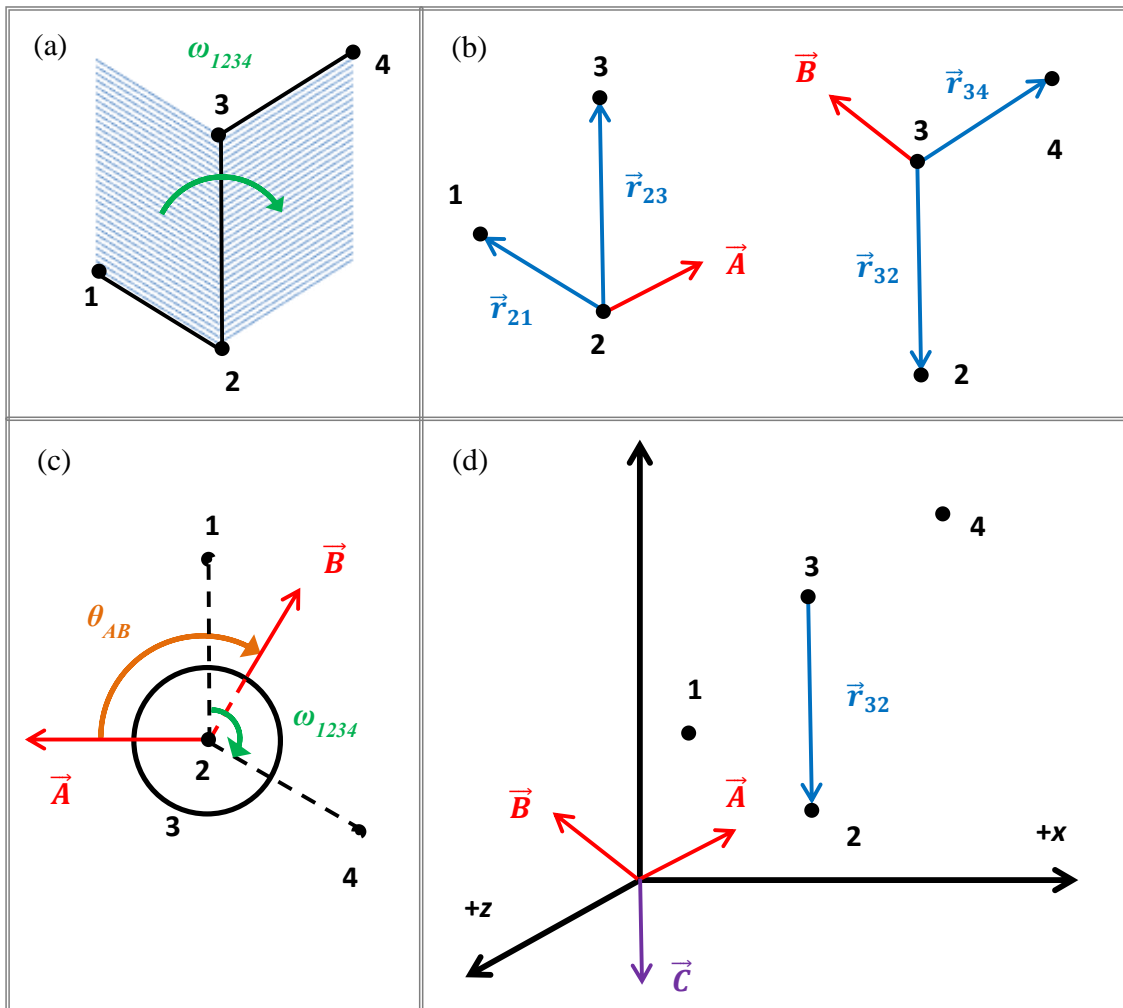


Figure 3.11: (a) The magnitude of the ω_{1234} dihedral angle is defined as the angle between atom planes 123 and 234. (b) Definition of two new vectors each separately perpendicular to the two planes shown in (a). (c) View down the bond between atoms 2 (foreground) and 3 (circle in the background) with the ω_{1234} and θ_{AB} angles indicated to illustrate their equal magnitudes. (d) The sign of ω_{1234} is determined by the angle between the vectors $\vec{C} = \vec{A} \times \vec{B}$ and \vec{r}_{32} , that is, if they point in the same ($\omega_{1234} > 0$), or opposite ($\omega_{1234} < 0$) direction.

Applying Eqs. 3.3-3.5 to models in Cartesian coordinate format, the internal coordinates necessary to specify the hydrogen atoms in Z-matrix format were determined. Coordinates with the same magnitude were collected and specified by a single variable, allowing for the sign of dihedral angles by specifying $abcd$ or $-abcd$. A Visual Basic script, to be discussed next, was composed in order to automate this process.

Chapter 3: Materials and methods

3.7 VB Script for generating a Z-matrix

To apply the formulae given in Section 3.6 recursively, a script was written in Visual Basic for use as a macro in Microsoft EXCEL (© Microsoft Corporation). Only key concepts thereof will be discussed here and the reader is referred to Section A.1.2 for the full script. First, a molecular representation is exported in Cartesian format and reordered so that non-hydrogen atoms are listed first. This was accomplished by importing the atom list to *cell#B2* of the spreadsheet followed by converting text to tables, sorting according to element and numbering (in column A). Figure 3.12 shows the layout of the spreadsheet used for executing the script.

A	B	C	D	E	F	G	H	I	J	K	L	M	N	O	
1	Atom1No	AtomType	X1	Y1	Z1	Atom2No	Atom2Type	R12	Atom3No	Atom3Type	A123	Atom4No	Atom4Type	Omega	W1234
17	16	O	0.99858	3.76707	0.90639										
18	17	O	3.76707	0.90639	0.99858										
19	18	O	-3.0924	0.90639	-3.1844										
20	19	O	-3.1844	-3.0924	0.90639										
21	20	O	0.90639	-3.1844	-3.0924										
22	21	H	0.67687	0.74546	2.95422										
23	22	H	0.84149	1.88414	3.77736										
24	23	H	-1.6471	-0.0777	2.82252										
25	24	H	-2.2851	-0.5016	1.40809										
26	25	H	-2.8352	1.75792	1.73049										

A	B	C	D	E	F	G	H	I	J	K	L	M	N	O	
1	Atom1No	AtomType	X1	Y1	Z1	Atom2No	Atom2Type	R12	Atom3No	Atom3Type	A123	Atom4No	Atom4Type	Omega	W1234
17	16	O	0.99858	3.76707	0.90639										
18	17	O	3.76707	0.90639	0.99858										
19	18	O	-3.0924	0.90639	-3.1844										
20	19	O	-3.1844	-3.0924	0.90639										
21	20	O	0.90639	-3.1844	-3.0924										
22	21	H	0.67687	0.74546	2.95422	15	O	0.8817450	12	N	13.172447	4	C	125.4842	125.4842
23	22	H	0.84149	1.88414	3.77736	15	O	0.8879946	12	N	114.137379	4	C	179.8345	-179.8345
24	23	H	-1.6471	-0.0777	2.82252	2	C	0.9852483	12	N	105.191464	4	C	55.9436	55.9436
25	24	H	-2.2851	-0.5016	1.40809	2	C	0.9974567	12	N	111.319663	4	C	61.3008	-61.3008
26	25	H	-2.8352	1.75792	1.73049	3	C	0.9673027	2	C	110.260662	12	N	174.9405	174.9405

Figure 3.12: Portion of spreadsheet used for the devised script to show the layout used. Top panel: sorted Cartesian coordinates and sequential numbering of atoms in a model; Bottom panel: specifications of internal coordinates of hydrogen atoms as determined through the script.

The aim of the script was (i) to automate the generation of the internal coordinates required to define all hydrogen atoms relative to non-hydrogen atoms, and (ii) to identify *unique* coordinates in order to specify their reoccurrences collectively with the same variable, thereby reducing the number of variables and enforcing a degree of symmetry. In this context “unique coordinates” refers to the internal coordinates of the asymmetric unit, from which molecular representations are generated according to symmetry operators. In Figure 3.13 it can be seen that the internal coordinates of each hydrogen atom (different rows in the depiction on the left) are specified according to unique variables (right-hand depiction) that are identified, named, and their occurrence counted during the macro’s execution.

Q	R	S	U	V	W	X	Y	Z	AA	AB	AC		
1	BondVariable	AngleVariable	TorsionVariable	BVarName	BVar	BVarCount	AVarName	AVar	AVarCount	TVarName	TVar	TVarCount	
31	B3	A3	T3	2	B1	0.88174502	6	A1	13.172447	3	T1	125.484200	3
32	B4	A4	-T4	3	B2	0.88799460	6	A2	114.137381	3	T2	179.834489	3
33	B5	A5	T5	4	B3	0.98524830	3	A3	105.191464	3	T3	55.943633	3
34	B6	A6	-T6	5	B4	0.99745671	3	A4	111.319665	3	T4	61.300803	3
35	B7	A7	-T7	6	B5	0.96730267	3	A5	110.260665	3	T5	174.940495	3
36	B8	A8	T8	7	B6	0.98106691	3	A6	108.849170	3	T6	67.287182	3
37	B9	A9	-T10	8	B7	0.97655648	3	A7	104.718075	3	T7	54.261478	3
38	B3	A3	T3	9	B8	0.99430586	3	A8	111.130571	3	T8	63.359874	3
39	B4	A4	-T4	10	B9	1.00347983	3	A9	112.288086	3	T9	8.224354	1
40	RF	TC	TC				A10	A10	A10	T10	T10	T10	

Figure 3.13: Snapshot of spreadsheet to show some output values at completion of the script. Left: each hydrogen atom (different rows) is assigned its internal coordinate variables; Right: unique variables are collected for inspection during execution of the macro.

Chapter 3: Materials and methods

3.7.1 Reading in Atom1-Number, -type, and XYZ coordinates

The keyword `Dim` is used to declare variables and to allocate storage space according to variable type: `String` for text (1 to 65 400 characters, number of bytes determined by string length) and `Single` for numbers ($-3.402823 \times 10^{-38} \leq \# \leq 3.402823 \times 10^{38}$, 4 bytes). The `String`-type declaration is also used to define arrays of the form $\Lambda(\lambda)$ wherein λ storage slots are allowed for variable- Λ values. In the following script excerpt, the total number of atoms in the model is determined to be *AtomCount* with the element and Cartesian coordinates of each atom sequentially stored in a memory slot of the arrays `Atomtype`, `X1`, `Y1` and `Z1`, starting from $\lambda = 1$.

```

Dim Atomtype(1000) As String
Dim AtomCount As Single
Dim X1(1000) As String
Dim Y1(1000) As String
Dim Z1(1000) As String

Counter_1 = 1
AtomCount = 0
Do Until Cells(Counter_1, 2) = ""
    Counter_1 = Counter_1 + 1
    AtomCount = AtomCount + 1
    Atomtype(AtomCount) = Cells(Counter_1, 2)
    X1(AtomCount) = Cells(Counter_1, 3)
    Y1(AtomCount) = Cells(Counter_1, 4)
    Z1(AtomCount) = Cells(Counter_1, 5)
Loop
AtomCount = AtomCount - 1

```

The `Loop` starts from the second row (*counter_1* = 2) and continues until an empty row is reached, requiring *AtomCount* – 1 (due to column headings). Now that all the coordinates have been saved to specific memory slots, the various vectors required to determine internal coordinates can be calculated. The simplest way of finding the correct atom sequence 1234 to specify bond length *R*₁₂, bond angle *A*₁₂₃ and dihedral angle *W*₁₂₃₄, is to find the successive nearest neighbor of Atom1. Non-hydrogen atoms remain specified in Cartesian coordinates. This ensures that hydrogen atoms are defined relative to previously defined atoms and reduces the execution time of the macro.

3.7.2 Determination of Atom2

The distances between all atoms are calculated in order to find the nearest neighbor of each hydrogen atom, that is, Atom2 for every Atom1. More variables are declared and a new loop initiated, as shown in the script excerpt below. The variable *Counter_1* represents the current Atom1 number (irrespective of element), while *Hcount* is stepped (current value +1) if the current `Atomtype` is hydrogen. *Counter_2* represents all possible Atom2's and is stepped from one to *AtomCount*, with the distance to Atom1 for each calculated through Eq. 3.3 and stored in the number-*Counter_2* memory slot of array `R`. The distances are halved, as comparisons between small numbers are less troublesome. Hydrogen atoms are removed as candidates for Atom2 by enlarging their distances to Atom1, along with the Atom1-Atom1 distance, to 10 Å.

Chapter 3: Materials and methods

To find the correct nearest neighbor, the smallest distance d_{21} must be identified. Two “counters” are used to sequentially scan the distance array \mathbf{R} and constraining the distance $R(Counter_3)$ to be smaller than all the *AtomCount*-number of $R(Counter_2)$ distances it is compared to. If $R(Counter_2)$ is smaller, *Counter_3* is set to *Counter_2*. Then, having identified the nearest neighbor as Atom1 = *Counter_3*, all the information about Atom2 required for upcoming calculations is saved into the *Hcount*-memory slot of various arrays.

```

Dim Counter_1 As Single
Dim Counter_2 As Single
Dim Counter_3 As Single
Dim Hcount As Single
Dim DX(1000) As String
Dim DY(1000) As String
Dim DZ(1000) As String
Dim R(1000) As String
Dim Atom2(1000) As String
Dim R12(1000) As String
Dim X2 As Single
Dim Y2 As Single
Dim Z2 As Single
Dim r21X As Single
Dim r21Y As Single
Dim r21Z As Single

Counter_1 = 0
Hcount = 0
Do Until Counter_1 = AtomCount
    Counter_1 = Counter_1 + 1
    Counter_2 = 0
    If Atomtype(Counter_1) = "H" Then
        Hcount = Hcount + 1
If Atom1 is a H, determine distance to every other (AtomCount - 1) atom and save to R(Counter_2)
    Do Until Counter_2 = AtomCount
        Counter_2 = Counter_2 + 1
        DX(Counter_2) = X1(Counter_1) - X1(Counter_2)
        DY(Counter_2) = Y1(Counter_1) - Y1(Counter_2)
        DZ(Counter_2) = Z1(Counter_1) - Z1(Counter_2)
        R(Counter_2) = ((DX(Counter_2) ^ 2 + DY(Counter_2) ^ 2 + DZ(Counter_2) ^ 2) ^ 0.5) / 2
Eliminate distances to itself and hydrogen atoms by enlarging R(Counter_2)
    If Counter_2 = Counter_1 Then
        R(Counter_2) = 5
    Elseif Atomtype(Counter_2) = "H" Then
        R(Counter_2) = 5
    End If
Loop
Sequentially compare all R(Counter_2) distances to find the smallest one: R(Counter_3)
    Counter_2 = 0
    Counter_3 = 1
    Do Until Counter_2 = AtomCount
        Counter_2 = Counter_2 + 1
        If R(Counter_3) > R(Counter_2) Then
            Counter_3 = Counter_2
        End If
    Loop
Store identified Atom2 information
    Atom2(Hcount) = Counter_3
    X2 = X1(Counter_3)
    Y2 = Y1(Counter_3)
    Z2 = Z1(Counter_3)
    r21X = DX(Counter_3)
    r21Y = DY(Counter_3)
    r21Z = DZ(Counter_3)
    R12(Hcount) = R(Counter_3) * 2
End If
Loop

```

The same procedure is used to identify Atom3 (nearest neighbor of Atom2, not Atom1, or a hydrogen atom) and Atom4 and to store information regarding vectors \vec{r}_{23} and \vec{r}_{34} . Note that all the script excerpts shown here form part of the same *Loop*. For the sake of completeness, the initial and final lines of this *Loop* are shown in each excerpt. All declarations are made at the start of the script, as shown in Section A.1.2.

Chapter 3: Materials and methods

The portions of the script used in (i) determining each dihedral angle ω_{1234} and (ii) identifying unique dihedral angles are discussed in Sections 3.7.3 and 3.7.4, respectively, as examples for the procedure used for all internal coordinates. The relevant lines from the script are shown for each section.

3.7.3 Determining dihedral angle W1234

As shown below, the vectors $\vec{A} = \vec{r}_{21} \times \vec{r}_{23}$ and $\vec{B} = \vec{r}_{32} \times \vec{r}_{34}$ (Eq. 3.5a) are defined in order to determine the magnitude of the dihedral angle (Eq. 3.5b). This value is saved into the array *Omega*. To obtain the sign of the dihedral angle, the vector $\vec{C} = \vec{A} \times \vec{B}$ must be defined and the angle between vectors \vec{C} and \vec{r}_{32} evaluated (Eq. 3.5c). The answer, either +1 or -1, is saved into the array *Sign*. The *W1234(Hcount)* dihedral angle is then determined by *Sign(Hcount) × Omega(Hcount)* (Eq. 3.5d).

```

Dim AX As Single
Dim AY As Single
Dim AZ As Single
Dim BX As Single
Dim BY As Single
Dim BZ As Single
Dim RA As Single
Dim RB As Single
Dim Omega(1000) As String
Dim CX As Single
Dim CY As Single
Dim CZ As Single
Dim RC As Single
Dim Sign(1000) As String
Dim W1234(1000) As String

Counter_1 = 0
Hcount = 0
Do Until Counter_1 = AtomCount
    Counter_1 = Counter_1 + 1
    Counter_2 = 0
    If Atomtype(Counter_1) = "H" Then
        Hcount = Hcount + 1

        AX = r21Y * r23Z - r21Z * r23Y
        AY = r21Z * r23X - r21X * r23Z
        AZ = r21X * r23Y - r21Y * r23X
        BX = r23Z * r34Y - r23Y * r34Z
        BY = r23X * r34Z - r23Z * r34X
        BZ = r23Y * r34X - r23X * r34Y
        RA = (AX ^ 2 + AY ^ 2 + AZ ^ 2) ^ 0.5
        RB = (BX ^ 2 + BY ^ 2 + BZ ^ 2) ^ 0.5
        Argument = (AX * BX + AY * BY + AZ * BZ) / (RA * RB)
        Omega(Hcount) = WorksheetFunction.Degrees(WorksheetFunction.Acot(Argument))
        CX = AY * BZ - AZ * BY
        CY = AZ * BX - AX * BZ
        CZ = AX * BY - AY * BX
        RC = (CX ^ 2 + CY ^ 2 + CZ ^ 2) ^ 0.5
        Sign(Hcount) = (CX * r23X + CY * r23Y + CZ * r23Z) / (RC * R23)
        W1234(Hcount) = Sign(Hcount) * Omega(Hcount)

    End If
Loop

```

The dihedral angles of each hydrogen atom are determined in this way. However, several recurring dihedral angles values might be present. To reduce the number of variables, and to enforce symmetry, all dihedral angles identical in magnitude and make-up (constituting atomtypes) are collectively given the same coordinate name.

Chapter 3: Materials and methods

3.7.4 Identifying unique dihedral angles

In the following excerpt the magnitudes of unique dihedral angles are identified, labelled and stored into the arrays **TVar** and **TVarname**. The dihedral angle magnitudes, $|W1234|$, from array **Omega** are evaluated and the (**single**-type) variable **Counter_6** is stepped (current value +1) when a unique $|W1234|$ value is encountered. For each **Counter_6** value, the unique dihedral angle is named by concatenation of “T” and variable $C_6 = Counter_6$ (where C_6 is a **string**-type variable) to yield a unique “ $T\#$ ” label. For the current hydrogen, namely **Hcount**, the corresponding entry in the **Sign** array is used to correctly specify “ $T\#$ ” or “ $-T\#$ ” in the Z-matrix.

In more detail, for each hydrogen atom, the “counters” **Counter_2** and **Counter_3** are first reset and then stepped to compare each $\Omega(Hcount)$ value to all previously identified **TVar** values, or until the value of **Counter_6** is reached. If $Counter_2 = Counter_6$, that is, if no previously identified unique $|W1234|$ was encountered, **Counter_6** is increased (current value +1) and a new **TVar** defined. **Counter_3** ensures **Counter_6** is stepped linearly without blank memory slots in **TVar**. If a previously identified **TVar** is encountered, the occurrence thereof is increased by appending an “i” to the array-entry **TVarCount(Counter_2)**. In a later portion of the script, the occurrence of each **TVar** is then simply calculated by the text function **Len(TVarCount(Counter_2))**.

```

Dim TVar(1000) As String
Dim TVarName(1000) As String
Dim TVarCount(1000) As String
Dim Counter_6 As Single
Dim C_6 As String
Dim HAtomT(1000) As String

Counter_1 = 0
Counter_6 = 0
Hcount = 0
Do Until Counter_1 = AtomCount
    Counter_1 = Counter_1 + 1
    Counter_2 = 0
    If Atomtype(Counter_1) = "H" Then

Identify unique Omega=|W1234| value
    Counter_2 = -1
    Counter_3 = -1
    Do Until Counter_2 = Counter_6
        Counter_2 = Counter_2 + 1
        If Omega(Hcount) = TVar(Counter_2) Then Exit Do A previously identified Omega encountered
        Counter_3 = Counter_3 + 1
        If Counter_3 = Counter_6 Then
            Counter_6 = Counter_6 + 1
Store and name unique Omega value
        TVar(Counter_6) = Omega(Hcount)
        C_6 = Counter_6
        TVarName(Counter_6) = "T" + C_6
    End If
Loop
Correctly store the sign of W1234, labelled T# for the current hydrogen atom into array HAtomT
    If Round(Sign(Hcount), 0) = -1 Then
        HAtomT(Hcount) = "-" + TVarName(Counter_2)
        Cells(Counter_1 + 1, 19) = HAtomT(Hcount)
    Else
        HAtomT(Hcount) = TVarName(Counter_2)
        Cells(Counter_1 + 1, 19) = HAtomT(Hcount)
    End If
Increase the count of current TVar
    TVarCount(Counter_2) = TVarCount(Counter_2) + "i"
End If
Loop

```

Chapter 3: Materials and methods

The macro stores the dihedral angle variable name (*TVarName*) of each hydrogen atom into the array **HAtomT** (memory slot *Hcount*). Similar arrays for bond lengths (*BVarName*) and valence angles (*AVarName*), **HAtomB** and **HAtomA**, respectively, are concurrently populated. There are *Counter_4*, *Counter_5* and *Counter_6* unique bond lengths (*BVar*), valence angles (*AVar*) and dihedral angles (*TVar*), respectively, identified by the script (cf. Section A.1.2). These arrays are used to compile a ready-for-use Z-matrix, as shown in Figure 3.14.

	I	J	K	L	M	N	O
18	O	-3.09243	0.90639	-3.18435			
19	O	-3.18435	-3.09243	0.90639			
20	O	0.90639	-3.18435	-3.09243			
21	H	15 B1		12 A1		4 T1	
22	H	15 B2		12 A2		4 -T2	
23	H	2 B3		12 A3		4 T3	
24	H	2 B4		12 A4		4 -T4	

	I	J	K	L	M	N	O
51	H		19 B2		5 A11		1 T13
52	H		20 B1		5 A10		1 -T12
53	H		20 B2		5 A11		1 T13
54							
55	B1		0.88175				
56	B2		0.88799				
57	B3		0.98525				

Figure 3.14: Example of Z-matrix generated by the script. The right-hand depiction is a continuation of the left-hand depiction.

Now that a Z-matrix with the order and internal coordinates of all the hydrogen atoms has been created, it is appended to the non-hydrogen atom list (in Cartesian coordinates) and can be used to optimize some or all of the variables. Other modifications as seen fit for a specific application can also be introduced, including but not limited to constraining certain variables to be equal or requiring one or more variables to be stepped to yield a one- or higher dimensional potential energy surface.

3.8 Anisotropic thermal expansion mechanistic model

Anomalous thermal expansion was identified in **1_{apo}** and a mechanism proposed concerning elongation of the $\cdots\text{Zn-O(H)-Zn-O(H)}\cdots$ coordination spiral (along the *c* axis), while coordinating ligands (**L₁**, largely parallel to the *ab* plane), acting as rigid linkers, pull the coordination spirals closer together.⁵ Here follows a discussion of a molecular model that was developed to reproduce the proposed convergent stretching mechanism of the coordination spiral in order to confirm this theory.

The 100 K crystal structure of **1_{apo}** was used to obtain a molecular representation in Cartesian coordinates. The model, depicted in Figure 3.15(c), consists of six zinc centres, with the hydroxide at one end of the coordination spiral converted to a coordinating water molecule for charge neutrality. To reduce computational expense, the ligand was truncated to coordinating imidazole and benzoate moieties. The model was translated to move the coordinating water onto the origin, and rotated so that all O(H) *x*-coordinates become zero, as shown in Figure 3.16. Every five atoms complete a turn and are separated by the distance *R_{AE}* initially equal to *c_{100K}*. By increasing this distance while simultaneously pulling all atoms closer to the *z*-axis, the elongation of the coordination spiral can be simulated. The translation variables of the *x*- and *y*-dimensions are defined in terms of the stepping variable (labelled *S*) in the *z* direction. The entire movement can therefore be controlled by one parameter.

Chapter 3: Materials and methods

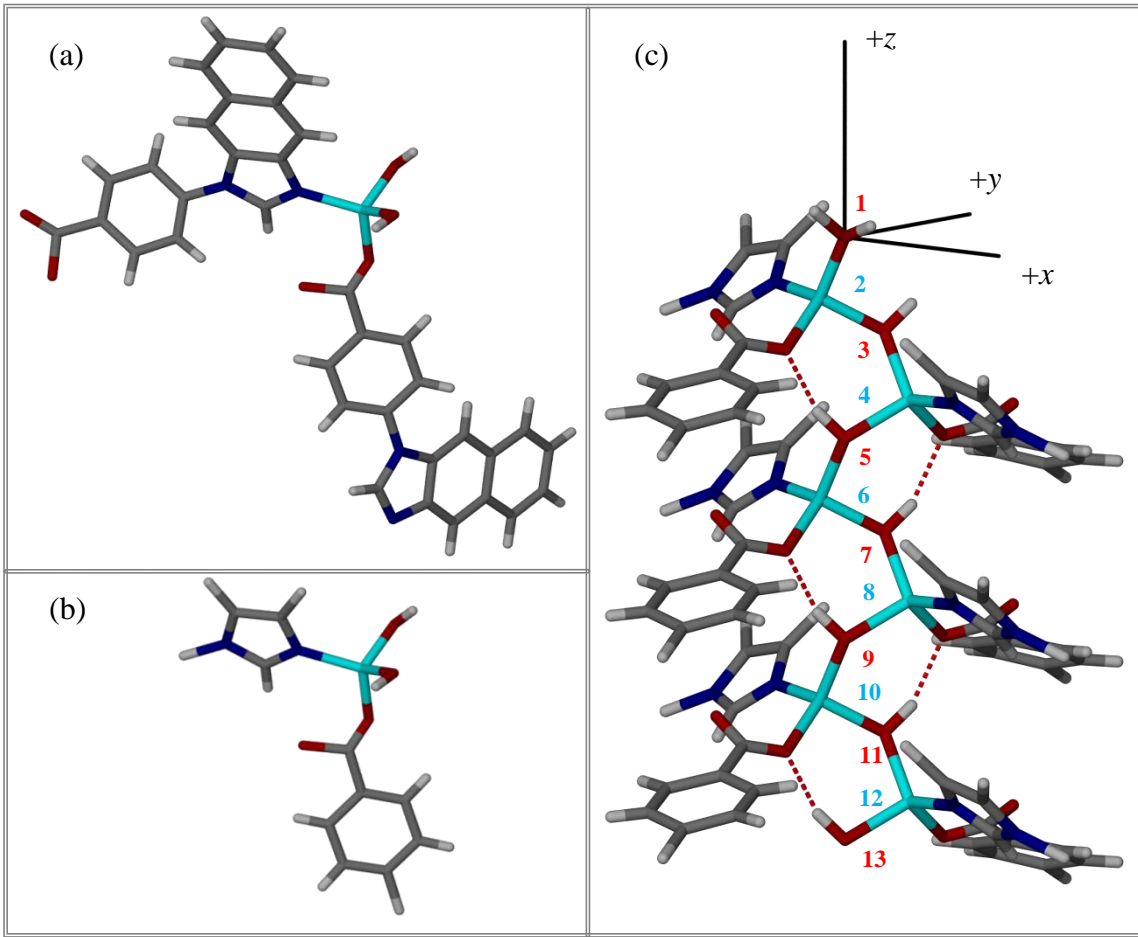


Figure 3.15: (a) Distorted tetrahedral coordination sphere around zinc in $\mathbf{1}_{\text{apo}}$ with two full coordinating ligands; (b) the truncated ligand used in the model shown in (c). Hydrogen bonds between the hydroxide and coordinating benzoate oxygen atoms are shown as red dashed lines. Note the coordinated water, with its oxygen labelled 1, on the origin to allow for charge neutrality.

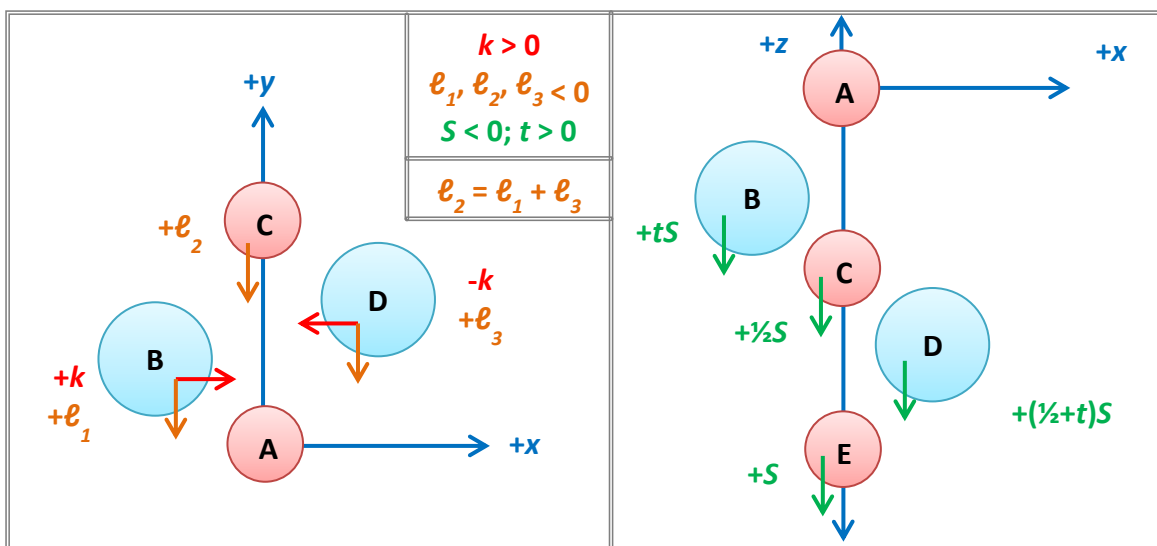


Figure 3.16: One turn (or five atoms) of the coordination spiral in the model depicted in Figure 3.15(c) with A, B, C, D, E corresponding to atoms O_1, Zn_2, O_3, Zn_4 and O_5 , respectively. Oxygen atoms of hydroxide groups are shown as pink spheres and zinc atoms as larger cyan spheres. On the left the variables controlling the convergent movement in the xy plane are shown, while those of the extension in the z direction are shown on the right. Note that atoms A and E have the same xy coordinates and do not move in the xy plane during the simulation. The separation R_{AE} represents the effective c unit cell length, which is stepped by variable S . The signs of the various parameters are indicated along with the relationship of the y -direction translation variables.

Chapter 3: Materials and methods

Table 3.2: Displacement of atoms (see text for details) labelled as in Figure 3.15(c) according to the parameters defined in Figure 3.16

Label Figure 3.15(c)	Group assignment Figure 3.16	Δx	Δy	Δz
1	A	0.0	0.0	0.0
2	B	$+k$	$+\ell_1$	$+tS$
3	C	0.0	$+\ell_2$	$+0.5S$
4	D	$-k$	$+\ell_3$	$+(0.5+t)S$
5	A/E	0.0	0.0	$+S$
6	B	$+k$	$+\ell_1$	$+(1+t)S$
7	C	0.0	$+\ell_2$	$+1.5S$
8	D	$-k$	$+\ell_3$	$+(1.5+t)S$
9	A/E	0.0	0.0	$+2S$
10	B	$+k$	$+\ell_1$	$+(2+t)S$
11	C	0.0	$+\ell_2$	$+2.5S$
12	D	$-k$	$+\ell_3$	$+(2.5+t)S$
13	A/E	0.0	0.0	$+3S$

The S_4 symmetry of **1_{apo}** ($I\bar{4}$ space group; asymmetric unit depicted in Figure 3.1) simplify matters significantly since $R_{AB} = R_{CD}$, $R_{BC} = R_{DE}$ and $R_{AC} = \frac{1}{2}R_{AE}$. The latter relationship allows for the rational z -direction translation shown in the right hand panel of Figure 3.16. The O₁-Zn₂ (labelled as in Figure 3.15(c)) interatomic separation is given by:

$$R_{AB}(c_{100K}) = \sqrt{(x_B - x_A)^2 + (y_B - y_A)^2 + (z_B - z_A)^2} \quad 3.6$$

where the Cartesian coordinates refer to those in the model derived from optimized the 100 K crystal structure. Taking the c -axis length of the 100 K structure as the initial value, and calling the z direction stepping variable S , the R_{AB} bond length for the incremented c -axis, $c_{eff} = c_{100K} + S$, is expressed as

$$\begin{aligned} R_{AB}^2(c_{eff}) &= R_{AB}^2(c_{100K}) + k^2 + 2k(x_B - x_A) + \ell_1^2 + 2\ell_1(y_B - y_A) \\ &\quad + 2tS(z_B - z_A) + t^2S^2 \end{aligned} \quad 3.7$$

where k and ℓ_1 are the stepping variables in the x and y directions, respectively, for B -group atoms. See Section A.1.3 for the derivation of the equations presented here. The dimensionless constant t (as yet unknown) is responsible for scaling the step size S over the five atoms making up one turn (see Figure 3.16). Atoms of subsequent turns are translated by an additional S in the z direction, but by identical translations in the xy plane as corresponding atoms of previous turns. Of the D -group atoms (numbered as in Figure 3.15(c) and listed in Table 3.2), for example, Zn₄ is moved by $[-k, +\ell_3, +(0.5+t)S]$, Zn₈ by $[-k, +\ell_3, +(1.5+t)S]$ and Zn₁₂ by $[-k, +\ell_3, +(2.5+t)S]$.

By assuming that the O₁-Zn₂ coordination bond length remains constant, that is: $R_{AB}(c_{100K} + S) = R_{AB}(c_{100K})$, Eq. 3.7 can be simplified to

$$k^2 + 2k(x_B - x_A) + \ell_1^2 + 2\ell_1(y_B - y_A) + 2tS(z_B - z_A) + t^2S^2 = 0 \quad 3.8$$

Chapter 3: Materials and methods

This assumption is validated by the theoretical investigations of anomalous thermal expansion discussed in Section 1.2. In MD simulations of MOF-5 Han *et al.*¹⁴ found negligible change in Zn-O coordination bond lengths, while Goodwin and co-workers¹⁵ ascribed anisotropic thermal expansion in Ag₃[Co(CN)₆] to the rigidity of the Co-CN-Ag-NC-Co linking units. Applying the same reasoning to the bond length for Zn₂-O₃, R_{BC} , the following is found:

$$k^2 - 2k(x_C - x_B) + \ell_3^2 + 2\ell_3(y_C - y_B) + (0.5 - t)S[2(z_C - z_B) + (0.5 - t)S] = 0 \quad 3.9$$

where ℓ_3 is the variable controlling the translation in the y direction for the D -group atoms. The y direction of the C -group atoms is controlled by the variable $\ell_2 = \ell_1 + \ell_3$. To solve for t , the maximum values of the variables are employed, that is, the values of the parameters that would render the coordination spiral fully stretched out on the z axis. This is the case when $c_{eff} = 2R_{AB} + 2R_{BC}$:

$$\begin{aligned} S^{max} &= -(2R_{AB} + 2R_{BC} - |z_{E,100K}|) = -2.5354 \text{ \AA} \\ k^{max} &= |x_{B,100K}| = 0.9389 \text{ \AA} \\ \ell_1^{max} &= -y_{B,100K} = -0.1403 \text{ \AA} \\ \ell_3^{max} &= -y_{D,100K} = -1.4152 \text{ \AA} \end{aligned} \quad 3.10$$

Substituting these values into either Eq. 3.8 or Eq. 3.9 yields $t = 0.0995$. To reduce their dimensionality, these two equations are equated to obtain

$$\begin{aligned} 2k[(x_B - x_A) + (x_{C,0} - x_B)] + \ell_1^2 - \ell_3^2 + 2\ell_1(y_B - y_A) - 2\ell_3(y_C - y_B) \\ + 2tS[(z_B - z_A) + (z_C - z_B)] - S(z_C - z_B) - (0.25 - t)S^2 = 0 \end{aligned} \quad 3.11$$

Within the accuracy of the reorientation, that should render $x_A = x_C = 0$ (*cf.* Figure 3.16), the first term in Eq. 3.11 is zero, leaving an expression in terms of variables in the y and z directions only. Substituting for $\ell_3 = R_3\ell_1$, where the constant scaling factor $R_3 = y_D/y_B = 10.85$, Eq. 3.11 becomes

$$\begin{aligned} (1 - R_3^2)\ell_1^2 + 2\ell_1[(y_B - y_A) - R_3(y_C - y_B)] + 2tS(z_C - z_A) - S(z_C - z_B) \\ - (0.25 - t)S^2 = 0 \end{aligned} \quad 3.12$$

Chapter 3: Materials and methods

By solving Eq. 3.12 quadratically, an expression for ℓ_1 in terms of S is obtained. Subsequent substitution of ℓ_1 into Eq. 3.8 yields a quadratic expression for k in terms of S . In both cases the $x = -(b + \sqrt{b^2 - 4ac}) \cdot (2a)^{-1}$ root was used. All the variables and, thereby, the group-specific movement of all atoms in the coordination spiral (*cf.* Table 3.2) are determined through only one variable, namely S .

In Figure 3.17 the model is depicted over the range $0 \text{ \AA} \leq S \leq 2.5 \text{ \AA} < S^{max}$. The truncated ligand remains rigid (in its crystallographic geometry) and is translated along with the zinc atom to which it coordinates. This simplified the generation of models in that the imidazole and benzoate moieties are then simply translated as a single *B*- or *D*-group entity. To complete the model, an unaltered hydrogen atom Z-matrix (obtained for the 100 K structure using the script described in Section 3.7) is appended to the Cartesian coordinates of non-hydrogen atoms for a specific value of variable S .

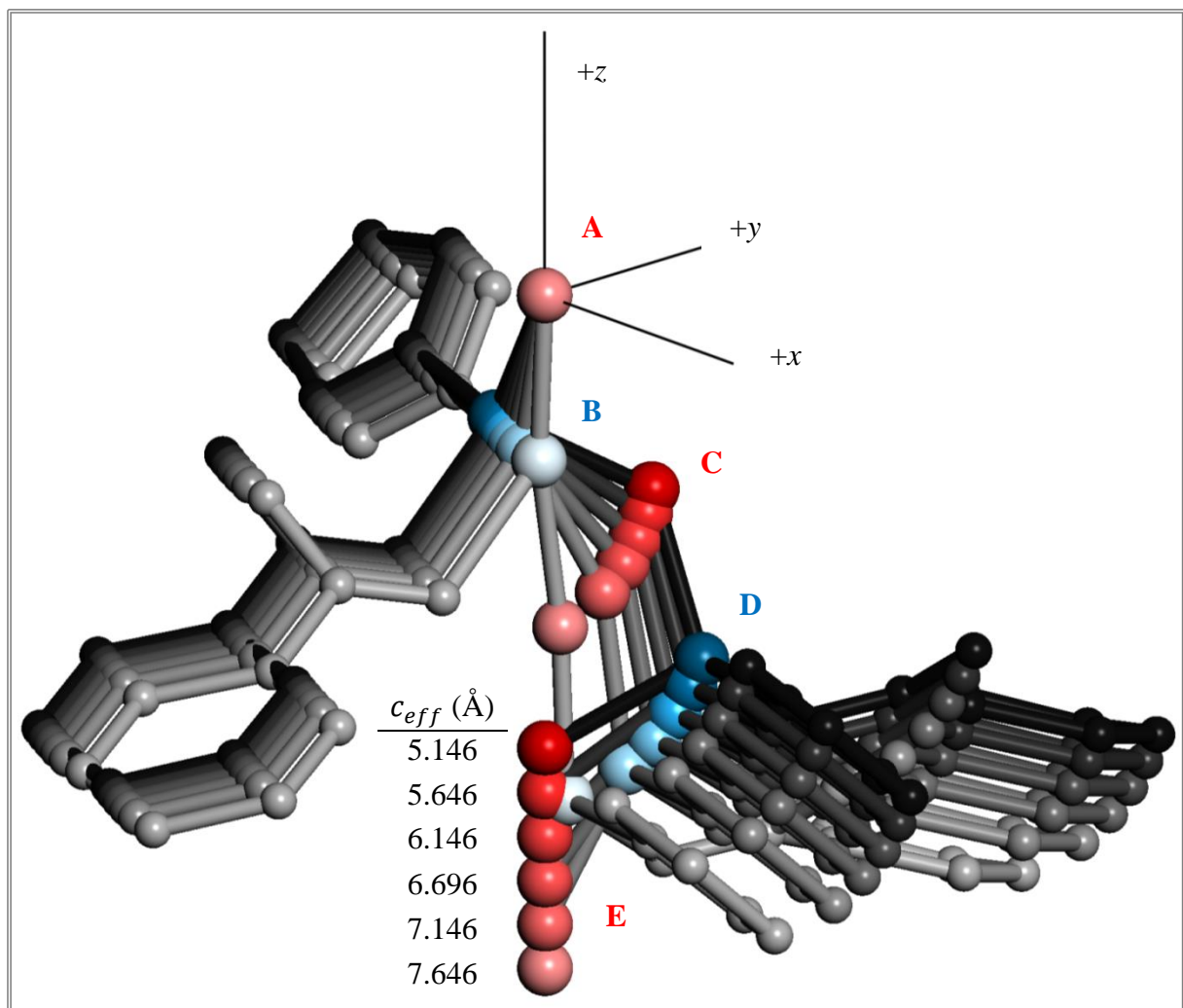


Figure 3.17: Overlay of the simulated model structures of one turn (atoms A to E) for variable S between 0.0 and 2.5 \AA in 0.5 \AA increments. Hydrogen atoms are omitted for clarity. Ligands are shown in grayscale while zinc atoms are colored blue and hydroxide-oxygen atoms red. The increasing brightness gradient infers movement as S is increased. Note that the atoms A and E are stationary in the xy plane, while the other atom of the coordination spiral converges onto the z axis. The effective c unit cell length $R_{AE} = c_{eff} = c_{100K} + S$ is also shown.

Chapter 3: Materials and methods

3.9 Density functionals and basis sets

In addition to the B97D and ω B97XD functionals discussed in Sections 2.4 and 2.5.3, respectively, the following density functionals were employed in this study: B3LYP;¹⁶ B3PW91;^{16a,17} mPW1PW91;¹⁷⁻¹⁸ CAM-B3LYP;¹⁹ LC- ω PBE;²⁰ M06L;²¹ M06;²² mPW1LYP;^{16b,c,18} O3LYP;^{16b,16d,23} PBEPBE;²⁴ mPW1PBE^{18,24b} and mPW3PBE.^{18,24b} The following all-electron basis sets were considered: STO-3G,²⁵ 6-31G,²⁶ 6-311G,²⁷ D95,²⁸ cc-PVDZ²⁹ and TZVP.³⁰ Effective core potential basis sets comprised the *compact effective potential* basis sets (CEP-4G, CEP-31G and CEP-121G),³¹ SDDAll³² wherein Stuttgart potentials are placed on non-hydrogen atoms, while Los Alamos potentials are employed in LANL2DZ³³ for non-hydrogen atoms.

For this study, *in vacuo*, 0 K molecular calculations were carried out using the Gaussian 09 software package. The bulk of the calculations presented in Chapter 4 were carried out using revision A.02,³⁴ while the calculations succeeding Section 4.6 (including results of the mechanistic model presented in Section 5.5) were carried out using revision D.01.³⁵ Theoretical evaluations of periodic structures were carried out with the Forcite and DMol³ modules³⁶ of the Materials Studio suite³⁷ for Molecular Modelling (encompassing Molecular Mechanics and Molecular Dynamics) and DFT calculations.

3.10 Summary

In this chapter, materials and methods used in this study are discussed. Synthetic routes and solvent-accessible space of the compounds investigated are presented, followed by a description of a novel volumetric SIT device previously developed in-house and a conventional gravimetric instrument used to carry out CO₂ adsorption experiments on **3_{apo}** and **4_{apo}** (results presented in Chapter 6). Rudimentary vector mathematics used for obtaining internal coordinates from Cartesian coordinates are presented and a VB script that automates the generation of a Z-matrix described along with illustrations of its application as a macro in Microsoft EXCEL. A procedure for investigating the mechanism of anisotropic thermal expansion observed in metal-organic framework **1_{apo}** (to be applied in Section 5.5) was also developed wherein the movement of all atoms in a computationally eligible model were solved as a function of only one variable, namely *S*.

Chapter 3: Materials and methods

3.11 References

1. (a) Connolly, M.L., *Science* **1983**, *221*, 709; (b) Connolly, M.L., *J. Mol. Graphics* **1993**, *11*, 139.
2. Bondi, A., *J. Phys. Chem.* **1964**, *68*, 441.
3. *POV-RAYTM for Windows*, Version 3.6, Persistence of vision Raytracer Pty. Ltd., Williamstown, Australia, **2004**, <http://www.povray.org>.
4. Barbour, L.J., *J. Supramol. Chem.* **2003**, *1*, 189.
5. Grobler, I.; Smith, V.J.; Bhatt, P.M.; Herbert, S.A.; Barbour, L.J., *J. Am. Chem. Soc.* **2013**, *135*, 6411.
6. Jacobs, T. PhD thesis, *Self-assembly of new porous materials*; Stellenbosch University, **2009**.
7. Dobrzańska, L.; Lloyd, G.O.; Raubenheimer, H.G.; Barbour, L.J., *J. Am. Chem. Soc.* **2006**, *128*, 698.
8. Atwood, J.L.; Barbour, L.J.; Thallapally, P.K.; Wirsig, T.B., *Chem. Commun.* **2005**, 51.
9. Marais, C.G. MSc thesis, *Thermodynamics and Kinetics of Sorption*; Stellenbosch University, **2008**.
10. Benham, M.J.; Ross, D.K., *Z. Phys. Chem.* **1989**, *163*, 25.
11. (a) Foley, N.J.; Thomas, K.M.; Forshaw, P.L.; Stanton, D.; Norman, P.R., *Langmuir* **1997**, *13*, 2083; (b) O'Koye, I.P.; Benham, M.; Thomas, K.M., *Langmuir* **1997**, *13*, 4054; (c) Reid, C.R.; O'Koye, I.P.; Thomas, K.M., *Langmuir* **1998**, *14*, 2415; (d) Harding, A.W.; Foley, N.J.; Norman, P.R.; Francis, D.C.; Thomas, K.M., *Langmuir* **1998**, *14*, 3858; (e) Fletcher, A.J.; Thomas, K.M., *Langmuir* **1999**, *15*, 6908; (f) Fletcher, A.J.; Thomas, K.M., *Langmuir* **2000**, *16*, 6253.
12. Busing, W.R.; Levy, H.A., *Acta Crystallogr.* **1964**, *17*, 142.
13. Schiller, C., *Fall, Flow and Heat In Motion Mountain, The Adventure of Physics*, 25 ed.; Creative Commons: Germany, **2012**; Vol. 1.
14. Han, S.S.; Goddard, W.A., III, *J. Phys. Chem. C* **2007**, *111*, 15185.
15. (a) Goodwin, A.L.; Calleja, M.; Conterio, M.J.; Dove, M.T.; Evans, J.S.O.; Keen, D.A.; Peters, L.; Tucker, M.G., *Science* **2008**, *319*, 794; (b) Calleja, M.; Goodwin, A.L.; Dove, M.T., *J. Phys. Condens. Matter* **2008**, *20*, 255226; (c) Conterio, M.J.; Goodwin, A.L.; Tucker, M.G.; Keen, D.A.; Dove, M.T.; Peters, L.; Evans, J.S.O., *J. Phys. Condens. Matter* **2008**, *20*, 255225.
16. (a) Becke, A.D., *Phys. Rev. A* **1988**, *38*, 3098; (b) Lee, C.; Yang, W.; Parr, R.G., *Phys. Rev. B* **1988**, *37*, 785; (c) Miehlich, B.; Savin, A.; Stoll, H.; Preuss, H., *Chem. Phys. Lett.* **1989**, *157*, 200; (d) Becke, A.D., *J. Chem. Phys.* **1993**, *98*, 5648; (e) Stephens, P.J.; Devlin, F.J.; Chabalowski, C.F.; Frisch, M.J., *J. Phys. Chem.* **1994**, *98*, 11623.
17. (a) Perdew, J.P.; Chevary, J.A.; Vosko, S.H.; Jackson, K.A.; Pederson, M.R.; Singh, D.J.; Fiolhais, C., *Phys. Rev. B* **1992**, *46*, 6671; (b) Perdew, J.P.; Chevary, J.A.; Vosko, S.H.; Jackson, K.A.; Pederson, M.R.; Singh, D.J.; Fiolhais, C., *Phys. Rev. B* **1993**, *48*, 4978; (c) Perdew, J.P.; Burke, K.; Wang, Y., *Physical Rev. B* **1996**, *54*, 16533.
18. Adamo, C.; Barone, V., *J. Chem. Phys.* **1998**, *108*, 664.
19. Yanai, T.; Tew, D.P.; Handy, N.C., *Chem. Phys. Lett.* **2004**, *393*, 51.
20. (a) Tawada, Y.; Tsuneda, T.; Yanagisawa, S.; Yanai, T.; Hirao, K., *J. Chem. Phys.* **2004**, *120*, 8425; (b) Vydrov, O.A.; Scuseria, G.E., *J. Chem. Phys.* **2006**, *125*, 234109; (c) Vydrov, O.A.;

Chapter 3: Materials and methods

- Heyd, J.; Krukau, A.V.; Scuseria, G.E., *J. Chem. Phys.* **2006**, *125*, 74106; (d) Vydrov, O.A.; Scuseria, G.E.; Perdew, J.P., *J. Chem. Phys.* **2007**, *126*, 154109.
21. Zhao, Y.; Truhlar, D.G., *J. Chem. Phys.* **2006**, *125*, 194101.
 22. Zhao, Y.; Truhlar, D.G., *Theor. Chem. Acc.* **2008**, *120*, 215.
 23. (a) Handy, N.C.; Cohen, A.J., *Mol. Phys.* **2001**, *99*, 403; (b) Hoe, W.M.; Cohen, A.J.; Handy, N.C., *Chem. Phys. Lett.* **2001**, *341*, 319.
 24. (a) Perdew, J.P.; Burke, K.; Ernzerhof, M., *Phys. Rev. Lett.* **1997**, *78*, 1396; (b) Perdew, J.P.; Burke, K.; Ernzerhof, M., *Phys. Rev. Lett.* **1996**, *77*, 3865.
 25. (a) Hehre, W.J.; Stewart, R.F.; Pople, J.A., *J. Chem. Phys.* **1969**, *51*, 2657; (b) Collins, J.B.; Schleyer, P.v.R.; Binkley, J.S.; Pople, J.A., *J. Chem. Phys.* **1976**, *64*, 5142.
 26. (a) Ditchfield, R.; Hehre, W.J.; Pople, J.A., *J. Chem. Phys.* **1971**, *54*, 724; (b) Hehre, W.J.; Ditchfield, R.; Pople, J.A., *J. Chem. Phys.* **1972**, *56*, 2257; (c) Hariharan, P.C.; Pople, J.A., *Theor. Chim. Acta* **1973**, *28*, 213; (d) Hariharan, P.C.; Pople, J.A., *Mol. Phys.* **1974**, *27*, 209; (e) Gordon, M.S., *Chem. Phys. Lett.* **1980**, *76*, 163; (f) Francil, M.M.; Pietro, W.J.; Hehre, W.J.; Binkley, J.S.; Gordon, M.S.; DeFrees, D.J.; Pople, J.A., *J. Chem. Phys.* **1982**, *77*, 3654; (g) Binning, R.C., Jr.; Curtiss, L.A., *J. Comput. Chem.* **1990**, *11*, 1206; (h) Blaudeau, J.-P.; McGrath, M.P.; Curtiss, L.A.; Radom, L., *J. Chem. Phys.* **1997**, *107*, 5016; (i) Rassolov, V.A.; Pople, J.A.; Ratner, M.A.; Windus, T.L., *J. Chem. Phys.* **1998**, *109*, 1223; (j) Rassolov, V.A.; Ratner, M.A.; Pople, J.A.; Redfern, P.C.; Curtiss, L.A., *J. Comput. Chem.* **2001**, *22*, 976.
 27. (a) Wachters, A.J.H., *J. Chem. Phys.* **1970**, *52*, 1033; (b) Hay, P.J., *J. Chem. Phys.* **1977**, *66*, 4377; (c) Krishnan, R.; Binkley, J.S.; Seeger, R.; Pople, J.A., *J. Chem. Phys.* **1980**, *72*, 650; (d) McLean, A.D.; Chandler, G.S., *J. Chem. Phys.* **1980**, *72*, 5639; (e) Raghavachari, K.; Trucks, G.W., *J. Chem. Phys.* **1989**, *91*, 2457; (f) McGrath, M.P.; Radom, L., *J. Chem. Phys.* **1991**, *94*, 511; (g) Curtiss, L.A.; McGrath, M.P.; Blaudeau, J.-P.; Davis, N.E.; Binning, r.C., Jr.; Radom, L., *J. Chem. Phys.* **1995**, *103*, 6104.
 28. (a) Huzinaga, S., *J. Chem. Phys.* **1965**, *42*, 1293; (b) Dunning, T.H., Jr., *J. Chem. Phys.* **1970**, *53*, 2823.
 29. (a) Dunning, T.H., Jr., *J. Chem. Phys.* **1989**, *90*, 1007; (b) Kendall, R.A.; Dunning, T.H., Jr.; Harrison, R.J., *J. Chem. Phys.* **1992**, *96*, 6796; (c) Woon, D.E.; Dunning, T.H., Jr., *J. Chem. Phys.* **1993**, *98*, 1358; (d) Peterson, K.A.; Woon, D.E.; Dunning, T.H., Jr., *J. Chem. Phys.* **1994**, *100*, 7410; (e) Wilson, A.K.; van Mourik, T.; Dunning, T.H., Jr., *J. Mol. Struct. THEOCHEM* **1996**, *388*, 339.
 30. (a) Schäfer, A.; Horn, H.; Ahlrichs, R., *J. Chem. Phys.* **1992**, *97*, 2571; (b) Schäfer, A.; Huber, C.; Ahlrichs, R., *J. Chem. Phys.* **1994**, *100*, 5829.
 31. (a) Stevens, W.J.; Basch, H.; Krauss, M., *The Journal of Chemical Physics* **1984**, *81*, 6026; (b) Stevens, W.J.; Krauss, M.; Basch, H.; Jasien, P.G., *Can. J. Chem.* **1992**, *70*, 612; (c) Cundari, T.R.; Stevens, W.J., *J. Chem. Phys.* **1993**, *98*, 5555.
 32. (a) Fuentealba, P.; Preuss, H.; Stoll, H.; Von Szentpaly, L., *Chem. Phys. Lett.* **1982**, *89*, 418; (b) Von Szentpaly, L.; Fuentealba, P.; Preuss, H.; Stoll, H., *Chem. Phys. Lett.* **1982**, *93*, 555; (c) Fuentealba, P.; Stoll, H.; Von Szentpaly, L.; Schwerdtfeger, P.; Preuss, H., *J. Phys. B* **1983**, *16*, L323; (d) Stoll, H.; Fuentealba, P.; Schwerdtfeger, P.; Flad, J.; Von Szentpaly, L.V.; Preuss, H., *J. Chem. Phys.* **1984**, *81*, 2732; (e) Fuentealba, P.; Von Szentpaly, L.; Preuss, H.; Stoll, H., *J. Phys. B* **1985**, *18*, 1287; (f) Wedig, U.; Dolg, M.; Stoll, H.; Preuss, H., *Quantum Chemistry: The Challenge of Transition Metals and Coordination Chemistry*. **1986**; (g) Dolg, M.; Wedig, U.; Stoll, H.; Preuss, H., *J. Chem. Phys.* **1987**, *86*, 866; (h) Igel-Mann, G.; Stoll, H.; Preuss, H., *Mol. Phys.* **1988**, *65*, 1321; (i) Dolg, M.; Stoll, H.; Preuss, H., *J. Chem. Phys.* **1989**, *90*, 1730; (j) Schwerdtfeger, P.; Dolg, M.; Schwarz, W.H.E.; Bowmaker,

Chapter 3: Materials and methods

- G.A.; Boyd, P.D.W., *J. Chem. Phys.* **1989**, *91*, 1762; (k) Dolg, M.; Stoll, H.; Savin, A.; Preuss, H., *Theor. Chim. Acta* **1989**, *75*, 173; (l) Andrae, D.; Haeussermann, U.; Dolg, M.; Stoll, H.; Preuss, H., *Theor. Chim. Acta* **1990**, *77*, 123; (m) Dolg, M.; Fulde, P.; Kuechle, W.; Neumann, C.S.; Stoll, H., *J. Chem. Phys.* **1991**, *94*, 3011; (n) Kaupp, M.; Schleyer, P.v.R.; Stoll, H.; Preuss, H., *J. Chem. Phys.* **1991**, *94*, 1360; (o) Kuechle, W.; Dolg, M.; Stoll, H.; Preuss, H., *Mol. Phys.* **1991**, *74*, 1245; (p) Dolg, M.; Stoll, H.; Flad, H.J.; Preuss, H., *J. Chem. Phys.* **1992**, *97*, 1162; (q) Dolg, M.; Stoll, H.; Preuss, H.; Pitzer, R.M., *J. Phys. Chem.* **1993**, *97*, 5852; (r) Dolg, M.; Stoll, H.; Preuss, H., *Theor. Chim. Acta* **1993**, *85*, 441; (s) Bergner, A.; Dolg, M.; Kuechle, W.; Stoll, H.; Preuss, H., *Mol. Phys.* **1993**, *80*, 1431; (t) Haeussermann, U.; Dolg, M.; Stoll, H.; Preuss, H.; Schwerdtfeger, P.; Pitzer, R.M., *Mol. Phys.* **1993**, *78*, 1211; (u) Kuechle, W.; Dolg, M.; Stoll, H.; Preuss, H., *J. Chem. Phys.* **1994**, *100*, 7535; (v) Nicklass, A.; Dolg, M.; Stoll, H.; Preuss, H., *J. Chem. Phys.* **1995**, *102*, 8942; (w) Leininger, T.; Nicklass, A.; Stoll, H.; Dolg, M.; Schwerdtfeger, P., *J. Chem. Phys.* **1996**, *105*, 1052; (x) Cao, X.; Dolg, M., *J. Chem. Phys.* **2001**, *115*, 7348; (y) Cao, X.; Dolg, M., *J. Mol. Struct. THEOCHEM* **2002**, *581*, 139.
33. (a) Hay, P.J.; Wadt, W.R., *J. Chem. Phys.* **1985**, *82*, 299; (b) Hay, P.J.; Wadt, W.R., *J. Chem. Phys.* **1985**, *82*, 270; (c) Wadt, W.R.; Hay, P.J., *J. Chem. Phys.* **1985**, *82*, 284.
34. *GAUSSIAN 09, Revision A.02*, Frisch, M.J.; Trucks, G.W.; Schlegel, H.B.; Scuseria, G.E.; Robb, M.A.; Cheeseman, J.R.; Scalmani, G.; Barone, V.; Mennucci, B.; Petersson, G.A.; Nakatsuji, H.; Caricato, M.; Li, X.; Hratchian, H.P.; Izmaylov, A.F.; Bloino, J.; Zheng, G.; Sonnenberg, J.L.; Hada, M.; Ehara, M.; Toyota, K.; Fukuda, R.; Hasegawa, J.; Ishida, M.; Nakajima, T.; Honda, Y.; Kitao, O.; Nakai, H.; Vreven, T.; Montgomery Jr., J.A.; Peralta, J.E.; Ogliaro, F.; Bearpark, M.; Heyd, J.J.; Brothers, E.; Kudin, K.N.; Staroverov, V.N.; Kobayashi, R.; Normand, J.; Raghavachari, K.; Rendell, A.; Burant, J.C.; Iyengar, S.S.; Tomasi, J.; Cossi, M.; Rega, N.; Millam, J.M.; Klene, M.; Knox, J.E.; Cross, J.B.; Bakken, V.; Adamo, C.; Jaramillo, J.; Gomperts, R.; Stratmann, R.E.; Yazyev, O.; Austin, A.J.; Cammi, R.; Pomelli, C.; Ochterski, J.W.; Martin, R.L.; Morokuma, K.; Zakrzewski, V.G.; Voth, G.A.; Salvador, P.; Dannenberg, J.J.; Dapprich, S.; Daniels, A.D.; Farkas, O.; Foresman, J.B.; Ortiz, J.V.; Cioslowski, J.; Fox, D.J.; Gaussian, Inc.: Wallingford CT, **2009**.
35. *GAUSSIAN 09, Revision D.01*, Frisch, M.J.; Trucks, G.W.; Schlegel, H.B.; Scuseria, G.E.; Robb, M.A.; Cheeseman, J.R.; Scalmani, G.; Barone, V.; Mennucci, B.; Petersson, G.A.; Nakatsuji, H.; Caricato, M.; Li, X.; Hratchian, H.P.; Izmaylov, A.F.; Bloino, J.; Zheng, G.; Sonnenberg, J.L.; Hada, M.; Ehara, M.; Toyota, K.; Fukuda, R.; Hasegawa, J.; Ishida, M.; Nakajima, T.; Honda, Y.; Kitao, O.; Nakai, H.; Vreven, T.; Montgomery Jr., J.A.; Peralta, J.E.; Ogliaro, F.; Bearpark, M.; Heyd, J.J.; Brothers, E.; Kudin, K.N.; Staroverov, V.N.; Keith, T.; Kobayashi, R.; Normand, J.; Raghavachari, K.; Rendell, A.; Burant, J.C.; Iyengar, S.S.; Tomasi, J.; Cossi, M.; Rega, N.; Millam, J.M.; Klene, M.; Knox, J.E.; Cross, J.B.; Bakken, V.; Adamo, C.; Jaramillo, J.; Gomperts, R.; Stratmann, R.E.; Yazyev, O.; Austin, A.J.; Cammi, R.; Pomelli, C.; Ochterski, J.W.; Martin, R.L.; Morokuma, K.; Zakrzewski, V.G.; Voth, G.A.; Salvador, P.; Dannenberg, J.J.; Dapprich, S.; Daniels, A.D.; Farkas, O.; Foresman, J.B.; Ortiz, J.V.; Cioslowski, J.; Fox, D.J.; Gaussian, Inc.: Wallingford CT, **2013**.
36. (a) Delley, B., *J. Chem. Phys.* **1990**, *92*, 508; (b) Delley, B., *J. Chem. Phys.* **2000**, *113*, 7756.
37. *Materials Studio Modeling Environment*, Release 6.0; Accelrys Software Inc.: San Diego, USA, **2011**.

Chapter 4: Investigation of eclipsed methyl in the solid state

In order to identify key concepts necessary to accurately model porous materials, the performance of various density functionals in predicting a nearly eclipsed $\text{C}_{\text{sp}^3}\text{-CH}_3$ group in the solid state is discussed. This anomalous methyl conformation is found in the crystal structure of the trihydrate of a tricyclicorthoamide ($\text{C}_{11}\text{H}_{21}\text{N}_3\cdot 3\text{H}_2\text{O}$, **2** \cdot $3\text{H}_2\text{O}$), reported along with its anhydrous form by Seiler *et al.*¹ As shown in Figure 4.1, the asymmetric unit of the anhydrous form comprises two full molecules of **2** in different configurations. The C-C bond lengths and H-C-C-N dihedral angles (ω_{hccn}) of the methyl group are also shown for comparison.

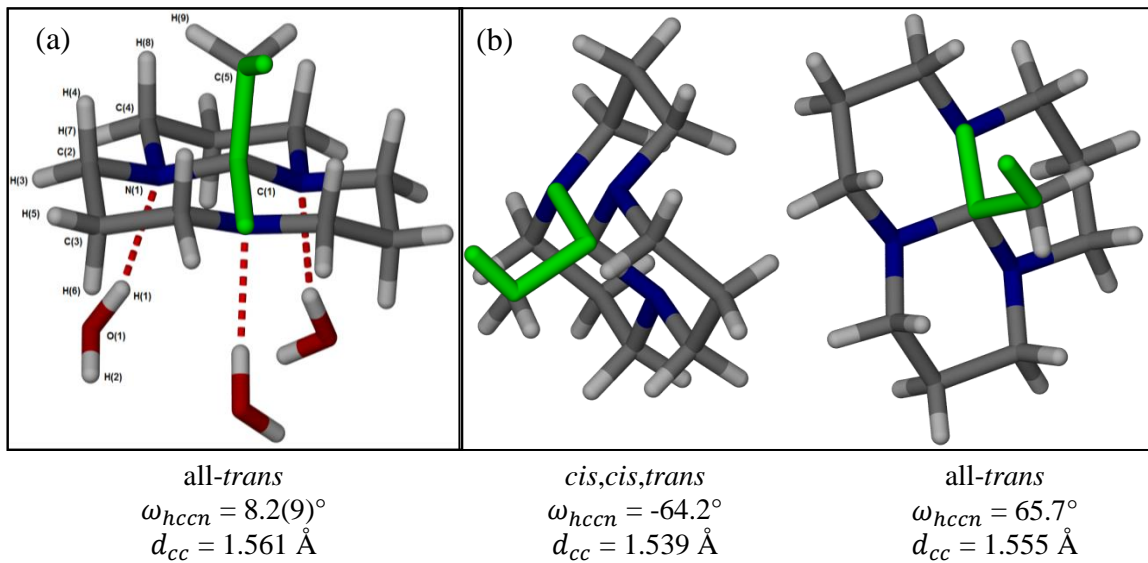


Figure 4.1: Comparison of the orientations of the methyl group in the crystal structures of (a) **2** \cdot $3\text{H}_2\text{O}$ with asymmetric unit labelled, and (b) its anhydrous form.¹ The ω_{hccn} dihedral angle is highlighted in green.

The anhydrous form crystallizes in the monoclinic space group $P2_1/c$ while the trihydrate crystallizes in the cubic space group $Pa\bar{3}$. The position of the hydrogen atoms were located from difference maps and assigned isotropic displacement parameters.¹ An $\text{OH}\cdots\text{N}$ hydrogen bond was identified in **2** \cdot $3\text{H}_2\text{O}$ with $d_{\text{O}\cdots\text{N}} = 2.874 \text{ \AA}$. Complexes of **2** \cdot $3\text{H}_2\text{O}$ are related to one another through an inversion centre to form hydrogen-bonded water hexamers (H_2O)₆ with $d_{\text{O}\cdots\text{O}} = 2.770 \text{ \AA}$, as shown in Figure 4.2(a). The eclipsed conformation seen in the hydrate is not an inherent molecular property since the all-*trans* molecule of the anhydrous form (right hand side of Figure 4.1(b)) displays a staggered conformation. One can therefore assume that the presence of water molecules is responsible for the eclipsed conformation of the methyl. Figure 4.2(b) shows that the methyl hydrogen points towards a water molecule to form an $\text{C}_{\text{sp}^3}\text{-CH}_3\cdots\text{OH}_2$ interaction with $\omega_{ncco} = 0.9^\circ$ and $d_{\text{C}\cdots\text{O}} = 3.638 \text{ \AA}$.

Chapter 4: Investigation of eclipsed methyl in the solid state

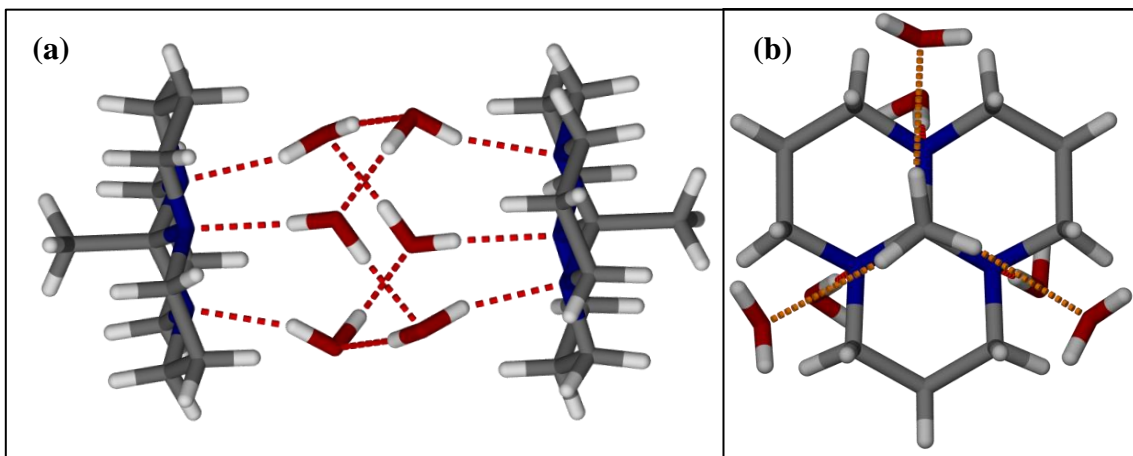


Figure 4.2: (a) Depiction of the hydrogen bonded water-hexamer ($d_{O\cdots O} = 2.770 \text{ \AA}$) in the crystal structure of **2**·3H₂O. (b) The methyl hydrogens point to water molecules with the weak C-H···O hydrogen bonds ($d_{C\cdots O} = 3.638 \text{ \AA}$) possibly responsible for the eclipsed conformation indicated by orange dashed lines.

In a seminal study of hydrogen bonding, Steiner searched the Cambridge Structural Database (CSD)² (October 2000 update) for hydrogen bonds wherein water molecules act as acceptors. The study was restricted to those where $\theta_{X-H\cdots OH_2} > 135^\circ$.³ For the C_{sp³}-CH₃···OH₂ interaction, Steiner found a mean C···O separation of 3.613(6) Å with 95% of the 533 structures having a separation > 3.35 Å. Based on these findings, the interaction in **2**·3H₂O with $d_{C\cdots O} = 3.638 \text{ \AA}$ is too long to be classified as a weak hydrogen bond. The C-H···Ow angle of 170.18° (**2**·3H₂O, X-ray data)¹ is, however, close to the linear-geometry criterion for strong hydrogen bonds, reducing the weight of the distance criterion.³ Steiner stated that in the solid state, hydrogen bonds are subject to crystal-packing forces that can easily distort them from optimal geometries.³ Such crystal-field effects arise from the numerous close contacts present in the condensed phase, while increased polarization through cooperative effects can also strengthen intermolecular interactions.³

Here follows a discussion of previous computational investigations of the C-H···O interaction in **2**·3H₂O. This chapter describes the potential energy surface of molecular representations of **2**·3H₂O obtained by way of scanning of the ω_{hccn} dihedral angle with all non-hydrogen atoms constrained to their crystallographic positions. Results of a CCSD (coupled cluster with singles and doubles) method evaluation **2**·H₂O is presented, followed by an assessment of the basis set dependence of results obtained at the Hartree-Fock level of theory. The ω_{hccn} potential energy profile obtained by various DFT exchange-correlation functionals is discussed, followed by a comparison of the dispersion correction of different DFT-D schemes to the correlation correction of the Møller-Plesset perturbation theory with second-order corrections (MP2). The counterpoise scheme is also discussed as an effective means towards obtaining geometries free of basis set superposition errors.

4.1 Background

The first study of **2·3H₂O** was conducted by Seiler *et al.*, who calculated the CH₄···OH₂ interaction for $d_{C\cdots O} = 3.64 \text{ \AA}$, as found in the **2·3H₂O**, to be -1.45 kcal.mol⁻¹ at the MP2/6-31G(d) level of theory.⁴ The C-H···O interaction energy increased to -1.98 kcal.mol⁻¹ in an enlarged model consisting of CH₄···O(H)H···NH₃, indicating that cooperative effects strengthen the interaction by increasing the accepting capability of the water molecule. Based on this, Seiler *et al.* concluded that the C-H···O interaction is responsible for the eclipsed methyl conformation in **2·3H₂O**.

Upon further investigation, Novoa *et al.* pointed out that the interaction energies calculated by Seiler *et al.* were plagued by the BSSE.⁵ They in turn reported an interaction energy of -0.59 kcal.mol⁻¹ based on MP2-level calculations with a near-HF-limit basis set for the CH₄···OH₂ model.⁶ In order to examine cooperative effects, they carried out MP2/6-31++G(d,p) calculations for the series CH₄···OH₂, CH₄···(OH₂)₂ and CH₄···(OH₂)₃, and found cp corrected interaction energies of -0.37, -0.61 and -0.86 kcal.mol⁻¹ for the respective models.⁵ The C-H···O interaction strength is therefore not additive, because the interaction energy of methane with three waters is not simply three times the interaction energy of CH₄···OH₂. Novoa *et al.* furthermore found a cp-corrected interaction energy of -0.52 kcal.mol⁻¹ [MP2/6-31++G(d,p)] for the CH₄···O(H)H···NH₃ model of **2·3H₂O**, as opposed to the interaction energy of -1.98 kcal.mol⁻¹ [MP2/6-31G(d)] found by Seiler *et al.*⁴

Using CH₃-C(NH₂)₃ to represent a molecule of **2**, Novoa *et al.* predicted the barrier to rotation, ΔE_{rot} , of the methyl group to be 5.44 kcal.mol⁻¹ at the HF/6-31++G(d,p) level of theory.⁵ They concluded that the overall C-H···O interaction, roughly -2.5 kcal.mol⁻¹ after scaling to allow for cooperative effects, is not strong enough to overcome the rotation barrier, and that the eclipsed conformation is simply a local minimum.

Chao *et al.* used a complete molecule of **2** to calculate a rotation barrier of 2.00 kcal.mol⁻¹ at the HF/6-31++G(d,p) level of theory.⁷ To explain this large reduction in the rotation barrier (*cf.* $\Delta E_{rot} = 5.44 \text{ kcal.mol}^{-1}$), they pointed out that the short contact between the staggered methyl and the axial methylene hydrogens present in **2** was not accounted for in the model used by Novoa *et al.* This is illustrated in Figure 4.3. The combined stabilization of the three C-H···O interactions extrapolated by Novoa *et al.* ($\sim 2.5 \text{ kcal.mol}^{-1}$) is therefore able to overcome the rotation barrier and is responsible for the unique eclipsed methyl found in the crystal structure of **2·3H₂O**.⁷

Chapter 4: Investigation of eclipsed methyl in the solid state

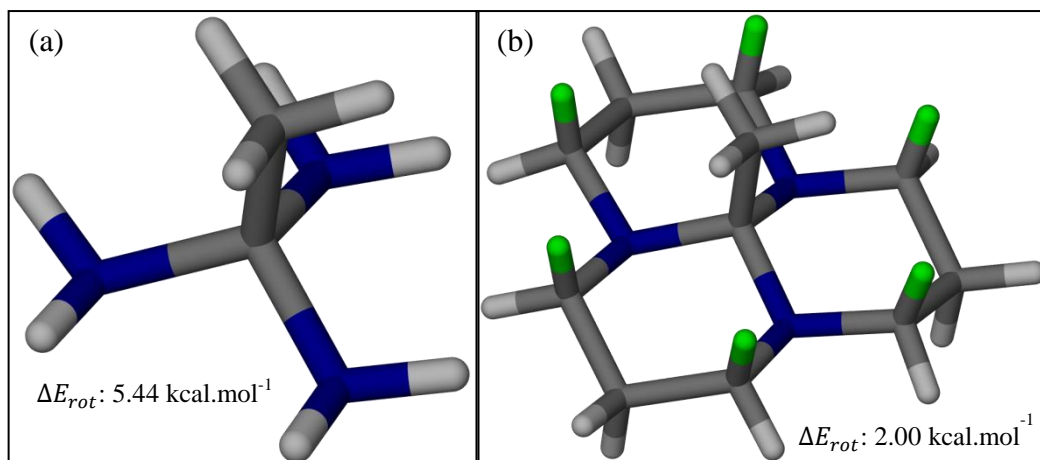


Figure 4.3: Comparison of the model employed by Novoa *et al.*⁵ $\text{CH}_3\text{-C}(\text{NH}_2)_3$ (a) and **2** (b), used by Chao *et al.*,⁷ with axial hydrogens highlighted in green, to calculate the barrier to rotation.

It is thus clear from the discussion above that a model of sufficient size to account for intramolecular close contacts, as well as cooperative effects, must be employed in order to correctly model the weak intermolecular interactions in **2**·3H₂O.

4.2 CCSD investigation

The ω_{hccn} dihedral angle was stepped in partially relaxed scans employing the B97D functional in combination with various basis sets, followed by CCSD single point energy calculations to yield potential energy profiles at the CCSD/basis set//B97D/basis set level of theory. Due to the high expense of the CCSD method, viable basis set choices are limited to very small all-electron basis sets, or those incorporating effective core potentials (ECPs) that replace core electrons with a single potential and introduce some degree of relativistic effects.⁸ In addition, the minimal model shown in Figure 4.4 was evaluated and the frozen noble gas core approximation used.⁹ In Figure 4.5 the energy profiles relative to the most stable conformer for each basis set are shown. The three-fold symmetry (point group C₃) of the model is evident with a period of 120° (*cf.* Figure A.4 for 0° < ω_{hccn} < 180° results). All basis sets found the eclipsed conformer ($\omega_{hccn} \approx 10^\circ$) to be most stable with a rotation barrier at ~85° whose basis set dependent magnitude ranges from 1.25 to 1.65 kcal·mol⁻¹. The profiles also show an inflection close to the staggered conformation (~50°) with the all-electron 6-31G and ECP SDDAll basis sets displaying the strongest inflections. This suggests the presence of a local minimum in this region.

In general eclipsed conformations (0°) have the highest energy due to repulsion of the methyl group, while staggered conformations (60°) are most stable.¹⁰ However, due to the favorable interaction with neighboring water molecules, the nearly eclipsed conformer becomes dominant in **2**·3H₂O. The pronounced barrier to rotation at ~85° can be ascribed to steric repulsion of the proximal axial hydrogens of methylene bridges. The shoulder in the dihedral angle profile at ~50° is due to a favorable dispersion interaction with both axial hydrogens, before steric repulsion starts to dominate. The reasoning for this behavior will become clear in the following sections, where it is shown that dispersion correction schemes are essential in reproducing the CCSD profile.

Chapter 4: Investigation of eclipsed methyl in the solid state

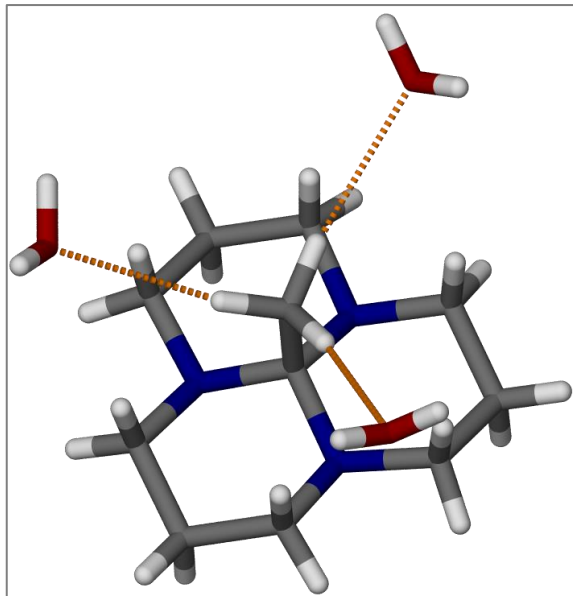


Figure 4.4: Minimal model of **2·3H₂O** used for computationally expensive calculations: CCSD and counterpoise corrected MP2 single point calculations and counterpoise corrected DFT and HF geometry optimizations. Weak C-H···O interactions are shown as dashed lines.

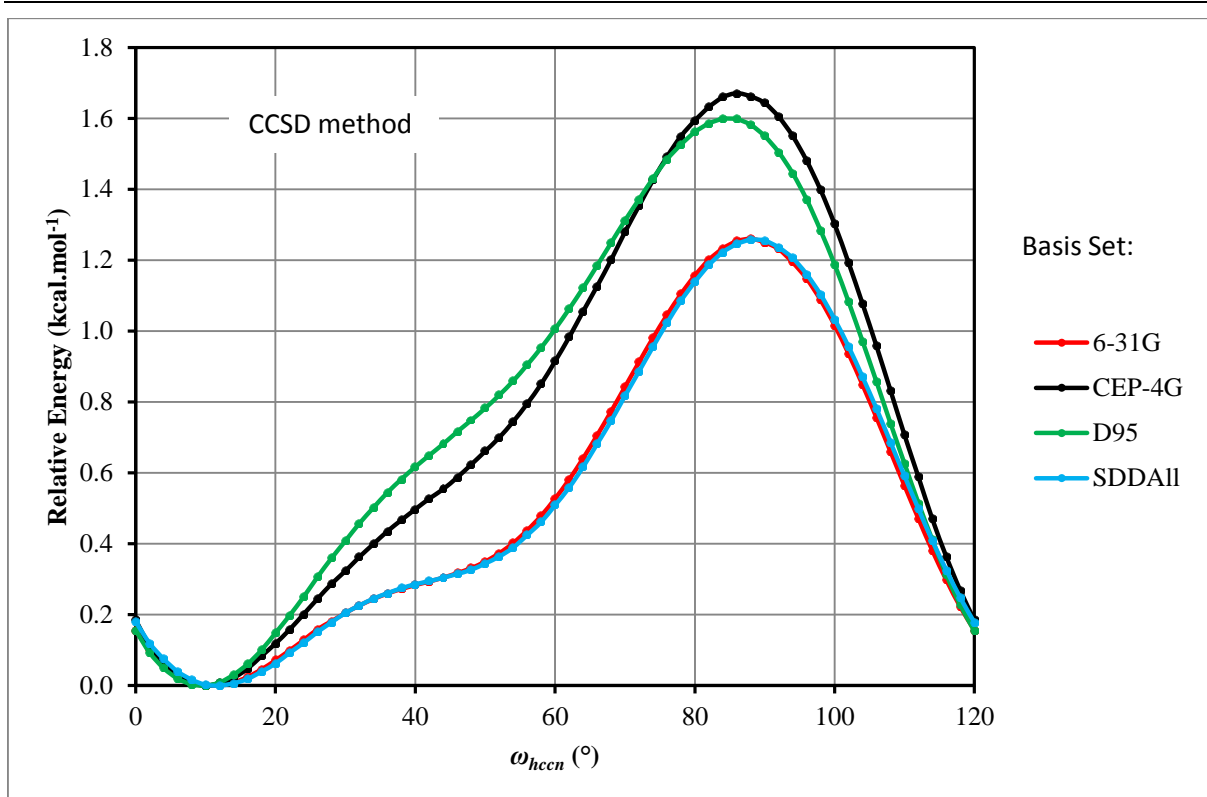


Figure 4.5: Relative potential energy profile of the ω_{hccn} dihedral angle stepped between 0° and 120° in 2° increments obtained using various basis sets at the CCSD/basis set/B97D/basis set level of theory.

Chapter 4: Investigation of eclipsed methyl in the solid state

4.3 Comprehensive model of 2·3H₂O

In order to better evaluate the potential energy profile of ω_{hccn} , the model shown in Figure 4.6 was employed. This model overcomes the limitations pointed out in Section 4.1 of using a smaller model for the orthoamide, and also allows accounting for cooperative effects. The interaction sphere of water molecules involved in the C-H···O interaction includes two water molecules and an ammonia molecule to approximate the hydrogen bonding to an orthoamide molecule.* All non-hydrogen atoms of appendage molecules were maintained in their crystallographic positions corresponding to those in the hexameric water units or orthoamide molecules.

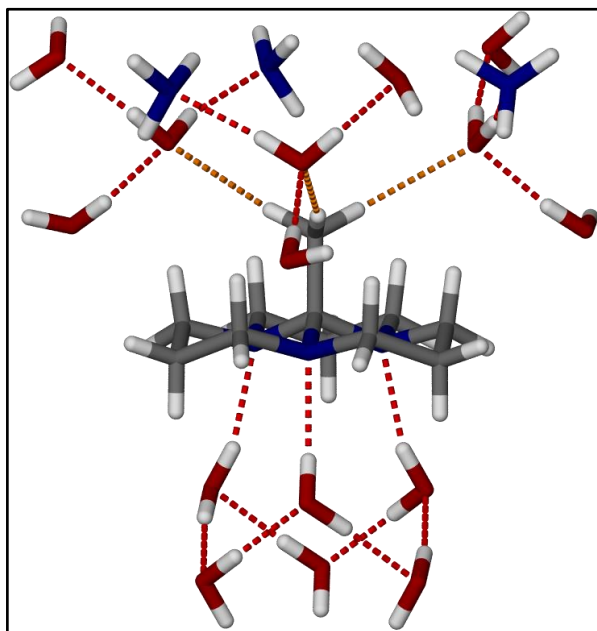


Figure 4.6: Comprehensive model of 2·3H₂O that encompasses steric and cooperative effects used to carry out scans of the ω_{hccn} dihedral angle at the HF and DFT levels of theory. Red dashed lines represent hydrogen bonds while the weak C-H···O interactions are shown in orange.

The following sequence of optimizations was performed at various HF (Section 4.4) and DFT (Section 4.5) levels of theory. All non-hydrogen atoms were kept fixed in their relative 2·3H₂O crystal structure positions throughout. Initially, the geometries of the water molecules were optimized in the hexameric conformation in the model shown in Figure 4.2(a). The optimized internal coordinate variables were then transferred to models of Figure 4.6 and all hydrogen atoms, except those of water molecules, optimized with ω_{hccn} fixed at 0.0°. Finally, scans from 0° to 120° in 2° steps of ω_{hccn} were performed with the water and ammonia molecules frozen in their geometries obtained in the first and second steps, respectively.

* In order to construct a Z-matrix with the minimum number of variables, all water molecules were defined relative to each other in a hexameric (H₂O)₆ unit. Dummy atoms on the O_w positions of omitted water molecules, as shown in Figure A.3, allow use of the same variables for incomplete hexamers. C₃ symmetry is thus maintained to speed up calculations.

4.4 Comparison of basis set performance at the HF level of theory

The basis set dependence of the ω_{hccn} potential energy profile obtained at the HF-level of theory is discussed in this section. As seen in Figure 4.7, all unaugmented (*vide infra*) basis sets correctly predict the $\omega_{hccn} \approx 85^\circ$ conformation to be least stable with a potential energy between 1.0 and 1.3 kcal. mol^{-1} higher than for the nearly eclipsed conformer. The very small CEP-4G basis set (—), however, overestimates the barrier to rotation to be 2.0 kcal. mol^{-1} . The basis sets can be augmented by adding diffuse functions and/or polarization functions to the non-hydrogen atom sets or to all sets. Diffuse functions have small exponents and decay slowly, allowing for improved modelling of long-range interactions, while polarization functions have high angular momentum components to improve the directionality of the basis set.¹¹ The effect of augmenting the CEP basis sets' non-hydrogen atoms with polarization functions is to shift the predicted minimum from the experimentally observed $\omega_{hccn} = 8.2^\circ$ to around 50° , except for the CEP-4G basis set which now predicts a potential energy profile similar to that obtained with the all-electron basis sets. The CCSD/SDDAll//B97D/SDDAll level of theory results obtained for the minimal model (●) are shown for comparison. The fact that the Hartee-Fock results correlate favorably with the CCSD results is due to a cancellation of errors (*vide infra*) in that it is not possible for the HF method to model the dynamic correlation responsible for dispersion interactions to which the inflection in the potential energy profile can be ascribed.

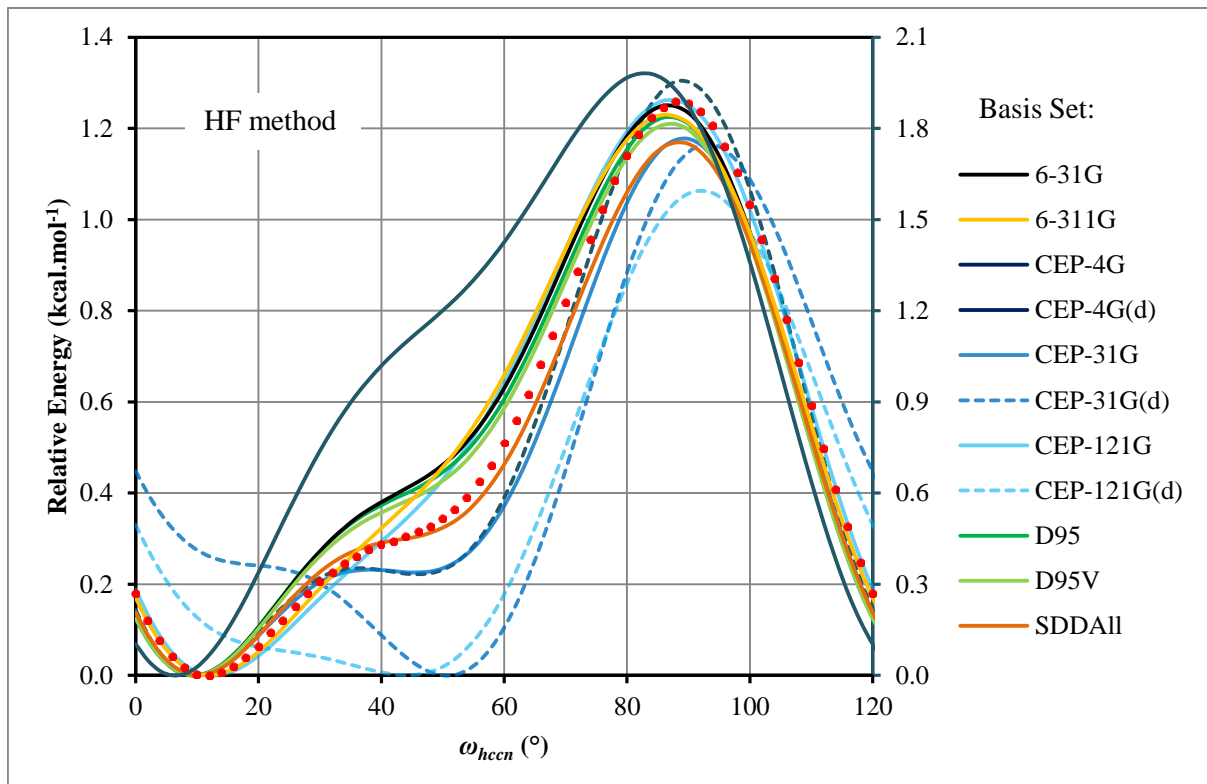


Figure 4.7: Graph of the potential energy profile for ω_{hccn} obtained with various basis sets at the HF level of theory. The relative energy of the CEP-4G basis set (—) is shown on the right hand ordinate. Also shown is the CCSD/SDDAll//B97D/SDDAll profile (●, minimal model of Figure 4.4).

Chapter 4: Investigation of eclipsed methyl in the solid state

The effect of augmentation for all-electron 6-31G and 6-311G basis sets is collectively shown in Figure 4.8. Adding either only diffuse or only polarization functions makes the local minimum at $\omega_{hccn} = 50^\circ$ more prominent (Figure 4.8(a) and (b)). This effect is enhanced if hydrogen atom basis sets are also augmented. Augmenting with both diffuse and polarization functions causes the predicted minimum energy conformation to shift from $\sim 8^\circ$ to $\sim 50^\circ$ (Figure 4.8(c) and (d)). These effects are more pronounced for the smaller double- ζ 6-31G basis set than for the triple- ζ 6-311G basis set.

Based on these results, it is clear the HF-level calculations are highly basis set dependent with the smallest, 6-31G, and largest, 6-311++G(d,p), basis sets* able to predict the nearly eclipsed conformer ($\omega \approx 10^\circ$) to be more stable. On the other hand, depending on the augmentation, some medium basis sets predict the staggered conformation ($\omega \approx 50^\circ$) to be more stable. In evaluating the conformation 1,2,3,6-tetrahydropyridinide by the HF, B3LYP and MP2 methods, Tran *et al.*¹² found the 6-31G(d) basis set to consistently predict the axial congener to be most stable, while the 6-31+G(d) and 6-311G(d,p) basis sets predict the equatorial congener to be most stable – in line with experiment.¹³

* For the comprehensive model shown in Figure 4.6 (with 288 electrons in spin-balanced pairs), 6-31G has 408 symmetry adapted basis functions while 6-311++G(d,p) has 1124.

Chapter 4: Investigation of eclipsed methyl in the solid state

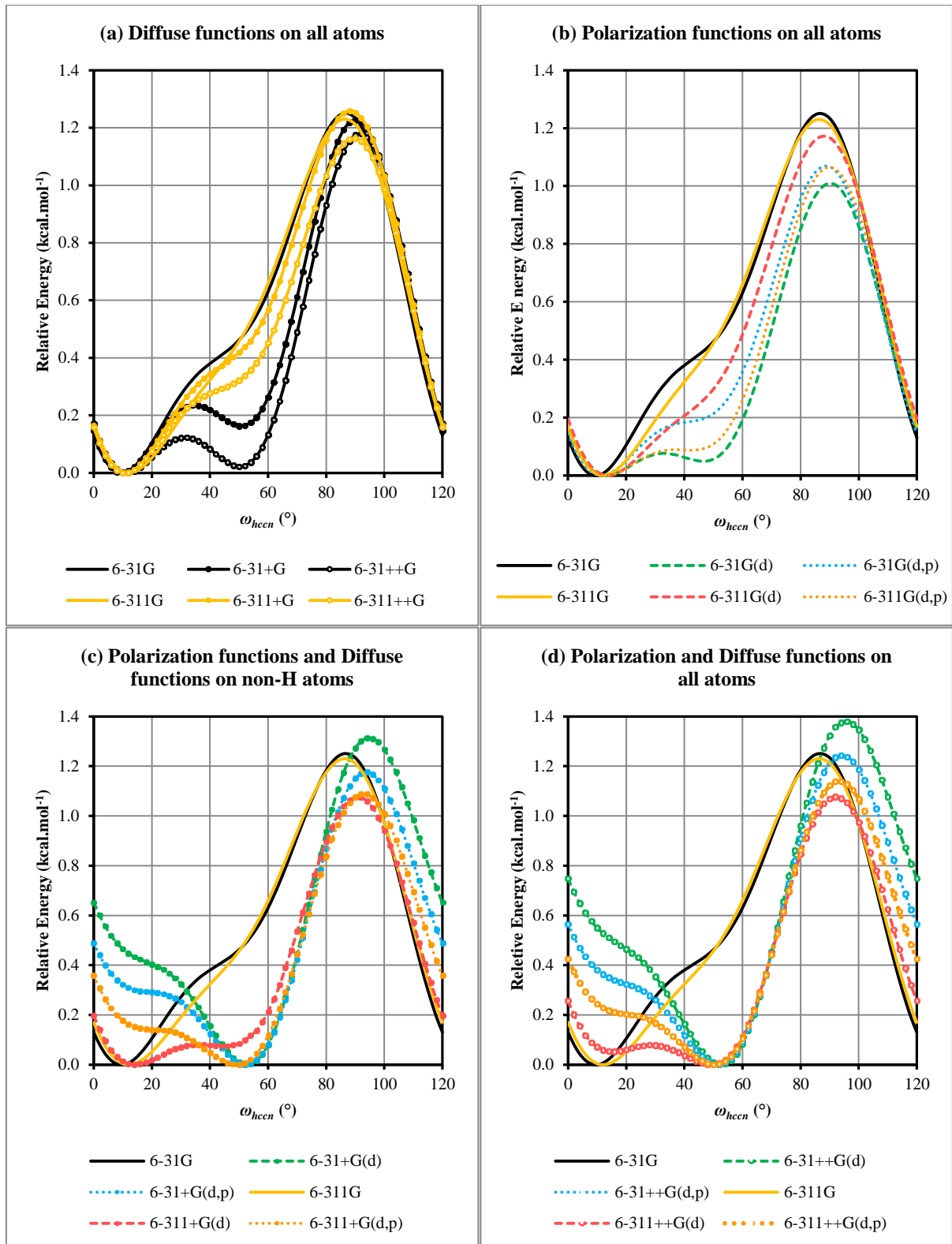


Figure 4.8: Graphs comparing effects of basis set augmentation on the potential energy profile of ω_{hccn} calculated at the HF level of theory. The following colors represent different levels of diffuse-function augmentation: Green curves depict the 6-31G(d) basis set; cyan the 6-31G(d,p); pink the 6-311G(d) and orange the 6-311G(d,p) basis set. The 6-31G (black) and 6-311G (yellow) potential energy profiles are shown in all plots for comparison.

4.5 Comparison of different DFT methods using various basis sets

A comparison of the ω_{hccn} potential energy profile obtained by numerous density functionals (listed in Section 3.9) is presented in this section. Unlike the HF case, the choice of basis set does not seem to influence the potential energy profile extensively other than changing the magnitude of the rotation barrier (*cf.* Figure A.5 for the B97D case). Figure 4.9 shows relative energies for scans of the ω_{hccn} dihedral angle employing the SDDAll basis set.

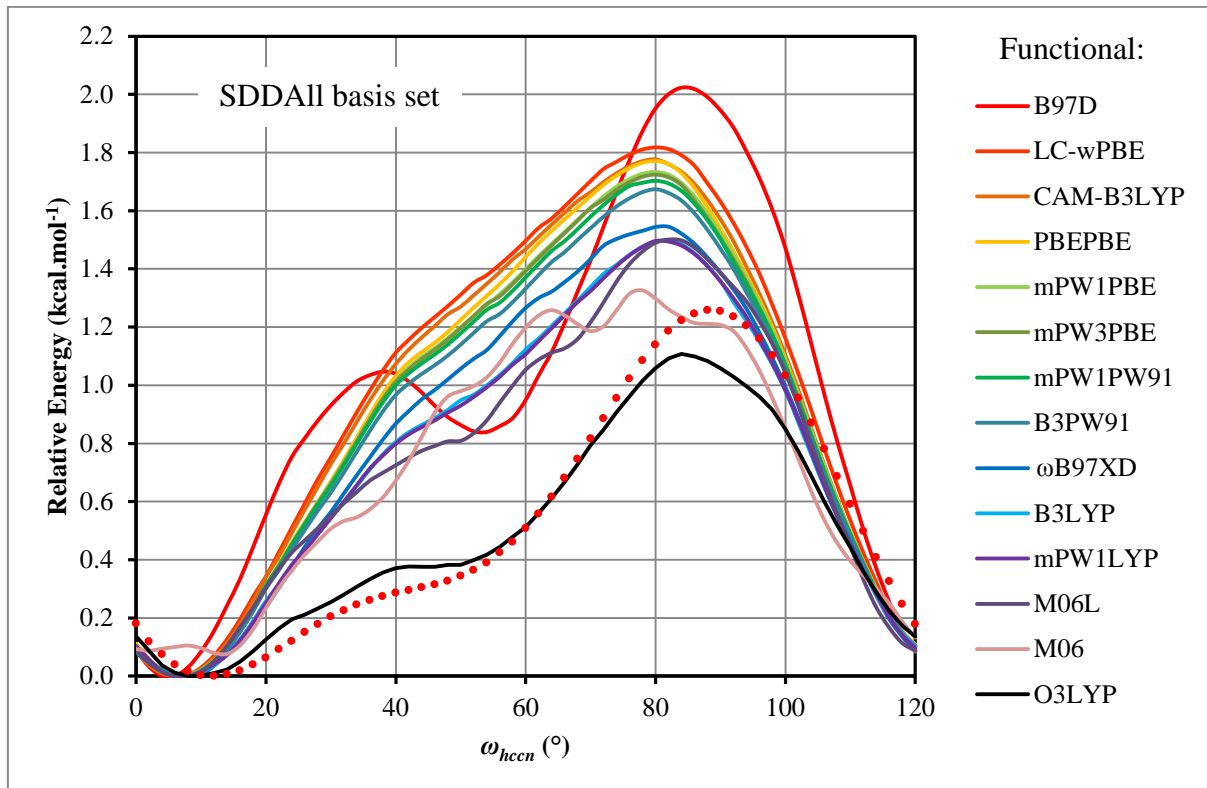


Figure 4.9: Relative potential energy profiles for the ω_{hccn} dihedral angle obtained for various density functionals in combination with the SDDAll basis set, along with the CCSD/SDDAll//B97D/SDDAll profile (●, minimal model of Figure 4.4) for comparison. Notice the inability of the M06 functional (—) to reproduce a profile with three-fold symmetry (0° vs. 120°) due to oscillations also present in the M06L profile (—).

All functionals show a shoulder near $\omega_{hccn} \approx 55^\circ$, with that of the O3LYP functional (—), which also shows the smallest ΔE_{rot} [$\approx \Delta E_{rot}^{HF}$], being the most prominent. A comparison, enabled by repeat of the CCSD/SDDAll//B97D/SDDAll profile (●) shows the accuracy of the O3LYP density functional for this model. Unfortunately, the high expense of this hybrid functional (with the same functional form as that of B3LYP, *cf.* Eq. 2.36) precludes its use for investigation of metal-organic frameworks. Closer inspection of Figure 4.9 reveals two unusual profiles: the spurious oscillations of M06 (—) and, to a lesser extent, M06L (—), and the deep local minimum of B97D (—). The spurious behavior of the M06 and M06L functionals, examples of the meta-GGA class of functionals, will be discussed in Section 4.5.1, followed by a discussion of the profile of the B97D functional, alongside the other dispersion corrected functional, ω B97XD, in Section 4.5.2.

4.5.1 Oscillations in potential energy surfaces of meta-GGAs

The oscillating behavior present in the M06 potential energy profile is a commonly observed phenomenon for functionals of the meta-GGA class. Roy *et al.*, for example, found oscillations in the interaction energy surface of the Ar₂ dimer for the M06L (pure)¹⁴ M06 (hybrid with $c_x = 0.27$), and M06-2X ($c_x = 0.54$)¹⁵ functionals.¹⁶ These functionals depend on the *kinetic-energy density*, $\tau_\sigma = \sum_i^{occ} |\nabla \psi_{i\sigma}|^2$, in addition to the electron-density, ρ_σ , and its reduced gradient, $s_\sigma = \frac{|\nabla \rho_\sigma|}{\rho_\sigma^{4/3}}$ (Eq. 2.38). Of most concern with this type of behavior is that a minimizer might get trapped in one of the many local minima. This is especially true for weakly bound complexes with very flat potential energy surfaces.

To solve the Schrödinger equation, a number of n -dimensional integrals need to be solved, where n depends on the method. However, the prohibitive size of systems of interest to chemist necessitates the use of numerical approximations to the analytical solutions of these integrals. Most Quantum Mechanics program packages use integration grids centred on the atoms of a system¹⁷ according to a partitioning scheme first introduced by Becke.¹⁸ An atom-centred integration grid is specified by (n_r, n_ℓ) , where n_r is the number of radial shells per atom, and n_ℓ the number of angular points per shell. A *pruned* grid is a grid that has been optimized to achieve a given accuracy with the minimum number of grid points.

However, using atom-centred integration grids causes the placement of grid points in the region between monomers to vary uncontrollably between successive increments of intermonomer separation. After examining the kinetic-energy dependent terms of various meta-GGA functionals Johnson *et al.* established the sparse distribution of grid points between monomers to be the origin of the observed erratic behavior. They found that the situation could be remedied by increasing the fineness of integration grids used during numerical integration.¹⁹

The expressions used for the kinetic-energy density terms in the M06 suite of functionals are identical to those of the VSXC²⁰ functional.* In order to reduce the problems that Johnson *et al.* pointed out, Zhao and Truhlar have set particular coefficients to zero for these terms in their Minnesota functionals.¹⁴⁻¹⁵ Sporadic oscillatory behavior is, however, still observed for these functionals,^{19b} as is also evident from Figure 4.9.

An assessment of the effect of grid size for the potential energy profile obtained for the medium model shown in Figure 4.2(b) employing the M06 functional is presented in Figure 4.10. The ω_{hccn} dihedral angle was incremented from 0° to 120° in 4° steps. Lebedev angular grids with $n_\ell = 302$ or 590 were used.²¹ The default grid used in Gaussian 09 is the pruned (75,302) grid. By specifying *Int=Ultrafine* the pruned (99,590) grid is used, while the finer, unpruned (250,590) grid is invoked through the keyword *Int=(Grid=250590)*.

* For the uniform electron gas, $\tau_\sigma^{LSDA} = \frac{3}{5} (6\pi^2)^{2/3} \rho_\sigma^{5/3}$ based on the Fermi momentum. In VSXC, the kinetic energy dependence is introduced through the function $f(s_\sigma, z_\sigma) = \frac{a_1}{\gamma_\sigma} + \frac{a_2 s_\sigma^2 + a_3 z_\sigma}{\gamma_\sigma^2} + \frac{a_4 s_\sigma^4 + a_5 s_\sigma^2 z_\sigma + a_6 z_\sigma^2}{\gamma_\sigma^3}$, where $z_\sigma = \frac{2\tau_\sigma}{\rho_\sigma^{5/3}} - \tau_\sigma^{LSDA}$ and $\gamma_\sigma = 1 + a_7(s_\sigma^2 + z_\sigma)$. The a_i coefficients are empirical fit parameters that are separately optimized for exchange and like- and opposite-spin correlation. In M06L $a_{x,6} = a_{c\sigma\sigma,6} = a_{ca\beta,6} = 0$, while in M06 $a_{x,4} = a_{x,5} = 0$ in addition to those of M06L and in M062X, all $a_{x,i}$ are set to zero.

Chapter 4: Investigation of eclipsed methyl in the solid state

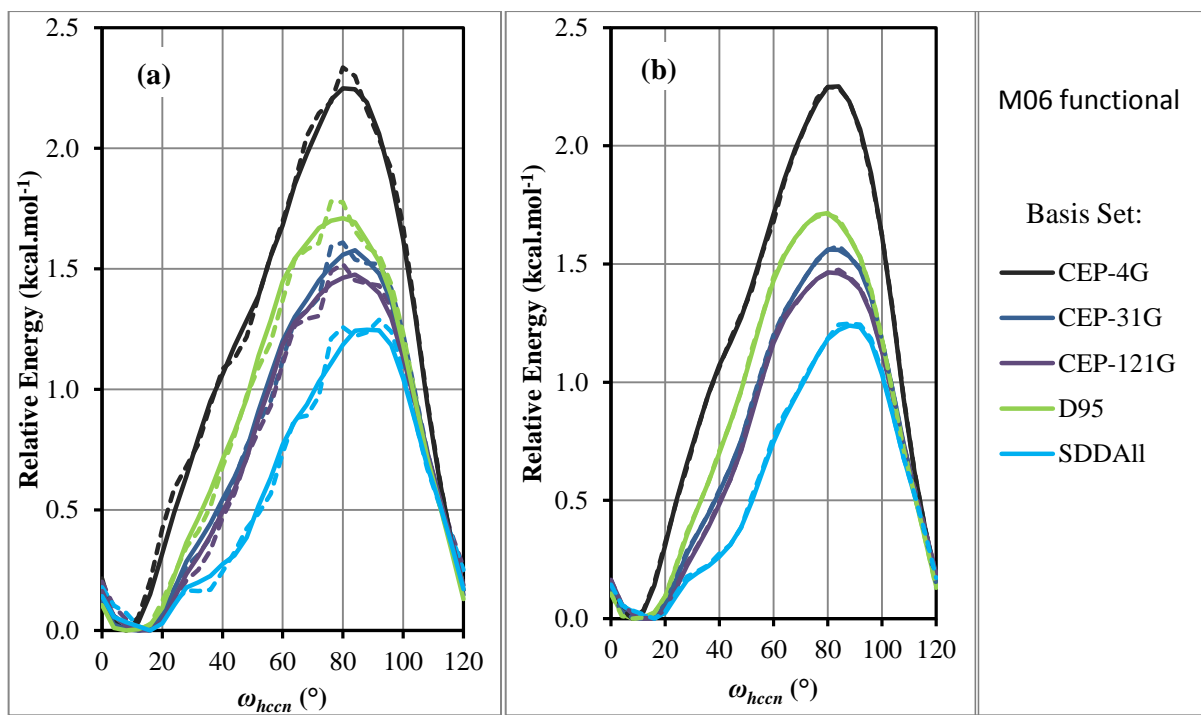


Figure 4.10: Effect of integration grid coarseness on the potential energy profile for ω_{hccn} of the M06 functional employing different effective core potential basis sets. The integration grids considered were the default 75,302 (---), ultrafine 99,590 (—) and finest 250,590 (···). The medium model of Figure 4.2(b) was evaluated.

From Figure 4.10(a) it is clear that using the ultrafine grid (—) diminishes the erratic oscillation observed with the default grid (---), while going to the (250,590) grid (···), with a corresponding increase in computational expense, does not show significant improvement (Figure 4.10(b)). Additional evaluations for this study (see Section A.2.4) have shown that the choice of integration grid influences the results obtained from all considered density functionals, albeit to a lesser extent for the non-meta-GGA classes. The ultrafine integration grid (250,590) was therefore applied in subsequent calculations.

4.5.2 Potential Energy profiles of dispersion-corrected B97D and ω B97XD

The parameterization of Grimme's B97D and Chai and Head-Gordon's ω B97XD functionals are discussed in Sections 2.4 and 2.5.3, respectively. The effect of the dispersion corrections on the potential energy profile of the ω_{hccn} dihedral angle calculated by the B97D and ω B97XD functionals are compared in Figure 4.11. The dispersion correction energy was deconvoluted from the potential energy profiles shown in Figure 4.9 for the comprehensive model of Figure 4.6.

In the absence of the dispersion correction, the B97D energy profile becomes similar to that of most other DFT functions for this model (*cf.* Figure 4.9). The dispersion correction scheme used in B97D, the previously discussed GD2 (Section 2.4.2), is maximal (shows greatest stabilization) at the eclipsed conformation while the ω B97XD-correction has a minimum close to $\omega_{hccn} = 0^\circ$. Both dispersion-correction schemes show a maximum near the staggered conformation ($\omega_{hccn} = 60^\circ$) with the GD2 $E_{disp}^{60^\circ}$ value three times as large as that of the ω B97XD-correction. It has been found before that the B97D functional tends to overestimate interaction energies of van der Waals complexes.²² A more thorough comparison between these and other correction schemes is presented in Section 4.8 for the minimal model.

Chapter 4: Investigation of eclipsed methyl in the solid state

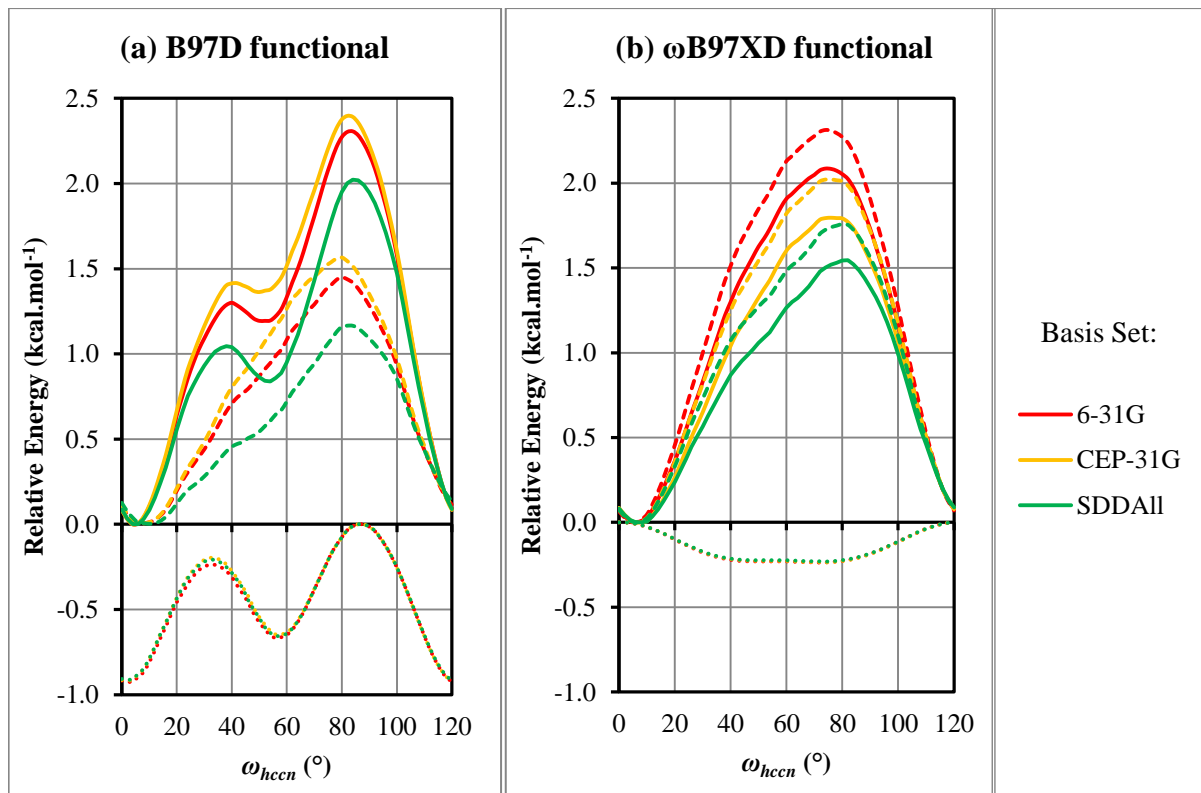


Figure 4.11: Comparison of the magnitude of the potential energy profile before (---) and after (—) addition of a dispersion correction (...) in (a) the B97D and (b) the ω B97XD functionals in combination with different basis sets.

4.6 Møller-Plesset perturbation theory with 2nd order corrections (MP2)

The HF and DFT potential energy profiles for ω_{hccn} were compared to that at the MP2 level of theory.²³ The comprehensive model shown in Figure 4.6 is, however, not computationally feasible at this level of theory, and the minimal model shown in Figure 4.4 was investigated. Although cooperative effects are ignored in this model, because hydrogen bonding pendant molecules and OH···N hydrogen bonding water molecules are absent, it still comprises a full orthoamide molecule, allowing for the repulsive steric effects of the proximal axial hydrogen atoms of methylene bridges.

MP2-level scans of ω_{hccn} in 2° increments between 0° and 120° are shown in Figure 4.12. The frozen core approximation was employed to speed up calculations. By treating the MP2 as a correlation correction to the HF method and deconvoluting the MP2 energy as $E_{MP2} = E_{HF} + E2$,²⁴ the HF level results for the minimal model (of Figure 4.4) are shown in Figure 4.12(c). Comparing these profiles to those of Figure 4.7 (obtained for the comprehensive model of Figure 4.6) provides support for the idea that cooperative effects increase the hydrogen bond accepting capability of the water molecules. The staggered conformer ($\omega_{hccn} \approx 50^\circ$) is predicted to be marginally more stable in the minimal model at the HF level of theory, while the magnitude, 1.2 kcal.mol⁻¹, and position, at $\omega_{hccn} \approx 85^\circ$, of the rotation barrier is maintained relative to the profiles of the comprehensive model (Figure 4.7). After the 2nd-order correlation correction shown in Figure 4.12(b) is applied, the eclipsed conformer ($\omega_{hccn} \approx 10^\circ$) is predicted to be more stable at the MP2-level of theory, Figure 4.12(a).

Chapter 4: Investigation of eclipsed methyl in the solid state

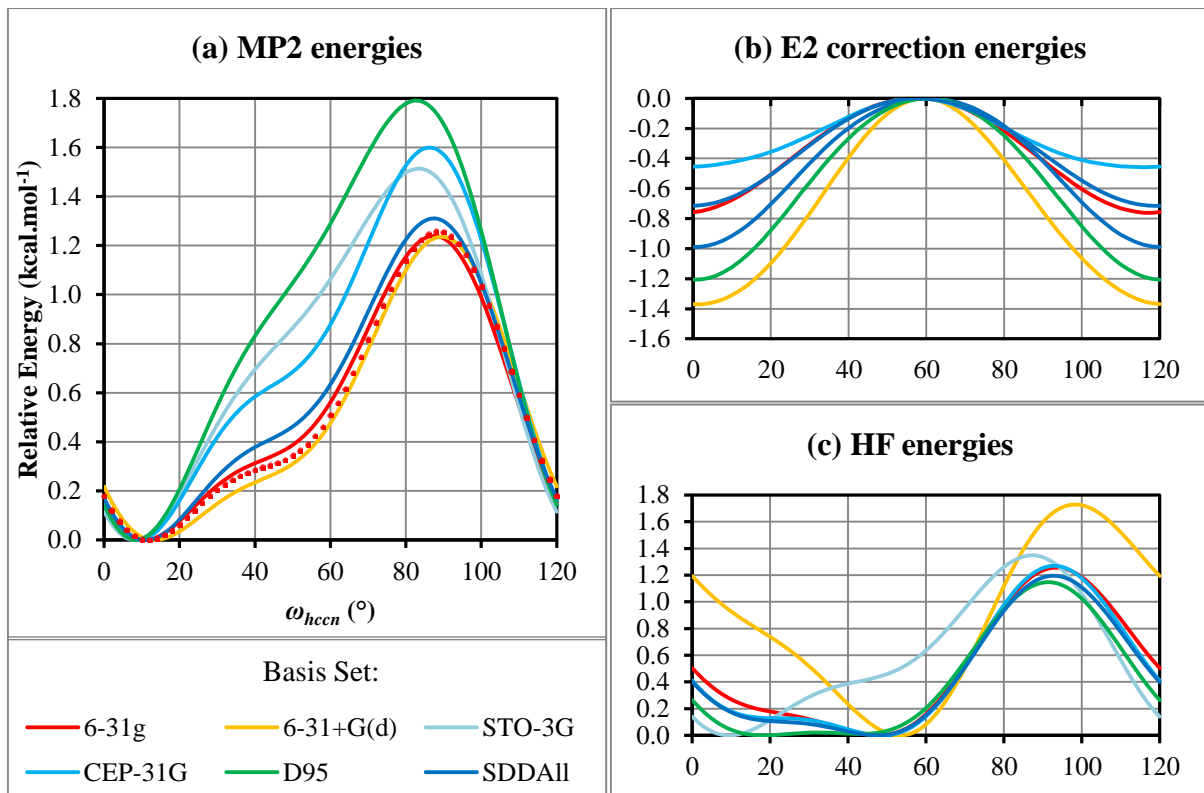


Figure 4.12: (a) Comparison of energy profile for ω_{hccn} in the minimal model of Figure 4.4 obtained at the MP2-level of theory employing various basis sets. The CCSD/SDDAll//B97D/SDDAll profile (●) is shown for comparison. The deconvoluted $E2$ correction and HF energies are shown in (b) and (c), respectively.

It is interesting to note that the smallest basis set, STO-3G, shows the eclipsed conformer to be more stable at the HF-level and also shows the smallest $E2$ correction. The reason for this could be a large basis set superposition error, the topic of the next section, which result in artificial binding that is significant in the case of van der Waals complexes.²⁵ In addition, the small virtual space (available unoccupied basis functions) of STO-3G, as opposed to that of 6-31+G(d), restrict the number of perturbations contributing to an $E2_{STO-3G}^{0^\circ}$ value that is three times smaller than $E2_{6-31+G(d)}^{0^\circ}$. A comparison to Figure 4.11 reveals that neither the GD2, nor the dispersion-correction energy in ω B97XD show profiles that corresponds to that of the $E2$ correction.

4.7 Eliminating the BSSE: the counterpoise scheme

The basis set superposition error arises when monomers within a complex augment their own incomplete basis sets with orbitals from neighboring monomers.²⁶ This expansion in the monomer centred basis sets is not a problem in itself, but has serious consequences for the calculation of interaction energies where artificial stabilization erroneously infers binding.[•] The BSSE can have adverse effects in the study of weakly bound complexes, since it not only influences relative energy values, but also geometries.²⁷ In a recent study, geometry optimization of noble gas dimers at the HF level of theory yielded local minima in the potential energy surface even though the HF method cannot describe dispersion, the only attractive interaction present between these spherical, nonpolar atoms.¹⁶

The most common method used to negate BSSE is the counterpoise (cp) scheme of Boys and Bernardi, wherein a system is reduced to fragments that are evaluated individually.²⁸ For a complex consisting of more than two monomers, the only unambiguous way to apply the counterpoise method is to individually define each monomer as a fragment.²⁹ The potential energy profile for ω_{hccn} of the model shown in Figure 4.2(b), wherein seven fragments had to be defined, is assessed in this section. See Section A.2.5 for more details. In order to correct a potential energy surface *a priori*, not just at the end as a final correction of the complex energy, Simon *et al.* developed an algorithm to implement the counterpoise scheme during geometry optimizations.³⁰

The influence of BSSE and the effect of how the counterpoise scheme is applied to the ω_{hccn} energy profile calculated using the B97D functional is shown in Figure 4.13. The ω_{hccn} dihedral angle was scanned in 1° increments between 30° and 60° to encompass the region of the local minimum where the profile is most basis set dependent (*cf.* Figure A.5). Results from geometry optimizations and *a posteriori* application of the counterpoise scheme in single point energy calculation are depicted by (—) and (■), respectively, while the potential energy profiles for different basis sets resulting from an *a priori* cp correction during geometry optimizations are represented by (---).

[•] To calculate the interaction energy, the energies of monomers (E_i , calculated individually) are subtracted from the energy of the complex ($E_{complex}$) according to $E_{int} = E_{complex} - \sum_i^n E_i$. The BSSE results from the fact that a comparison is made between $E_{complex}$ at distances where exploitation of neighboring orbitals plays a role, and $E_{complex}$ at infinite separation where such augmentation is not possible.²⁴

Chapter 4: Investigation of eclipsed methyl in the solid state

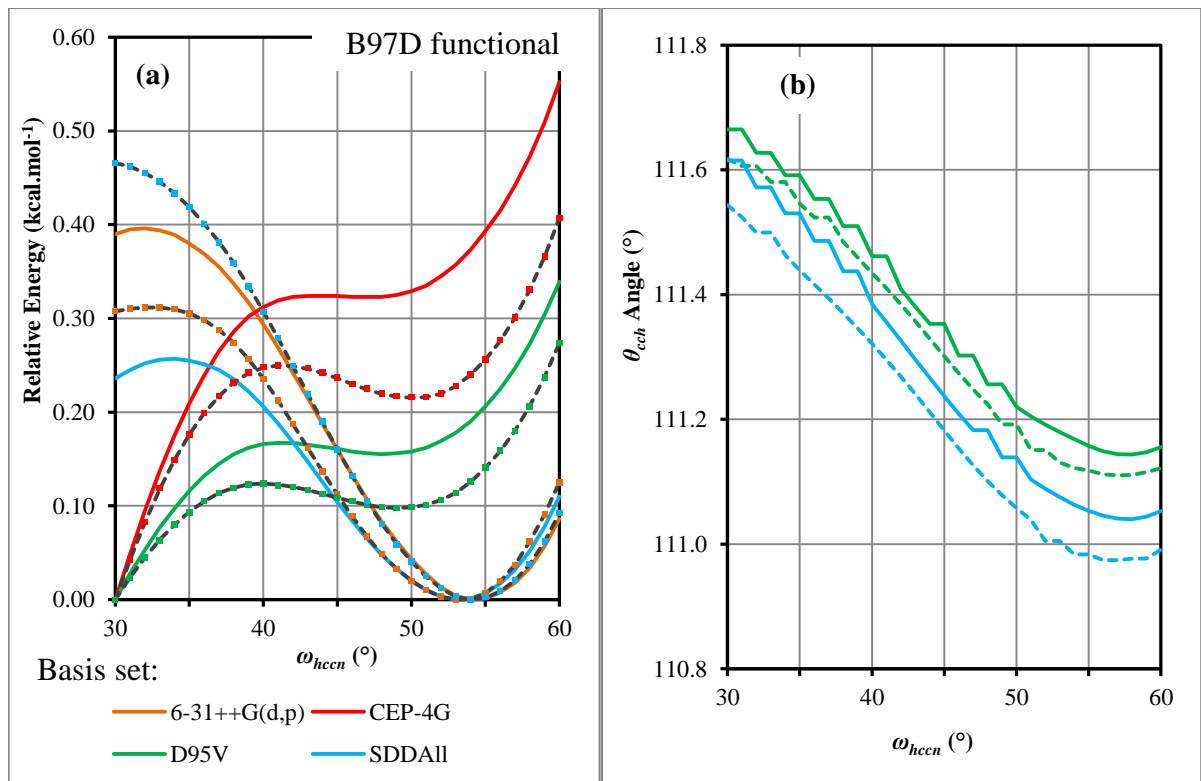


Figure 4.13: Influence of how the counterpoise scheme is applied, either during geometry optimizations (---, black), or after geometry optimizations as a single point calculation (■, colored), or not at all (—, colored) on (a) the energies and (b) valence angles calculated by the B97D functional as a function of the ω_{hccn} dihedral angle. The medium model of Figure 4.2(b) was evaluated. Data colored according to basis set.

It can be seen from Figure 4.13(a) that the interaction energies obtained through the *a priori* and *a posteriori* application of the counterpoise scheme are indistinguishable – the black dashed profiles (---) overlay the blocked profiles colored according to basis set (■) exactly. This is due to the fact that non-hydrogen atoms were kept fixed in their crystallographic positions for $2\cdot 3\text{H}_2\text{O}$.¹ There is, however, still a small, but definite effect on the geometries of the model, with the methyl θ_{cch} valence angle shown as an example in Figure 4.13(b). It is also interesting to note that, although the energy profiles of the D95V and SDDAll basis sets are dissimilar, their predicted trends of the θ_{cch} valence angle, offset by a constant amount, match. The *a priori* cp corrected traces (---) of Figure 4.13(b) are furthermore smoother than those of geometry optimizations without cp correction (—).

In a thorough analysis of the $\text{CH}_4\cdots\text{H}_2\text{O}$ dimer at the HF-level, Novoa *et al.* found that the diffuse functions on oxygen are essential, due most likely for the proper description of the hydrogen bond accepting oxygen lone pair electrons.⁶ The interaction energies are consistently overestimated by basis sets without diffuse functions on non-hydrogen atoms, while the counterpoise correction was found to bring the E_{int} values of all basis sets closer to the MP2/nHFL result of -0.59 kcal.mol⁻¹ (nHFL³¹ ≡ near Hartree-Fock limit quality basis set of Lee and Schaefer).⁶

Since monomer geometries and separation greatly influence shallow potential energy surfaces where weak interactions such as dispersion dominate, it was decided to apply the counterpoise scheme in an *a priori* fashion.

4.8 Choice of dispersion correction scheme

Various attempts have been made in the literature to improve the DFT description of dispersion bound complexes. The most popular is Grimme's DFT-D scheme, wherein a dispersion correction term is simply added to the density dependent energy: $E_{DFT-D} = E_{DFT} + E_{disp}$. The dispersion-correction energy profiles for ω_{hccn} in the minimal model (Figure 4.4) for the GD2 (discussed in Section 2.4.2), GD3 (Section 2.6.1) and GD3BJ schemes applied to the B97D functional are compared in this section in addition to the dispersion correction of the ω B97XD functional (Section 2.5.3).³² In the GD3³³ scheme “zero-damping” is used (*cf.* Eq. 2.72), while it was found that the rational damping function proposed by Becke and Johnson³⁴ improved nonbonded distances of benchmark molecular databases.³⁵ Other than the damping function, the GD3BJ scheme employs the same reference values and fractional coordination number interpolation scheme as GD3 to infer chemical environment. The functional expressions for the DFT-D schemes are collected in Eq. 4.1, with the scaling parameters that have been optimized for augmenting different density functionals shown in boxes. These parameters, listed in Table 4.1, were employed without change for this study. Results for the ω_{hccn} dihedral angle (stepped between 0° and 120° in 2° increments) of the minimal model (Figure 4.4) are shown in Figure 4.14 (*cf.* Figure 4.11 for the GD2 and ω B97XD results for the comprehensive model Figure 4.6).

$$E_{disp}^{GD2} = -[S_6] \sum_A^{N_{at}-1} \sum_{B>A}^{N_{at}} \frac{C_{AB,6}}{R_{AB}^6} \frac{1}{1 + e^{-20(R_{AB}/R_{AB,0}-1)}} \quad 4.1a$$

$$E_{disp}^{GD3} = - \sum_A^{N_{at}-1} \sum_{B>A}^{N_{at}} \left\{ \frac{C_{AB,6}}{R_{AB}^6 \left[1 + 6 \left(\frac{R_{AB}}{\boxed{S_{r,6}} R_{AB,0}} \right)^{-14} \right]} + \frac{[S_8] C_{AB,8}}{R_{AB}^8 \left[1 + 6 \left(\frac{R_{AB}}{R_{AB,0}} \right)^{-16} \right]} \right\} \quad 4.1b$$

$$E_{disp}^{GD3BJ} = - \sum_A^{N_{at}-1} \sum_{B>A}^{N_{at}} \frac{C_{AB,6}}{R_{AB}^6 + (\boxed{a_1} R_{AB,0} + \boxed{a_2})^6} + \frac{[S_8] C_{AB,8}}{R_{AB}^8 + (a_1 R_{AB,0} + a_2)^8} \quad 4.1c$$

$$E_{disp}^{\omega B97XD} = - \sum_A^{N_{at}-1} \sum_{B>A}^{N_{at}} \frac{C_{6}^{ij}}{R_{AB}^6} \frac{1}{1 + 6 \left(\frac{R_{AB}}{R_{AB,0}} \right)^{-12}} \quad 4.1d$$

Table 4.1: Density functional specific scaling parameters of the GD2, GD3 and GD3BJ dispersion correction schemes.

Functional	GD2 scheme Eq. 4.1a		GD3 scheme Eq. 4.1b		GD3BJ scheme Eq. 4.1c	
	S_6	$S_{r,6}$	S_8	S_8	a_1	a_2
B97D	1.25	0.892	0.909	2.261	0.555	3.230
B3LYP	1.05	1.261	1.703	1.989	0.398	4.421
PBEPBE	0.75	1.217	0.722	0.788	0.429	4.441

Chapter 4: Investigation of eclipsed methyl in the solid state

The effect of the damping function is evident from the similar, but differently scaled, profiles of the GD3 (---) and GD3BJ (···) schemes in Figure 4.14(a). The correction schemes show very little basis set dependence for the current model wherein all non-hydrogen atoms are frozen in their crystallographic positions. The profile of the GD3 correction (---) is the most similar (in shape, but not magnitude) to that of the E_2 correction of the MP2 level of theory (Figure 4.12(b)). The profiles of the GD2 and GD3 dispersion-correction energy as applied to different density functionals are compared in Figure 4.14(b) and (c), respectively. It is clear that the s_6 parameter effectively scales the GD2 correction energy for the series of DFs (Figure 4.14(b)), while the two parameters $s_{r,6}$ and s_8 in the GD3 scheme modify the shape of the correction energy profile (Figure 4.14(c)).

Figure 4.15 shows a comparison of the GD2 (—) and GD3 (---) augmented B3LYP and PBEPBE counterpoise corrected potential energy profiles for the ω_{hccn} dihedral angle in the minimal model. A comparison of the B97D potential energy profiles in conjunction with the GD2, GD3 and GD3BJ dispersion correction schemes is presented in Figure A.11. It is clear that the examined DFT methods only consistently yield similar energy profiles to that calculated with the CCSD (Figure 4.5) and MP2 (Figure 4.12(a)) *ab initio* methods when used in conjunction with the GD2 correction scheme.

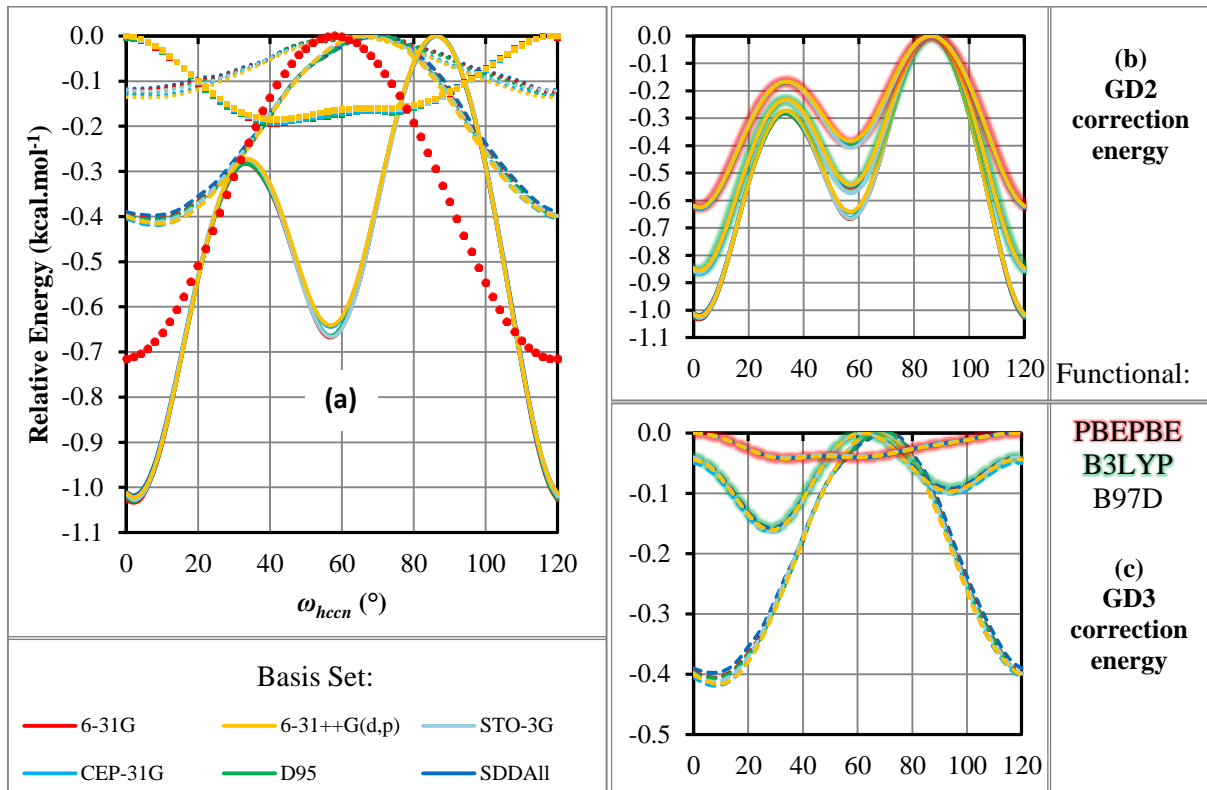


Figure 4.14: (a) Comparison of the E_{disp} profile for the dispersion correction schemes: GD2 (—), GD3 (---), GD3BJ (···) as applied to the B97D functional and the dispersion correction in ω B97XD (■). The deconvoluted E_2 correction of the MP2/SDDAll level of theory (●) is shown for comparison. A comparison of the relative GD2 and GD3 correction energies applied to various density functionals are compared in (b) and (c), respectively. The ω_{hccn} dihedral angle was stepped in the minimal model by 2° increments.

Chapter 4: Investigation of eclipsed methyl in the solid state

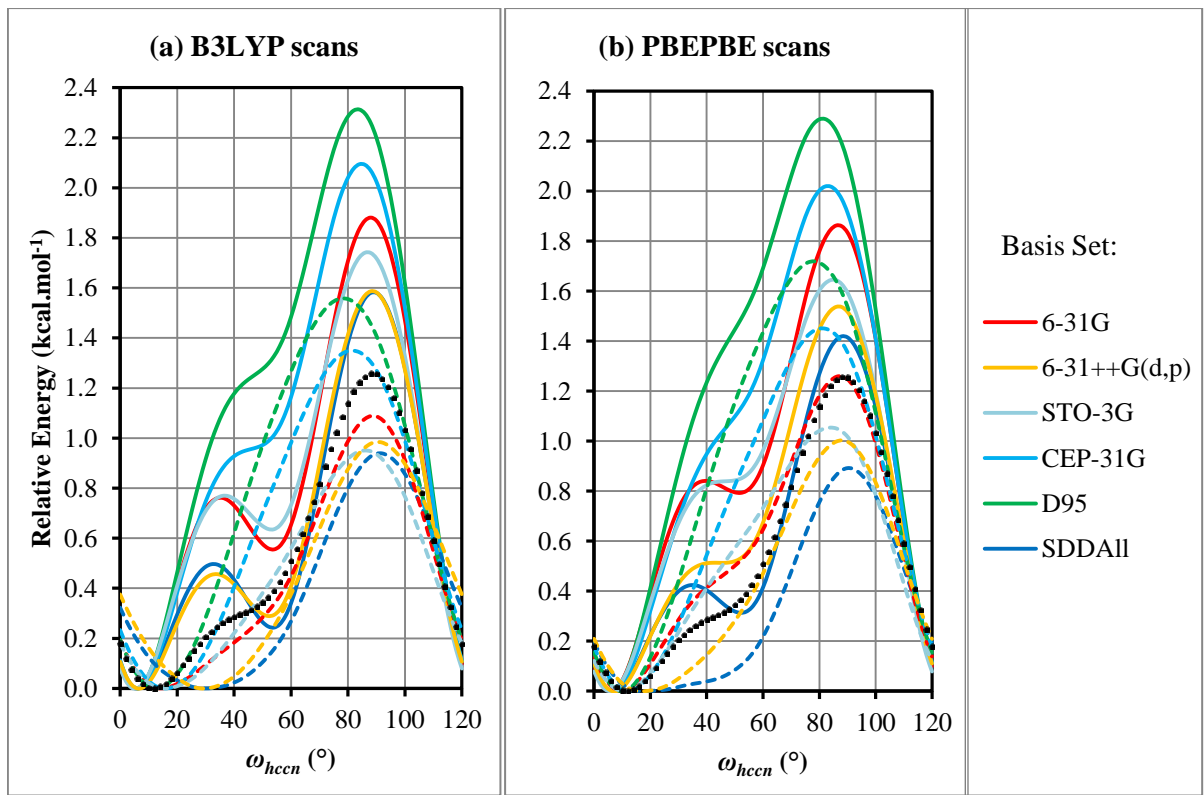


Figure 4.15: Comparison of the potential energy profiles obtained with application of the GD2 (—) and GD3 (---) dispersion correction schemes to the B3LYP (a) and PBEPBE (b) density functionals. The CCSD/SDDAll//B97D/SDDAll profile (●) is shown for comparison

4.9 Summary

Results from an analysis of the **2·3H₂O** crystal structure with an anomalous nearly eclipsed methyl are presented in this chapter. It is shown that it is important to allow for intramolecular close contacts in a molecular representation in order to obtain potential energy surfaces with minima that correspond to experimental results. Insights into the influence of cooperative effects that increase the polarization of heterobonds have been gained by comparing results obtained for a comprehensive model with hydrogen bonding pendant molecules to results obtained for a minimal representation. The necessity of using atom-centred integration grids of sufficient fineness to improve the accuracy of numerical quadrature and to eliminate erratic oscillations in the potential energy profiles obtained for functionals of the meta-GGA class is highlighted. When using incomplete basis sets, as is generally the case, it is necessary to apply the counterpoise correction scheme *a priori* during atom-position optimizations to minimize the influence of the basis set superposition error on the obtained geometry. At the conclusion of this chapter various semi-empirical dispersion correction schemes, whereby a E_{disp} correction is simply added to E_{DFT} , is evaluated. Although the GD3 scheme was found to compare most favorably to the correlation correction of MP2 theory, only the GD2 scheme was consistently effective in augmenting DFT functionals to reproduce CCSD level of theory results.

The insights presented above are used in the following chapter during the investigation of anomalous thermal expansion behavior of a metal-organic framework recently synthesized in our group.

Chapter 4: Investigation of eclipsed methyl in the solid state

4.10 References

1. Seiler, P.; Dunitz, J.D., *Helv. Chim. Acta* **1989**, 72, 1125.
2. Cambridge Structural Database and Cambridge Structural Database System, Version 5.20, October **2000**, Cambridge Crystallographic Data Centre, University Chemical Laboratory, Cambridge England. Allen, F.H.; Kennard, O., *Chem. Des. Autom. News.* **1993**, 8, 1.
3. Steiner, T., *Angew. Chem. Int. Ed.* **2002**, 41, 48.
4. Seiler, P.; Weisman, G.R.; Glendening, E.D.; Weinhold, F.; Johnson, V.B.; Dunitz, J.D., *Angew. Chem. Int. Ed.* **1987**, 26, 1175.
5. Novoa, J.J.; Constans, P.; Whangbo, M.-H., *Angew. Chem. Int. Ed.* **1993**, 32, 588.
6. Novoa, J.J.; Tarron, B.; Whangbo, M.-H.; Williams, J.M., *J. Chem. Phys.* **1991**, 95, 5179.
7. Chao, I.; Chen, J.-C., *Angew. Chem. Int. Ed.* **1996**, 35, 195.
8. (a) Dolg, M.; Wedig, U.; Stoll, H.; Preuss, H., *J. Chem. Phys.* **1987**, 86, 866; (b) Dolg, M.; Stoll, H.; Preuss, H., *J. Chem. Phys.* **1989**, 90, 1730; (c) Dolg, M.; Stoll, H.; Savin, A.; Preuss, H., *Theor. Chim. Acta* **1989**, 75, 173; (d) Bergner, A.; Dolg, M.; Kuechle, W.; Stoll, H.; Preuss, H., *Mol. Phys.* **1993**, 80, 1431.
9. Austin, A.J.; Frisch, M.J.; Montgomery, J.A., Jr.; Petersson, G.A., *Theor. Chem. Acc.* **2002**, 107, 180.
10. Clayden, J.; Greeves, N.; Warren, S., *Organic Chemistry*. Second Edition.; Oxford University Press: Oxford, **2012**.
11. Frisch, M.J.; Pople, J.A.; Binkley, J.S., *J. Chem. Phys.* **1984**, 80, 3265.
12. Tran, T.; Malloy, T.B., *J. Mol. Struct.* **2010**, 970, 66.
13. Chao, S.; Avirah, T.K.; Cook, R.L.; Malloy, T.B., Jr., *J. Phys. Chem.* **1976**, 80, 1141.
14. Zhao, Y.; Truhlar, D.G., *J. Chem. Phys.* **2006**, 125, 194101.
15. Zhao, Y.; Truhlar, D.G., *Theor. Chem. Acc.* **2008**, 120, 215.
16. Roy, D.; Marianski, M.; Maitra, N.T.; Dannenberg, J.J., *J. Chem. Phys.* **2012**, 137, 134109.
17. Malagoli, M.; Baker, J., *J. Chem. Phys.* **2003**, 119, 12763.
18. Becke, A.D., *J. Chem. Phys.* **1988**, 88, 2547.
19. (a) Johnson, E.R.; Wolkow, R.A.; DiLabio, G.A., *Chem. Phys. Lett.* **2004**, 394, 334; (b) Johnson, E.R.; Becke, A.D.; Sherrill, C.D.; DiLabio, G.A., *J. Chem. Phys.* **2009**, 131, 34111.
20. Van Voorhis, T.; Scuseria, G.E., *J. Chem. Phys.* **1998**, 109, 400.
21. (a) Lebedev, V.I., *Zh. Vychisl. Mat. Mat. Fiz.* **1976**, 16, 293; (b) Lebedev, V.I., *Russian Acad. Sci. Dokl. Math.* **1992**, 45, 587.
22. Yang, K.; Zheng, J.-J.; Zhao, Y.; Truhlar, D.G., *J. Chem. Phys.* **2010**, 132, 164117.
23. (a) Møller, C.; Plesset, M.S., *Phys. Rev.* **1934**, 46, 618; (b) Head-Gordon, M.; Pople, J.A.; Frisch, M.J., *Chem. Phys. Lett.* **1988**, 153, 503; (c) Saebo, S.; Almlöf, J., *Chem. Phys. Lett.* **1989**, 154, 83; (d) Frisch, M.J.; Head-Gordon, M.; Pople, J.A., *Chem. Phys. Lett.* **1990**, 166, 281; (e) Head-Gordon, M.; Rico, R.J.; Oumi, M.; Lee, T.J., *Chem. Phys. Lett.* **1994**, 219, 21.
24. Chałasiński, G.; Szczęśniak, M.M., *Chem. Rev.* **1994**, 94, 1723.
25. Deligkaris, C.; Rodriguez, J.H., *Phys. Chem. Chem. Phys.* **2012**, 14, 3414.
26. van Duijneveldt, F.B.; van Duijneveldt-van de Rijdt, J.G.C.M.; van Lenthe, J.H., *Chem. Rev.* **1994**, 94, 1873.

Chapter 4: Investigation of eclipsed methyl in the solid state

27. (a) Xantheas, S.S., *J. Chem. Phys.* **1996**, *104*, 8821; (b) Hobza, P.; Bludsky, O.; Suhai, S., *Phys. Chem. Chem. Phys.* **1999**, *1*, 3073; (c) Salvador, P.; Simon, S.; Duran, M.; Dannenberg, J.J., *J. Chem. Phys.* **2000**, *113*, 5666.
28. Boys, S.F.; Bernardi, F., *Mol. Phys.* **1970**, *19*, 553.
29. Turi, L.; Dannenberg, J.J., *J. Phys. Chem.* **1993**, *97*, 2488.
30. Simon, S.; Duran, M.; Dannenberg, J.J., *J. Chem. Phys.* **1996**, *105*, 11024.
31. Lee, T.J.; Schaefer, H.F., III, *J. Chem. Phys.* **1985**, *83*, 1784.
32. Chai, J.-D.; Head-Gordon, M., *Phys. Chem. Chem. Phys.* **2008**, *10*, 6615.
33. Grimme, S.; Antony, J.; Ehrlich, S.; Krieg, H., *J. Chem. Phys.* **2010**, *132*, 154104.
34. (a) Becke, A.D.; Johnson, E.R., *J. Chem. Phys.* **2005**, *123*, 154101; (b) Johnson, E.R.; Becke, A.D., *J. Chem. Phys.* **2005**, *123*, 24101; (c) Johnson, E.R.; Becke, A.D., *J. Chem. Phys.* **2006**, *124*, 174104.
35. Grimme, S.; Ehrlich, S.; Goerigk, L., *J. Comput. Chem.* **2011**, *32*, 1456.

Chapter 5: Anisotropic thermal expansion in a MOF

This chapter presents a computational investigation into the anomalous thermal expansion observed for the metal-organic framework **1_{apo}**. The low expense of Molecular Modelling (encompassing Molecular Mechanics and Molecular Dynamics) allows for the full crystallographic system to be studied. In Molecular Modelling, classical expressions are used to approximate bonded (extent of bond stretching, angle bending and torsion twisting relative to an *atomtype*-specific reference value) and nonbonded (van der Waals and electrostatic interactions calculated using a distance-dependent summation over atom-pairs) potential energy contributions.¹ A set of atom-types, assigned to atoms in a system under investigation based on element and chemical environment, and their reference parameters, constitute a *force field*. To decide on a suitable force field for the investigation of **1_{apo}**, the tricyclicorthoamide crystal structure, **2·3H₂O**, was again considered.

First, a brief introduction to the vibrational origin of thermal expansion is given, followed by a discussion of the anisotropic thermal expansion of **1_{apo}** in Section 5.2. Molecular Mechanics (MM) results obtained for a molecular representation of **2·3H₂O** is followed by an MM and DFT potential energy surface evaluation of the crystal structure of **2·3H₂O** in Section 5.3. Results from Molecular Dynamics simulations of **1_{apo}**, employing the force field identified to be accurate in Section 5.3, are presented in Section 5.4. The chapter is concluded with results obtained for the mechanistic model discussed in Section 3.8 to gain insight into the reasons for the anomalous thermal expansion of **1_{apo}**.

5.1 Vibrational origin of thermal expansion

A topical review by Barrera *et al.* was used extensively in compiling this section.² The volume dependence of entropy can be derived by applying Maxwell relations to the *volumetric thermal expansion* coefficient, β , defined as

$$\begin{aligned}\beta &= \frac{1}{V} \left(\frac{\partial V}{\partial T} \right)_P \\ &= -\frac{1}{V} \left(\frac{\partial S}{\partial P} \right)_T \\ &= -\frac{1}{V} \left(\frac{\partial V}{\partial P} \right)_T \left(\frac{\partial S}{\partial V} \right)_T = \chi_T \left(\frac{\partial S}{\partial V} \right)_T\end{aligned}\quad 5.1$$

The isothermal compressibility, χ_T , defined in the last line of Eq. 5.1, is always a positive quantity. It is furthermore expected that entropy would increase with an isothermal increase in volume to yield a positive β , or positive thermal expansion. Following this convention, negative thermal expansion with $\beta < 0$ is considered anomalous. Since β is positive for an ideal gas, negative thermal expansion is a consequence of the interactions between particles. In water, for example, the increase in entropy upon compression below 4 °C, $\left(\frac{\partial S}{\partial V} \right)_T < 0$, that

Chapter 5: Anisotropic thermal expansion in a MOF

causes negative thermal expansion, is ascribed to the interruption of extensive hydrogen bonding that offset $\left(\frac{\partial S}{\partial V}\right)_T > 0$ contributions to β .²

The thermal expansion of a material is its elastic response to the total thermal stress. As the temperature increases, the amplitude of vibrational movement increases.³ At the atomic level three vibrational mechanisms that give rise to thermal stress have been identified.⁴ These are discussed below, along with a libration motion found for rigid motion groups.

5.1.1 Bond-stretching effect

Consider vibrational displacements along a line connecting two atoms. When the distance \mathbf{r}_0 between the mean atomic positions, $\mathbf{r}_0 = \langle \mathbf{r}_A \rangle - \langle \mathbf{r}_B \rangle$, remains constant, \mathbf{r} continues to sample values both greater and less than \mathbf{r}_0 . Due to the asymmetry of the interatomic potential, the repulsion between the atoms when $\mathbf{r} < \mathbf{r}_0$ is greater than the attraction when $\mathbf{r} > \mathbf{r}_0$, as shown in Figure 5.1. A net repulsive force is therefore generated, the magnitude of which increases as the amplitude of vibration increases.

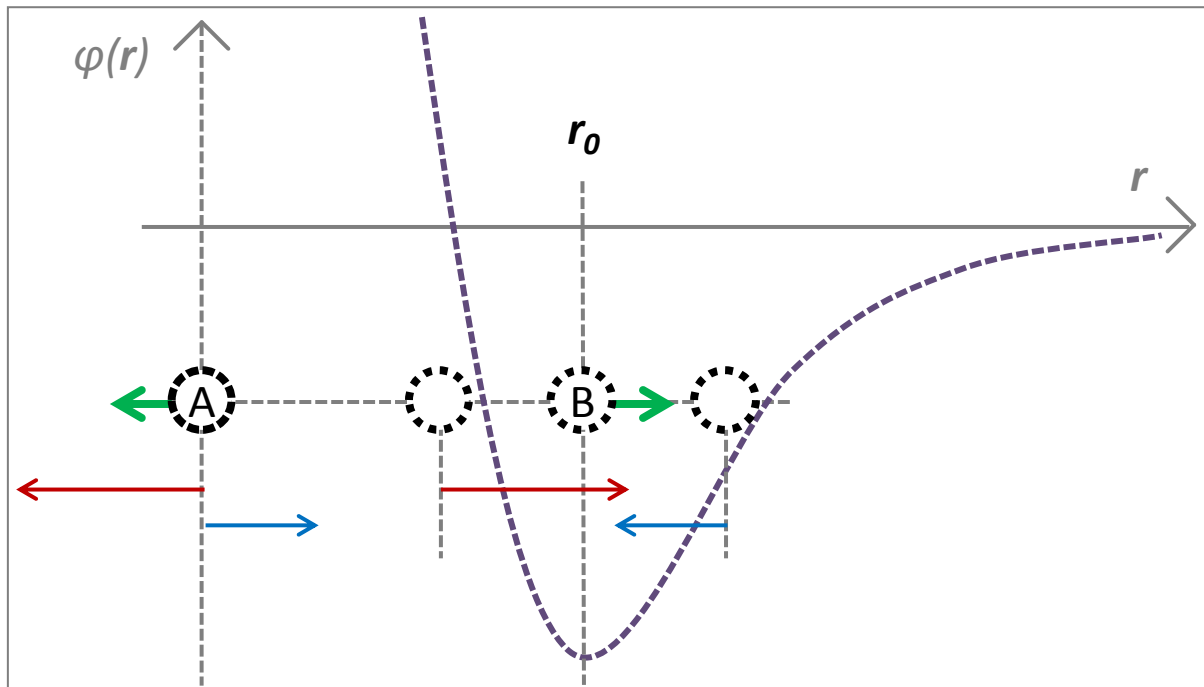


Figure 5.1: Shape of a typical anharmonic pair potential (—). When the mean separation between atoms A and B (\mathbf{r}_0 , full circles) is kept constant, vibrational displacements of atom B (dashed circles) along the interatomic direction produce a net repulsive force (→). Instantaneous forces: → repulsive > ← attractive.

5.1.2 Tension effect

Upon keeping the distance between the mean atomic positions fixed, relative motion normal to the bond increases the time-averaged distance between the atoms. This induces a net attractive force, as evident from Figure 5.2, that contribute negatively to β .

Chapter 5: Anisotropic thermal expansion in a MOF

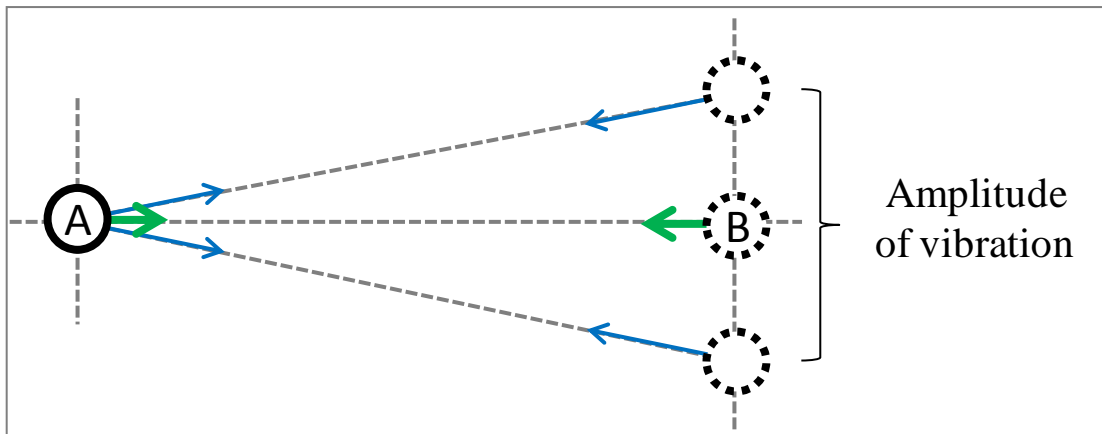


Figure 5.2: Vibrational displacements of atom B (dashed circles) normal to the bond produce a net attractive force (→). Instantaneous attractive force: →. Adapted from reference [2].

5.1.3 Bond-rotation effect

Vibrational movement with components along the bond and transverse to it affect both the bond-stretch and tension effects. In addition, a net torque is produced that tends to rotate the bond away from the direction of relative motion. This effect is usually trivial since different vibrational modes tend to rotate the bond in different directions.⁴

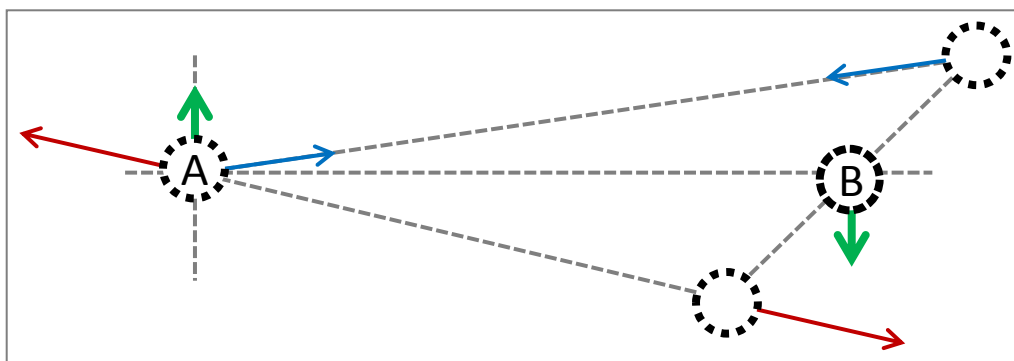


Figure 5.3: Thermal displacements in a direction acute to the AB-bond produce a net torque on the bond in addition to the forces shown in Figures 5.1 and 5.2. Dashed circles represent the amplitude of motion of B relative to A. Instantaneous forces: → repulsive, → attractive; → time-averaged force. Adapted from reference [2].

5.1.4 Rigid bonds

When the bond between two atoms is strong enough to be considered rigid, bond-stretching and rotation effects are prevented. The bond is however free to librate, or swivel about its centre point, with motions transverse to the bond affecting the tension effect of Figure 5.2. As depicted in Figure 5.4, the mean separation of the atoms midway in the libration amplitude is given by

$$\langle d_{AB} \rangle_T = \mathbf{r}_0 \langle \cos \theta \rangle_T \quad 5.2$$

where θ is the displacement of the bond from its mean orientation. The apparent bond length, as obtained from a diffraction measurement (*cf.* Section 1.2), is the true bond length, \mathbf{r}_0 , reduced by a factor $\langle \cos \theta \rangle_T$. This factor and, therefore, d_{app} decrease as the libration amplitude increases with temperature.

Chapter 5: Anisotropic thermal expansion in a MOF

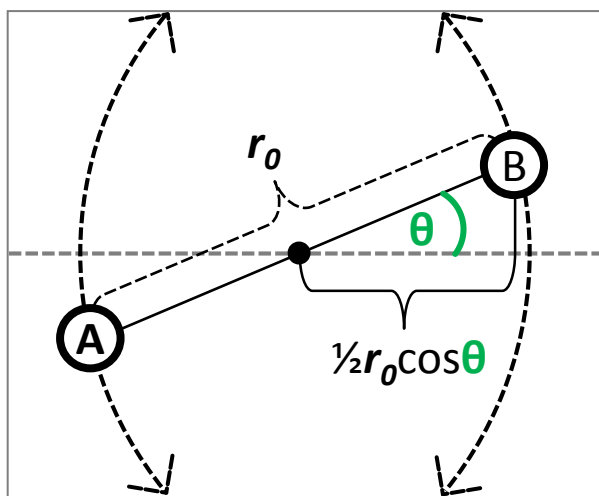


Figure 5.4: Libration of the A-B bond with fixed length r_0 reduces the distance between the mean positions of atoms A and B by a factor $\cos \theta$, where θ is the angular displacement of the AB-bond from its mean orientation. Adapted from reference [2].

The collective outcome of the effects discussed in this section, along with considerations of the strength of the inter- and intramolecular bonds, will determine the sign and magnitude of β . Volumetric expansion of a crystal can furthermore be isotropic (universal expansion or contraction along all three axes) or anisotropic depending on the expansion in different directions.

5.2 Anisotropic thermal expansion in a MOF

Anisotropic thermal expansion was identified in a novel MOF (**1**) synthesized in our research group.⁵ It was shown that the methanol guest can be exchanged for a range of other solvent molecules or removed under reduced pressure with heating (150 °C) to yield the apohost (**1_{apo}**).⁶ Variable temperature single crystal X-ray diffraction under static vacuum (Figure 5.5) revealed anisotropic thermal expansion: positive along the *c* axis and negative along the equal *a* and *b* axes. The linear thermal expansion coefficients,² defined as $\alpha = \frac{1}{L} \left(\frac{\partial L}{\partial T} \right)_P$, were determined to be $\alpha_a = \alpha_b = -21 \text{ MK}^{-1}$ and $\alpha_c = 123 \text{ MK}^{-1}$ for the temperature range 100-370 K (where 1 MK = 1×10^6 K). The exceptionally large α_c results in an overall positive volumetric thermal expansion with $\beta = 87 \text{ MK}^{-1}$.⁵

Chapter 5: Anisotropic thermal expansion in a MOF

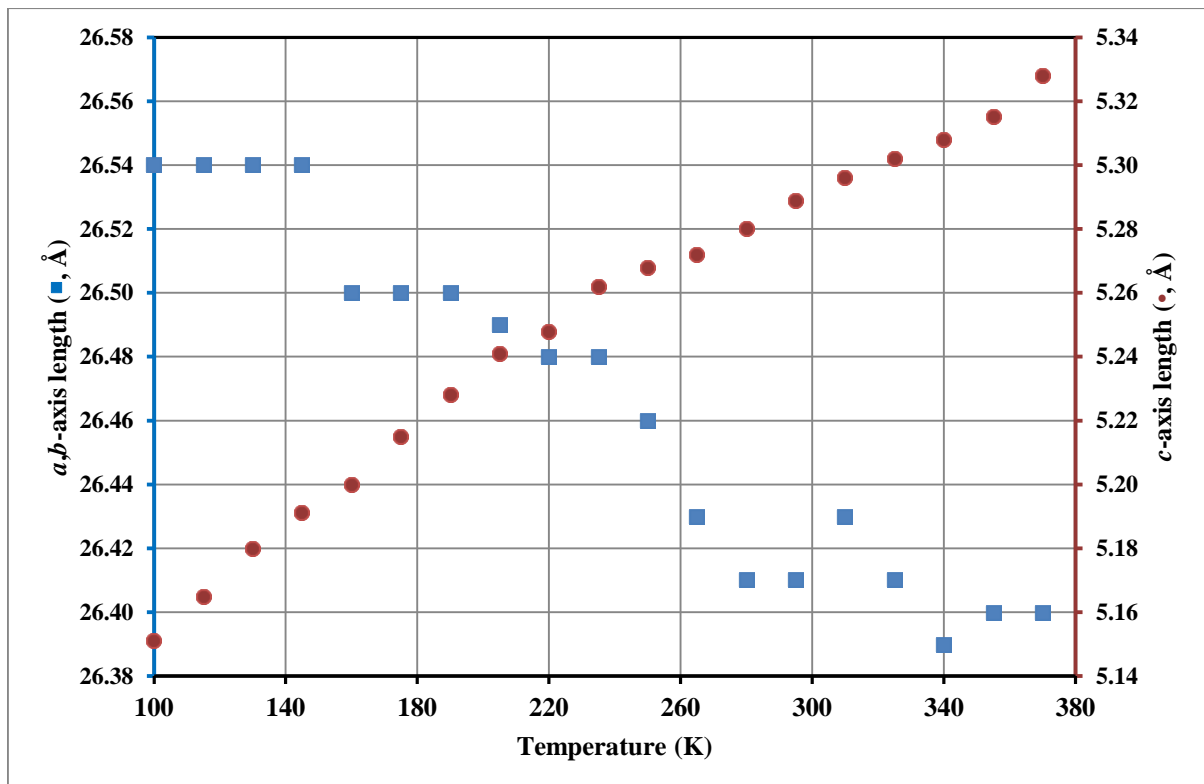


Figure 5.5: Graph of unit cell lengths determined by single crystal X-ray diffraction on the same crystal of $\mathbf{1}_{\text{apo}}$ under static vacuum, showing variation with temperature.⁵

Full structure determinations were performed at four temperatures with a crystal kept under static vacuum for the duration of the experiment.⁵ Table 5.1 shows the determined unit cell parameters, along with specific internal coordinates. An overlay of the four structures revealed only minor changes in the geometries of the ligand (see Figure A.13). The assumption made during derivation of the mechanistic model to treat the ligand as a rigid linker is supported by the fact that the Zn…Ligand…Zn distance remains essentially constant, decreasing by less than 0.09 Å in the temperature range considered. A systematic increase in the Zn-O(H)-Zn valence angle confirms stretching of the coordination spiral with increasing temperature.

Table 5.1: Summary of unit cell parameters and selected internal coordinates of full structure determinations of $\mathbf{1}_{\text{apo}}$ at different temperatures.⁵

Temperature (K)	<i>a</i> , <i>b</i> axes (Å)	<i>c</i> axis (Å)	Zn…(L ₁)…Zn (Å)	Zn-O(H)-Zn (°)	N-Zn-O _{Carb} (°)
100	26.5937(11)	5.1462(2)	12.1969(6)	126.7(1)	111.6(1)
190	26.5112(9)	5.2351(1)	12.2056(6)	128.5(1)	112.0(1)
280	26.4574(9)	5.2854(2)	12.1958(6)	129.6(2)	112.4(1)
370	26.4366(9)	5.3287(2)	12.1926(7)	130.7(2)	113.5(3)

5.2.1 Comparison to mechanistic model

A model to test the proposed mechanism responsible for the observed anisotropic thermal expansion was introduced in Section 3.8. In the derivation it was assumed that all bond lengths (covalent and coordination) remain constant and that the (truncated) ligands move with the zinc atoms they are bonded to. The latter assumption infers that the N-Zn-O_{Carb} valence angle remains constant at its value in the 100 K structure during simulations. This is in contrast to the crystal structure data (Table 5.1) where this angle is found to increase slightly with temperature. Attempts to reproduce the observed trend in the N-Zn-O_{Carb} valence angle introduced undue complexity to the model and was therefore discarded.*

A direct comparison to the crystal structure data can be made by considering how the model predicts variation in the unit cell parameters. Due to C₄ symmetry, there are four ...Zn-O(H)-Zn-O(H)... coordination spirals present in a unit cell of **1_{apo}**. The simultaneous change in unit cell length with $\Delta c = S$ is then $\Delta a = \Delta b = -2k + \ell_2$ (recall from Figure 3.16 that $k > 0$ and $\ell_n < 0$). In Figure 5.6 it can be seen that the model underestimates the decrease in the a (equal to b) unit cell parameters with respect to the c parameter. Attempts to improve the model's agreement with experimental data again unduly increased the complexity of the model and were rejected.♦

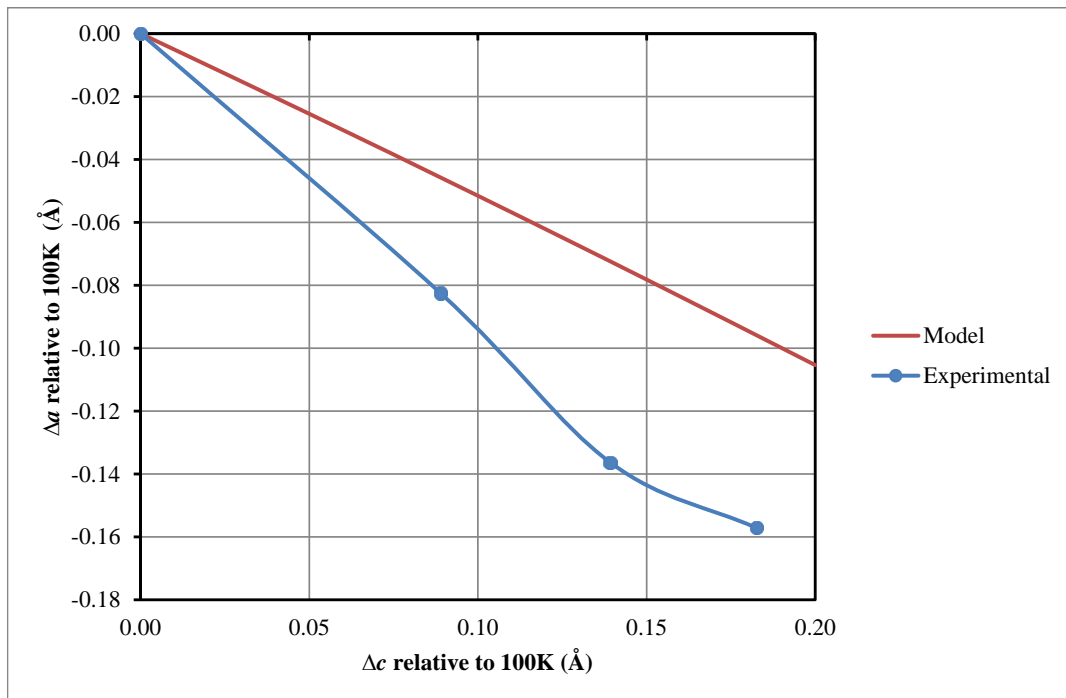


Figure 5.6: Comparison of change in unit cell parameters as determined from variable temperature single crystal X-ray structure determinations⁵ and a mechanistic model (see text for details) attempting to reproduce expansion of the coordination spiral of **1_{apo}**.

* Alternative models wherein the ligands' downward translation (in the z direction) is controlled by an additional lagging/accelerating factor to scale the movement of the imidazole and/or benzoate ligand were unsuccessful since the tetrahedral coordination sphere of zinc was unduly distorted.

♦ One option pursued was to introduce a scaled elongation of the Zn-O(H), Zn-O_{carb} and Zn-N_{imidazole} coordination bond lengths, instead of maintaining them at their values in the 100 K crystal structure. However, inclusion of such a scaling factors prohibited manipulation of the distance equations to relate all atom movements of the model to the value of one variable (S), and such a model was dismissed.

5.2.2 Considerations for theoretical modelling

The disorder of the benzoate group (shown in Section 3.2.1) persisted in all four variable temperature structures.⁵ Closer inspection of the atomic displacement parameters with increasing temperature revealed a disproportionate increase in the thermal motion of the benzoate moiety relative to the rest of the structure. In line with this, the benzoate is expected to undergo rapid libration, as described in Section 5.1.4. The libration mechanism should, however, not dominate the observed thermal expansion behavior. The two positions of equal occupancy identified for the benzoate during structure elucidation are shown in different colors in Figure 5.7. For computational applications, the position wherein the uncoordinated oxygen forms a hydrogen bond with the acidic proton of the imidazole coordinating to the same zinc atom (— in Figure 5.7) was retained, while the other component was omitted. This was decided on to reduce crystal field effects of divergent hydrogen bonding that cannot be incorporated into the mechanistic model, as opposed to the convergent hydrogen bonding across the coordination spiral.

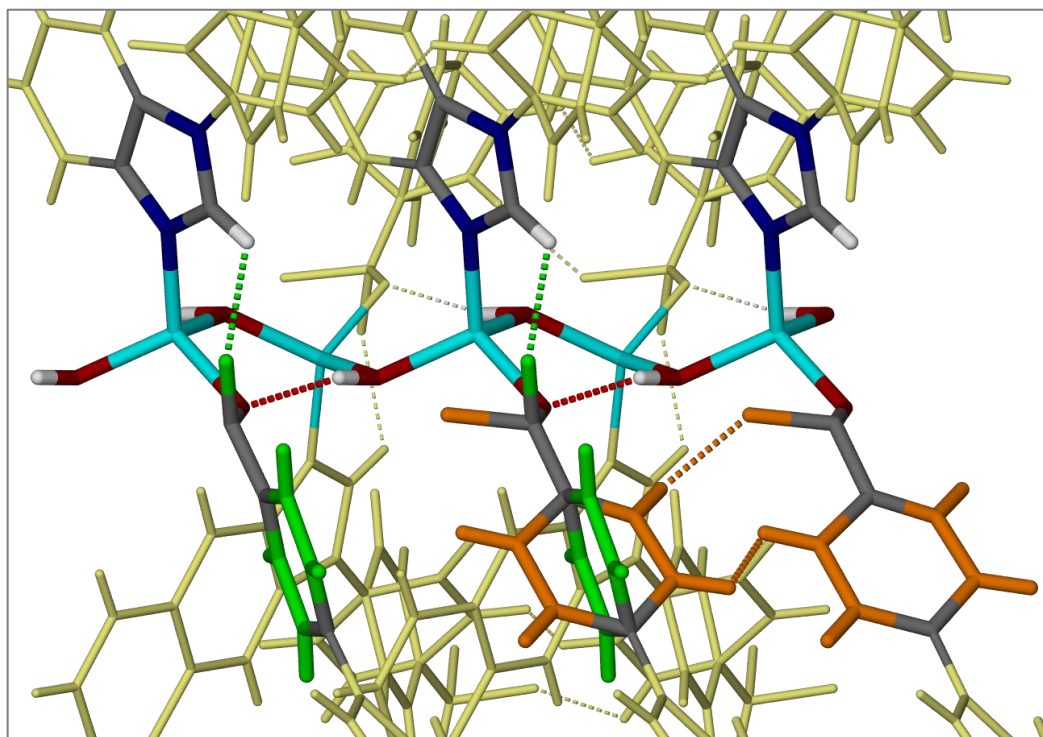


Figure 5.7: Depiction of two positions of equal occupancy of the disordered benzoate moiety of ligand \mathbf{L}_1 in compound **1**.⁵ Hydrogen bonds are shown as dashed lines. In one position (left, —), a hydrogen bond is formed with the acidic proton of the imidazole coordinating to the same zinc; in the other (right, —), hydrogen bonds are formed between neighboring benzoate moieties. Hydrogen bonds between the bridging hydroxide groups and the coordinating oxygen atoms are shown as red dashed lines.

Elucidation of the mechanism of thermal expansion in **1** could provide insight into the design of thermo-responsive materials for use in sensors and attenuators. In the following sections results from a theoretical investigation of $\mathbf{1}_{\text{apo}}$ are given. However, first a MM investigation of $\mathbf{2}\cdot 3\text{H}_2\text{O}$, undertaken in order to identify a suitable force field to employ during Molecular Dynamics simulations of $\mathbf{1}_{\text{apo}}$, is first presented.

5.3 Investigation of the crystal structure of **2·3H₂O**

Results obtained in a MM analysis of the crystal structure of **2·3H₂O** are reported and compared to the Quantum Mechanics molecular results obtained in Chapter 4. These simulations were carried out using the Force module of the Materials Studio suite of programs. Periodic DFT calculations were subsequently carried out with the DMol³ module in order to assess crystal field effects on the ω_{hccn} potential energy profile. Insights gained for the organic **2·3H₂O** system will be used in Molecular Dynamics simulations and periodic DFT evaluations of **1_{apo}** in later sections.

5.3.1 Molecular Mechanics (MM) investigation of **2·3H₂O**

The following general purpose force fields suitable for application to zinc were considered: Universal,⁷ COMPASS⁸ and Dreiding.⁹ Initially the minimal model of Figure 4.4 was evaluated to allow profile comparison to CCSD (Figure 4.5) and MP2 (Figure 4.12) levels of theory results. Non-hydrogen atoms were frozen in their crystallographic positions and the *charge equilibration* scheme (QE)¹⁰ was employed.* The MM profiles for 1° steps of the ω_{hccn} dihedral angle from 0° to 180° are compared to each other in Figure 5.8.* All the force fields considered predict the eclipsed conformer ($\omega_{hccn} \approx 0^\circ$) to be more stable with the Universal and COMPASS force fields predicting a barrier of rotation roughly four (22.60 kcal.mol⁻¹) and three (18.40 kcal.mol⁻¹) times larger than that of the Dreiding force field (5.37 kcal.mol⁻¹). Only the Dreiding force field (—) gives the same profile as that found for the higher levels of theory by showing an inflection around 50° in the potential energy profile for ω_{hccn} . As discussed in Chapter 4, this shoulder is due to a favorable dispersion interaction between the methyl hydrogen atoms and the proximal axial hydrogen atoms of the methylene bridges, before steric repulsion starts to dominate, leading to the barrier of rotation for the methyl at ~85°.

* Molecular Mechanics (and Dynamics) results obtained employing either Mulliken^{11(a)(b)} or Hirshfeld^{12(a)(b)} charges, as obtained from single point DFT population analysis on periodic structures with MM-optimized hydrogen atom positions, were not consistent with experimental results.

* A copy of the Perl scripts used to automate stepping of ω_{hccn} in the molecular representation and crystal structure (*vide infra*) of **2·3H₂O** is given in Sections A.3.2.1 and A.3.2.2, respectively. Atom-based summation of nonbonded interactions was used for the molecular representation, while the Ewald summation scheme was employed for the periodic calculations. The position of hydrogen atoms were optimized for each step with the *ultra-fine* threshold values of 2.0×10⁻⁵ kcal.mol⁻¹, 0.001 kcal.mol⁻¹.Å⁻¹ and 1.0×10⁻⁵ Å for the change in energy, maximum force and maximum displacement criteria, respectively.

Chapter 5: Anisotropic thermal expansion in a MOF

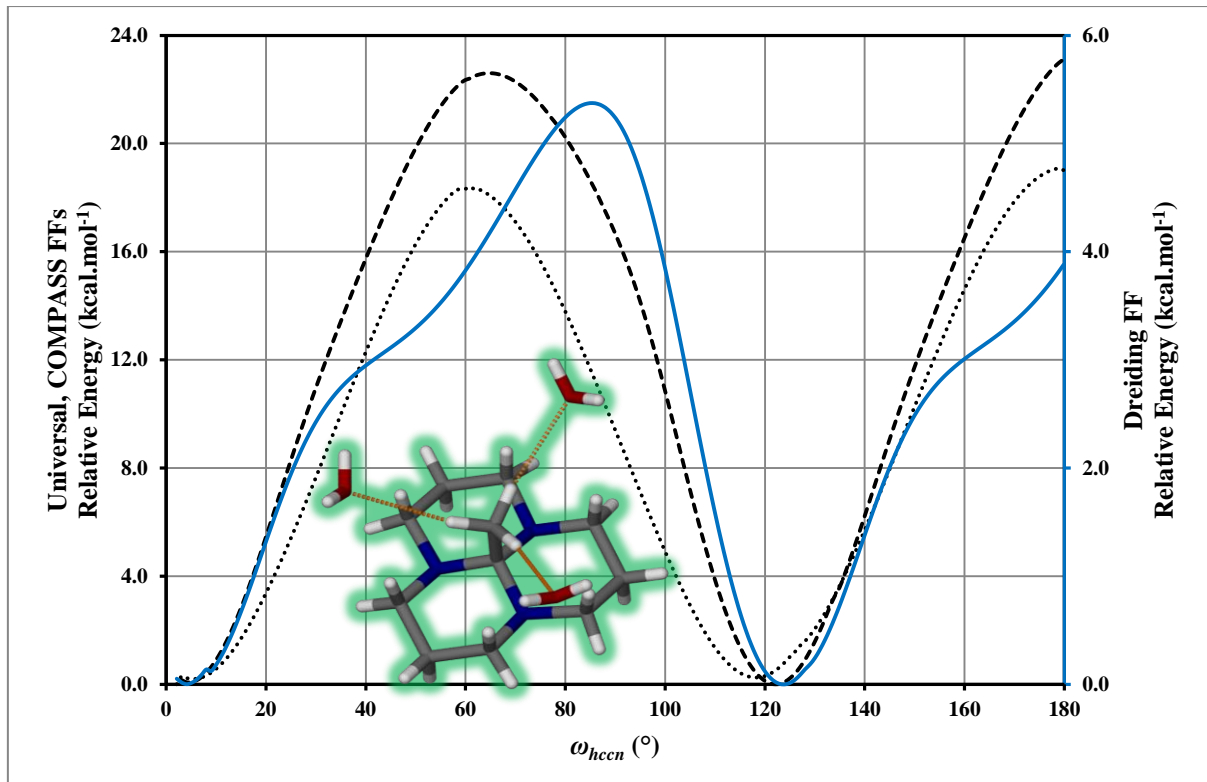


Figure 5.8: Comparison of potential energy profiles for the ω_{hccn} dihedral angle stepped in 1° increments employing the Universal (---), COMPASS (...) and Dreiding (—, right hand ordinate) force fields and QEq charges. The minimal model of $\text{2}\cdot\text{3H}_2\text{O}$ used in the simulation is also shown.

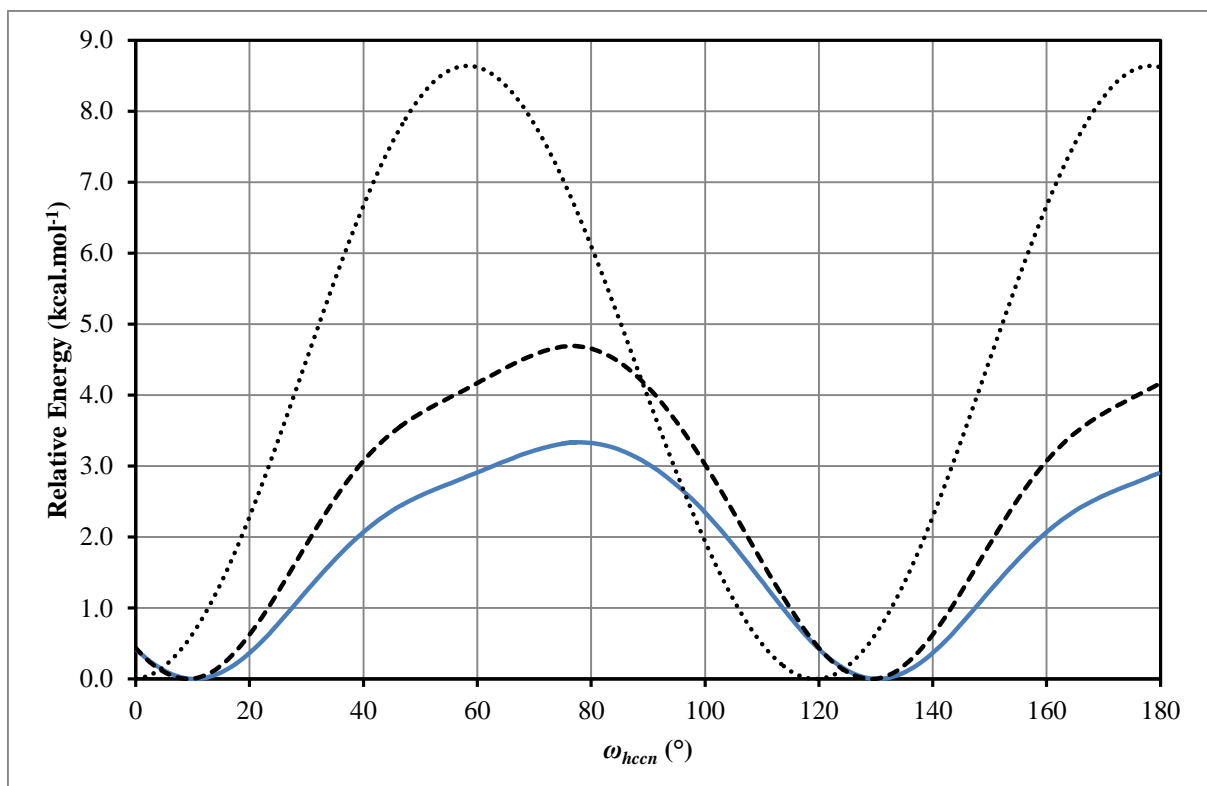


Figure 5.9: Comparison of the potential energy profiles for the crystal structure of $\text{2}\cdot\text{3H}_2\text{O}$ as a function of the ω_{hccn} dihedral angle (stepped in 0.1° increments) obtained by the Universal (---), COMPASS (...) and Dreiding (—) force fields using QEq charges.

Chapter 5: Anisotropic thermal expansion in a MOF

Application of the force fields to the full crystal structure of **2**·3H₂O yielded the profiles presented in Figure 5.9. The results were scaled by a factor of $\frac{1}{8}$ to allow comparison with the molecular results, as there are 8 complexes of **2**·3H₂O per unit cell. It was necessary to decrease the ω_{hccn} step increment to 0.1° to eliminate spurious oscillations in the potential energy. The profile obtained with the COMPASS force field remains unaltered, but with ΔE_{rot} reduced from 18.40 kcal.mol⁻¹ (for the molecular representation) to 8.64 kcal.mol⁻¹. This reduction in the calculated stability of the eclipsed conformer in the crystal structure relative to the gas phase molecular representation can be ascribed to the fact that the methylene hydrogens of **2** are not free to move out of the way of the methyl hydrogens in the crystal structure due to close contacts with surrounding complexes. This was examined by generating Hirshfeld surfaces in the Crystal Explorer package.¹³ Hirshfeld surfaces are determined by both the enclosed molecule and its closest neighbors and an interaction is indicated by a color scale ranging from blue (no interaction) to red (strong interaction).¹⁴ As shown in Figure 5.10, weak interactions are present between neighboring molecules of **2** in the region of the methylene bridges.

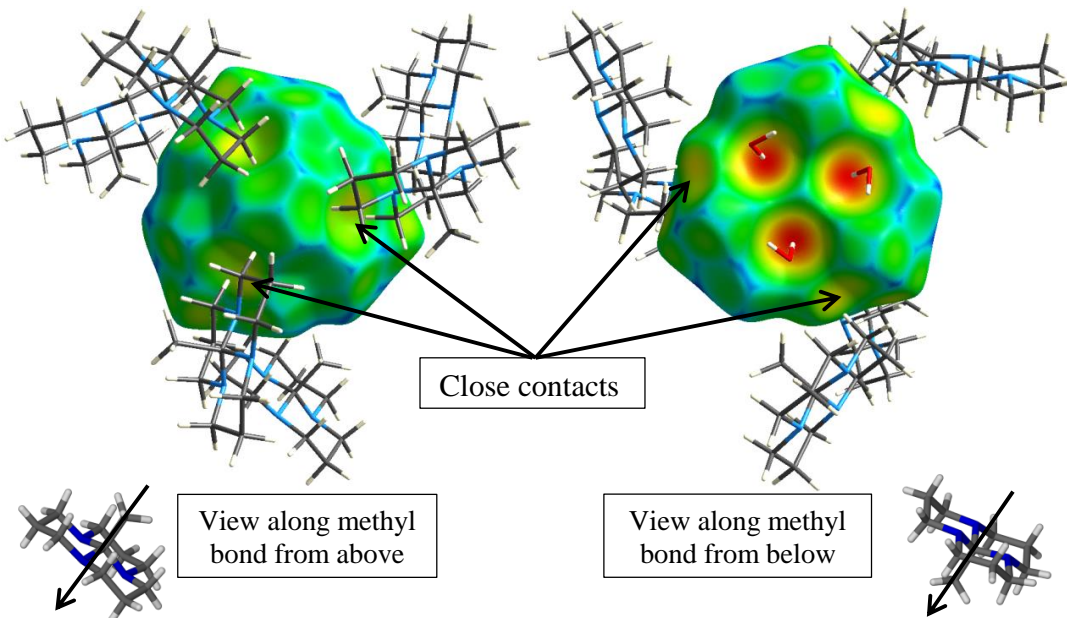


Figure 5.10: Different views of the Hirshfeld surface of the same molecule of **2** in the **2**·3H₂O crystal structure showing close contacts with three surrounding neighbors. The strong intermolecular interaction with water molecules (hydrogen bond) is shaded an intense red.

The ω_{hccn} potential energy profiles predicted by the Universal and Dreiding force fields also show a reduction in ΔE_{rot} relative to the molecular results, with both profiles presenting a shoulder in the 50° region as expected from the Quantum Mechanics results.

Chapter 5: Anisotropic thermal expansion in a MOF

5.3.2 DFT-D investigation of the crystal structure and minimal model of 2·3H₂O

The crystal structure and minimal model (Figure 4.4) of 2·3H₂O was investigated by employing the PBE/PBE nonhybrid GGA functional as implemented in DMOL³ (accessed via Materials Studio). Other density functionals were assessed, but only the PBE/PBE functional, in the presence of a dispersion energy correction, yielded profiles similar to the high-level of theory molecular results presented in Chapter 4. For the PBE/PBE functional, GD2¹⁵ (discussed in Section 2.4.2) and the correction scheme of Tkatchenko and Scheffler (TS, Section 2.6.2)¹⁶ are available in DMOL³.

For the periodic structure calculations the default *Medium* quality setting[•] was used, along with effective core potentials (ECPs) that replace core electrons with a single potential and introduce some degree of relativistic effects.¹⁷ To expedite calculations, DIIS (Direct Inversion in an Iterative Subspace) with a subspace size of 6 was used. After an initial geometry optimization of one unit cell of 2·3H₂O, with non-hydrogen atoms and unit cell parameters frozen, the ω_{hccn} dihedral angle was stepped between 0° and 120° in 5° increments and single-point energy evaluations carried out. Results, scaled by a factor 1/8, are shown in Figure 5.11. The potential energy profiles for ω_{hccn} in the minimal model were obtained in DMol³ using the same quality settings as the crystallographic studies with ω_{hccn} stepped in 2° increments. The profile at the CCSD/D95//B97D/D95 level of theory (●) obtained in Section 4.2 for the minimal model is shown for comparison (note that the inflection around 50° is less obvious due to scaling effects).

[•] SCF tolerance : 1.0×10⁻⁵

Numerical Basis set : DND (double numeric plus d-functions): One atomic orbital-function for each occupied atomic orbital plus a second set of valence AOs and a polarization d-function on all non-hydrogen atoms.

k-point separation : 0.08 Å⁻¹

Geometry Optimization Convergence Tolerance

Energy : 2.0×10⁻⁵ Ha

Maximum force : 0.004 Ha/Å

Maximum displacement : 0.005 Å

Chapter 5: Anisotropic thermal expansion in a MOF

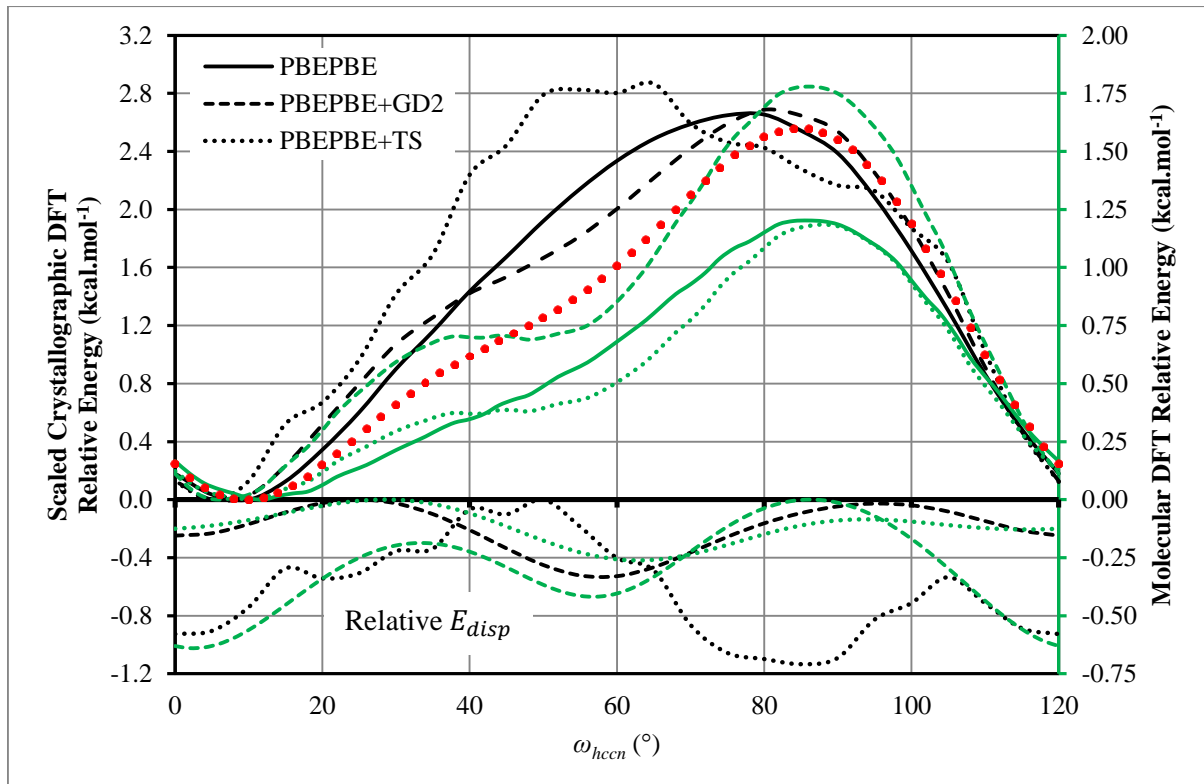


Figure 5.11: Comparison of the potential energy profiles for the ω_{hccn} dihedral angle in the crystal structure of **2**· $3\text{H}_2\text{O}$ (left hand ordinate) and minimal molecular representation (right hand ordinate, colored green) obtained with the PBEPBE density functional alone (—) and in conjunction with the GD2 (---) and TS (···) dispersion correction schemes. The deconvoluted dispersion-correction energy profiles are shown, along with the profile obtained at the CCSD/D95//B97D/D95 level of theory (●, right hand ordinate) for the minimal model.

At the molecular level, the TS and GD2 dispersion-correction energy (E_{disp}) profiles are similar in shape, with the magnitude of the GD2 correction-energy about four times that of the TS scheme at $\omega_{hccn} = 0^\circ$ (see Figure 4.14(b) and Figure 4.15(b) for Gaussian09 PBEPBE+GD2 results). At the crystallographic level, the shape of the E_{disp}^{GD2} profile is largely maintained, but its magnitude at $\omega_{hccn} = 0^\circ$ is reduced from $E_{disp,model}^{GD2,0^\circ} = -0.63 \text{ kcal.mol}^{-1}$ (---, left-hand ordinate) to $E_{disp,crystal}^{GD2,0^\circ} = -0.25 \text{ kcal.mol}^{-1}$ (---, right-hand ordinate), whereas the $E_{disp,crystal}^{TS}$ profile (···) becomes erratic with a shift in its maximum to $\sim 85^\circ$. This points towards an inefficient damping of the TS dispersion-correction ($S_r^{PBEPBE} = 0.94$ parameter of Eq. 2.87 too large), causing an excessive contribution of close contacts to be included in E_{disp}^{TS} . As a result the crystallographic PBEPBE/DNP+TS potential energy profile (···) shows erratic oscillations and the maximum of the rotation barrier is shifted from $\sim 80^\circ$ to $\sim 60^\circ$.* It has been noted before that the PBEPBE functional performs better than other GGAs for dispersion-bound complexes and care must be taken in parameterizing dispersion correction to avoid double-counting effects.¹⁸

* These oscillations could not be remedied (as was suggested for meta-GGA density functionals in Section 4.5.1) by improving the integration grid coarseness from *Medium* (where 1000 grid points are assigned to each atom) to *Fine*.

Chapter 5: Anisotropic thermal expansion in a MOF

Only in combination with GD2 does the PBEPBE energy profile (---) of the ω_{hccn} dihedral angle echo that of the molecular CCSD-level of theory results. This is in line with the discussion in Section 1.1 of a recent investigation by Appalakondaiah *et al.* who found PBEPBE+GD2 to be able to reproduce experimental pressure dependent structural and vibrational results of FOX-7.¹⁹ Closer inspection of Figure 5.11 reveals that the magnitude of the rotation barrier increases from 1.76 kcal.mol⁻¹ for the molecular representation (---) to a value of 2.7 kcal.mol⁻¹ for the periodic structure (PBEPBE/DND+GD2 scaled by 1/8). This increase is attributable to crystal-field effects (many-body effects in the solid state) that increase the polarizability of heterobonds.²⁰ This is counter to what was found for the molecular (Figure 5.8, Dreiding/QEq 5.2 kcal.mol⁻¹) and crystallographic (Figure 5.9, 3.2 kcal.mol⁻¹) results obtained using MM, where such polarization effects do not offset the close-contact interactions of neighboring molecules in the periodic structure.

5.4 Molecular Dynamics (MD) on MOF **1_{apo}**

To investigate the temperature dependence of the unit cell parameters in **1_{apo}**, Molecular Dynamics simulations were carried out in the NTP ensemble using Force (accessed via Materials Studio). The Parrinello-Rahman barostat was used since it allows for change of both unit cell shape and volume during a simulation under a constant external pressure.²¹ This is essential for attempting to reproduce the experimentally observed *anisotropic* thermal expansion of **1_{apo}**. The Berendsen thermostat²² was found to best regulate temperature for the system under investigation.

Simulations were carried out in the range 100-400 K in 25 K increments on the geometry optimized 100 K crystal structure of **1_{apo}** (see Section 5.5 for details regarding periodic DFT calculations).[▲] Results of the Dreiding force field using QEq charges are shown in Figure 5.12. The observed anisotropic thermal expansion trend (*cf.* Figure 5.5 for experimental variable temperature powder X-ray diffraction unit cell parameters) is reproduced. The comparison in Figure 5.12(b) possibly hides the fact that the simulated change in unit cell volume, $\Delta V_{sim} \approx 23 \text{ \AA}^3$, is a factor 3.6 times smaller than the experimental change, $\Delta V_{exp} \approx 88 \text{ \AA}^3$, in the 100 K to 370 K temperature range. Even though this is reflected in similarly reduced simulated unit cell length changes, the successful reproduction of the experimentally observed trends was unexpected. Numerous other combinations of available force fields and charge schemes (based on periodic DFT or molecular *ab initio* calculations) were attempted, but all yielded isotropic positive thermal expansion.

[▲] The Parrinello-Rahman barostat cell time constant was set to 1.0 ps, while the decay constant of the Berendsen thermostat was set to 0.1 ps. Simulations were carried out for 200 ps with 1 fs steps. The frame output frequency was set to 1.0 ps and the average values of the last 100 structures used to calculate the unit cell parameters for the set temperature. The first 100 ps therefore represent equilibration of the system in the NTP ensemble, with results produced in the second 100 ps.

Chapter 5: Anisotropic thermal expansion in a MOF

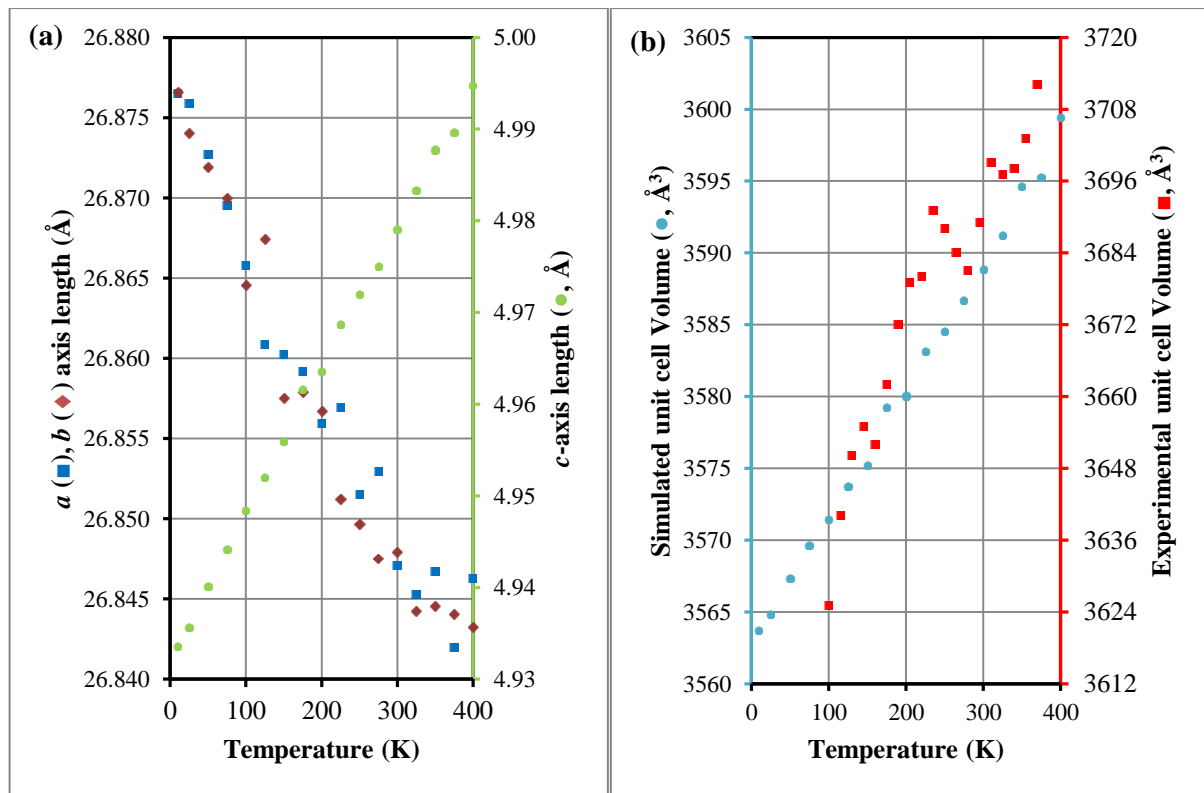


Figure 5.12: Unit cell (a) dimensions and (b) volumes of $\mathbf{1}_{\text{apo}}$ calculated in the NTP ensemble employing the Dreiding force field and the QEq charge scheme. The Parrinello-Rahman barostat and Berendsen thermostat were employed. In (b) the experimental volume change is plotted from data of Figure 5.5.⁵

5.5 Mechanistic model for anisotropic thermal expansion in $\mathbf{1}_{\text{apo}}$

In the paper wherein Grobler *et al.* reported the 100, 190, 280 and 370 K crystal structures of $\mathbf{1}_{\text{apo}}$, it was suggested that the mechanism responsible for the anisotropic thermal expansion is associated with stretching of the zinc-hydroxide-zinc coordination spiral along the crystallographic c -axis.⁵ A rigid-bond model that can be stretched out by varying a single variable in order to test this hypothesis was introduced in Section 3.8. DFT results obtained for this mechanistic model are compared here to periodic DFT calculations on $\mathbf{1}_{\text{apo}}$.

The increased thermal motion of the benzoate moiety decreased the quality of the X-ray data at higher temperatures, with hydrogen atoms poorly positioned or even absent. It was therefore decided to generate the higher temperature structures by imposing their unit cell parameters on the geometry-optimized 100 K structure and using the same fractional coordinates. Subsequent reoptimization of all atomic positions (with fixed unit cell parameters) resulted in structures that were nearly identical to those obtained from geometry optimization of each experimental structure (requiring certain atoms to be placed in chemically intuitive positions).

Chapter 5: Anisotropic thermal expansion in a MOF

The positions of atoms in the crystal structures of **1_{apo}** were optimized in DMol³ employing the PBE/PBE density functional augmented with the GD2 dispersion correction. To speed up calculations, geometry optimizations were carried out on the primitive cell, that is, for the tetragonal class, half the original unit cell. Calculations were performed at the default *Fine* quality setting^{*} of DMol³ with ECP approximations and a DIIS subspace size of 6. To expedite SCF convergence, a smearing parameter of 0.005 Ha was used.[♦] After geometry optimization of the primitive cell, the conventional cell (space group *I*⁴) was redefined and single point energy calculations were carried out with the same quality setting. Potential energies relative to the 100 K structure are shown in Figure 5.13.

A model of the representation shown in Figure 3.15(c) (insert in Figure 5.13) was obtained from the optimized 100 K structure and the initial hydrogen atom Z-matrix generated using the VB script presented in Section 3.7. The variable *S* was stepped between 0.00 and 0.20 Å in 0.05 Å increments to yield an effective *c*-axis length range of 5.146 Å to 5.346 Å, which corresponds to the experimental *c*-axis length variation in the temperature range 100–370 K (*cf.* Table 5.1).⁵ After translation of non-hydrogen atoms in Cartesian coordinates, the unaltered initial hydrogen atom Z-matrix was appended to yield a mixed coordinate input file for GAUSSIAN 09, Revision D.01. For each value of *S* only the hydroxide and water hydrogen atom positions were optimized. Energies of the model, scaled by a factor $\frac{4}{3}$ to allow comparison to the unit cell single point energy values (8 zinc atoms per unit cell of **1_{apo}** *vs.* 6 in the mechanistic model), are shown in Figure 5.13 relative to the *S* = 0.0 Å model energy (*cf.* Figure A.14 for additional results). Also depicted in Figure 5.13 is the profile obtained for the hydrogen atom position optimized model (—) in DMol³ using the same settings as the crystallographic single point calculations (*i.e.*, footnote ♦ plus DIIS (subspace size: 6) and orbital smearing (factor: 0.005 Ha)). It can be seen that the magnitude of the results for the TZVP Gaussian-type orbital (GTO) basis set matches the numerical DNP basis set results, with the ωB97XD (---) potential energy profile closely resembling the PBE/PBE+GD2 profile.

* SCF tolerance : 1.0×10^{-6}

Numerical Basis set : DNP (double numeric plus polarization): DND augmented with a polarization p-function on all hydrogen atoms.

k-point separation : 0.07 Å⁻¹

Geometry Optimization Convergence Tolerance

Energy : 1.0×10^{-5} Ha

Maximum force : 0.002 Ha/Å

Maximum displacement : 0.05 Å

♦ In thermal smearing, the default procedure used by DMol³ in Materials Studio, a fractional occupancy is assigned to one-electron states near the Fermi-level ($T = \beta/k_B$, with β the *smearing parameter* and k_B Boltzmann's constant) to allow orbitals to relax more rapidly.

Chapter 5: Anisotropic thermal expansion in a MOF

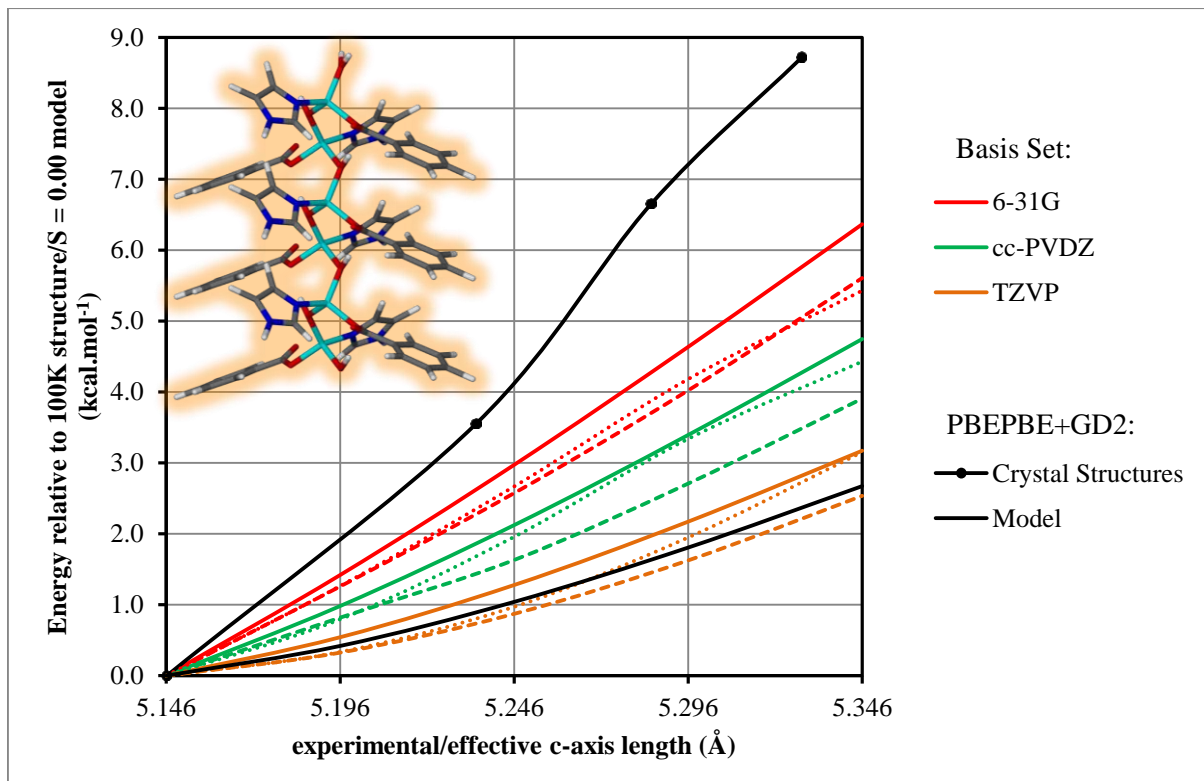


Figure 5.13: Comparison of single point energy values for one unit cell of $\mathbf{1}_{\text{apo}}$ (●) and the scaled results obtained for hydrogen atom position optimizations of the simplified model (inset) using B3LYP + GD2 (—, colored), ωB97XD (---) and M06 + GD3 (···) in conjunction with various basis sets. The abscissa shows the effective *c*-axis length calculated as $c_{\text{eff}} = c_{100K} + S$ to correspond to the experimental *c*-axis length in the temperature range 100–370 K (Table 5.1). The variable *S* was stepped between 0.00 Å and 0.20 Å in 0.05 Å (yielding $5.146 \text{ \AA} \leq c_{\text{eff}} \leq 5.346 \text{ \AA}$). Also shown is the profile obtained for the model (—) using the same settings as the crystallographic single point calculations.

Although a number of gross assumptions were made in the model, which ignores crystal field and certain stereo-electronic effects (for instance, the ligand was severely truncated, a hydroxide group was converted into a coordinating water (inset in Figure 5.13) and all bond lengths were kept constant), the correlation between the model and the crystallographic energies (obtained as previously discussed in this section) are gratifying. In Figure 5.6 it was moreover shown that the model underestimates Δa as a function of Δc . These results indicate that a concerted change in the coordination sphere of the zinc centre so as to elongate the coordination spiral in the *c* direction ($\text{O(H)}-\text{Zn}-\text{O(H)}$ angles enlarge), while pulling the largely unaltered rigid ligands ($\text{Zn}\cdots\text{Ligand}\cdots\text{Zn}$ distance constant) closer together in the *ab* plane is a dominating causative factor for the observed anisotropic thermal expansion of the MOF $\mathbf{1}_{\text{apo}}$ ($\alpha_a = \alpha_b = -21 \text{ MK}^{-1}$ and $\alpha_c = 123 \text{ MK}^{-1}$ for the temperature range 100–370 K).

5.6 Summary

A brief overview of vibrational mechanisms contributing to thermal stress is presented at the start of this chapter and more details of the anomalous thermal expansion of **1_{apo}** given in Section 5.2. A MM investigation of **2·3H₂O** (minimal model and crystallographic) reveal the accuracy of the general purpose Dreiding force field to reproduce Quantum Mechanics results of Chapter 4. DFT calculations of one unit cell of **2·H₂O** are presented in Section 5.3.2 employing the PBEPBE functional. Only in conjunction with the GD2 dispersion correction is the potential energy profile for ω_{hccn} obtained at CCSD level of theory for the minimal model reproduced. It is shown that the anisotropic thermal expansion of **1_{apo}** can be reproduced by Molecular Dynamics simulations in the NTP ensemble employing the Dreiding force field and QEq charges. Lastly, in Section 5.5 it is shown that the observed energy trend in the anisotropically expanding unit cell of **1_{apo}** with increasing temperature is successfully reproduced using a simple mechanistic model with fixed bond lengths that simulate the concomitant expansion and convergence of the coordination spiral in the crystallographic *c* direction.

Chapter 5: Anisotropic thermal expansion in a MOF

5.7 References

1. Jensen, F., *Introduction to Computational Chemistry*. Second Edition.; Wiley: West Sussex, England, **2007**.
2. Barrera, G.D.; Bruno, J.A.O.; Barron, T.H.K.; Allan, N.L., *J. Phys. Condens. Matter* **2005**, *17*, R217.
3. (a) Brown, I.D., *Acta Crystallogr.* **1992**, *B48*, 553; (b) Brown, I.D.; Dabkowski, A.; McCleary, A., *Acta Crystallogr.* **1997**, *B53*, 750.
4. Barron, T.H.K.; Gibbons, T.G., *J. Phys. C* **1974**, *7*, 3260.
5. Grobler, I.; Smith, V.J.; Bhatt, P.M.; Herbert, S.A.; Barbour, L.J., *J. Am. Chem. Soc.* **2013**, *135*, 6411.
6. Grobler, I. PhD thesis, *Solid-State Dynamics of Porous Materials*; Stellenbosch University, **2013**.
7. (a) Rappé, A.K.; Casewit, C.J.; Colwell, K.S.; Goddard III, W.A.; Skiff, W.M., *J. Am. Chem. Soc.* **1992**, *114*, 10024; (b) Casewit, C.J.; Colwell, K.S.; Rappé, A.K., *J. Am. Chem. Soc.* **1992**, *114*, 10035; (c) Casewit, C.J.; Colwell, K.S.; Rappé, A.K., *J. Am. Chem. Soc.* **1992**, *114*, 10046; (d) Rappé, A.K.; Colwell, K.S.; Casewit, C.J., *Inorg. Chem.* **1993**, *32*, 3438.
8. (a) Rigby, D.; Sun, H.; Eichinger, B.E., *Polym. Int.* **1997**, *44*, 311; (b) Sun, H., *J. Phys. Chem. B* **1998**, *102*, 7338; (c) Sun, H.; Ren, P.; Fried, J.R., *Comput. Theor. Polym. Sci.* **1998**, *8*, 229; (d) Sun, H.; Ren, P.; Fried, J.R., *Comput. Theor. Polym. Sci.* **1998**, *8*, 363.
9. Mayo, S.L.; Olafson, B.D.; Goddard, W.A., III, *J. Phys. Chem.* **1990**, *94*, 8897.
10. Rappé, A.K.; Goddard III, W.A., *J. Phys. Chem.* **1991**, *95*, 3358.
11. (a) Mulliken, R.S., *J. Chem. Phys.* **1955**, *23*, 1833; (b) Sanchez-Portal, D.; Artacho, E.; Soler, J.M., *Solid State Commun.* **1995**, *95*, 685.
12. (a) Ritchie, J.P., *J. Am. Chem. Soc.* **1985**, *107*, 1829; (b) Ritchie, J.P.; Bachrach, S.M., *J. Comput. Chem.* **1987**, *8*, 499.
13. *Crystal Explorer 2.1 (381)*, Wolff, S.K.; Grimwood, D.J.; McKinnon, J.J.; Jayatilaka, D.; Spackman, M.A.; University of Western Australia: **2007**.
14. Spackman, M.A.; Jayatilaka, D., *CrystEngComm* **2009**, *11*, 19.
15. Grimme, S., *J. Comput. Chem.* **2006**, *27*, 1787.
16. Tkatchenko, A.; Scheffler, M., *Phys. Rev. Lett.* **2009**, *102*, 73005.
17. (a) Dolg, M.; Wedig, U.; Stoll, H.; Preuss, H., *J. Chem. Phys.* **1987**, *86*, 866; (b) Dolg, M.; Stoll, H.; Preuss, H., *J. Chem. Phys.* **1989**, *90*, 1730; (c) Dolg, M.; Stoll, H.; Savin, A.; Preuss, H., *Theor. Chim. Acta* **1989**, *75*, 173; (d) Bergner, A.; Dolg, M.; Kuechle, W.; Stoll, H.; Preuss, H., *Mol. Phys.* **1993**, *80*, 1431.
18. Antony, J.; Grimme, S., *Phys. Chem. Chem. Phys.* **2006**, *8*, 5287.
19. Appalakondaiah, S.; Vaitheeswaran, G.; Leb  gue, S., *J. Chem. Phys.* **2014**, *140*, 014105/1.
20. (a) Chao, I.; Chen, J.-C., *Angew. Chem. Int. Ed.* **1996**, *35*, 195; (b) Van de Bovenkamp, J.; Matxain, J.M.; Van Duijneveldt, F.B.; Steiner, T., *J. Phys. Chem. A* **1999**, *103*, 2784; (c) Chuev, I.I.; Atovmyan, E.G.; Aldoshin, S.M., *J. Mol. Struct.* **1999**, *474*, 177.
21. Martyna, G.J.; Tobias, D.J.; Klein, M.L., *J. Chem. Phys.* **1994**, *101*, 4177.
22. Berendsen, H.J.C.; Postma, J.P.M.; Van Gunsteren, W.F.; DiNola, A.; Haak, J.R., *J. Chem. Phys.* **1984**, *81*, 3684.

Chapter 6: Adsorption techniques and methodologies

Isosteric heats of adsorption, Q_{st} , are generally compared in order to predict the performance of adsorbents in industrial applications. Materials exhibiting a large Q_{st} should show a high selectivity, but then high temperatures are required in order to regenerate the activated material. This chapter compares various methodologies currently used to determine Q_{st} values from isothermal adsorption data. Thermodynamic parameters of carbon dioxide sorption on compounds **3** and **4** previously determined using the volumetric SIT device are compared to Q_{st} values determined for gravimetric CO₂ sorption by the same compounds.

6.1 Isotherm models

A general equation for describing the adsorption process has the following form:

$$n = F(P, T) \quad 6.1$$

where n represents the amount adsorbed, or occupancy, at equilibrium pressure P and absolute temperature T . Knowledge of this relationship allows for the estimation of the basic thermodynamic characteristics of the adsorption process and the prediction of adsorption occupancy as a function of pressure and temperature. To circumvent the temperature dependence of this process, adsorption experiments are carried out under constant temperature conditions:

$$n = [F(P)]_T \quad 6.2$$

hence the convention of calling plots of occupancy as a function of pressure *adsorption isotherms*.¹ The analytical form of the relationship given in Eq. 6.2 is unknown *a priori* and various isotherm equations exist that relate the fractional occupancy θ (defined as the ratio of the current occupancy n to the occupancy at saturation n_{sat}) to pressure. The most commonly applied equation is that of Irving Langmuir:²

$$\theta = \frac{n}{n_{sat}} = \frac{bP}{1 + bP} \quad 6.3$$

where the affinity parameter b is related to the strength of adsorption. The simple Langmuir model has been extended to account for surface heterogeneity by incorporating a heterogeneity parameter c in various ways. Modified versions of the standard isotherm equations; wherein n_{sat} is allowed to vary, were used in this study, namely the Freundlich³ (Eq. 6.4), Sips⁴ (Eq. 6.5) and Tóth⁵ (Eq. 6.6) equations:

Chapter 6: Adsorption techniques and methodologies

$$n = n_{sat} P^{\frac{1}{c}} \quad 6.4$$

$$n = \frac{n_{sat} (bP)^c}{1 + (bP)^c} \quad 6.5$$

$$n = \frac{n_{sat} bP}{[1 + (bP)^c]^{\frac{1}{c}}} \quad 6.6$$

The best isotherm equation to apply to experimental adsorption data can be identified based on goodness-of-fit considerations.⁶ In this study the parameters R_{adj}^2 (adjusted coefficient of determination) and χ_{red}^2 (reduced ratio of residual sum of squares to degrees of freedom) were considered and an interdependence of parameters (that indicate over-parameterization) avoided. Non-linear fitting for this work was carried out using the OriginPro 9.0 software package (© OriginLab Corporation, Massachusetts, USA).⁷ This programme employs the Levenberg-Marquardt least-squares fitting algorithm that combines the steepest-descent and Gauss-Newton methods to adjust the parameter values in order to minimize χ_{red}^2 . The maximum number of iterations was set to 400, with a change in χ_{red}^2 tolerance of 10^{-9} .

6.2 Thermodynamic parameters of adsorption

The thermodynamic quantities ΔH_{ad}^0 , ΔS_{ad}^0 and ΔG_{ad}^0 representing the enthalpy of adsorption, the entropy of adsorption and the Gibbs free energy of adsorption, respectively, can be related to the change in pressure and temperature based on the following physico-chemical principles. For the general adsorption reaction between guest G (adsorbate) on host H (adsorbent)



the equilibrium constant is given by

$$K_{eq}^{ad} = \frac{a_{HG}}{a_H a_G} = \frac{1}{a_G} \quad 6.8$$

where a_{HG} is the activity for the $HG_n(s)$ complex, a_H is the activity for $H(s)$ and a_G is the activity for $nG(g)$.⁸ Assuming the activity of solids are unity, the equilibrium constant of the adsorption reaction is only related to the activity of the adsorbate.

Integration of the following thermodynamic relationship:⁹

$$\left(\frac{\partial G}{\partial P} \right)_{T,n} = V \quad 6.9$$

gives an expression for the Gibbs free energy in terms of pressure:

Chapter 6: Adsorption techniques and methodologies

$$\int_{G^0}^G dG = G - G^0 = \int_{P^0}^P VdP \quad 6.10$$

The initial pressure is chosen to be the standard state pressure: $P^0 = 1$ bar. Assuming ideal gas behavior, $V = nRT/P$, and constant temperature, Eq. 6.10 becomes

$$G = G^0 + nRT \ln P \quad 6.11$$

Consider the following generic gaseous reaction:⁸



with arbitrary partial pressures P_A , P_B , P_C and P_D for the respective species. The change in the Gibbs free energy for this reaction (Eq. 6.11) is given by

$$\begin{aligned} \Delta G_{rxn} &= G_C + G_D - G_A - G_B \\ &= G_C^0 + \gamma RT \ln P_C + G_D^0 + \delta RT \ln P_D - G_A^0 - \alpha RT \ln P_A - G_B^0 - \beta RT \ln P_B \end{aligned} \quad 6.13$$

Collecting the logarithmic terms results in

$$\Delta G_{rxn} = \Delta G_{rxn}^0 + RT \ln \frac{\left(\frac{P_C}{P^0}\right)^\gamma \left(\frac{P_D}{P^0}\right)^\delta}{\left(\frac{P_A}{P^0}\right)^\alpha \left(\frac{P_B}{P^0}\right)^\beta} = \Delta G_{rxn}^0 + RT \ln Q_P \quad 6.14$$

where Q_P is the reaction quotient of partial pressures. At equilibrium $\Delta G_{rxn} = 0$; therefore

$$\Delta G_{rxn}^0 = -RT \ln K_{eq} \quad 6.15$$

which is generally applicable for any reaction.⁸

Returning to the adsorption reaction of Eq. 6.7, the equilibrium constant can be written as

$$K_{eq}^{ad} = \frac{1}{a_G} = \frac{1}{P^n} \quad 6.16$$

where it is assumed that the activity of a pure gaseous species can be approximated by its pressure. The thermodynamic parameters of the adsorption reaction are thus calculated:

$$\Delta G_{ad}^0 = nRT \ln P = \Delta H_{ad}^0 - T\Delta S_{ad}^0 \quad 6.17$$

For the adsorption process to be spontaneous ($\Delta G_{ad}^0 < 0$), physisorption (as opposed to chemisorption) must necessarily be exothermic. During physical adsorption, molecules from a bulk phase pass to a more ordered adsorbed state where they are restricted to a surface or confined to a pore. The system therefore experiences a decrease in entropy ($\Delta S_{ad}^0 < 0$) that must be compensated for by a negative ΔH_{ad}^0 . The physisorption process is therefore favored by a decrease in temperature.⁹

6.3 Volumetric SIT study of CO₂ sorption on compounds 3 and 4

Gravimetric adsorption data obtained in this work were compared to those generated by Marais¹⁰ on a novel volumetric sorption isosteric technique (SIT) device constructed by Barbour.¹¹ The device and its modes of operation are described in Section 3.3. The low pressure adsorption isotherms obtained by Marais for compounds **2** and **3** using the volumetric SIT device are shown in Figure 6.1.¹⁰ The Sips equation was found to fit the adsorption data best and the fitting parameters are shown in Figure 6.1.

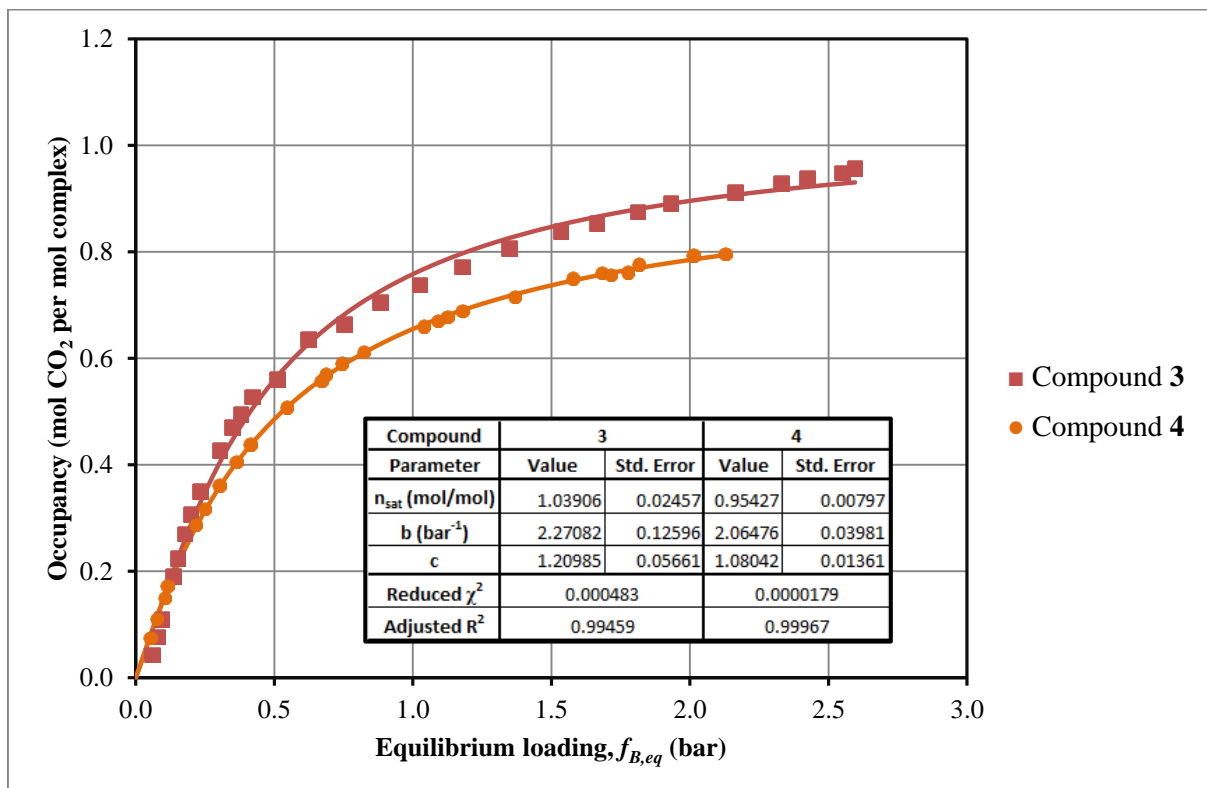


Figure 6.1: Adsorption isotherms (25 °C) obtained using the volumetric SIT device.¹⁰ The solid lines represent fits of the Sips equation to the adsorption data [$N(3) = 28$; $N(4) = 26$] with the goodness-of-fit found to be superior for compound **4**.

As discussed in Section 3.3.2, the volumetric SIT device can readily be used to determine the thermodynamic parameters of adsorption. Rewriting the thermodynamic relation $\Delta G_{ad}^0 = \Delta H_{ad}^0 - T\Delta S_{ad}^0$ (Eq. 6.17) as

$$n \ln P = \frac{\Delta H_{ad}^0}{R} \frac{1}{T} - \frac{\Delta S_{ad}^0}{R} \quad 6.18$$

allows for the determination of ΔH_{ad}^0 from the slope and ΔS_{ad}^0 from the intercept of a linear fit to the plot of $n \ln P$ against $1/T$. Here n represents the stoichiometric factor of guest uptake in the gas adsorption reaction: $H(s) + nG(g) \rightleftharpoons HG_n(s)$ (Eq. 6.7) when full occupancy is reached.

Chapter 6: Adsorption techniques and methodologies

Jacobs carried out an *in situ* controlled pressure single-crystal X-ray diffraction study on compound **3** and found a host-complex to CO₂ guest ratio of 1:2 for a CO₂ loading of 10 bar.¹² A similar study was carried out on compound **4** by Lloyd, who found a limiting host to guest ratio of 1:1.¹³ Marais reported the thermodynamic parameters of adsorption based on these stoichiometries,¹⁰ but, in the absence of crystallographic data, potential users of the volumetric SIT device will have to rely on the n_{sat} fitting parameter of a suitable isotherm equation to scale the thermodynamic quantities. Therefore, a maximum occupancy of one, as inferred from fitting of the Sips equation (Figure 6.1), was used to generate the thermodynamic parameters as a function of occupancy for CO₂ adsorption on compounds **3** and **4** (shown in Figure 6.2).

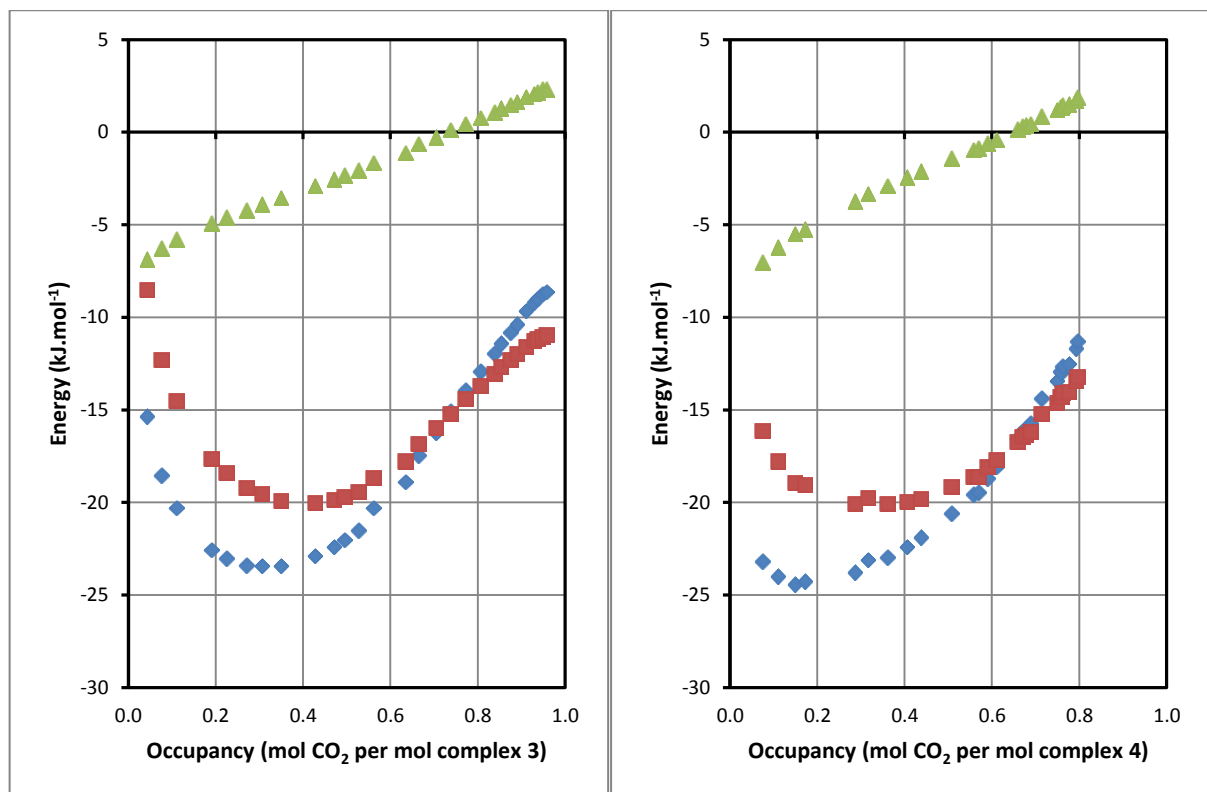


Figure 6.2: Thermodynamic parameters of adsorption for compounds **3** (left) and **4** (right) as a function of occupancy: ΔH_{ad}^0 (◆), ΔS_{ad}^0 (■) and ΔG_{ad}^0 (▲).

The ΔH_{ad}^0 profile has a minimum for both compounds, with the minimum reached at a higher occupancy for compound **3** ($n \approx 0.3$) than compound **4** ($n \approx 0.2$). This profile indicates the presence of attractive guest-guest interactions as pockets in the microporous material are filled sequentially, before these interactions are overcome by steric repulsion.¹⁴ The larger voids present in **3_{apo}** ($\sim 118 \text{ \AA}^3$ (Section 3.2.2) compared to $\sim 107 \text{ \AA}^3$ in **4_{apo}** (Section 3.2.3)) therefore allow more CO₂ to be adsorbed before either steric repulsion or framework rearrangement to accommodate more adsorbate offset the exothermic physisorption process.

Chapter 6: Adsorption techniques and methodologies

6.4 The isosteric heat of adsorption

The adsorption enthalpy, ΔH_{ad}^0 , is a measure of the strength of the adsorbent-adsorbate interactions and can be approximated by the isosteric heat of adsorption, $\Delta H_{ad}^0 \approx -Q_{st}$ discussed briefly in this section. Q_{st} represents the average binding energy of an adsorbing molecule at a specific surface coverage. By recording isotherms at various temperatures the Q_{st} for a given occupancy can be obtained from the Clausius-Clapeyron approximation:¹⁵

$$Q_{st} = RT^2 \left(\frac{\partial \ln P}{\partial T} \right)_n \quad 6.19$$

Assuming Q_{st} to be temperature invariant, integration of Eq. 6.19 yields

$$\ln P = \frac{-Q_{st}}{R} \frac{1}{T} + C \quad 6.20$$

In the *graphical interpolation* method the experimental isotherms are fitted individually to the chosen isotherm model and the fitting parameters used to calculate the pressures for a specific occupancy. The Q_{st} value is then obtained from the slope of a linear fit to the graph of $\ln p$ versus $1/T$. Adsorption isotherms are generally recorded at three or more temperatures to improve the accuracy of the Q_{st} profiles.

Here follows a discussion of the application of this methodology to gravimetric CO₂ adsorption isotherms of compounds **3** and **4** recorded at 20, 30, 40 and 50 °C. Since CO₂ is expected to deviate considerably from ideal gas behavior, pressure values were converted to fugacities by employing the van der Waals approximation for a real gas:

$$P = \frac{nRT}{V - nb_{vdW}} - \frac{n^2 a_{vdW}}{V^2} \quad 6.21$$

The molecular attraction parameter a_{vdW} represents the reduction in pressure due to intermolecular interactions, and the molecular exclusion parameter b_{vdW} the reduction in volume due to the non-negligible size of the particles constituting real gases.¹⁶ These parameters are calculated from the critical point temperature T_c and pressure P_c according to

$$a_{vdW} = 27R^2T_c^2/(64P_c) \quad \text{and} \quad b_{vdW} = RT_c/(8P_c)$$

to yield $a_{vdW}^{CO_2} = 3.658 \text{ bar.L}^2.\text{mol}^{-2}$ and $b_{vdW}^{CO_2} = 0.0426 \text{ L.mol}^{-1}$.¹⁶ The fugacity was then calculated from the virial equation of state truncated after the second term:¹⁷

$$f = Pe^{\left[\left(b - \frac{a}{RT} \right) P + \left(ab - \frac{a^2}{2RT} \right) \left(\frac{P}{RT} \right)^2 \right] / (RT)} \quad 6.22$$

Chapter 6: Adsorption techniques and methodologies

6.4.1 Graphical interpolation of gravimetric CO₂ adsorption data

The adsorption data obtained for an activated powder sample of compound **3** were fitted to the Sips equation, as shown in Figure 6.3. The CO₂ sorption data for, encompassing both adsorption and desorption (showing negligible hysteresis, hence both sets were included to statistically improve curve fitting), compound **4** was fitted to the Tóth equation as shown in Figure 6.4. From these figures it can be seen that compound **4** yielded superior fitting results. In order to calculate Q_{st} , pressure must be calculated as a function of occupancy. To this end, the Sips equation (Eq. 6.5) was rearranged to yield

$$P = \frac{n^{\frac{1}{c}}}{b[n_{sat} - n]^{\frac{1}{c}}} \quad 6.23$$

while rearrangement of the Tóth equation (Eq. 6.6) gives

$$P = \frac{n}{b[n_{sat}^c - n^c]^{\frac{1}{c}}} \quad 6.24$$

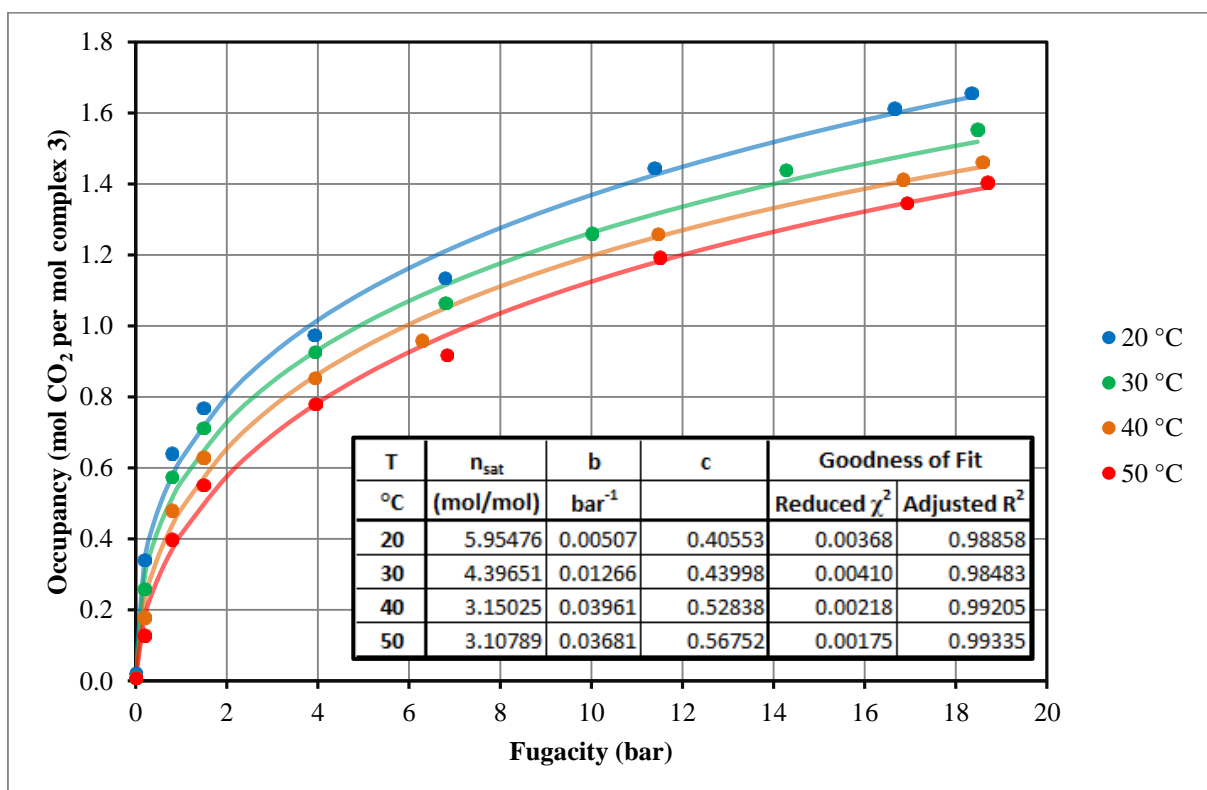


Figure 6.3: Isotherm plots of carbon dioxide adsorption (filled circles) on compound **3**. Solid lines represent least-squares fitting of the Sips equation to each isotherm ($N = 9$ in each case).

The Q_{st} for a specific occupancy is then calculated from Eq. 6.20 as the negative of the slope of $\ln P$ versus $1/T$ plots (shown in Figure 6.5 for compound **4**) multiplied by R , the universal gas constant $8.31447 \text{ J.K}^{-1}.\text{mol}^{-1}$. Figure 6.6 summarizes the Q_{st} results obtained for compounds **3** and **4** by the graphical interpolation method.

Chapter 6: Adsorption techniques and methodologies

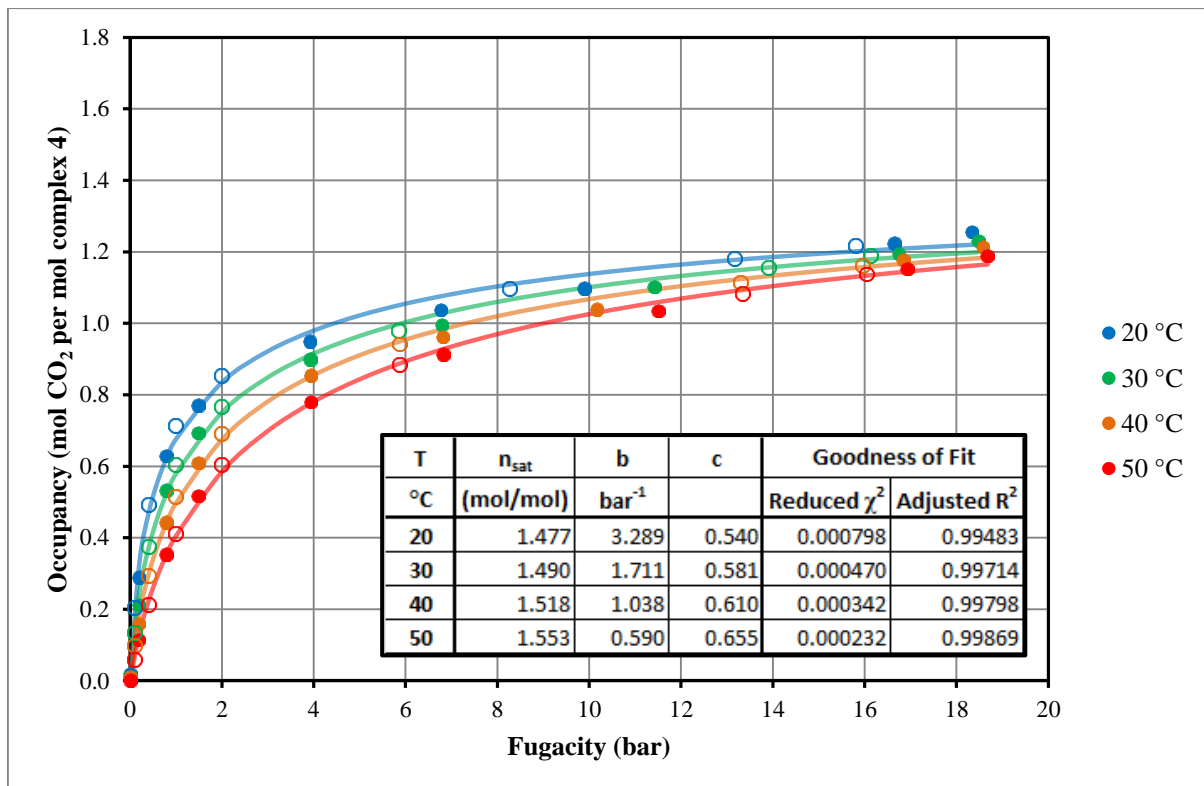


Figure 6.4: Isotherm plots of carbon dioxide adsorption (filled circles) and desorption (open circles) on compound 4. Solid lines represent fits of the Tóth equation to the individual isotherms ($N = 16$ in each case).

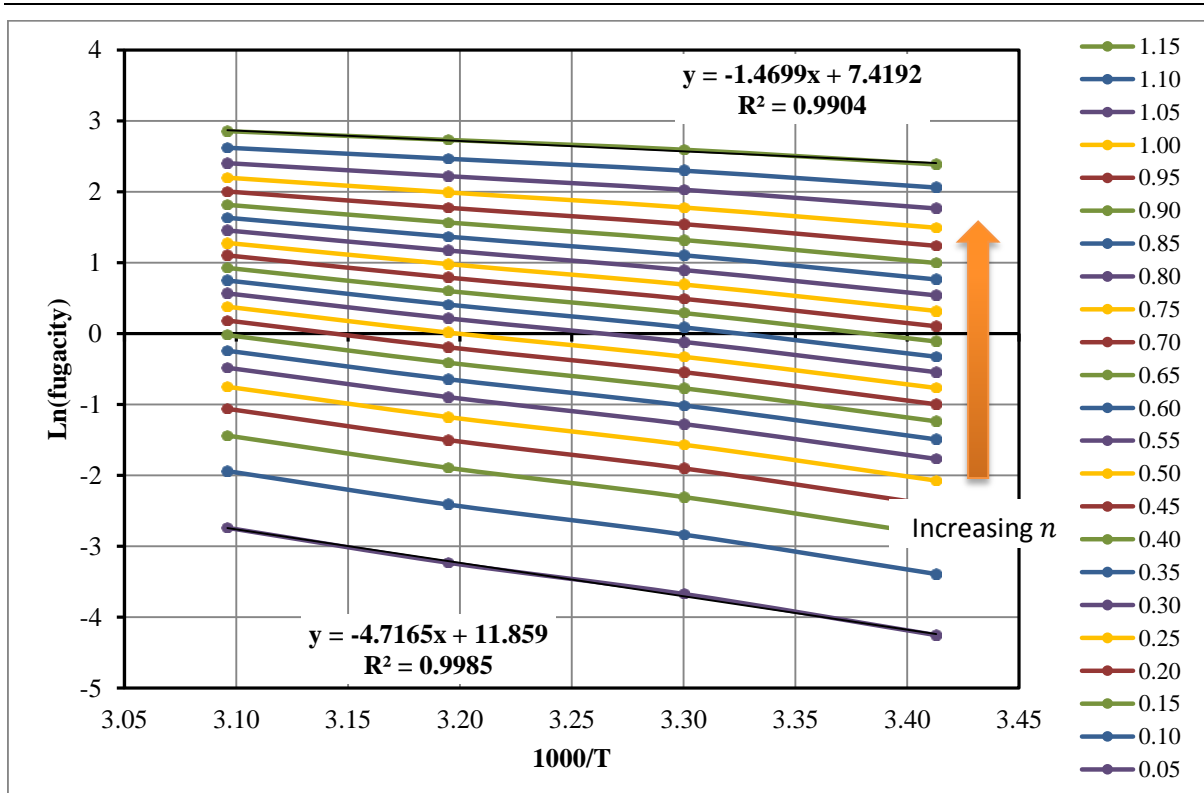


Figure 6.5: Plots of $\ln P$ versus $1/T$ for specific occupancies for the CO_2 sorption data of compound 4 fitted to the Tóth equation. The coefficient of determination of the linear fits to the graphs of occupancies 0.05 and 1.15 are also shown.

Chapter 6: Adsorption techniques and methodologies

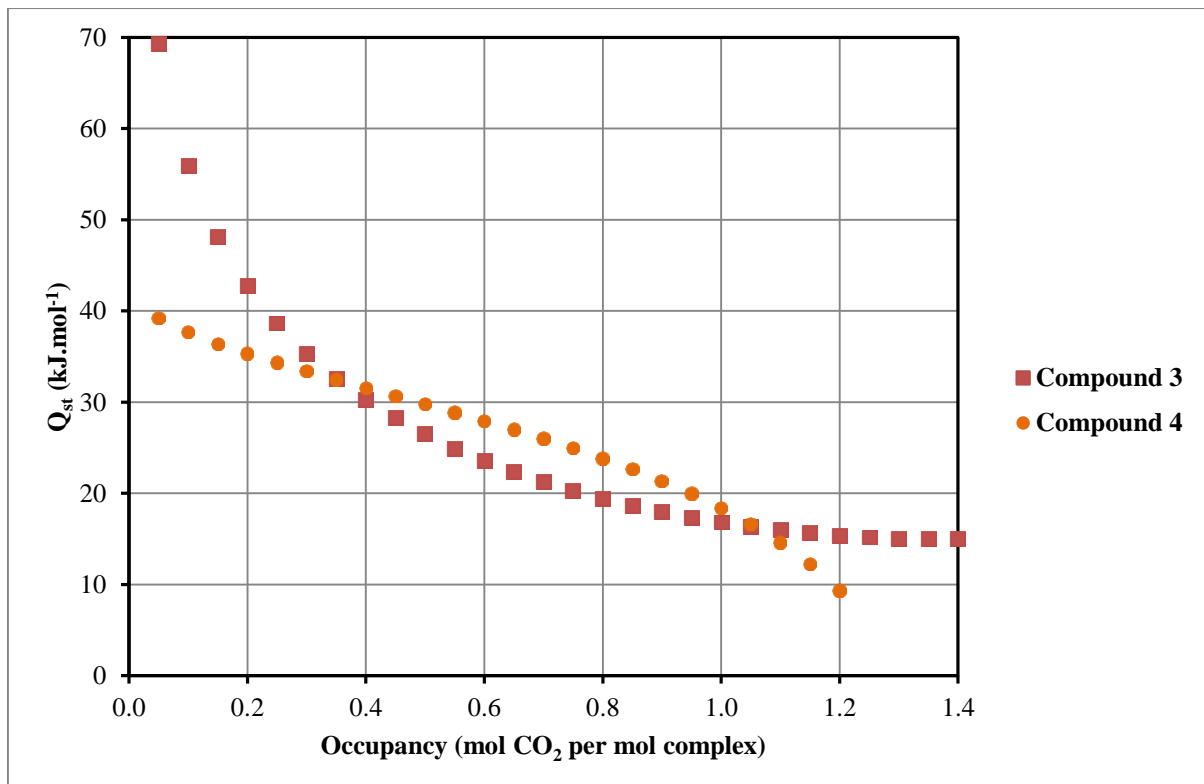


Figure 6.6: Isosteric heat of CO₂ adsorption by compounds **3** and **4** calculated through the graphical interpolation method. The adsorption data of compound **3** were fitted according to the Sips equation, while the sorption data of compound **4** were fitted to the Tóth equation.

From Figure 6.6 it can be seen that the Q_{st} profile of compound **3** exhibits asymptotic behavior. This makes a comparison of the Q_{st} value at zero loading challenging. Application of other isotherm equations (see Section A.4) yielded similar profiles.

To avoid the cumbersome graphical interpolation method, the affinity parameter can be assumed to follow an Arrhenius relationship:¹⁸

$$b = b_0 \exp\left(\frac{E}{RT}\right) \quad 6.25$$

where E is related to the enthalpy of adsorption and b_0 to the entropy of adsorption.^{6a} By incorporating the Arrhenius relationship into an isotherm equation, global fits over the entire temperature range can be carried out. Then, by solving the temperature dependent isotherm equation, the isosteric heat of adsorption as a function of occupancy can be obtained directly. In this work the temperature dependent dual-site Langmuir equation of Mason *et al.*¹⁹ and the commonly applied virial-type isotherm equation²⁰ were employed to perform global fits to adsorption data. These equations were chosen as both give analytical expressions for Q_{st} as a function of occupancy.

Chapter 6: Adsorption techniques and methodologies

6.4.2 Temperature-dependent dual-site Langmuir (dsL) adsorption equation

The temperature-dependent dsL equation is an extension of the single-site Langmuir equation given in Eq. 6.3 that allows for a heterogeneous adsorbent surface with two distinct adsorption sites:

$$n = \frac{n_{sat,1}b_1P}{1 + b_1P} + \frac{n_{sat,2}b_2P}{1 + b_2P} \quad 6.26$$

Introduction of the Arrhenius relationship (Eq. 6.25) gives the temperature dependent dsL equation:¹⁹

$$n = \frac{n_{sat,1}b_{0,1}\exp\left(\frac{E_1}{RT}\right)P}{1 + b_{0,1}\exp\left(\frac{E_1}{RT}\right)P} + \frac{n_{sat,2}b_{0,2}\exp\left(\frac{E_2}{RT}\right)P}{1 + b_{0,2}\exp\left(\frac{E_2}{RT}\right)P} \quad 6.27$$

where parameters E_1 and E_2 are related to the enthalpy of adsorption of the adsorption sites 1 and 2, respectively. This enables the simultaneous fitting of all adsorption data to yield one set of parameters for the entire temperature range investigated. In order to determine Q_{st} using the Clausius-Clapeyron approximation (Eq. 6.19) an expression for $\ln P$ is required. Rewriting Eq. 6.26 as

$$(n_{sat,1} + n_{sat,2} - n)b_1b_2P^2 + [(n_{sat,1} - n)b_1 + (n_{sat,2} - n)b_2]P - n = 0 \quad 6.28$$

and setting

$$\alpha = (n_{sat,1} + n_{sat,2} - n)b_1b_2 \quad 6.29$$

$$\beta = (n_{sat,1} - n)b_1 + (n_{sat,2} - n)b_2$$

the quadratic equation can be solved

$$P = \frac{\sqrt{\beta^2 + 4\alpha n} - \beta}{2\alpha} \quad 6.30$$

to yield an analytical expression for $\ln P$:

$$\ln P = \ln(\gamma - \beta) - \ln(2\alpha) \quad 6.31$$

where $\gamma = \sqrt{\beta^2 + 4\alpha n}$.

Chapter 6: Adsorption techniques and methodologies

The derivative necessary to calculate Q_{st} can now be obtained:¹⁹

$$\left(\frac{\partial \ln P}{\partial T}\right)_n = \frac{1}{\gamma - \beta} \left[\frac{1}{\gamma} \left(\beta \frac{\partial \beta}{\partial T} + 2n \frac{\partial \alpha}{\partial T} \right) - \frac{\partial \beta}{\partial T} \right] - \frac{1}{\alpha} \frac{\partial \alpha}{\partial T} \quad 6.32$$

with

$$\begin{aligned} \frac{\partial}{\partial T} \alpha &= b_{0,1} b_{0,2} (n - n_{sat,1} - n_{sat,2}) \frac{E_1 + E_2}{RT^2} \exp\left(\frac{E_1 + E_2}{RT}\right) \\ \frac{\partial}{\partial T} \beta &= b_{0,1} (n - n_{sat,1}) \frac{E_1}{RT^2} \exp\left(\frac{E_1}{RT}\right) + b_{0,2} (n - n_{sat,2}) \frac{E_2}{RT^2} \exp\left(\frac{E_2}{RT}\right) \end{aligned} \quad 6.33$$

The temperature invariance of Q_{st} was verified for interpolation within the temperature range investigated (293 to 323 K) with the Q_{st} values reported for $T = 298$ K. Note that in the simultaneous regression fit to all isotherms the thermal behavior of the adsorbate is included and fitting results should be extrapolated with caution.²¹

6.4.3 The virial-type isotherm equation

The virial isotherm equation was derived by Czepirski and Jageillo.²² By rewriting the Clausius-Clapeyron relation in the following equivalent form:

$$Q_{st} = RT^2 \left(\frac{\partial \ln P}{\partial T} \right)_n = -R \left[\frac{\partial \ln P}{\partial (1/T)} \right]_n \quad 6.34$$

they defined the temperature invariant function $g(n)$ as

$$\left[\frac{\partial \ln P}{\partial (1/T)} \right]_n = g(n) \quad 6.35$$

Integrating Eq. 6.35 twice gives the general relationship

$$\ln P = g(n)/T + f(n) \quad 6.36$$

where $g(n)$ and $f(n)$ are temperature-invariant functions dependent only on the amount adsorbed. Without prior knowledge of the analytical forms of these functions, they are estimated as polynomials of n and Eq. 6.36 assumes the following form:

$$\ln P = \ln n + \frac{1}{T} \sum_{i=0}^k a_i n^i + \sum_{i=0}^l b_i n^i \quad 6.37$$

Chapter 6: Adsorption techniques and methodologies

The expansion order of both functions is arbitrary and k is not necessarily equal to, but usually larger than l . In the spirit of Occam's razor, the values of k and l are chosen when the addition of more variables is deemed statistically insignificant. The analytical expression for isosteric heat of adsorption as a function of occupancy is then given by $-Rg(n)$, or

$$Q_{st}(n) = -R \sum_{i=0}^k a_i n^i \quad 6.38$$

6.5 Global fits to gravimetric data for CO₂ sorption on 3 and 4

The gravimetric CO₂ adsorption isotherms of compound **3** were fitted simultaneously by the temperature dependent dsL and virial isotherm equations to yield the parameters shown in Figure 6.7, while the fits to sorption isotherms of compound **4** are presented in Figure 6.8. Note that one set of fitting parameters for each of the two global fitting equations was used to plot the temperature specific colored lines in these figures.

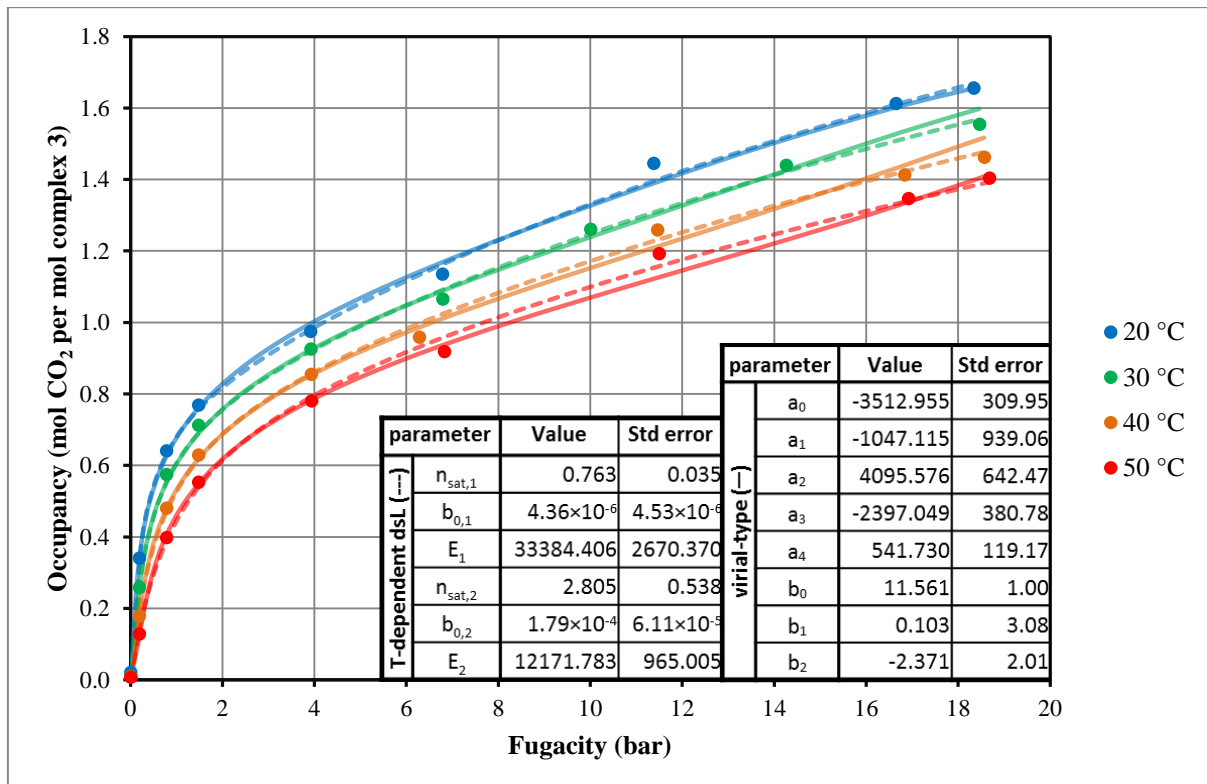


Figure 6.7: Isotherm plots of CO₂ adsorption on compound **3** (filled circles). The dashed and solid lines represent the global fit to all adsorption data by the temperature dependent dsL ($N = 36$, $R_{adj}^2 = 0.99836$, $\chi^2 = 4.37 \times 10^{-4}$) and virial isotherm equations ($N = 36$, $R_{adj}^2 = 0.99871$, $\chi^2 = 6.98 \times 10^{-3}$), respectively. The data and fit-equation plots (one set of parameters for each of the two models) are colored according to temperature.

Chapter 6: Adsorption techniques and methodologies

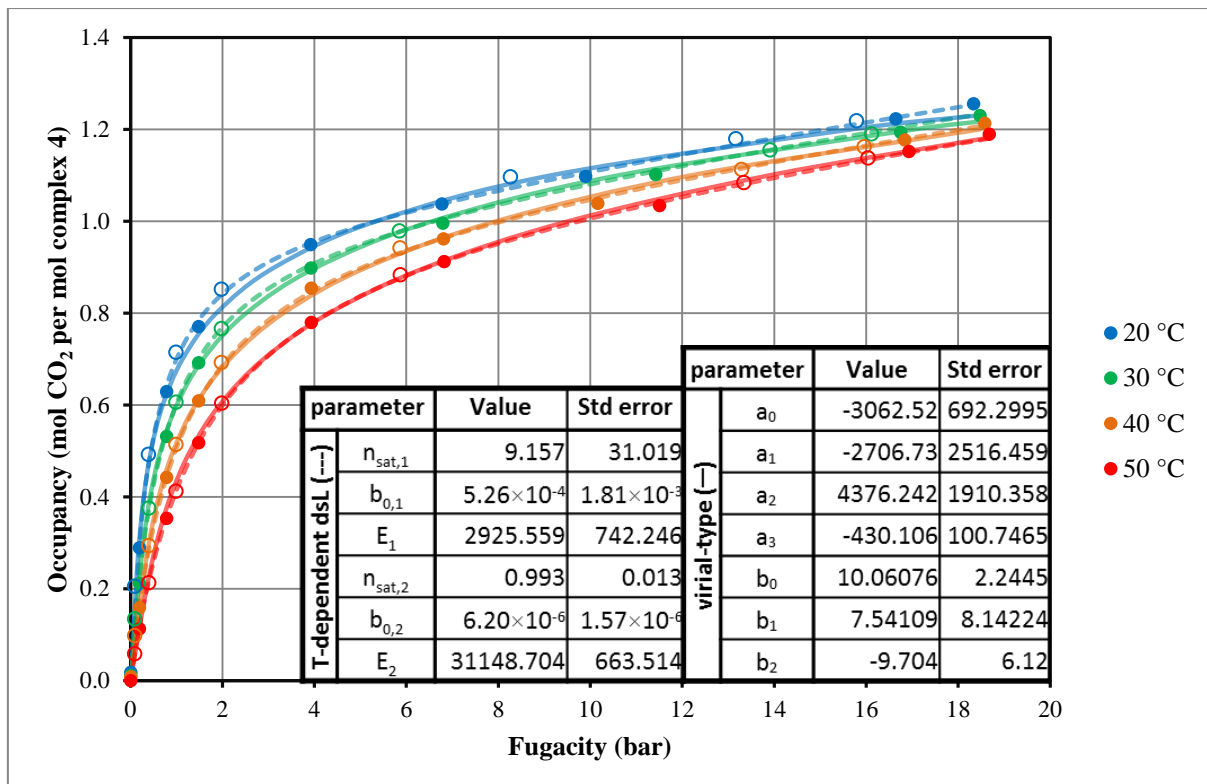


Figure 6.8: Isotherm plots of CO_2 adsorption (full circles) and desorption (open circles) on compound **4**. Dashed lines represent the temperature dependent dsL equation, which was globally fitted to all the sorption data ($N = 64$, $R^2_{\text{adj}} = 0.99946$, $\chi^2 = 8.85 \times 10^{-5}$), while the parameters obtained by a fit of the virial isotherm equation to the 30 °C and 40 °C sorption data ($N = 32$, $R^2_{\text{adj}} = 0.99881$, $\chi^2 = 5.30 \times 10^{-3}$) were used to plot the solid lines. Data and fit-equation results are colored according to temperature.

6.6 Discussion

The occupancy dependent Q_{st} profiles calculated from Eqs. 6.32 and 6.38 for the temperature dependent dsL and virial-type isotherm equations, respectively, are shown in Figure 6.9 for compounds **3** and **4**, along with the volumetric SIT (where $Q_{st} = -\Delta H_{ad}^0$) and graphical interpolation Q_{st} profiles obtained in Sections 6.3 and 6.4.1, respectively. It can be seen that the temperature-dependent dsL equation (—) smoothly steps from heterogeneous site 1 to site 2, while the virial isotherm equation (—) echoes this step in a continuous fashion. For compound **4** this step is not yet completed in the experimental pressure range considered.

The limiting Q_{st} value at zero loading can be obtained directly from the virial isotherm equation by $\lim_{n \rightarrow 0} Q_{st} = -Ra_0$ to yield 29.2 kJ.mol⁻¹ for compound **3** and 25.5 kJ.mol⁻¹ for compound **4**. These values are within the expected range for CO_2 adsorption on microporous materials.²³ From Figure 6.9 it can be seen that Q_{st}^3 is initially predicted to be $> Q_{st}^4$ by all gravimetric sorption data fit results. This infers the presence of stronger host-guest and/or guest-guest interactions in compound **3** than in compound **4**. A closed-shell interaction with the chloride anions in these compounds could be responsible for this discrepancy since the anions point into the one-dimensional columns formed by stacked metallocyclic complexes of compound **3**, and outward from the walls of the columns similarly formed by stacked metallocycles of compound **4**. This is illustrated in Figure 6.10.

Chapter 6: Adsorption techniques and methodologies

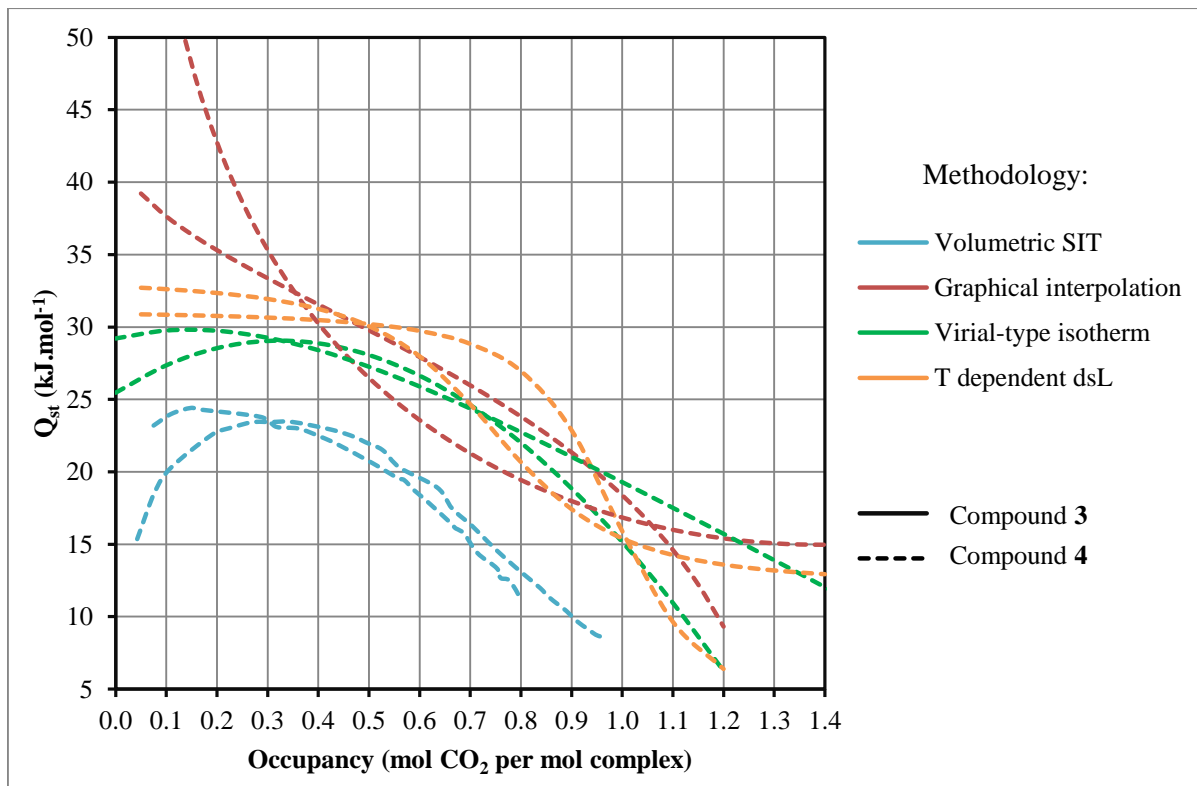


Figure 6.9: Comparison of Q_{st} profiles determined through the methodologies discussed in this chapter. Thermodynamic data for CO₂ adsorption previously obtained using a volumetric SIT device¹⁰ (with — representing $Q_{st} = -\Delta H_{ad}^0$) is compared to results from fitting various equations to conventional gravimetric CO₂ sorption data for compounds 3 (—) and 4 (---). A comparison of the profiles obtained by graphical interpolation of gravimetric sorption data is given in Figure 6.6.

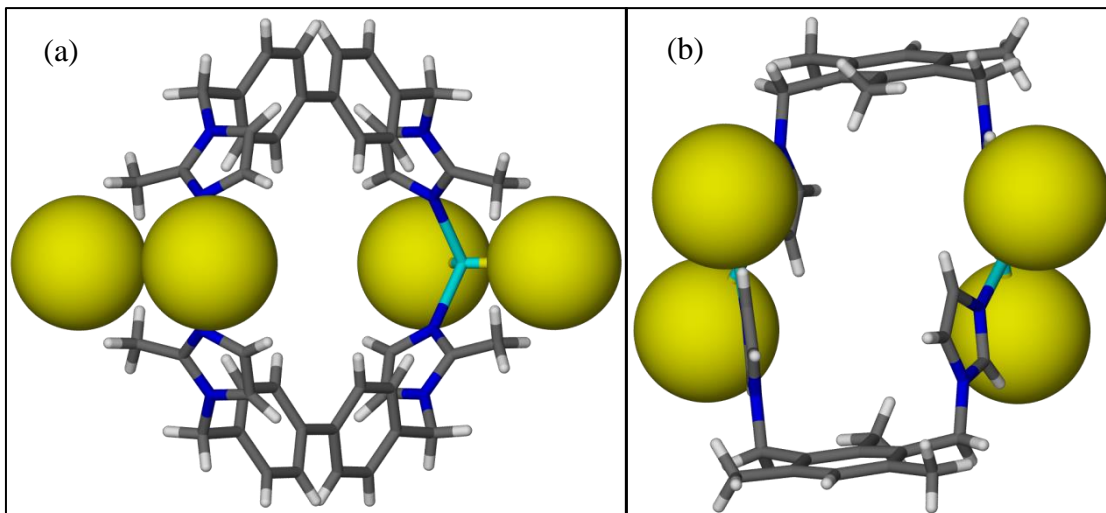


Figure 6.10: Comparison of columns formed along [001] and [100] by stacked metallocycle complexes 3 (a) and 4 (b), respectively, to illustrate inward and outward protrusion of the chloride anions (shown in van der Waals representation).

Chapter 6: Adsorption techniques and methodologies

As discussed in Section 3.2.3 (*cf.* Figures 3.5 and 3.7), a substantial structural adjustment takes place upon desolvation of **4_{MeOH·H₂O}** (with voids of 142 Å³) to yield **4_{apo}** (with voids of 107 Å³). This is in contrast to the more subtle reduction in void volume (from 124 Å³ to 118 Å³) upon evacuation of **3_{MeOH}** to yield **3_{apo}**. A larger energy penalty in **4** than in **3** upon expansion of the host to accommodate guest molecules (reverse of the desolvation process) could also contribute to the initial order of Q_{st} profiles, $Q_{st}^3 > Q_{st}^4$, observed in Figure 6.9. In order to explain the opposite initial Q_{st} profile-order obtained by the volumetric SIT device, the aforementioned framework adjustment of compound **4** can be thought of as taking place in a continuous fashion during the isochoric temperature ramp mode of operation of the device. This is in contrast to the isothermal equilibration period at a specific pressure allowed for in the conventional gravimetric instrument.

A switch in the Q_{st} orders to $Q_{st}^3 < Q_{st}^4$ is observed in Figure 6.9 in the range $0.5 < n < 1.0$ and $0.3 < n < 0.7$ for the temperature dependent dSL and virial isotherm equations, respectively. This is rationalized as follows. After the initial high energy penalty of opening the host **4** structure, its resulting larger voids reduce the effect of guest-guest steric repulsion. Then, for the fit results to gravimetric sorption data, the profile order switches back to $Q_{st}^3 > Q_{st}^4$, while this order is found in the case of results from the volumetric SIT device for $n > 0.3$. The larger pores of compound **3** render its uptake of CO₂ still incomplete at 20 bar, as is evident from Figure 6.3. In an *in situ* controlled 10 bar pressure single-crystal X-ray diffraction study at 233 K, Jacobs could model two CO₂ guest molecules within the host **3** complex, albeit that they are highly disordered.¹² Again, a different experimental set-up was used in that a single crystal of **3_{apo}** was exposed to high pressure CO₂ overnight. Recall that a maximum occupancy of one, as found by a fit of the Sips equation, was used in the determination of thermodynamic parameters from data of the volumetric SIT device (*cf.* Section 6.3).

Although the findings of this study are promising, it can be concluded that due to the unique modes of operation, a more thorough study is required of the novel volumetric SIT device's application to a wider range of materials. Such an evaluation should be conducted in the same manner presented in this study, and it should additionally substantiated with theoretical predictions.

6.7 Summary

Here a brief introduction to different adsorption isotherm models to describe physisorption process is presented, followed by a discussion of the thermodynamics of such a reaction. Carbon dioxide adsorption isotherms and thermodynamic parameters obtained by the volumetric SIT device are presented in Section 6.3. A description of the isosteric heat of adsorption and the graphical interpolation method, as applied to gravimetric CO₂ sorption on compounds **3** and **4**, are presented next. A summary is then given of the derivations of the temperature dependent dual-site Langmuir (Section 6.4.2) and virial-type isotherm (Section 6.4.3) equations that allow for global fitting to all adsorption isotherms and have analytical expressions for Q_{st} as a function of occupancy. Resulting Q_{st} profiles are discussed in Section 6.6 and rational structural reasons are given for the observed trends.

Chapter 6: Adsorption techniques and methodologies

6.8 References

1. Sing, K.S.W.; Everett, D.H.; Haul, R.A.W.; Moscou, L.; Pierotti, R.A.; Rouquerol, J.; Siemieniewska, T., *Pure Appl. Chem.* **1985**, *57*, 603.
2. Langmuir, I., *J. Am. Chem. Soc.* **1918**, *40*, 1361.
3. Freundlich, H., *Z. Phys. Chem.* **1906**, *57*, 385.
4. Sips, R., *J. Chem. Phys.* **1948**, *16*, 490.
5. Tóth, J., *Acta Chim.* **1971**, *69*, 311.
6. (a) Sharpe, J.E.; Bimbo, N.; Ting, V.P.; Burrows, A.D.; Jiang, D.; Mays, T.J., *Adsorption* **2013**, *19*, 643; (b) Bimbo, N.; Ting, V.P.; Sharpe, J.E.; Mays, T.J., *Colloids Surf., A* **2013**, *437*, 113; (c) Bimbo, N.; Sharpe, J.E.; Ting, V.P.; Noguera-Diaz, A.; Mays, T.J., *Adsorption* **2014**, *20*, 373.
7. (a) Stevenson, K.J., *J. Am. Chem. Soc.* **2011**, *133*, 5621; (b) Seifert, E., *J. Chem. Inf. Model.* **2014**, *54*, 1552.
8. Engel, T.; Reid, P., *Thermodynamics, Statistical Thermodynamics, & Kinetics*. Pearson: Upper Saddle River, NJ, **2010**.
9. Roque-Malherbe, R.M.A., *Adsorption and Diffusion in Nanoporous Materials*. CRC Press: USA, **2007**.
10. Marais, C.G. MSc thesis, *Thermodynamics and Kinetics of Sorption*; Stellenbosch University, **2008**.
11. Atwood, J.L.; Barbour, L.J.; Thallapally, P.K.; Wirsig, T.B., *Chem. Commun.* **2005**, 51.
12. Jacobs, T. PhD thesis, *Self-assembly of new porous materials*; Stellenbosch University, **2009**.
13. Lloyd, G.O. MSc thesis, *Crystal Engineering of Porosity*; Stellenbosch University, **2006**.
14. Babarao, R.; Hu, Z.; Jiang, J.; Chempath, S.; Sandler, S.I., *Langmuir* **2007**, *23*, 659.
15. Atkins, P.; de Paula, J., *Atkin's Physical Chemistry*. Seventh Edition.; Oxford University Press: Oxford, **2002**.
16. Eberhart, J.G., *J. Chem. Educ.* **1989**, *66*, 990.
17. Wakefield, C.B.; Phillips, C., *J. Chem. Educ.* **2000**, *77*, 1371.
18. Arrhenius, S., *Z. Phys. Chem.* **1889**, *4*, 226.
19. Mason, J.A.; Sumida, K.; Herm, Z.R.; Krishna, R.; Long, J.R., *Energy Environ. Sci.* **2011**, *4*, 3030.
20. Rowsell, J.L.C.; Yaghi, O.M., *J. Am. Chem. Soc.* **2006**, *128*, 1304.
21. (a) Richard, M.A.; Benard, P.; Chahine, R., *Adsorption* **2009**, *15*, 53; (b) Richard, M.A.; Benard, P.; Chahine, R., *Adsorption* **2009**, *15*, 43.
22. Czepirski, L.; Jagiełło, J., *Chem. Eng. Sci.* **1989**, *44*, 797.
23. Sumida, K.; Rogow, D.L.; Mason, J.A.; McDonald, T.M.; Bloch, E.D.; Herm, Z.R.; Bae, T.-H.; Long, J.R., *Chem. Rev.* **2012**, *112*, 724.

Chapter 7: Concluding remarks

Evaluation of different molecular representations of a tricyclicorthoamide ($C_{11}H_{21}N_3$, labelled **2** in this work), which has a staggered methyl ($\omega_{hccn} = 65^\circ$) in the all-*trans* conformation of the anhydrous form and a nearly eclipsed methyl ($\omega_{hccn} = 8.2^\circ$) in the trihydrate form (**2**·3H₂O), revealed that cooperative effects enhance the strength of the C-H···O interaction responsible for the eclipsed conformation. At the B97D/D95 level of theory, for example, the minimal, medium and comprehensive models' (see Figure A.3) barriers to rotation of the methyl group (ΔE_{rot}) were calculated to be 2.12, 2.22 and 2.48 kcal.mol⁻¹, respectively. Since non-hydrogen atoms were kept frozen in their crystallographic positions, no zero-point energy corrections were included in the results presented in this work.

It was shown in Chapter 4 that the shallow potential energy surface of van der Waals complexes, where dispersion is the dominant intermolecular force, necessitates the use of very fine atom-centred grids for numerical quadrature. This is especially true for functionals of the meta-GGA class where erratic oscillations were observed when coarse grids were employed. It was furthermore shown that even though identical energies are obtained when the counterpoise BSSE-correction scheme is applied *a priori* or *a posteriori* (a consequence of keeping non-hydrogen atoms frozen), there is a clear difference in geometries and the application of cp during geometry optimizations is recommended.

Standard density functionals fail to correctly account for dispersion and several atom-pairwise dispersion correction schemes, wherein a density-independent correction energy is simply added to the DFT energy, $E_{DFT-D} = E_{DFT} + E_{disp}$, were evaluated. Although E_{disp}^{GD3} was found to be most similar in shape and magnitude to the *E*2 correction of MP2 theory ($E_{MP2} = E_{HF} + E2$), only in conjunction with GD2 do functionals yield potential energy profiles that correspond to those of the CCSD level of theory. In Figure 7.1 the constituting energy components of counterpoise (..., left-hand ordinate) and GD2 (---, left-hand ordinate) corrected B97D/TZVP and PBEPBE/TZVP potential energy profiles (●, right-hand ordinate) are both compared to the *E*2 correction (—, left-hand ordinate) at the MP2/6-31+G(d) level of theory with potential energy profile — (right-hand ordinate).

Chapter 7: Concluding remarks

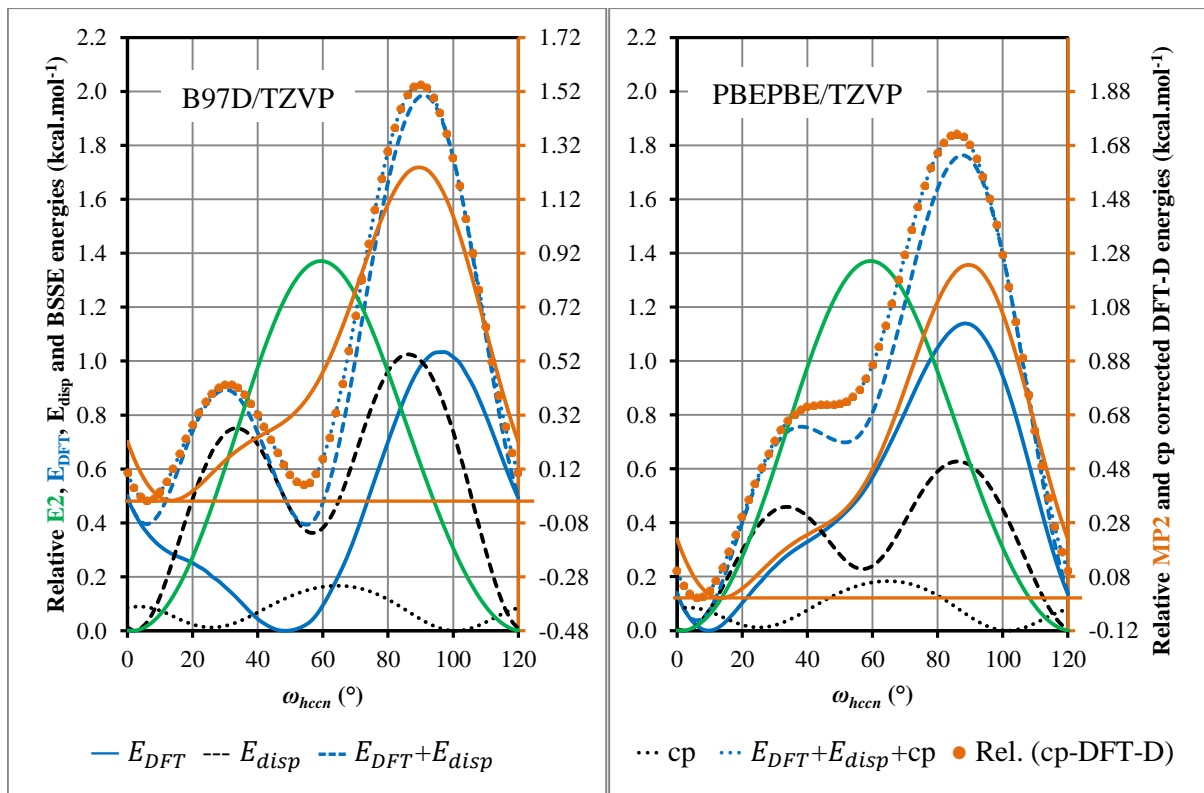


Figure 7.1: Comparison of constituting energy components of counterpoise and GD2 corrected B97D/TZVP and PBEPBE/TZVP potential energy profiles for ω_{hccn} in the minimal model.

It can be seen that the PBEPBE functional already accounts for some dispersion to yield a potential energy profile (—, left-hand ordinate) with the near-eclipsed conformer most stable. The E_{GD2}^{PBEPBE} correction (---) is accordingly much reduced in comparison to E_{GD2}^{B97D} . The TZVP basis set shows a maximum in its BSSE profile of 0.18 kcal.mol⁻¹ at $\omega_{hccn} = 62^\circ$ as estimated by *a priori* application of the counterpoise scheme during hydrogen atom position optimizations.

The insights gained above were used in the assessment of a MOF that displays anisotropic thermal expansion in the temperature range 100–370 K, namely **1_{apo}**. Initially, it was found that Molecular Dynamic simulations in the NTP ensemble with the Dreiding force field employing QEq charges could successfully reproduce the observed trends in the unit cell parameters of **1_{apo}**. A rigid-bond mechanistic model was envisioned in order to reproduce the convergent elongation of the zinc-hydroxide-zinc coordination spiral along the crystallographic *c*-axis. The molecular representation comprises six zinc centres with **L₁** ligands truncated to imidazole and benzoate moieties and a terminating hydroxide was converted into a coordinating water for charge neutrality. During the development of the mechanistic model the three-dimensional movement of all atoms of the coordination spiral were controlled by a single variable, namely *S*, while truncated ligand moieties were moved as the zinc atoms they are coordinated to were displaced upon changing the value of *S*. The stepping variable *S* was defined to elongate the coordination spiral from its 100 K single-crystal X-ray diffraction value to a new value $c_{eff} = c_{100K} + S$.

Chapter 7: Concluding remarks

In order to correspond to the experimental 100–370 K *c*-axis length range of 5.146–5.3287 Å, *S* was stepped from 0.00 to 0.20 Å in 0.05 Å increments. Previously obtained 100, 190, 280 and 370 K crystal structures of **1_{apo}** were evaluated by periodic DFT and a sensible trend in the lattice energy could only be obtained in conjunction with the GD2 dispersion correction, as opposed to when the TS dispersion-correction scheme is applied, or in the absence of dispersion correction. Evaluations of the mechanistic model successfully reproduced the observed energy trend. From this favorable comparison it can be concluded that a concerted change in the coordination sphere of the zinc centre so as to elongate the coordination spiral in the *c* direction, while simultaneously pulling the linking ligands closer together in the *ab* plane is a dominating causative factor contributing to the observed anomalous thermal expansion of **1_{apo}**. Development and application of a similar mechanistic models to reproduce energy changes observed for other compounds that exhibit anomalous thermal expansion will be undertaken in the future.

A volumetric SIT device previously developed for the simplified determination of thermodynamic parameters of adsorption from readily available components was described in Section 3.3. The thermodynamic parameters obtained using the volumetric SIT device were compared to those determined through conventional means by obtaining gravimetric carbon dioxide adsorption isotherms of two metallocyclic compounds, namely **3** and **4**, at 20, 30, 40 and 50 °C. Initially the weight-percentages were converted to occupancies (*n*, mol CO₂/mol complex) and pressures to fugacities through the van der Waals real-gas equation. In order to determine isosteric heats of adsorption from plots of ln *f* vs. 1/*T* according to the graphical interpolation method, the isotherm plots of compounds **3** and **4** were fitted to the Sips and Tóth adsorption equations using least-squares fitting. The so-obtained *Q_{st}*³ plots show asymptotic behavior as the occupancy approach zero, making it difficult to draw conclusions.

Alternatively, the isotherms can be simultaneously fitted to a temperature-dependent isotherm equation. For this study the temperature-dependent dual-site Langmuir and the virial-type isotherm equations were employed since both have analytical expressions for *Q_{st}* as a function of occupancy. This is the first direct comparison of these two equations to the best of the author's knowledge. Results for the compounds investigated show that these two equations complement each other. The temperature-dependent dsL equation predicts a step in the *Q_{st}* as a function of occupancy profile when the more favorable adsorption sites become saturated and the less favored adsorption sites starts to be occupied. The virial isotherm equation reproduces this step in a smooth fashion.

Chapter 7: Concluding remarks

From the virial isotherm equation, $\lim_{n \rightarrow 0} Q_{st}$ values of 29.2 and 25.5 kJ.mol⁻¹ were obtained for compounds **3** and **4**, respectively, indicating that stronger host-guest interactions are present in **3**. The orientation of the chlorine anions inward and outward of the pockets formed by metallocycles of compound **3** and **4**, respectively, could be the reason for this. Evaluation of the strength of these proposed closed-shell interactions will be carried out in the near future. Furthermore, the Q_{st} as a function of occupancy plots obtained from gravimetric data by the different methodologies all initially predict $Q_{st}^3 > Q_{st}^4$, followed by an inversion to $Q_{st}^4 > Q_{st}^3$ in the region $0.4 < n < 0.8$ and a subsequent return to $Q_{st}^3 > Q_{st}^4$ until saturation is reached. This order is ascribed to a greater structural adjustment in compound **4** upon guest uptake (initial $Q_{st}^3 > Q_{st}^4$) followed by stronger attractive guest-guest interactions in the more open **4** (intermediate $Q_{st}^4 > Q_{st}^3$) before steric repulsion invert the order again (final $Q_{st}^3 > Q_{st}^4$). Theoretical evaluation of such framework rearrangements and guest-guest interactions will be undertaken.

Results from the volumetric SIT device, on the other hand, have $Q_{st}^4 > Q_{st}^3$ initially, followed by an inversion to $Q_{st}^3 > Q_{st}^4$ at $n = 0.3$. This is ascribed to the different experimental setups: an isochoric temperature ramp is used in the volumetric SIT device as opposed to an isothermal equilibration period at a specific pressure in the conventional gravimetric instrument. A continuous framework adjustment of compound **4** might therefore be overlooked by the volumetric SIT device. The trends in Q_{st} as a function of occupancy were, however, qualitatively established by the volumetric SIT device. Although the findings of this study are encouraging, a more versatile range of materials needs to be assessed before conclusions regarding the accuracy of the volumetric SIT device can be drawn.

Appendix A.1: Addendum to Chapter 3

Appendix A.

Supplements to discussions in order of appearance in main-text

A.1 Addendum to Chapter 3

A.1.1 Calibration of volumetric SIT device

Calibration of the chamber volumes V_A and V_B was carried out by Marais at 25 °C using low pressure nitrogen gas.¹ It is expected that N₂ exhibits near ideal behavior under these conditions and the ideal gas equation, $PV = nRT$, was thus employed. The calibration procedure is illustrated in Figure A.1.

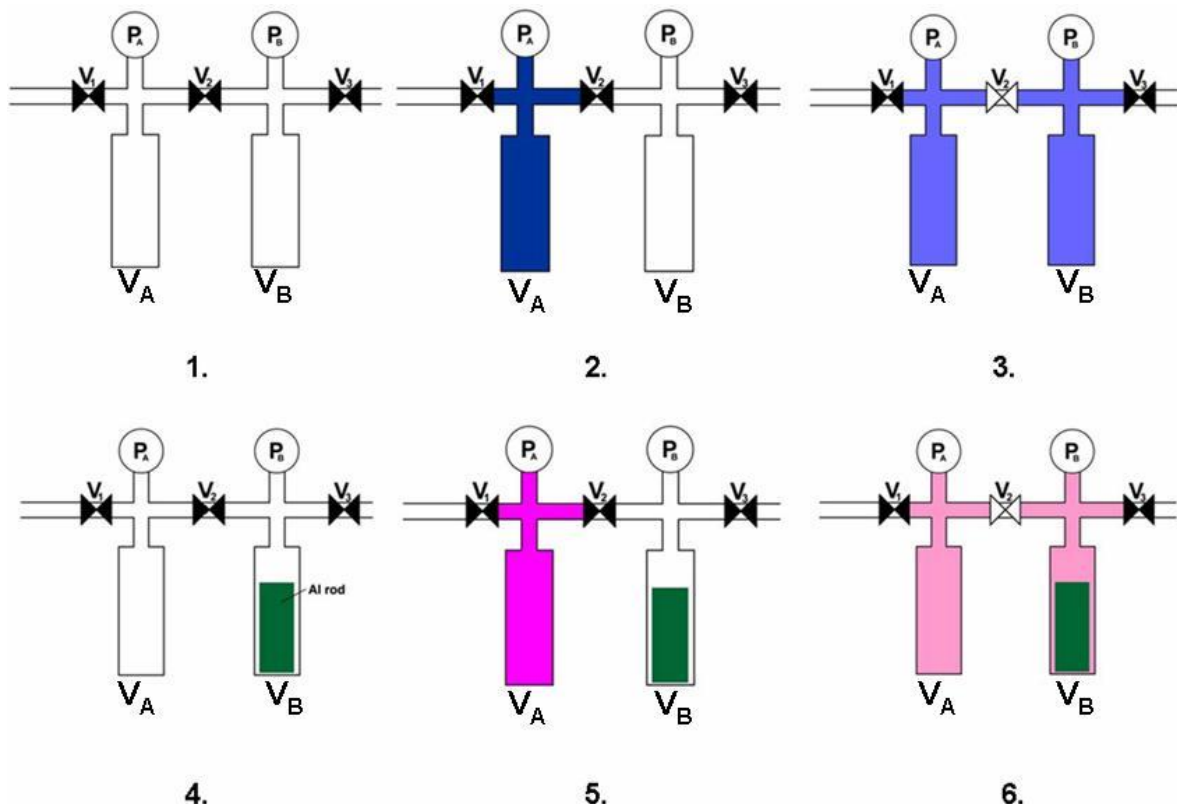


Figure A.1: Schematic representation of the sequence used to calibrate volumes V_A and V_B . In steps 3 and 6 ball valve V_2 is shown to be open. Adapted from Marais.¹

The system is connected to a high pressure nitrogen gas cylinder through valve V_1 and to a vacuum pump through valve V_3 . In step 1 the system is evacuated by opening valves V_2 and V_3 . All valves are subsequently closed and pressure readings P_A and P_B should be close to zero. N₂ gas (n moles, blue in Figure A.1.2) is introduced into chamber A during step 2 by opening and closing valve V_1 . The reading of pressure transducer P_A is recorded as P_1 after the system is allowed to stabilise.

Appendix A.1: Addendum to Chapter 3

In step 3 valve V_2 is opened to allow the n moles of N_2 gas to fill both chambers A and B. The pressure reading, which should be the same for both pressure transducers, is recorded as P_2 . By applying the ideal gas equation the following relationship is obtained (with n and T constant):

$$P_1 V_A = P_2 (V_A + V_B) \quad \text{A.1}$$

which on rearrangement yields

$$\frac{P_1}{P_2} = \frac{V_A + V_B}{V_A} = 1 + \frac{V_B}{V_A} \quad \text{A.2}$$

The nitrogen gas is released from the system and an aluminium rod of known volume V_x (determined from its density and weight) is placed in chamber B. Steps 1 through 3 are repeated as shown in Figure A.1.4-Figure A.1.6. The two pressures are recorded as P_3 (step 5) and P_4 (step 6) for n' moles of N_2 gas (pink in Figure A.1.5). Applying the ideal gas equation results in the following relationship:

$$P_3 V_A = P_4 (V_A + V_B - V_x) \quad \text{A.3}$$

$$\frac{P_3}{P_4} = \frac{V_A + V_B - V_x}{V_A} = 1 + \frac{V_B}{V_A} - \frac{V_x}{V_A} \quad \text{A.4}$$

V_A can now be determined by combining Eqs. A.2 and A.4,

$$\frac{P_1}{P_2} - \frac{P_3}{P_4} = \frac{V_x}{V_A} \quad \text{A.5}$$

followed by determination of V_B by substituting V_A into Eq. A.2.

References

1. Marais, C.G. MSc thesis, *Thermodynamics and Kinetics of Sorption*; Stellenbosch University, **2008**.

Appendix A.1: Addendum to Chapter 3

A.1.2 VB script for determining internal coordinates

Here follows a copy of the Visual Basic script to (i) determine the internal coordinates of hydrogen atoms relative to non-hydrogen atoms and (ii) identify unique coordinates to collectively call their reoccurrences with the same variable. In the lines determining and storing internal coordinates the function `Round(#,n)` is used to reduce the accuracy (for the purpose of correctly identifying the expected number of unique variables and their reoccurrences) by varying the number of decimal places, n, to which a coordinate is specified.

```

Private Sub zMatrix_Click()
    Reading in atom#, type and xyz coordinates
    Dim Atomtype(1000) As String
    Dim AtomCount As Single
    Dim X1(1000) As String
    Dim Y1(1000) As String
    Dim Z1(1000) As String
    Determining Atom2No
    Dim Counter_1 As Single
    Dim Counter_2 As Single
    Dim Counter_3 As Single
    Dim Hcount As Single
    Dim DX(1000) As String
    Dim DY(1000) As String
    Dim DZ(1000) As String
    Dim R(1000) As String
    Dim Argument As Single
    Dim Atom2(1000) As String
    Dim R12(1000) As String
    Dim X2 As Single
    Dim Y2 As Single
    Dim Z2 As Single
    Dim r21X As Single
    Dim r21Y As Single
    Dim r21Z As Single
    Determining Atom3No
    Dim Atom3(1000) As String
    Dim R23 As Single
    Dim X3 As Single
    Dim Y3 As Single
    Dim Z3 As Single
    Dim r23X As Single
    Dim r23Y As Single
    Dim r23Z As Single
    Determining Atom4No
    Dim Atom4(1000) As String
    Dim R34 As Single
    Dim X4 As Single
    Dim Y4 As Single
    Dim Z4 As Single
    Dim r34X As Single
    Dim r34Y As Single
    Dim r34Z As Single
    Determining angle 1-2-3
    Dim A123(1000) As String
    Determining torsion 1-2-3-4
    Dim AX As Single
    Dim AY As Single
    Dim AZ As Single

```

Appendix A.1: Addendum to Chapter 3

```

Dim BX As Single
Dim BY As Single
Dim BZ As Single
Dim RA As Single
Dim RB As Single
Dim Omega(1000) As String
Dim CX As Single
Dim CY As Single
Dim CZ As Single
Dim RC As Single
Dim Sign(1000) As String
Dim W1234(1000) As String
Determining unique bonds
Dim BVar(1000) As String
Dim BVarName(1000) As String
Dim BVarCount(1000) As String
Dim Counter_4 As Single
Dim C_4 As String
Dim HAtomB(1000) As String
Determining unique angles
Dim AVar(1000) As String
Dim AVarName(1000) As String
Dim AVarCount(1000) As String
Dim Counter_5 As Single
Dim C_5 As String
Dim HAtomA(1000) As String
Determining unique torsions
Dim TVar(1000) As String
Dim TVarName(1000) As String
Dim TVarCount(1000) As String
Dim Counter_6 As Single
Dim C_6 As String
Dim HAtomT(1000) As String
#####
Reading in atomNo, type and xyz coordinates
Counter_1 = 1
AtomCount = 0
Do Until Cells(Counter_1, 1) = ""
    Counter_1 = Counter_1 + 1
    AtomCount = AtomCount + 1
    Atomtype(AtomCount) = Cells(Counter_1, 2)
    X1(AtomCount) = Cells(Counter_1, 3)
    Y1(AtomCount) = Cells(Counter_1, 4)
    Z1(AtomCount) = Cells(Counter_1, 5)
Loop
AtomCount = AtomCount - 1
#####
Determining Atom2No
Counter_1 = 0
Hcount = 0
Counter_4 = 0
Counter_5 = 0
Counter_6 = 0
Do Until Counter_1 = AtomCount
    Counter_1 = Counter_1 + 1
    Counter_2 = 0
    If Atomtype(Counter_1) = "H" Then
        Hcount = Hcount + 1
        Do Until Counter_2 = AtomCount
            Counter_2 = Counter_2 + 1
            DX(Counter_2) = X1(Counter_1) - X1(Counter_2)
            DY(Counter_2) = Y1(Counter_1) - Y1(Counter_2)

```

Appendix A.1: Addendum to Chapter 3

```

DZ(Counter_2) = Z1(Counter_1) - Z1(Counter_2)
Argument = DX(Counter_2) ^ 2 + DY(Counter_2) ^ 2 + DZ(Counter_2) ^ 2
R(Counter_2) = Argument ^ 0.5 / 2
If Counter_2 = Counter_1 Then
    R(Counter_2) = 5
ElseIf Atomtype(Counter_2) = "H" Then
    R(Counter_2) = 5
End if
Loop
Counter_2 = 0
Counter_3 = 1
Do Until Counter_2 = AtomCount
    Counter_2 = Counter_2 + 1
    If R(Counter_3) > R(Counter_2) Then
        Counter_3 = Counter_2
    End if
Loop
Atom2(Hcount) = Counter_3
X2 = X1(Counter_3)
Y2 = Y1(Counter_3)
Z2 = Z1(Counter_3)
r21X = DX(Counter_3)
r21Y = DY(Counter_3)
r21Z = DZ(Counter_3)
R12(Hcount) = Round(R(Counter_3) * 2, 3)
#####
Determining Atom3No
Counter_2 = 0
Do Until Counter_2 = AtomCount
    Counter_2 = Counter_2 + 1
    DX(Counter_2) = X1(Counter_2) - X2
    DY(Counter_2) = Y1(Counter_2) - Y2
    DZ(Counter_2) = Z1(Counter_2) - Z2
    Argument = DX(Counter_2) ^ 2 + DY(Counter_2) ^ 2 + DZ(Counter_2) ^ 2
    R(Counter_2) = Argument ^ 0.5 / 2
    If Counter_2 = Atom2(Hcount) Then
        R(Counter_2) = 5
    ElseIf Atomtype(Counter_2) = "H" Then
        R(Counter_2) = 5
    End if
Loop
Counter_2 = 0
Counter_3 = 1
Do Until Counter_2 = AtomCount
    Counter_2 = Counter_2 + 1
    If R(Counter_3) > R(Counter_2) Then
        Counter_3 = Counter_2
    End if
Loop
Atom3(Hcount) = Counter_3
X3 = X1(Counter_3)
Y3 = Y1(Counter_3)
Z3 = Z1(Counter_3)
r23X = DX(Counter_3)
r23Y = DY(Counter_3)
r23Z = DZ(Counter_3)
R23 = R(Counter_3) * 2
#####
Determining Atom4No
Counter_2 = 0
Do Until Counter_2 = AtomCount
    Counter_2 = Counter_2 + 1

```

Appendix A.1: Addendum to Chapter 3

```

DX(Counter_2) = X1(Counter_2) - X3
DY(Counter_2) = Y1(Counter_2) - Y3
DZ(Counter_2) = Z1(Counter_2) - Z3
Argument = DX(Counter_2) ^ 2 + DY(Counter_2) ^ 2 + DZ(Counter_2) ^ 2
R(Counter_2) = Argument ^ 0.5 / 2
If Counter_2 = Atom3(Hcount) Then
    R(Counter_2) = 5
ElseIf Counter_2 = Atom2(Hcount) Then
    R(Counter_2) = 5
ElseIf Atomtype(Counter_2) = "H" Then
    R(Counter_2) = 5
End if
Loop
Counter_2 = 0
Counter_3 = 1
Do Until Counter_2 = AtomCount
    Counter_2 = Counter_2 + 1
    If R(Counter_3) > R(Counter_2) Then
        Counter_3 = Counter_2
    End if
Loop
If Cells(Counter_1 + 1, 12) <> "" Then
    Counter_3 = Cells(Counter_1 + 1, 12)
End if
Atom4(Hcount) = Counter_3
X4 = X1(Counter_3)
Y4 = Y1(Counter_3)
Z4 = Z1(Counter_3)
r34X = DX(Counter_3)
r34Y = DY(Counter_3)
r34Z = DZ(Counter_3)
R34 = R(Counter_3) * 2
#####
Determining angle 1-2-3
Argument = (r21X * r23X + r21Y * r23Y + r21Z * r23Z) / (R12(Hcount) * R23)
A123(Hcount) = Round(WorksheetFunction.Degrees(WorksheetFunction.Acos(Argument)), 3)
#####
Determining torsion 1-2-3-4
AX = r21Y * r23Z - r21Z * r23Y
AY = r21Z * r23X - r21X * r23Z
AZ = r21X * r23Y - r21Y * r23X
BX = r23Z * r34Y - r23Y * r34Z
BY = r23X * r34Z - r23Z * r34X
BZ = r23Y * r34X - r23X * r34Y
RA = (AX ^ 2 + AY ^ 2 + AZ ^ 2) ^ 0.5
RB = (BX ^ 2 + BY ^ 2 + BZ ^ 2) ^ 0.5
Argument = (AX * BX + AY * BY + AZ * BZ) / (RA * RB)
Omega(Hcount) = Round(WorksheetFunction.Degrees(WorksheetFunction.Acos(Argument)), 3)
CX = AY * BZ - AZ * BY
CY = AZ * BX - AX * BZ
CZ = AX * BY - AY * BX
RC = (CX ^ 2 + CY ^ 2 + CZ ^ 2) ^ 0.5
Sign(Hcount) = Round((CX * r23X + CY * r23Y + CZ * r23Z) / (RC * R23), 0)
W1234(Hcount) = Sign(Hcount) * Omega(Hcount)
#####
Identify unique bonds
Counter_2 = -1
Counter_3 = -1
Do Until Counter_2 = Counter_4
    Counter_2 = Counter_2 + 1
    If R12(Hcount) = BVar(Counter_2) Then Exit Do
        Counter_3 = Counter_3 + 1

```

Appendix A.1: Addendum to Chapter 3

```

If Counter_3 = Counter_4 Then
    Counter_4 = Counter_4 + 1
    BVar(Counter_4) = R12(Hcount)
    C_4 = Counter_4
    BVarName(Counter_4) = "B" + C_4
End if
Loop

BVarCount(Counter_2) = BVarCount(Counter_2) + "i"
HAtomB(Hcount) = BVarName(Counter_2)
#####
Identify unique angles
Counter_2 = -1
Counter_3 = -1
Do Until Counter_2 = Counter_5
    Counter_2 = Counter_2 + 1
    If A123(Hcount) = AVar(Counter_2) Then Exit Do
    Counter_3 = Counter_3 + 1
    If Counter_3 = Counter_5 Then
        Counter_5 = Counter_5 + 1
        AVar(Counter_5) = A123(Hcount)
        C_5 = Counter_5
        AVarName(Counter_5) = "A" + C_5
    End if
Loop
AVarCount(Counter_2) = AVarCount(Counter_2) + "i"
HAtomA(Hcount) = AVarName(Counter_2)
#####
Identify unique torsion
Counter_2 = -1
Counter_3 = -1
Do Until Counter_2 = Counter_6
    Counter_2 = Counter_2 + 1
    If Omega(Hcount) = TVar(Counter_2) Then Exit Do
    Counter_3 = Counter_3 + 1
    If Counter_3 = Counter_6 Then
        Counter_6 = Counter_6 + 1
        TVar(Counter_6) = Omega(Hcount)
        C_6 = Counter_6
        TVarName(Counter_6) = "T" + C_6
    End if
Loop
TVarCount(Counter_2) = TVarCount(Counter_2) + "i"
If Sign(Hcount) = -1 Then
    HAtomT(Hcount) = "-" + TVarName(Counter_2)
Else
    HAtomT(Hcount) = TVarName(Counter_2)
End if
End if
Loop
#####
Writing z-matrix with Variables
Counter_1 = 0
Counter_2 = 0
Do Until Counter_1 = AtomCount
    Counter_1 = Counter_1 + 1
    Worksheets("zMatrix").Cells(Counter_1, 9) = Atomtype(Counter_1)
    If Atomtype(Counter_1) = "H" Then
        Counter_2 = Counter_2 + 1
        Worksheets("zMatrix").Cells(Counter_1, 10) = Atom2(Counter_2)
        Worksheets("zMatrix").Cells(Counter_1, 11) = HAtomB(Counter_2)
        Worksheets("zMatrix").Cells(Counter_1, 12) = Atom3(Counter_2)
    End if
End if

```

Appendix A.1: Addendum to Chapter 3

```

Worksheets("zMatrix").Cells(Counter_1, 13) = HAtomA(Counter_2)
Worksheets("zMatrix").Cells(Counter_1, 14) = Atom4(Counter_2)
Worksheets("zMatrix").Cells(Counter_1, 15) = HAtomT(Counter_2)
Else
    Worksheets("zMatrix").Cells(Counter_1, 10) = X1(Counter_1)
    Worksheets("zMatrix").Cells(Counter_1, 11) = Y1(Counter_1)
    Worksheets("zMatrix").Cells(Counter_1, 12) = Z1(Counter_1)
End if
Loop
There are respectively Counter_4, Counter_5 Counter_6 unique R12, A123, T1234 variables
Counter_1 = Counter_1 + 1
Counter_2 = 0
Do Until Counter_2 = Counter_4
    Counter_2 = Counter_2 + 1
    Counter_1 = Counter_1 + 1
    Worksheets("zMatrix").Cells(Counter_1, 9) = BVarName(Counter_2)
    Worksheets("zMatrix").Cells(Counter_1, 10) = BVar(Counter_2)
Loop
Counter_2 = 0
Do Until Counter_2 = Counter_5
    Counter_2 = Counter_2 + 1
    Counter_1 = Counter_1 + 1
    Worksheets("zMatrix").Cells(Counter_1, 9) = AVarName(Counter_2)
    Worksheets("zMatrix").Cells(Counter_1, 10) = AVar(Counter_2)
Loop
Counter_2 = 0
Do Until Counter_2 = Counter_6
    Counter_2 = Counter_2 + 1
    Counter_1 = Counter_1 + 1
    Worksheets("zMatrix").Cells(Counter_1, 9) = TVarName(Counter_2)
    Worksheets("zMatrix").Cells(Counter_1, 10) = TVar(Counter_2)
Loop
End Sub

```

Appendix A.1: Addendum to Chapter 3

A.1.3 Derivation of key equations for mechanistic thermal expansion model

Here the derivations of equations that result in those shown in Section 3.8 are given. For illustrative purposes, Figure 3.16 is repeated below.

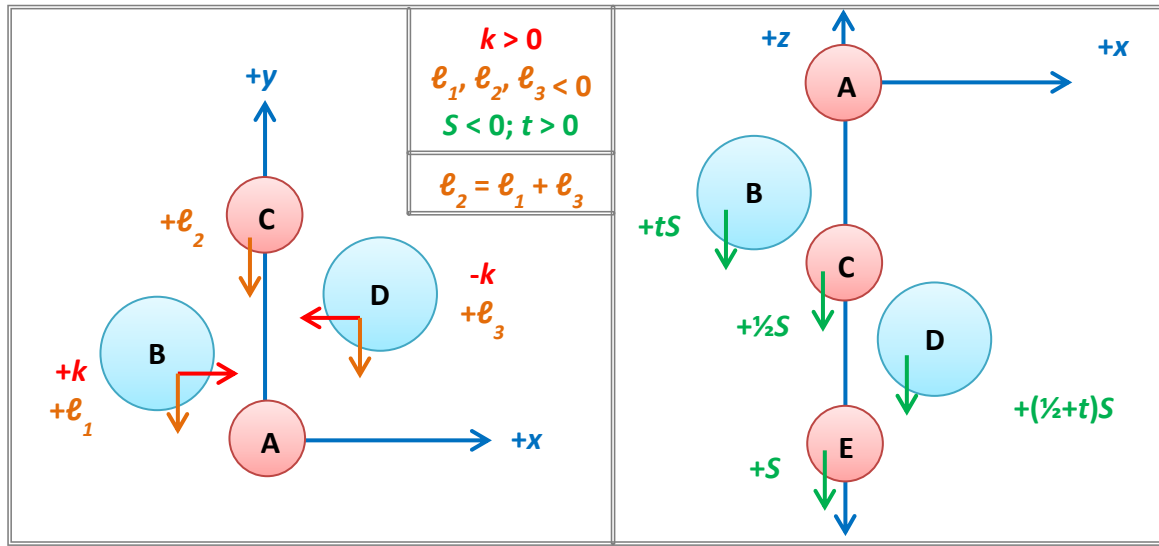


Figure A.2: Repeat of Figure 3.16 that depicts one turn of the coordination spiral in the mechanistic model (Figure 3.15(c)) of $\mathbf{1}_{\text{apo}}$.

In the initial, $S = 0.0$ model derived from the optimized the 100 K crystal structure,

$$R_{AB} = \sqrt{(x_B - x_A)^2 + (y_B - y_A)^2 + (z_B - z_A)^2} \quad \text{A.6}$$

The R_{AB} bond length for the c axis lengthened by S ($c_{\text{eff}} = c_{100K} + S$), is given by

$$R_{AB,\text{eff}} = \sqrt{[(x_B + k) - x_A]^2 + [(y_B + \ell_1) - y_A]^2 + [(z_B + tS) - z_A]^2} \quad \text{A.7}$$

Here, the 100 K-model Cartesian coordinates are stepped by the direction-specific stepping variables of Figure A.2. For the B -group atoms, for example, $(x_B^{\text{eff}}, y_B^{\text{eff}}, z_B^{\text{eff}})$ is specified by $(x_B + k, y_B + \ell_1, z_B + tS)$. Taking the square of Eq. A.7 and simplifying yields

$$\begin{aligned} R_{AB,\text{eff}}^2 &= (x_B + k)^2 - 2(x_B + k)x_A + x_A^2 + (y_B + \ell_1)^2 - 2(y_B + \ell_1)y_A + \\ &\quad y_A^2 + (z_B + tS)^2 - 2z_A(z_B + tS) + z_A^2 \\ &= x_B^2 + 2kx_B + k^2 - 2x_Ax_B - 2kx_A + x_A^2 + y_B^2 + 2\ell_1y_B + \ell_1^2 - \\ &\quad 2y_Ay_B - 2\ell_1y_A + y_A^2 + z_B^2 + 2tSz_B + t^2S^2 - 2z_Az_B - 2tSz_A + z_A^2 \quad \text{A.8} \\ &= (x_B - x_A)^2 + (y_B - y_A)^2 + (z_B - z_A)^2 + k^2 + 2k(x_B - x_A) + \\ &\quad \ell_1^2 + 2\ell_1(y_B - y_A) + t^2S^2 + 2tS(z_B - z_A) \\ &= R_{AB}^2 + k^2 + 2k(x_B - x_A) + \ell_1^2 + 2\ell_1(y_B - y_A) + t^2S^2 + \\ &\quad 2tS(z_B - z_A) \end{aligned}$$

Appendix A.1: Addendum to Chapter 3

The boldface terms are combined to give \mathbf{R}_{AB}^2 with the last line of Eq. A.8 corresponding to Eq. 3.7. Implementing the assumption that all bond lengths remain constant within the temperature range investigated, $R_{AB,eff} = R_{AB}$, yields:

$$k^2 + 2k(x_B - x_A) + \ell_1^2 + 2\ell_1(y_B - y_A) + 2tS(z_B - z_A) + t^2S^2 = 0 \quad \text{A.9}$$

which is a repeat of Eq. 3.8. Similarly, for the R_{BC} bond distance,

$$\begin{aligned} R_{BC,eff}^2 &= [x_C - (x_B + k)]^2 + [(y_C + \ell_2) - (y_B + \ell_1)]^2 + [(z_C + 0.5S) - (z_B + tS)]^2 \\ &= x_C^2 - 2x_C(x_B + k) + (x_B + k)^2 + (y_C + \ell_2)^2 - 2(y_C + \ell_2)(y_B + \ell_1) + (y_B + \ell_1)^2 + (z_C + 0.5S)^2 - 2(z_C + 0.5S)(z_B + tS) + (z_B + tS)^2 \\ &= \mathbf{x}_C^2 - 2\mathbf{x}_C\mathbf{x}_B - 2kx_C + \mathbf{x}_B^2 + 2kx_B + k^2 + \mathbf{y}_C^2 + 2\ell_2y_C + \ell_2^2 - 2\mathbf{y}_C\mathbf{y}_B - 2\ell_1y_C - 2\ell_2y_B - 2\ell_1\ell_2 + \mathbf{y}_B^2 + 2\ell_1y_B + \ell_1^2 + \mathbf{z}_C^2 + Sz_C + 0.25S^2 - 2\mathbf{z}_C\mathbf{z}_B - 2tSz_C - Sz_B - tS^2 + \mathbf{z}_B^2 + 2tSz_B + t^2S^2 \quad \text{A.10} \\ &= (\mathbf{x}_C - \mathbf{x}_B)^2 + (\mathbf{y}_C - \mathbf{y}_B)^2 + (\mathbf{z}_C - \mathbf{z}_B)^2 + k^2 - 2k(x_C - x_B) + \ell_2^2 - 2\ell_1\ell_2 + \ell_1^2 + 2\ell_2(y_C - y_B) - 2\ell_1(y_C - y_B) + S(z_C - z_B) - 2tS(z_C - z_B) + (0.25 - t + t^2)S^2 \\ &= \mathbf{R}_{BC}^2 + k^2 - 2k(x_C - x_B) + (\ell_2 - \ell_1)^2 + 2(\ell_2 - \ell_1)(y_C - y_B) + (1 - 2t)S(z_C - z_B) + (0.5 - t)^2S^2 \end{aligned}$$

Again the boldface terms are combined to give \mathbf{R}_{BC}^2 in the last line which is further reduced by recognizing from Figure A.2 that $\ell_2 - \ell_1 = \ell_3$. Implementing $R_{BC,eff} = R_{BC}$ along with $(1 - 2t) = 2(0.5 - t)$ yields Eq. 3.9:

$$k^2 - 2k(x_C - x_B) + \ell_3^2 + 2\ell_3(y_C - y_B) + (0.5 - t)S[2(z_C - z_B) + (0.5 - t)S] = 0 \quad \text{A.11}$$

which is a repeat of Eq. 3.9. Subsequent equations in Section 3.8 follow from those shown by simple manipulation and will therefore not be expanded on.

Appendix A.2: Addendum to Chapter 4

A.2 Addendum to Chapter 4**A.2.1 Utility of Dummy atoms**

As stated in the footnote on page 78, water molecules were defined relative to each other in a hexameric unit with dummy atoms on the Ow positions of omitted water molecules as shown in Figure A.3. Hydrogen atoms of water molecules were optimized in the hydrogen bonded hexamer, Figure A.3(a). The optimized internal coordinate variables were then transferred to all other models (Figure A.3(b)-(d)) through dummy atoms.

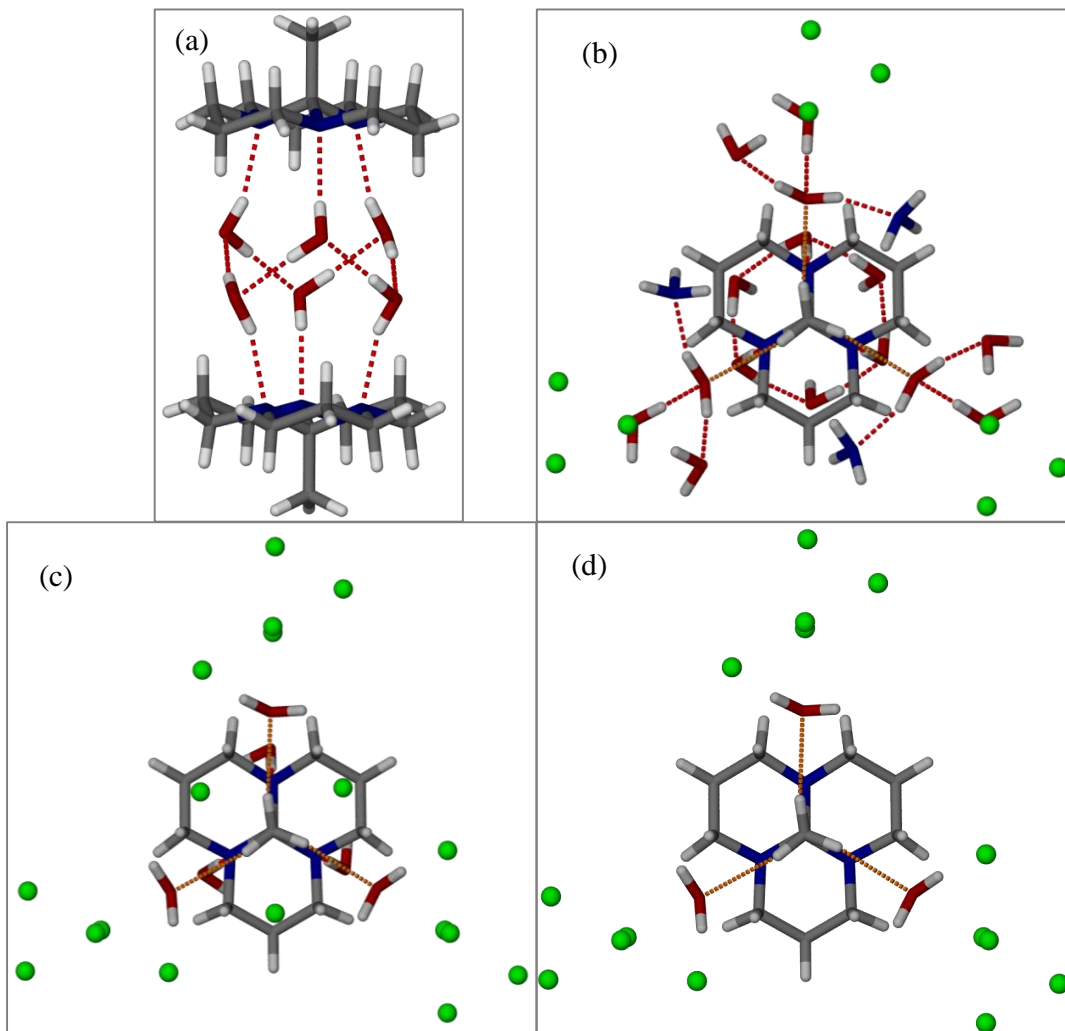


Figure A.3: Depiction of (a) hydrogen bonded water hexamer and (b) comprehensive, (c) medium and (d) minimal models of $\mathbf{2 \cdot 3H_2O}$ with molecular formulas $\mathbf{2 \cdot (H_2O)_6 \cdot 2}$ ($C_{22}H_{54}N_6O_6$, S_6 point-group symmetry 276 electrons), $\mathbf{2 \cdot (H_2O)_6 \cdot \{H_2O \cdot [(H_2O)_2(NH_3)\}_3}$ ($C_{11}H_{60}N_6O_{15}$, C_3 symmetry, 288 electrons), $\mathbf{2 \cdot 6H_2O}$ ($C_{11}H_{33}N_3O_6$, C_3 symmetry, 168 electrons) and $\mathbf{2 \cdot 3H_2O}$ ($C_{11}H_{27}N_3O_3$, C_3 symmetry, 138 electrons), respectively. Dummy atoms are shown as green spheres.

The models shown in Figure A.3 was used in the following sections: the comprehensive model (b) was used in HF (Section 4.4) and DFT (Section 4.5, Section A.2.3) basis set dependence studies; the medium model (c) was used for assessing the effect of integration grid coarseness (M06 functional, Section 4.5.1) and to evaluate the BSSE (B97D functional, Section 4.7); the minimal model (d) was used in CCSD (Section 4.2) and MP2 (Section 4.6) calculations as well as in Section 4.8 where different dispersion corrections to density functionals are evaluated.

Appendix A.2: Addendum to Chapter 4

A.2.2 CCSD investigation

A comparison of the potential energy profile for the ω_{hccn} dihedral angle using the minimal model at the B97D/basis set and CCSD/basis set//B97D/basis set levels of theory is made in Figure A.4. From the figure the 120° periodicity due to the C_3 symmetry of $\mathbf{2}\cdot 3\text{H}_2\text{O}$ is also evident.

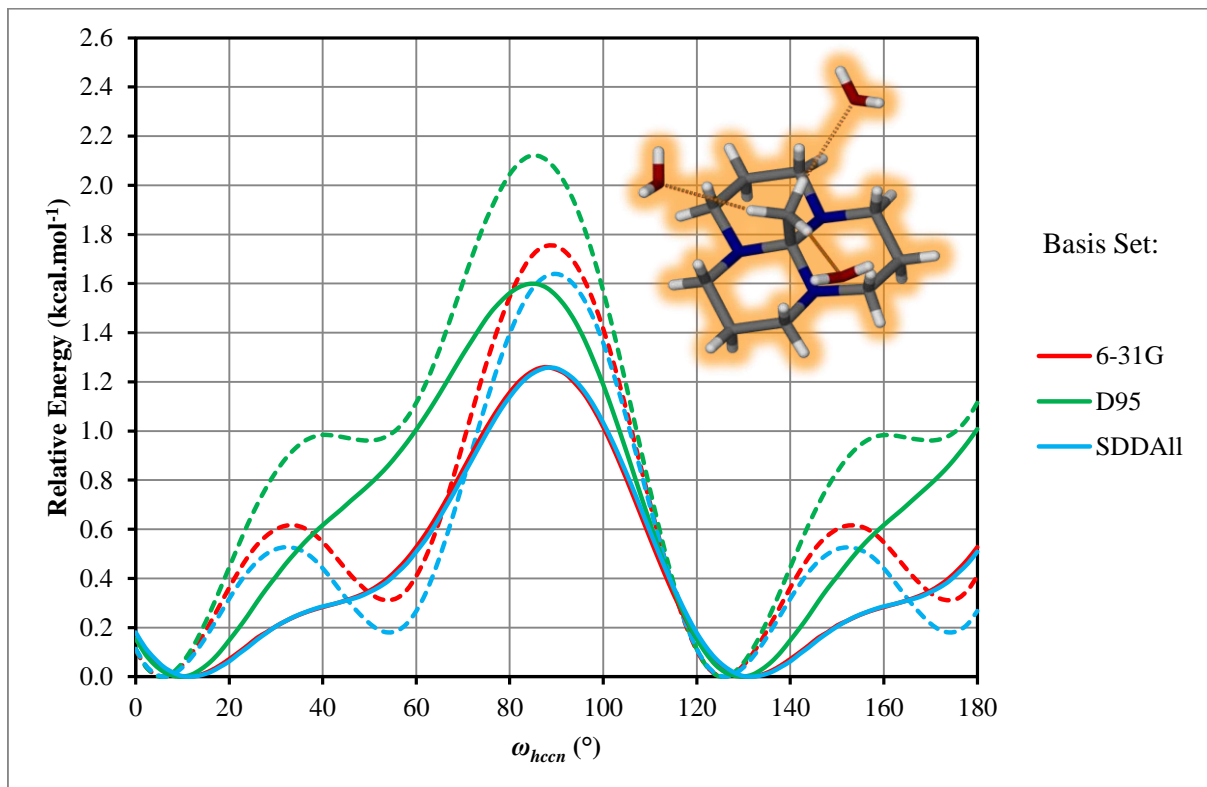


Figure A.4: Relative potential energy profiles for the ω_{hccn} dihedral angle obtained for the B97D functional (---), followed by single point energy calculations at the CCSD level of theory (—). The minimal model of $\mathbf{2}\cdot 3\text{H}_2\text{O}$ that was evaluated (Figure 4.4) is also shown.

Appendix A.2: Addendum to Chapter 4

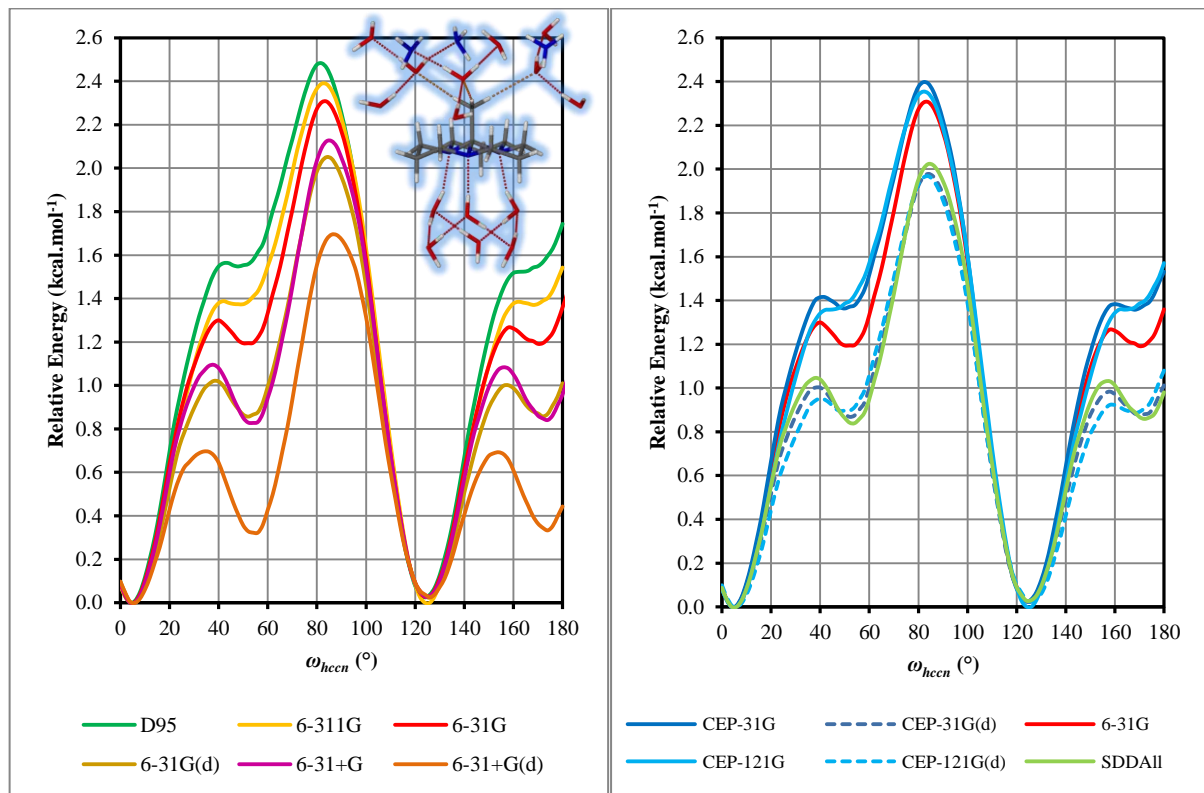
A.2.3 Basis set dependence of potential energy profile for the B97D functional

Figure A.5: Relative potential energy profiles for the ω_{hccn} dihedral angle obtained for the B97D functional in combination with various basis sets. All-electron basis sets are compared on the left and effective core potential basis sets on the right with the 6-31G profile repeated to facilitate comparison. Inset shows the comprehensive model that was evaluated (Figure 4.6) with hydrogen bonds represented by dashed lines.

A comparison between Figure A.5 (comprehensive) and Figure A.4 (minimal model) reveals that the rotation barrier is enhanced in the comprehensive model (*e.g.*, 2.3 kcal. mol^{-1} vs. 1.75 kcal. mol^{-1} for 6-31G), providing support for the suggested strengthening of the C-H \cdots O interaction through cooperative effects. In contrast to the HF case (*cf.* Figure 4.7), augmentation of the CEP basis sets leads to a reduction in the rotation barrier, while the potential energy profile is maintained in Figure A.5. Furthermore, a comparison of the HF/6-31+G(d) (dot-dash line --- of Figure 4.8(c)) and B97D/6-31+G(d) (— in Figure A.5) profiles suggest an enhanced BSSE for the HF method that shows the nearly eclipsed conformer ($\omega_{hccn} \approx 55^\circ$) to be most stable.

Appendix A.2: Addendum to Chapter 4

A.2.4 Integration-grid effects on DFT potential energy profiles

In Figure A.6 the potential energy profiles for ω_{hccn} stepped between 0° and 120° in 2° increments using different density functionals in conjunction with the SDDAll basis set are shown. The default (75,302) and ultrafine (99,590) integration grids of Gaussian09 were evaluated.

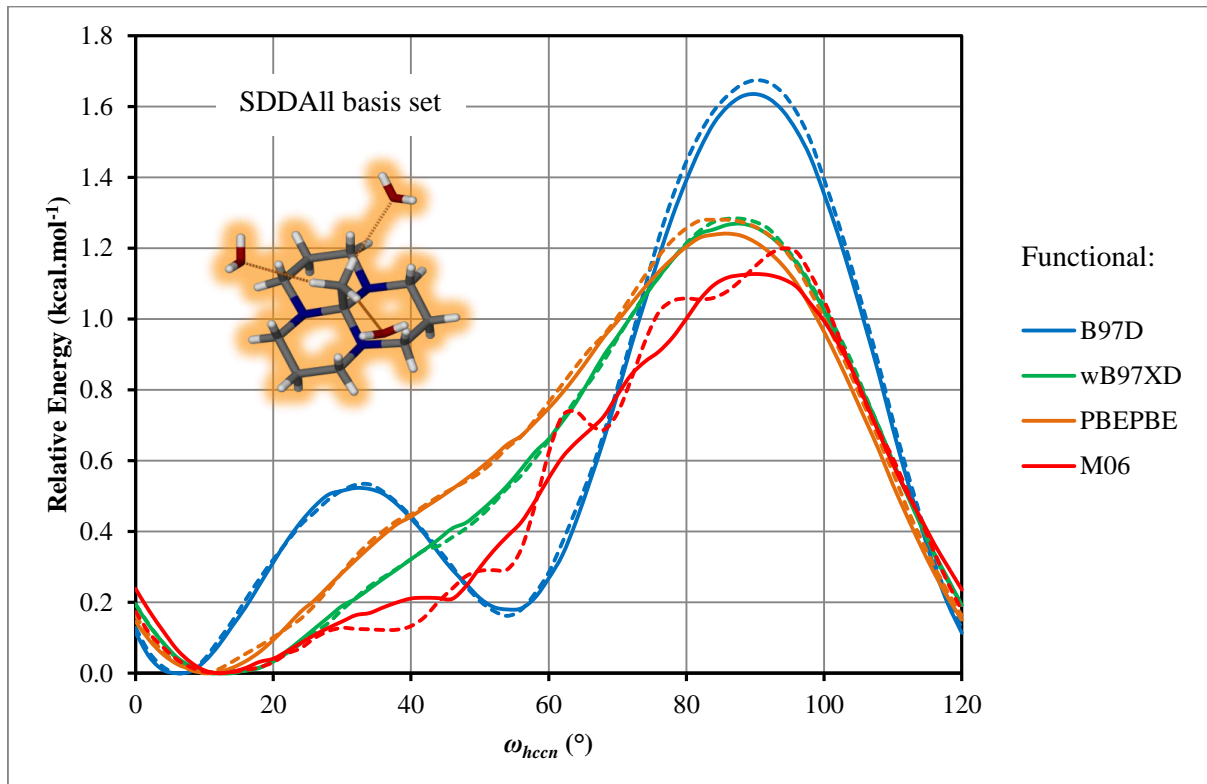


Figure A.6: Comparison of relative potential energy profiles for ω_{hccn} of the minimal model (inset) obtained for different functionals in combination with the SDDAll basis set employing the default (---) and ultrafine (—) integration grids.

It can be seen that the integration-grid coarseness influence the energies of all the evaluated density functionals, making it essential to consistently use the same grid for energy comparisons.

Appendix A.2: Addendum to Chapter 4

A.2.5 The counterpoise correction for BSSE

BSSE originates from the unphysical augmentation of monomer basis sets due to their close proximity in the complex.¹ It is a consequence of using finite-sized basis sets and results in artificial stabilization.² The magnitude of the BSSE can be estimated through the counterpoise scheme of Boys and Bernardi.³ For a complex consisting of n monomers, the BSSE is given by

$$BSSE = \sum_{i=1}^n [E_i(i) - E_{i*}(i)] \quad \text{A.12}$$

where $E_i(i)$ is the energy of monomer i calculated with its basis set alone (*i.e.*, the complex at infinite separation) and $E_{i*}(i)$ represents the energy of monomer i in the basis set of the complex wherein the atom-centred basis sets of the other $n - 1$ monomers are located on *ghost atoms*. Since $E_i(i) > E_{i*}(i)$ due to artificial stabilization (with $|E_i(i)| < |E_{i*}(i)|$), the $BSSE > 0$. The counterpoise corrected energy ($|E_{\text{complex}}^{\text{cp}}| < |E_{\text{complex}}|$) of the complex is then calculated from

$$E_{\text{complex}}^{\text{cp}} = E_{\text{complex}} + BSSE \quad \text{A.13}$$

It is therefore necessary to carry out $2n + 1$ single point calculations in order to obtain $E_{\text{complex}}^{\text{cp}}$. This is depicted in Figure A.7 for the medium model of **2·3H₂O** (Figure 4.2(b) or Figure A.3(c)) that required 15 (single point) energy evaluations of seven fragments per geometry optimization step.

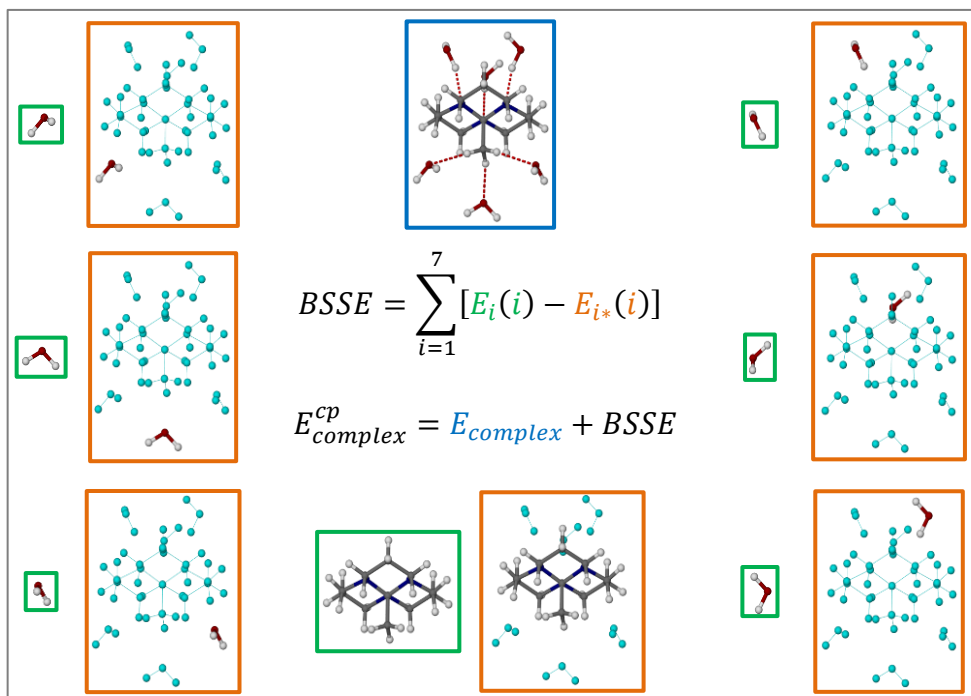


Figure A.7: Illustration of the 15 single point energies required to determine the counterpoise corrected energy of the complex boxed in blue. Molecules are shown in ball-and-stick representation with *ghost atoms* colored cyan.

Appendix A.2: Addendum to Chapter 4

The counterpoise correction is usually applied *a posteriori* to correct the final energy of a complex. Simon *et al.* developed an algorithm that allows application of the counterpoise correction during geometry optimizations to obtain an *a priori* corrected complex energy and geometry.⁴ This algorithm uses the derivatives of $E_{\text{complex}}^{\text{cp}}$ with respect to all internal coordinates to guide the optimizer to a stationary point - where all first derivatives are zero, within a certain threshold.

References

1. Liu, B.; McLean, A.D., *J. Chem. Phys.* **1989**, *91*, 2348.
2. van Duijneveldt, F.B.; van Duijneveldt-van de Rijdt, J.G.C.M.; van Lenthe, J.H., *Chem. Rev.* **1994**, *94*, 1873.
3. Boys, S.F.; Bernardi, F., *Mol. Phys.* **1970**, *19*, 553.
4. Simon, S.; Duran, M.; Dannenberg, J.J., *J. Chem. Phys.* **1996**, *105*, 11024.

A.2.6 BSSE of the minimal model at the MP2 and HF levels of theory

The Hartree-Fock potential energy profiles for ω_{hccn} in the minimal model (Figure 4.4) are shown in Figure A.8. The same basis sets as that of Section 4.6 were employed to allow for comparison to MP2 profiles not cp corrected. Note that the HF profiles of Figure 4.12(c) was deconvoluted from the MP2 energy using $E_{\text{MP2}} = E_{\text{HF}} + E2$.

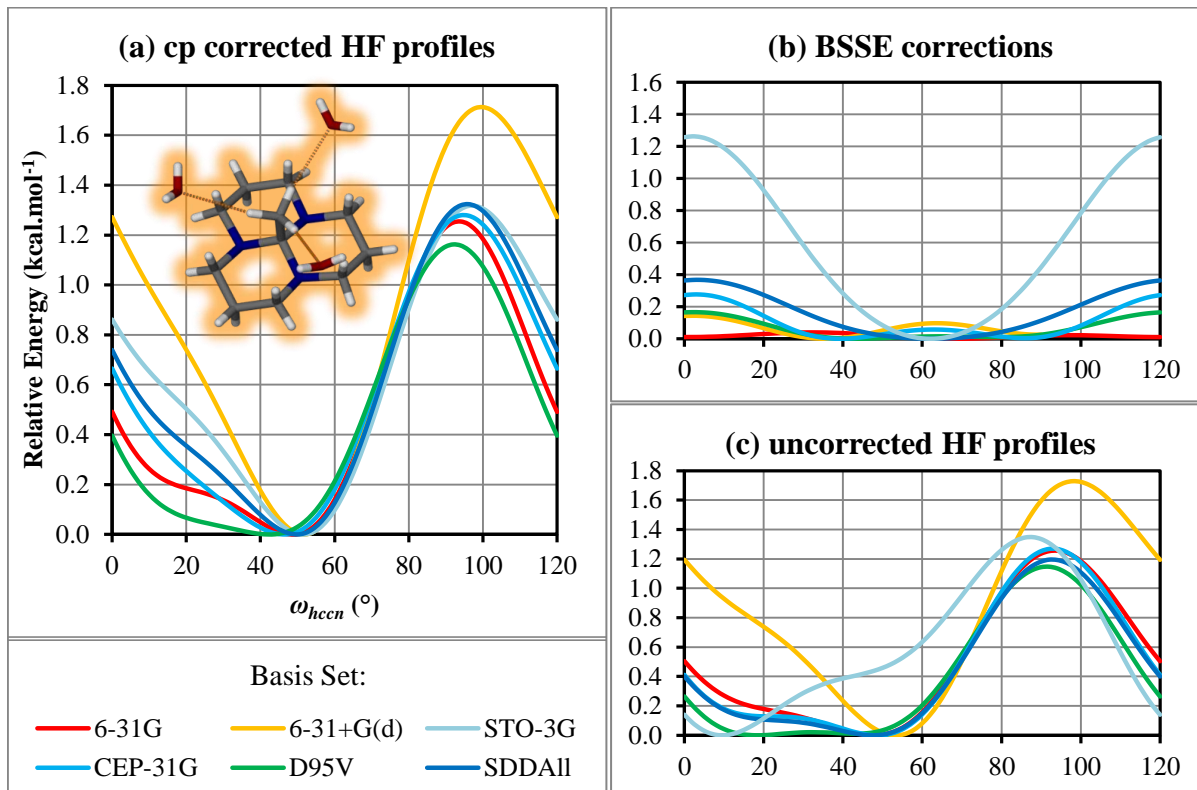


Figure A.8: Comparison of the counterpoise estimated BSSE values (b) to correct the HF profiles of (c) to yield those of (a). The cp scheme was applied *a priori* during hydrogen-atom position optimizations of the model shown.

Appendix A.2: Addendum to Chapter 4

The very small STO-3G basis set shows the largest BSSE, as estimated by the counterpoise scheme (Figure A.8(c)), with its uncorrected potential energy profile uniquely showing the nearly eclipsed conformer to be most stable. However, the *a priori* cp-corrected potential energy profiles of all basis sets show the nearly staggered conformer ($\omega_{hccn} \approx 55^\circ$) to be most stable. A comparison of Figure A.8(c) with results from Section 4.4 again substantiate the idea that the appendage molecules of the comprehensive model strengthen the C-H \cdots O interaction through cooperative polarization effects to yield ω_{hccn} profiles with the nearly eclipsed conformer most stable in Figure 4.7. The basis set dependent barrier to rotation remains in the 1.1 kcal. mol^{-1} to 1.3 kcal. mol^{-1} region except for the 6-31+G(d) basis set (Figure A.8(c), minimal model, — profile) where $\Delta E_{rot} = 1.75$ kcal. mol^{-1} in comparison to 1.30 kcal. mol^{-1} (Figure 4.8(c), comprehensive model, dash dot --- profile).

Results from an MP2 level of theory evaluation of the effects of BSSE on the ω_{hccn} potential energy profile of the minimal model are shown in Figure A.9. The counterpoise estimated BSSE magnitudes of MP2 is on average double that of the HF level of theory. The shape and magnitude of the *a priori* and *a posteriori* cp-corrected $E2$ corrections is, however, indistinguishable (see Figure A.10; cf. Figure 4.12(b)), confirming the invariance of the energy to the application method of the counterpoise correction scheme in the current model with all non-hydrogen atoms frozen (as stated in Section 4.7).

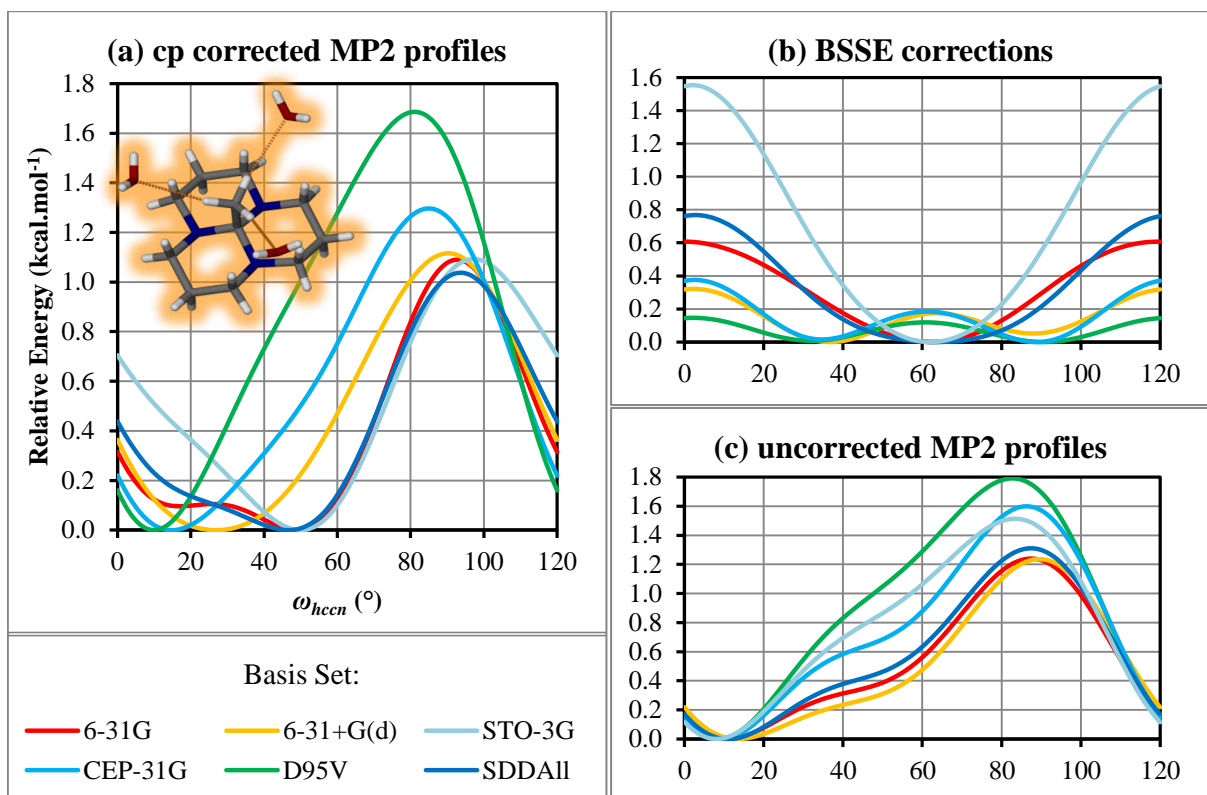


Figure A.9: Comparison of the counterpoise estimated BSSE values (b) to correct the MP2 ω_{hccn} potential energy profiles of (c) to yield those of (a). The cp scheme was applied *a priori* during geometry optimizations of hydrogen atom positions of the model shown as an insert.

Appendix A.2: Addendum to Chapter 4

Several reports in the literature have suggested that the counterpoise scheme overestimates the BSSE at the correlated level.¹ Cook *et al.* presented evidence towards the duality of ghost orbitals: they improve the system's basis set, but unphysically increase the virtual space.² For SCF-level calculations, *i.e.* at the HF and DFT levels of theory, the second influence has no effect, but it complicates the application of the counterpoise scheme at the correlated level. Wieczorek *et al.*, however, showed that the counterpoise scheme do not overestimate the BSSE if it is applied *a priori*, but the so obtained BSSE is generally larger and slower to converge than for SCF-level calculations.³ They looked at water clusters up to tetrameric size using basis sets of cc-PVDZ quality or better. For the system under investigation in this work, the BSSE obtained for MP2 by counterpoise renders the MP2 profiles incomparable to those of the (uncorrected) CCSD/basis set//B97D/basis set level of theory results, Figure 4.5.

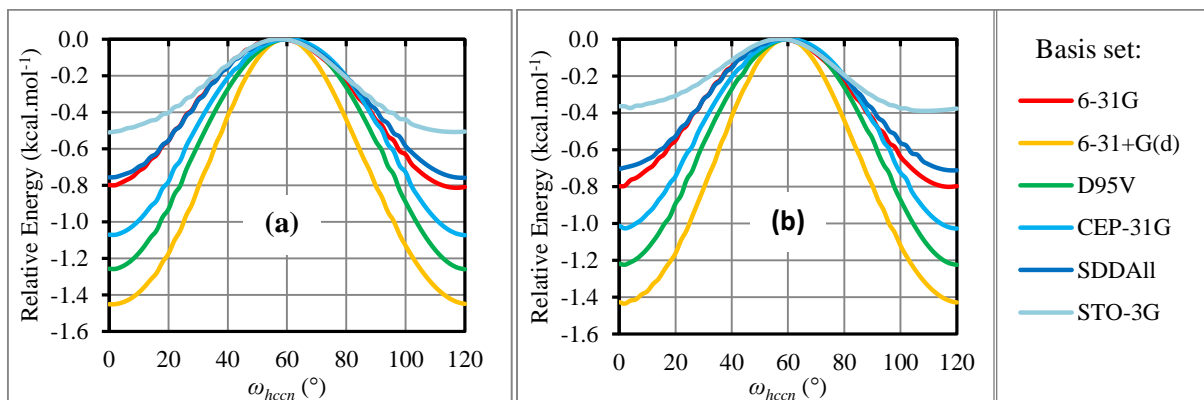


Figure A.10: Comparison of the second-order correlation correction of MP2 theory in the absence (a) and presence (b) of *a priori* counterpoise correction.

References

1. Simon, S.; Duran, M.; Dannenberg, J.J., *J. Phys. Chem. A* **1999**, *103*, 1640.
2. Cook, D.B.; Sordo, J.A.; Sordo, T.L., *Int. J. Quantum Chem.* **1993**, *48*, 375.
3. Wieczorek, R.; Haskamp, L.; Dannenberg, J.J., *J. Phys. Chem. A* **2004**, *108*, 6713.

Appendix A.2: Addendum to Chapter 4

A.2.7 B97D in conjunction with GD2, GD3 and GD3BJ potential energy profiles

In Figure A.11 a comparison of the counterpoise corrected potential energy profile for the ω_{hccn} dihedral angle of the minimal model (stepped between 0° and 120° in 2° increments) is made for the B97D functional in conjunction with the GD2 (default), GD3 and GD3BJ (the B97D3 functional of Gaussian 09) dispersion correction schemes using various basis sets.

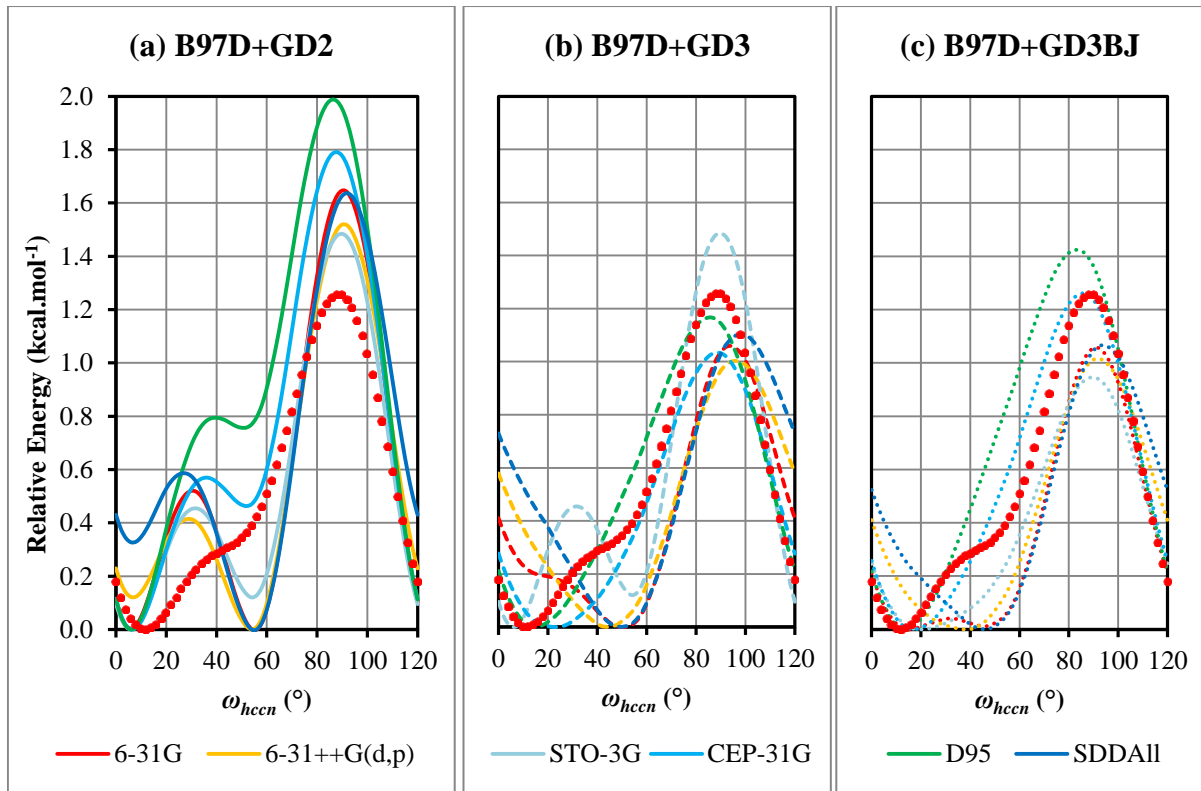


Figure A.11: Comparison of the B97D potential energy profiles for the ω_{hccn} dihedral angle of the minimal model augmented with the GD2 (—), GD3 (---) and GD3BJ (...) dispersion correction schemes for various basis sets. The CCSD/SDDAll//B97D/SDDAll profile (●) is shown for comparison.

A comparison to the not-counterpoise corrected potential energy profiles of the minimal model with the B97D+GD2 method in Figure A.4 (depicted by ---) reveals that the local minimum at $\omega_{hccn} \approx 55^\circ$ is enhanced on the *a priori* counterpoise corrected potential energy surface. This is especially true for the SDDAll basis set (—) where the nearly staggered conformation is predicted to be most stable in Figure A.11(a) as opposed to the nearly-eclipsed conformer in Figure A.4 (---). In Figure A.12 the deconvoluted energy contributions are compared for each basis set. The dispersion corrected energy profiles (*raw+disp*, depicted by colored --- relative to the uncorrected potential energy (*raw*) minimum) correlate to those of Figure A.4. It can be seen that the cp-estimated BSSE of the SDDAll basis set ($0.51 \text{ kcal.mol}^{-1}$ at $\omega_{hccn} \approx 0^\circ$) is about twice that of the 6-31G ($0.33 \text{ kcal.mol}^{-1}$) and D95 ($0.21 \text{ kcal.mol}^{-1}$) basis sets, while the STO-3G ($1.59 \text{ kcal.mol}^{-1}$) cp-estimated BSSE is three times larger again. The GD2 dispersion-correction energy profile (---) is basis set independent, while the uncorrected potential energy profile (*raw*, —, colored) is basis set dependent: the 6-31G, SDDAll and 6-31++G(d,p) basis sets predict the nearly staggered conformation to be most stable, while the *raw* STO-3G, D95 and CEP-31G profiles have the nearly eclipsed conformation most stable.

Appendix A.2: Addendum to Chapter 4

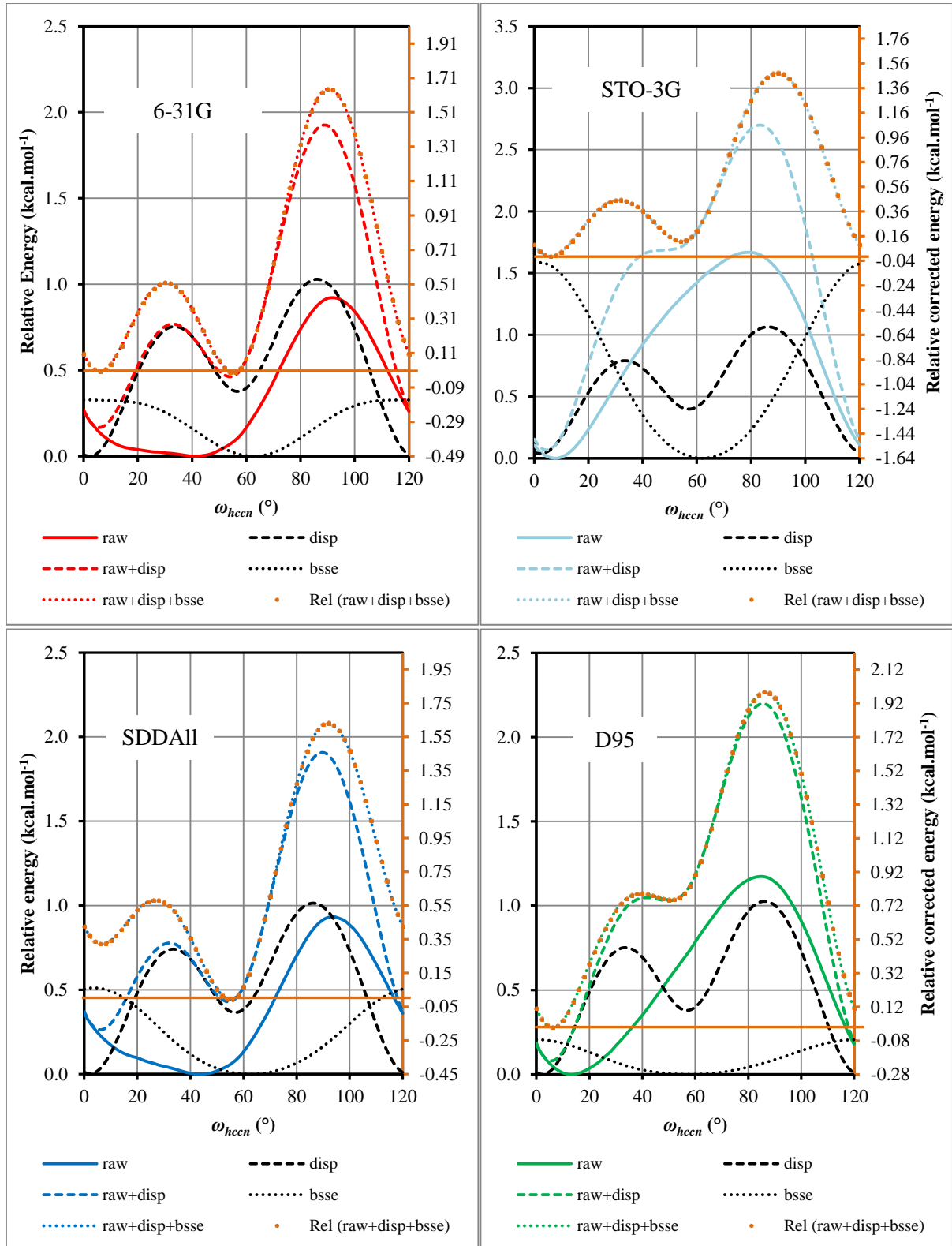
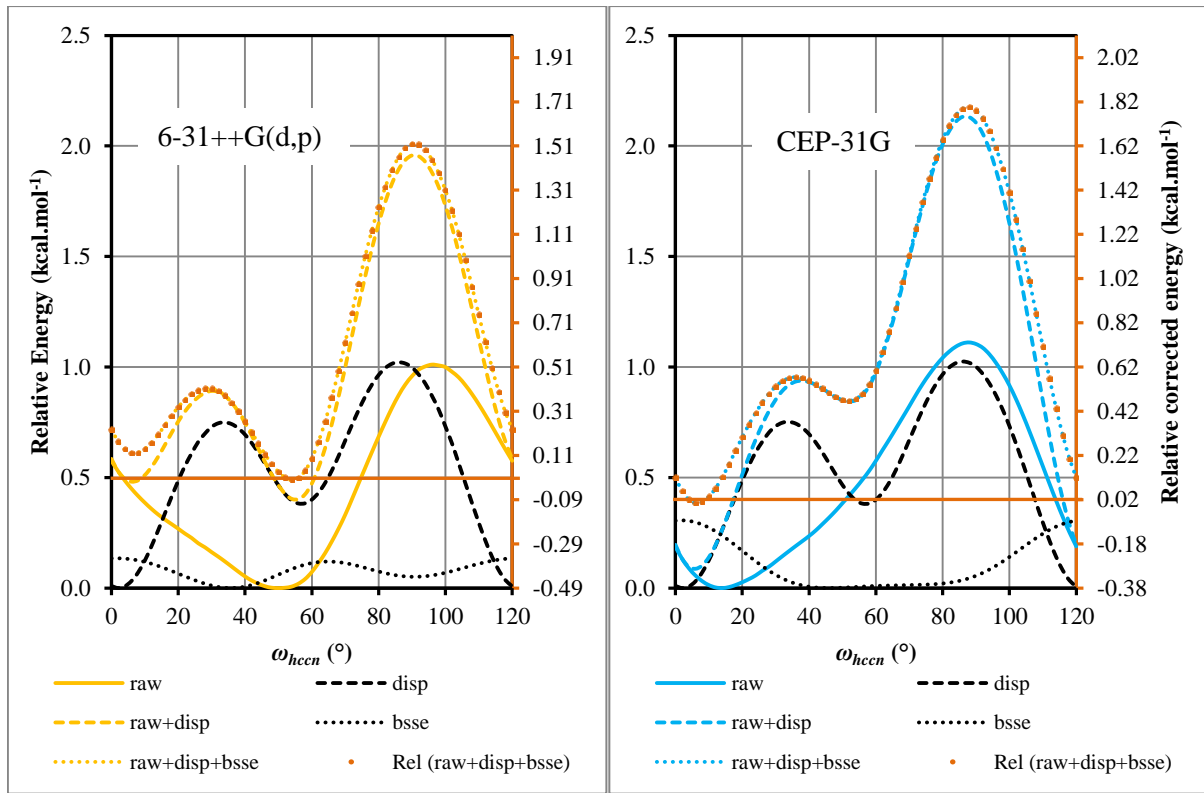


Figure A.12: Comparison of the deconvoluted energy contributions to the counterpoise corrected B97D plus GD2 potential energy profiles for the ω_{hccn} dihedral angle of the minimal model. Here *raw* refers to the uncorrected potential energy, *disp* refers to the dispersion-correction energy and *bsse* to the cp estimate of the BSSE. In each case the relative counterpoise and dispersion corrected potential energy is shown on the right-hand ordinate, overlaying the sum of energy contributions plot: ..., colored according to basis set.

Appendix A.2: Addendum to Chapter 4

**Figure A.12** continued.

The number of basis functions for the minimal model (138 electrons; 104 valence) is 207, 485, 112, and 224 for the 6-31G, 6-31++G(d,p), STO-3G and D95 all-electron basis sets and 190 and 199 for the CEP-31G and SDDAll ECP basis sets, respectively. It can be seen that the largest basis set, that of 6-31++G(d,p) shows the smallest BSSE with a unique profile in that its minimum at $\omega_{hccn} = 35^{\circ}$ is offset from the minimum of the smaller basis sets rather than 62° . Also see Figure 7.1 for the B97D/TZVP (default + GD2) results that shows a cp-estimated BSSE profile similar to that of 6-31++G(d,p). This is expected since it also has 485 basis functions for the minimal model.

Appendix A.3: Addendum to Chapter 5

A.3 Addendum to Chapter 5

A.3.1 Comparison of variable temperature $\mathbf{1}_{\text{apo}}$ crystal structures

An overlay of the variable temperature single-crystal X-ray diffraction structures of $\mathbf{1}_{\text{apo}}$ are shown in Figure A.13.¹ As decided in Section 5.2.2, the orientation of the disordered benzoate wherein a hydrogen bond is formed with the imidazole moiety bonding to the same zinc atom is shown. It is apparent that the internal coordinates of the ligand change only minimally, validating the assumption (of Section 5.2) that it can be treated as a rigid linker in the temperature range investigated.

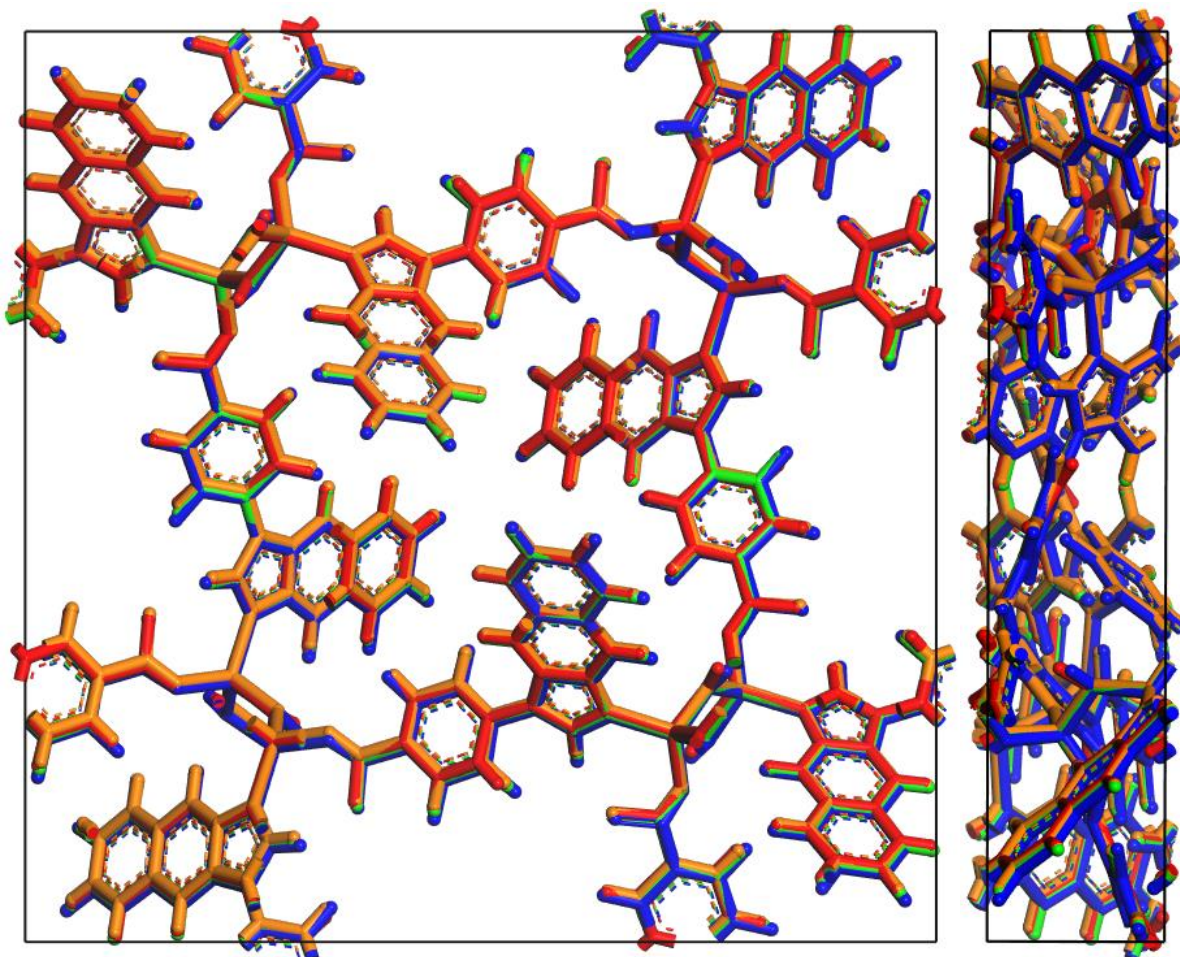


Figure A.13: Overlay of single crystal X-ray diffraction structures of $\mathbf{1}_{\text{apo}}$ determined at 100 K (blue), 190 K (green), 280 K (orange) and 370 K (red) viewed down [001] on the left and [010] on the right.

References

1. Grobler, I.; Smith, V.J.; Bhatt, P.M.; Herbert, S.A.; Barbour, L.J., *J. Am. Chem. Soc.* **2013**, *135*, 6411.

Appendix A.3: Addendum to Chapter 5

A.3.2 Perl Scripts to scan the W_{hccn} dihedral angle in 2·3H₂O

Here follows the Perl scripts used for Molecular Mechanics simulations on 2·3H₂O using the Forcite module of Materials Studio. Section A.3.2.1 presents the script used for a molecular representation with one dihedral angle defined (results shown in Figure 5.8), while the dihedral angle is defined during application of the script given in Section A.3.2.2 to the crystal structure (*cf.* Figure 5.9).

A.3.2.1 Molecular Model

```
#!perl
use strict;
use Getopt::Long;
use MaterialsScript qw(:all);
my $doc = $Documents->New("Tors.xsd");
my $Studytable = $Documents->New("Summary.std");
my $calcsheet = $Studytable->Sheets->Item(0);
$calcsheet->ColumnHeading(0) = "Structure";
$calcsheet->ColumnHeading(1) = "SetAngle";
$calcsheet->ColumnHeading(2) = "Torsion->Angle";
$calcsheet->ColumnHeading(3) = "PotentialEnergy";
$calcsheet->ColumnHeading(4) = "NonBond energy";
$calcsheet->ColumnHeading(5) = "Electrostatic energy";
$calcsheet->ColumnHeading(6) = "vdW energy";
$calcsheet->ColumnHeading(7) = "Restraint energy";
my $Forcite = Modules->Forcite;
my $opt = $Forcite->GeometryOptimization;
$Forcite->ChangeSettings(Settings(CurrentForcefield => "Universal"));
$Forcite->ChangeSettings(["NonPeriodicElectrostaticSummationMethod" => "Atom based"]);
$Forcite->ChangeSettings(["NonPeriodicvdWSummationMethod" => "Atom based"]);
$Forcite->ChangeSettings(Settings(ChargeAssignment => "Charge using QEq"));
$Forcite->ChangeSettings(Settings(AssignForcefieldTypes => "Yes"));
$Forcite->ChangeSettings(Settings(Quality => "Ultra-fine"));
my $torsions = $doc->Torsion;
for (my $angle = 0; $angle < 181; ++$angle) {
    Tools->Symmetry->FindSymmetry->Find($doc);
    $doc->Restraints->Delete();
    $torsion->CreateRestraint("Harmonic"), [HarmonicMinimum => $angle];
    $opt->Run($doc);
    $doc->UpdateViews;
    $doc->Save;
    $calcsheet->Cell($angle,0) = $doc;
    $calcsheet->Cell($angle,1) = $angle;
    $calcsheet->Cell($angle,2) = $doc->Torsion->Angle;
    $calcsheet->Cell($angle,3) = $doc->PotentialEnergy;
    $calcsheet->Cell($angle,4) = $doc->NonBondEnergy;
    $calcsheet->Cell($angle,5) = $doc->ElectrostaticEnergy;
    $calcsheet->Cell($angle,6) = $doc->VanDerWaalsEnergy;
    $calcsheet->Cell($angle,7) = $doc->RestraintEnergy;
    $Studytable->Save;
}
}
```

Appendix A.3: Addendum to Chapter 5

A.3.2.2 Crystallographic representation

```

#!/perl
use strict;
use Getopt::Long;
use MaterialsScript qw(:all);
my $doc = $Documents{"Tors.xsd"};
my $Studytable = $Documents->New("Summary.std");
my $calcsheet = $Studytable->Sheets->Item(0);
    $calcsheet->ColumnHeading(0) = "Structure";
    $calcsheet->ColumnHeading(1) = "SetAngle";
    $calcsheet->ColumnHeading(2) = "Torsion->Angle";
    $calcsheet->ColumnHeading(3) = "PotentialEnergy";
    $calcsheet->ColumnHeading(4) = "NonBond energy";
    $calcsheet->ColumnHeading(5) = "Electrostatic energy";
    $calcsheet->ColumnHeading(6) = "vdW energy";
    $calcsheet->ColumnHeading(7) = "Restraint energy";
my $Forcite = Modules->Forcite;
my $sopt = $Forcite->GeometryOptimization;
    $Forcite->ChangeSettings(Settings(CurrentForcefield => "Universal"));
    $Forcite->ChangeSettings(["3DPeriodicElectrostaticSummationMethod" => "Ewald"]);
    $Forcite->ChangeSettings(["3DPeriodicvdWSummationMethod" => "Ewald"]);
    $Forcite->ChangeSettings(Settings(ChargeAssignment => "Charge using QEeq"));
    $Forcite->ChangeSettings(Settings(AssignForcefieldTypes => "Yes"));
    $Forcite->ChangeSettings(Settings(Quality => "Ultra-fine"));
my $atom1 = $doc->Unitcell->Atoms("N1");
my $atom2 = $doc->Unitcell->Atoms("C1");
my $atom3 = $doc->Unitcell->Atoms("C5");
my $atom4 = $doc->Unitcell->Atoms("H9");
my $torsions = $doc->Createtorsion([$atom1, $atom2, $atom3, $atom4]);
for (my $angle = 0; $angle < 181; ++$angle) {
    Tools->Symmetry->FindSymmetry->Find($doc);
    $doc->UnitCell->Restraints->Delete();
    $torsion->CreateRestraint("Harmonic"), [HarmonicMinimum => $angle];
    $sopt->Run($doc);
    $doc->UpdateViews;
    $doc->Save;
    $calcsheet->Cell($angle,0) = $doc;
    $calcsheet->Cell($angle,1) = $angle;
    $calcsheet->Cell($angle,2) = $torsion->Angle;
    $calcsheet->Cell($angle,3) = $doc->PotentialEnergy;
    $calcsheet->Cell($angle,4) = $doc->NonBondEnergy;
    $calcsheet->Cell($angle,5) = $doc->ElectrostaticEnergy;
    $calcsheet->Cell($angle,6) = $doc->VanDerWaalsEnergy;
    $calcsheet->Cell($angle,7) = $doc->RestraintEnergy;
    $Studytable->Save;
}

```

Appendix A.3: Addendum to Chapter 5

A.3.3 Additional evaluations of mechanistic model

Figure A.14 shows supplementary results to Section 5.5 of variable S stepped in the range 0.0 Å to 0.25 Å in 0.05 Å increments for the effective core potential basis sets LANL2DZ and SDDAll. Geometry optimizations were carried out with the hybrid B3LYP functional in combination with GD2 (—) and GD3 (●), the ωB97XD functional (---) and the M06 functional augmented by GD3 (···). GD2 is not parameterized for the M06 functional while problematic SCF-convergence prohibited evaluation of the model using the pure GGA PBEPBE in Gaussian09.

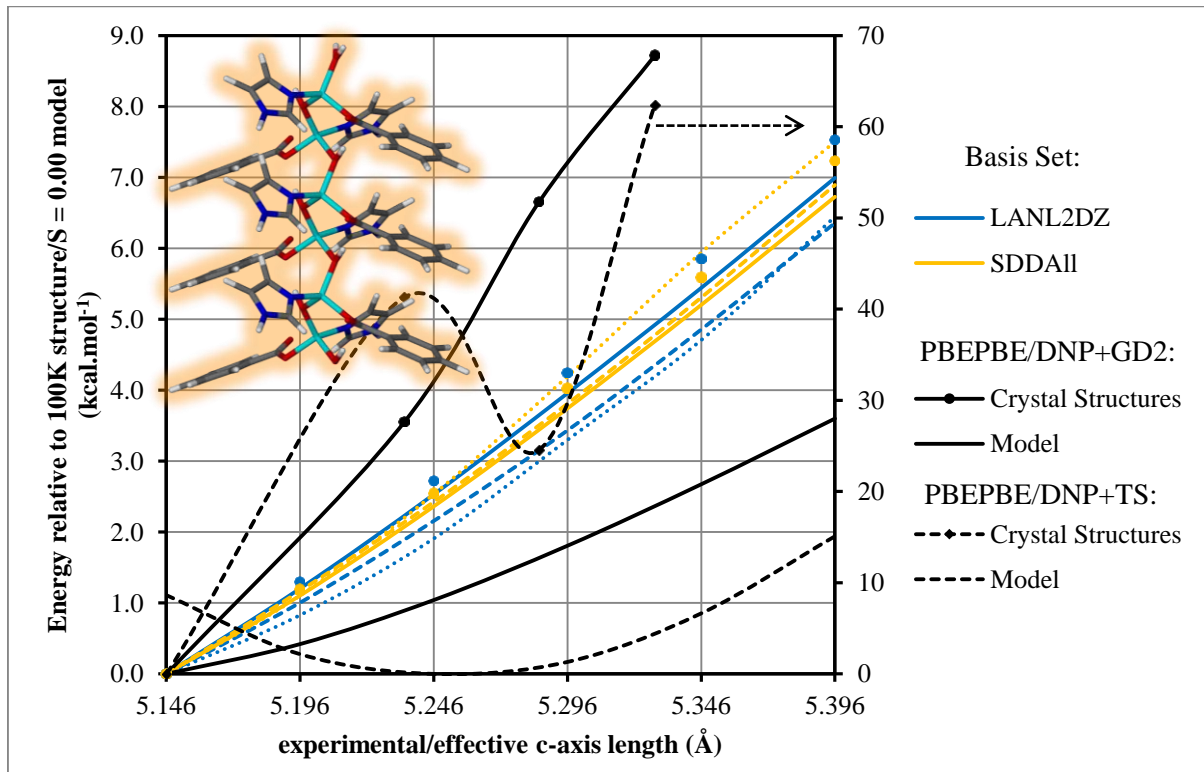


Figure A.14: Comparison of single point energy values for one unit cell of $\mathbf{1}_{\text{apo}}$ (solid lines with ● and ◆ for PBEPBE/DNP in conjunction with GD2 and TS dispersion correction schemes, respectively) and the scaled results obtained for hydrogen atom position optimizations of the mechanistic model (inset): B3LYP + GD2 (—, colored), B3LYP + GD3 (●, colored), ωB97XD (---) and M06 + GD3 (···) employing various basis sets. The right hand ordinate shows the relative energy of the PBEPBE/DNP+TS crystallographic calculations. The variable S was stepped between 0.00 Å and 0.25 Å in 0.05 Å increments, corresponding to the c_{eff} range 5.146 Å to 5.396 Å. Also shown is the profile obtained for the model (— and --- for PBEPBE/DNP in conjunction with GD2 and TS, respectively) in DMol³ using the same settings as the crystallographic single point calculations.

From Figure A.14 it is clear that the results obtained with the TS dispersion correction (discussed in Section 2.6.2) are erratic with no clear trend, making it difficult to draw conclusions. A comparison to Figure 5.13 reveals that the LANL2DZ (—) and SDDAll (—) ECP basis set plots correspond to those of the all-electron 6-31G (—) basis set.

Appendix A.4: Additional fittings to gravimetric sorption data

A.4 Additional fittings to gravimetric sorption data

Different isotherm equations were evaluated with the Sips and Tóth equations yielding statistically superior fitting results for compounds **3** (Figure 6.3) and **4** (Figure 6.4), respectively. In addition, the Langmuir-Freundlich equation was considered:

$$n = \frac{n_{sat} b P^{\frac{1}{c}}}{1 + n_{sat} b P^{\frac{1}{c}}} \quad \text{A.14}$$

that upon rearrangement yields

$$P = \left[\frac{n}{b(n_{sat} - n)} \right]^c \quad \text{A.15}$$

Additional fitting results are shown in Figure A.15 for compound **3** and in Figure A.16 for compound **4**.

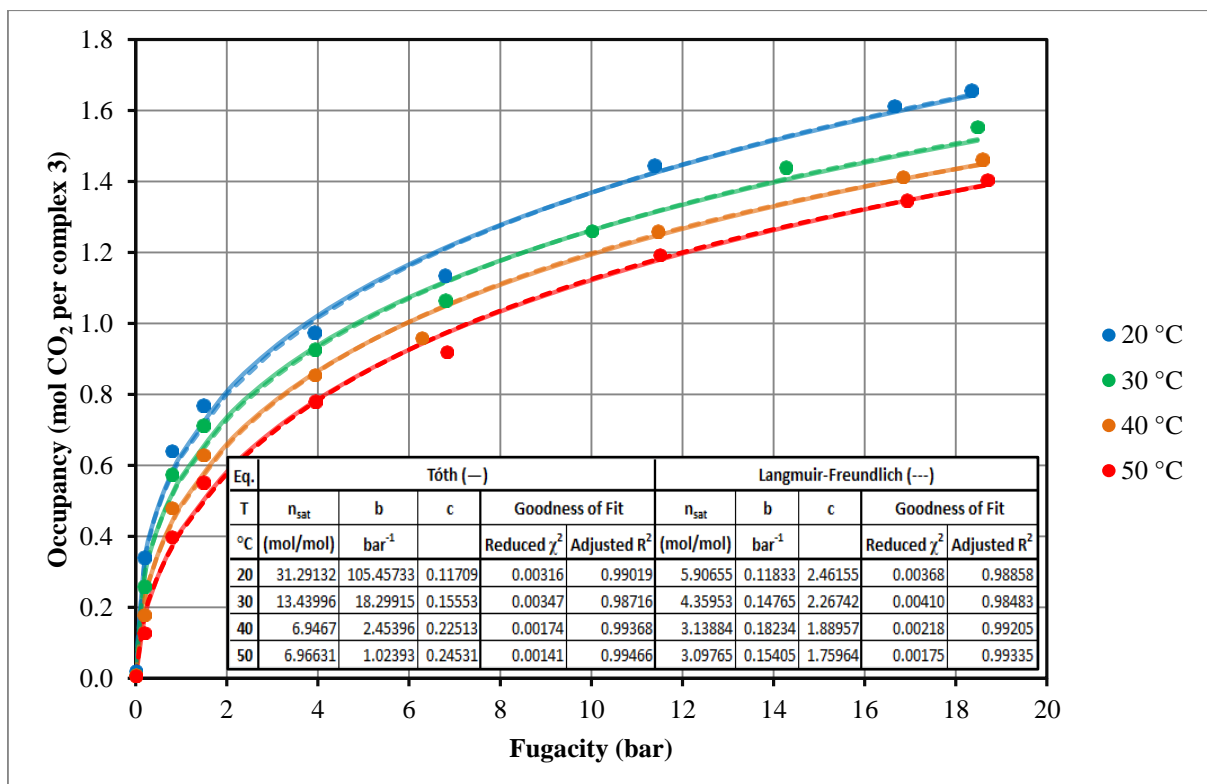


Figure A.15: Isotherm plots of carbon dioxide adsorption on compound **3** (filled circles). Solid and dashed lines represent fits of the Tóth and Langmuir-Freundlich equations, respectively, with $N = 9$ in each case.

Appendix A.4: Additional fittings to gravimetric sorption data

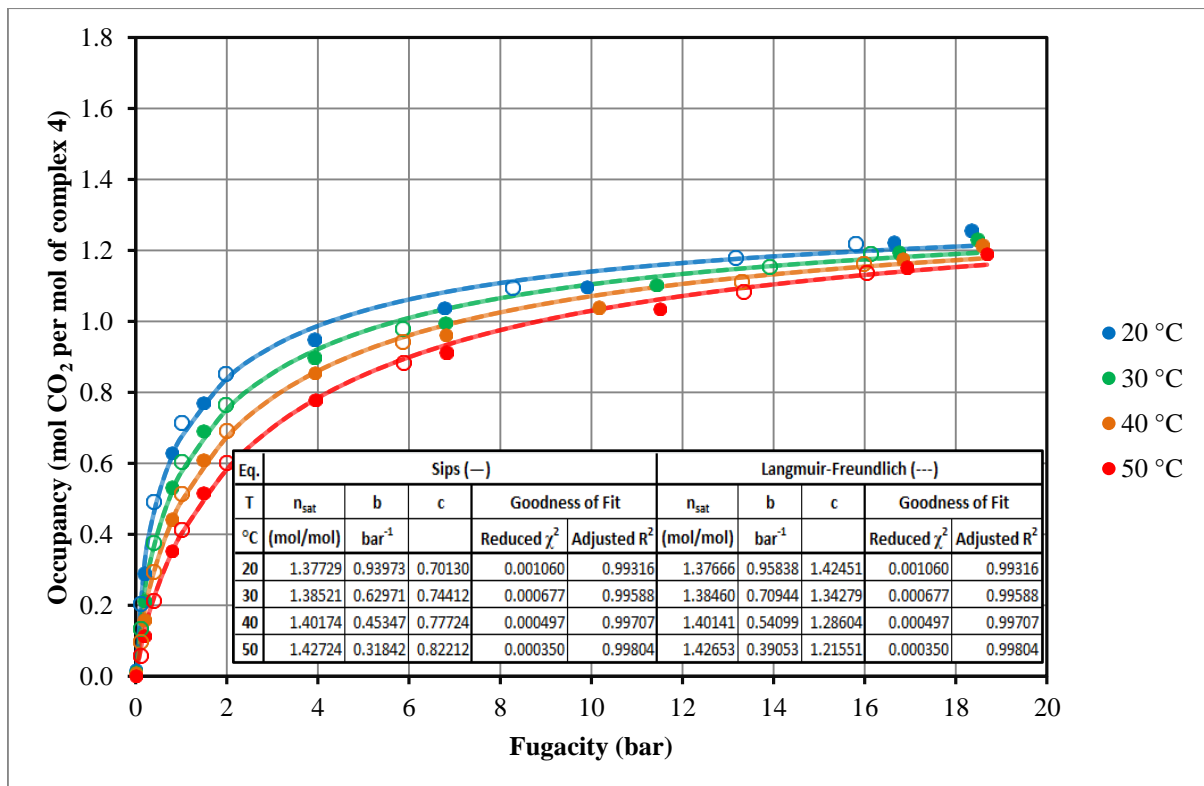


Figure A.16: Least-squares fitting results of the Sips (solid lines) and Langmuir-Freundlich (dashed lines) equations to the carbon dioxide sorption [adsorption (filled circles) and desorption (open circles)] on compound 4 with $N = 16$ in each case.

The occupancy-dependent isosteric heat of CO_2 adsorption profiles obtained through the graphical interpolation method for the isotherm equations considered are compared in Figure A.17. The asymptotic behavior of the Q_{st} profile of compound 3 persisted. Despite their different fundamental origins, the functional forms of the Sips and Langmuir-Freundlich equations yield near identical Q_{st} profiles. The poor fitting of common isotherm equations to the adsorption isotherms of compound 3, especially by the Tóth equation (that gave very large parameters), imply an uncommon CO_2 adsorption mechanism for this compound.

Appendix A.4: Additional fittings to gravimetric sorption data

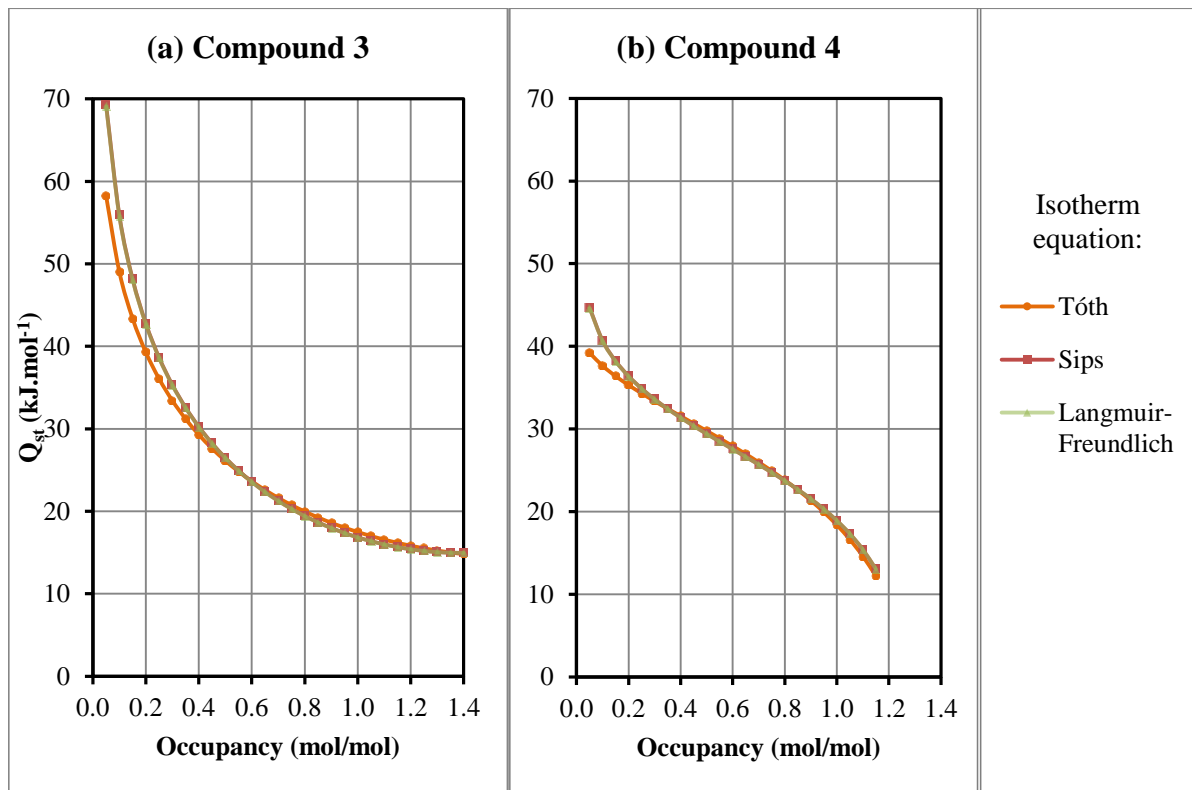


Figure A.17: Isosteric heats of CO_2 sorption on compounds **3** (a) and **4** (b) determined through graphical interpolation employing different isotherm equations.

Appendix B: Contents of Supplementary DVD

Appendix B. Contents of Supplementary DVD

The supplementary DVD contains the output files of results presented in this work. Gaussian 09 and DMol³ output files, *.log and *.outmol, respectively along with *.txt files from Forcite (accessed via Materials Studio) are given descriptive names and ordered according to discussions of this work. Note that result files are presented at their first appearance.

Result-files for Chapter 4

As summarized and named in Figure A.3, various models of **2**·3H₂O were evaluated in this study. In the following headings (and included in the names of folders of the supplementary DVD) the minimal (d), medium (c) and comprehensive (b) models refers to those of molecular formula 2·3H₂O, 2·6H₂O, 2·(H₂O)₆·{H₂O·[(H₂O)₂(NH₃)]}₃, respectively, while the hexameric conformation (a) refers to 2·(H₂O)₆·2.

Section 4.2: CCSD investigation on minimal model

- B97D/6-31G scan
- B97D/CEP-4G scan
- B97D/D95 scan
- B97D/SDDAll scan
- CCSD/6-31G single points
- CCSD/CEP-4G single points
- CCSD/D95 single points
- CCSD/SDDAll single points

Section 4.4: HF evaluation of comprehensive model

These calculations were carried out in three steps: first geometries of water molecules were optimized in the hexameric conformation, followed by optimization of the non-water hydrogen atoms in the comprehensive model; finally, the ω_{hccn} dihedral angle was incremented in partially relaxed scans with water and ammonia molecules frozen. The *.log files of the following basis sets are shown in the *1_OPT in hexamer*, *2_ModelOPT* and *3_Scans* subfolders:

6-31G	CEP-121G
6-311G	CEP-121G(d)
CEP-4G	D95
CEP-4G(d)	D95V
CEP-31G	SDDAll
CEP-31G(d)	

Appendix B: Contents of Supplementary DVD

Then, within each of these folders there is an *augmentation* subfolder containing the *.log files of the following basis sets:

6-31G(d)	6-311G(d)
6-31G(d,p)	6-311G(d,p)
6-31+G	6-311+G
6-311+G(d)	6-311+G(d)
6-311+G(d,p)	6-311+G(d,p)
6-311++G	6-311++G
6-311++G(d)	6-311++G(d)
6-311++G(d,p)	6-311++G(d,p)

Section 4.5: DFT/SDDAll evaluation of comprehensive model

Here *.log files of 13 density functionals in conjunction with the SDDAll basis set are presented in evaluating the ω_{hccn} dihedral angle of the comprehensive model, with the files again separated into the folders *1_OPT in hexamer*, *2_ModelOPT* and *3_Scans*. Some of the relaxed scan calculations were interrupted with the 0° to 180° range spanned in different result files. Here follows a list of the 13 density functionals' result-files with the range of the the ω_{hccn} dihedral angle covered by it included in the name if the relaxed scan was interrupted.

B3LYP, 3 files: 0 to 142; 140 to 160; 158 to 180.
 B3PW91, 2 files: 0 to 72; 70 to 180.
 B97D, 2 files: 0 to 106; 104 to 180.
 CAM-B3LYP, 2 files: 0 to 110; 108 to 180.
 LC- ω PBE, 2 files: 0 to 144; 142 to 180.
 M06, 1 file.
 mPW1LYP, 2 files: 0 to 52; 50 to 180.
 mP1PBE, 1 file.
 mPW2PW91, 2 files: 0 to 22; 22 to 180.
 mPW3PBE, 2 files: 0 to 60; 60 to 180.
 O3LYP, 3 files: 0 to 36; 30 to 176; 174 to 180.
 PBEPBE, 1 file.
 ω B97XD, 1 file.

Section 4.5.1: Integration grid effect on medium model

The result-files from evaluating integration grids of different coarseness's on the M06 functional's ω_{hccn} potential energy profiles are collected here. The subfolder *M06scan_75.302* contains results in the range 0° to 120° in 4° steps using the default pruned (75,302) grid of Gaussian 09, while result-files of the pruned (99,590) grid are given in subfolder *M06scan_99.590*. The expense of the unpruned (250,590) grid caused certain relaxed scans to be interrupted. Here follows a list of the result-files in the *M06scan_250.590* subfolder:

M06/CEP-4G, 1 file.
 M06/CEP-31G, 1 file.
 M06/CEP-121G, 1 file.
 M06/D95V, 2 files: 0 to 44; 40 to 120.
 M06/SDDAll, 2 files: 0 to 40; 36 to 120.

Appendix B: Contents of Supplementary DVD

Section 4.5.2: Dispersion correction in comprehensive model

Employing the same procedure as outlined in Section 4.3, the result-files of ω_{hccn} stepped between 0° and 180° in 2° increments are spread out in the *3_Scans* subfolder as follows:

- B97D/6-31G, 3 files: 0 to 14; 12 to 164; 162 to 200.
- B97D/CEP-31G, 2 files: 0 to 132; 130 to 180.
- ω B97XD/6-31G, 2 files: 0 to 110; 2209 to 180,
- ω B97XD/CEP-31G, 1 file.

Section 4.6: MP2 analysis of minimal model

- MP2/6-31G_Scan 0° to 86°
- MP2/6-31G_Scan 86° to 120°
- MP2/6-31+G(d)_Scan
- MP2/CEP-31G_Scan
- MP2/D95V_Scan
- MP2/SDDAll_Scan
- MP2/STO-3G_Scan

Section 4.7: Counterpoise corrected B97D profiles of medium model

Result-files with the cp scheme employed *a priori* during hydrogen atom geometry optimizations are collected in the subfolder *B97DScans_cpOPT*, while the uncorrected geometry optimizations' *.log files are collected in *B97DScans_noCP*. Application of the cp scheme *a posteriori* as single point energy calculation of uncorrected complex geometries yielded the result-files collected in *B97DScans_SPcp*. Files with the following names can be found in each subfolder:

- 6-31++G(d,p).log
- CEP-4G.log
- D95V.log
- SDDAll.log

Appendix B: Contents of Supplementary DVD

Section 4.8: Dispersion correction in minimal model

The GD2 and GD3 augmented B3LYP and PBEPBE results-files of scans of ω_{hccn} in the range 0° to 120° in 2° increments are collected here:

B3LYP/6-31G/GD2	PBEPBE/6-31G/GD2
B3LYP/6-31G/GD3	PBEPBE /6-31G/GD3
B3LYP/6-31++G(d,p)/GD2	PBEPBE /6-31++G(d,p)/GD2
B3LYP/6-31++G(d,p)/GD3	PBEPBE /6-31++G(d,p)/GD3
B3LYP/CEP-31G/GD2	PBEPBE /CEP-31G/GD2
B3LYP/CEP-31G/GD3	PBEPBE /CEP-31G/GD3
B3LYP/D95/GD2	PBEPBE /D95/GD2
B3LYP/D95/GD3	PBEPBE /D95/GD3
B3LYP/SDDAll/GD2	PBEPBE /SDDAll/GD2
B3LYP/SDDAll/GD3	PBEPBE /SDDAll/GD3
B3LYP/STO-3G/GD2	PBEPBE /STO-3G/GD2
B3LYP/STO-3G/GD3	PBEPBE /STO-3G/GD3

In the *B97D2*, *B97D3* and *B97D3BJ* subfolders are given the B97D+GD2, B97D+GD3 and B97D+GD3BJ result-files, respectively, in addition to those of the ω B97XD functional, for the following basis sets:

- 6-31G.log
- 6-31++G(d,p).log
- CEP-31G.log
- D95.log
- SDDAll.log
- STO-3G.log

Result-files for Chapter 5

Section 5.3.1: Molecular Mechanics investigation of 2·3H₂O

In the *Molecular* subfolder are listed Forcite result-files from a Molecular Mechanics investigation of the minimal model (*vide supra*), while the *Crystallographic* subfolder collect result-files of an evaluation of the crystal structure:

- COMPASS.txt
- Dreiding.txt
- Universal.txt

The Perl script files used to step the ω_{hccn} in the range 0° to 180° by 1° or 0.1° increments for the molecular and crystallographic investigations, respectively, were given in Section A.3.2.

Appendix B: Contents of Supplementary DVD

Section 5.3.2: Molecular and Crystallographic DFT investigation of 2·3H₂O

After an initial geometry optimization in one unit cell of 2·3H₂O with non-hydrogen atoms frozen (result-file: *GeometryOptimization.outmol*), the ω_{hccn} dihedral angle was stepped between 0° to 120° in 5° increments and single-point energy evaluations carried out. The subfolders 00, 05, 10, 15, 20, 25, 30, 35, 40, 45, 50, 55, 60, 65, 70, 75, 80, 85, 90, 95, 100, 105, 110, 115 and 120 contains the DMol³ result-files from the PBEPBE functional alone and in conjunction with the GD2 and TS dispersion correction schemes:

PBEPBE.outmol
 PBEPBE+GD2.outmol
 PBEPBE+TS.outmol

Within the subfolders *Molecular_GD2* (PBEPBE+GD2) and *Molecular_TS* (PBEPBE+TS) are collected the result-files of single-point energy evaluations of the minimal model.

Section 5.4: Molecular Dynamics investigation of 1_{apo}

In this folder are collected the *.txt files containing the input settings for the MD simulation for each set temperature along with a *.csv file summarizing the unit cell parameters as a function of time:

10 K Cell.csv	200 K.txt
10 K.txt	225K Cell.csv
25K Cell.csv	225K.txt
25K.txt	250 K Cell.csv
50 K Cell.csv	250 K.txt
50 K.txt	275K Cell.csv
75K Cell.csv	275K.txt
75K.txt	300 K Cell.csv
100 K Cell.csv	300 K.txt
100 K.txt	325K Cell.csv
125K Cell.csv	325K.txt
125K.txt	350 K Cell.csv
150 K Cell.csv	350 K.txt
150 K.txt	375K Cell.csv
175K Cell.csv	375K.txt
175K.txt	400 K Cell.csv
200 K Cell.csv	400 K.txt

In the subfolder *FinalPointStatus* are given files with information regarding the final 200 ps step of each simulation:

10 K.txt	225K.txt
25K.txt	250 K.txt
50 K.txt	275K.txt
75K.txt	300 K.txt
100 K.txt	325K.txt
125K.txt	350 K.txt
150 K.txt	375K.txt
175K.txt	400 K.txt
200 K.txt	

Appendix B: Contents of Supplementary DVD

Section 5.5: Mechanistic Model and crystallographic **1_{apo}** DFT results

In the directory *PBEPBEplusGD2/CrystalStructures* are given the PBEPBE functional in conjunction with the GD2 dispersion correction DMol³ result-files of geometry optimizations of the crystal structures of **1_{apo}** with fixed unit cell parameters in the primitive cell, along with single point energy evaluations of the redefined *I*⁴ unit cell:

```
100 K_primitive cell GeomOPT.outmol
100 K_conventional cell SP.outmol
190 K_primitive cell GeomOPT.outmol
190 K_conventional cell SP.outmol
280 K_primitive cell GeomOPT.outmol
280 K_conventional cell SP.outmol
370 K_primitive cell GeomOPT.outmol
370 K_conventional cell SP.outmol
```

Result-files of the PBEPBE plus GD2 hydrogen-atom position optimization of the mechanistic model in DMol³ are collected in the directory *PBEPBEplusGD2/Model* labelled according to the value of the *S* variable:

```
S_0_00.outmol
S_0_05.outmol
S_0_10.outmol
S_0_15.outmol
S_0_20.outmol
S_0_25.outmol
```

The similarly labelled Gaussian09 Revision D.01 *.log result-files are collected in the following subfolders

<i>B3LYP_6_31G_GD2</i>	: B3LYP/6-31G + GD2
<i>B3LYP_ccPVDZ_GD2</i>	: B3LYP/cc-PVDZ + GD2
<i>B3LYP_tzvp_GD2</i>	: B3LYP/TZVP + GD2
<i>M06_6_31G_GD3</i>	: M06/6-31G + GD3
<i>M06_ccPVDZ_GD3</i>	: M06/ccPVDZ + GD3
<i>M06_tzvp_GD3</i>	: M06/TZVP + GD3
<i>ωB97XD_6_31G</i>	: ωB97XD/6-31G
<i>ωB97XD_ccPVDZ</i>	: ωB97XD/cc-PVDZ
<i>ωB97XD_tzvp</i>	: ωB97XD/TZVP

Result-files for Chapter 7

Counterpoise corrected B97D/TZVP and PBEPBE/TZVP+GD2 *.log files are collected here.

Appendix B: Contents of Supplementary DVD

Result-files for Appendix A

A.2: Addendum to Chapter 4

Section A.2.3: B97D evaluation of comprehensive model

The ω_{hccn} potential energy profiles of the comprehensive model were obtained through the procedure outlined in Section 4.3. In addition to the 6-31G, CEP-31G (Section 4.5.2) and SDDAll (Section 4.5) basis sets, the *.log result-files of ω_{hccn} stepped between 0° and 180° in 2° increments are spread out in the 3_Scans subfolder as follows:

- 6-31G(d), 3 files: 0-88; 86-152; 150-180.
- 6-31+G, 5 files: 0-46; 44-80; 78-114; 112-170; 168-180;
- 6-31+G(d), 6 files: 0-20; 18-46; 44-64; 62-78; 76-110; 108-200.
- 6-311G, 4 files: 0-112; 110-140; 136-164; 162-180.
- CEP-31G(d), 2 files: 0-26, 102-180.
- CEP-121G, 6 files: 0-38; 36-66; 64-90; 88-136; 134-154; 152-180.
- CEP-121G(d), 2 files: 0-154; 152-180.
- D95, 2 files: 0-116; 114-180.

Section A.2.4: Integration grid effects on energies of minimal model

Here result-files for evaluating the default (75,302) and ultrafine (99,590) Lebedev integration grids are collected:

- B97D default
- M06 default
- PBEPBE default
- ω B97XD default
- B97D ultrafine
- M06 ultrafine
- PBEPBE ultrafine
- ω B97XD ultrafine

Section A.2.6: cp evaluation of minimal model

In the subfolders *HFscans_cpOPT*, *HFscans_noCP* and *MP2scans_cpOPT* are collected the *.log result-files of geometry optimization (non-hydrogen atoms maintained in their crystallographic positions) with and without counterpoise correction at the HF level of theory and with *a priori* cp correction at the MP2 level of theory, respectively:

- 6-31G.log
- 6-31+G(d).log
- CEP-31G.log
- D95V.log
- SDDAll.log
- STO-3G.log

Appendix B: Contents of Supplementary DVD

A.3: Addendum to Chapter 5**Section A.3.3: Mechanistic Model and crystallographic **1_{apo}** DFT results**

In the directory *PBEPBEplusTS/CrystalStructures* are given the PBEPBE/DNP in conjunction with the TS dispersion correction DMol³ result-files of geometry optimizations of the crystal structures of **1_{apo}** with fixed unit cell parameters in the primitive cell, along with subsequent single point energy evaluations of the redefined conventional unit cell:

- 100 K_primitive cell GeomOPT.outmol (3 files)
- 100 K_conventional cell SP.outmol
- 190 K_primitive cell GeomOPT.outmol
- 190 K_conventional cell SP.outmol
- 280 K_primitive cell GeomOPT.outmol (2 files)
- 280 K_conventional cell SP.outmol
- 370 K_primitive cell GeomOPT.outmol
- 370 K_conventional cell SP.outmol

Result-files of the PBEPBE/DNP plus TS geometry optimization of the mechanistic model are collected in the directory *PBEPBEplusTS/Model* labelled according to the value of the stepping variable *S*:

- S_0_00.outmol
- S_0_05.outmol
- S_0_10.outmol
- S_0_15.outmol
- S_0_20.outmol
- S_0_25.outmol

The similarly labelled *.log result-files of DFT geometry optimization with non-hydrogen atom positions frozen are collected in the subfolders according to level of theory as follows:

<i>B3LYP_lanl2dz_GD2</i>	: B3LYP/LANL2DZ + GD2
<i>B3LYP_sddall_GD2</i>	: B3LYP/SDDAll + GD2
<i>M06_lanl2dz_GD3</i>	: M06/LANL2DZ + GD3
<i>M06_sddall_GD3</i>	: M06/SDDAll + GD3
<i>ωB97XD_6_31G</i>	: ωB97XD/6-31G
<i>ωB97XD_lanl2dz</i>	: ωB97XD/LANL2DZ
<i>ωB97XD_sddall</i>	: ωB97XD/SDDAll

-----END-----